Application of N-doped TiO$_2$/Bi$_2$O$_3$/rGO nanocomposites as a photoanode material in dye-sensitized solar cells

UNIVERSITY OF KWAZULU-NATAL

INYUVESI YAKWAZULU-NATALI

Submitted in fulfillment of the academic requirements for the degree of Master of Science in Chemistry to the School of Chemistry and Physics, University of KwaZulu-Natal, Durban

by

Simphiwe Ntokozo Ngwenya

August 2021

Abstract

A series of nitrogen-doped titanium dioxide/bismuth oxide/reduced graphene oxide (NTiBi/rGO) nanocomposites were prepared *via* a hydrothermal method, in which the amount of reduced graphene oxide (rGO) added to nitrogen-doped titanium dioxide bismuth oxide (NTiBi) nanoparticles was varied. These nanocomposites were characterised for their physicochemical properties by using a wide range of techniques, including scanning electron microscopy (SEM), transmission electron microscopy (TEM), high-resolution transmission electron microscopy (HRTEM), energy dispersive X-ray spectroscopy (EDX), powder X-ray diffraction (P-XRD), ultraviolet-visible (UV-Vis) spectroscopy, photoluminescence (PL) spectroscopy, Raman spectroscopy, inductively coupled plasma-optical emission spectroscopy (ICP-OES), Brunauer-Emmett-Teller (BET) surface area analysis, thermogravimetric analysis (TGA), and elemental analysis. The nanocomposites were then used to fabricate photoanodes *via* a Doctor Blade method, and assembled into a dye-sensitized solar cell (DSSC) with an aluminium coated counter electrode and polyvinyl acetate (PVAc) doped with lithium iodide (LiI) as the gel electrolyte. The DSSC devices prepared were tested under simulated solar radiation and dark conditions to investigate their photovoltaic performance.

These NTiBi/rGO nanocomposites demonstrated good charge carrier separation and electron transfer as determined by PL analyses. Particularly good charge carrier separation was observed in the NTiBi/rGO 10 wt.% nanocomposite prepared. It was found that an excess amount of rGO induced poor charge carrier separation. Also, all the nanocomposites synthesised showed an extended light absorption. The incorporation of rGO caused the enhancement of charge carrier separation in the NTiBi nanoparticles. The incorporation of rGO into the NTiBi nanocomposites also produced a significant increase in the surface area up to 116.39 m^2 g^{-1}, and good thermal stability up to 735 °C. The NTiBi/rGO-based DSSCs prepared were found to have power conversion efficiencies (PCEs) of 4.93 - 7.20%, which were significantly greater than 4.26% for the pristine NTiBi-based DSSC. The NTiBi/rGO 10 wt.% nanocomposite-based DSSC demonstrated the highest PCE of 7.20%. When the amount of rGO was increased, as in the case of the NTiBi/rGO 15 wt.%-based DSSC, the resulting PCE was negatively affected. This is ascribed to the fact that rGO can absorb more incoming light and act as a recombination centre. On the other hand, the measurements carried out under dark conditions, where no sunlight was available, demonstrated that these devices might

operate in cold weather upon a high loading of rGO into the photoanodes. Thus, this NTiBi/rGO nanocomposite material has immense potential for designing and preparing highly efficient photoanodes for DSSCs.

Preface

The experimental work discussed in this dissertation was carried out in the School of Chemistry and Physics, University of KwaZulu-Natal, Westville Campus, from May 2018 to May 2021 under the supervision of Prof. V.O. Nyamori and Prof. B.S. Martincigh.

The studies represent original work by the author and have not been submitted in any form for any degree or diploma to any tertiary institution. Where use has been made of the work of others, it is duly acknowledged in the text.
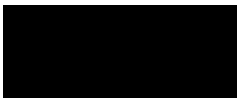
Signed:…………………………………….… Date:.…23 August 2021………………

Declaration 1: Plagiarism

I, **Simphiwe Ntokozo Ngwenya**, declare that

1. The research reported in the thesis, except where otherwise indicated, is my original research.

2. This dissertation has not been submitted for any degree or examination at any other University.

3. This dissertation does not contain other person's data, pictures, graphs or other information unless specifically acknowledged as being sourced from the persons.

4. This dissertation does not contain another person's writing unless specifically acknowledged as being sourced from other researchers. Where other written sources have been quoted, then:

   a. Their words have been re-written but, the general information attributed to them has been referenced.

   b. Where exact words have been used, then their writing has been placed in italics and inside quotation marks and referenced.

5. This dissertation does not contain text, graphics or tables copied and pasted from the internet, unless specifically acknowledged, and the source being detailed in the dissertation and in the references sections.

Signed:… … …………………………......…. Date:…23 August 2021………………………

Declaration 2: Presentations and publications

Presentation

1. **Postgraduate research and innovation symposium (PRIS) 2019**

   Title: Synthesis and characterisation of the physicochemical properties of reduced-graphene oxide-N-TiO_2/Bi_2O_3 nanocomposites
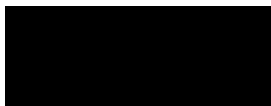
   University of KwaZulu-Natal, Westville Campus, 6-7 September 2019.

Poster

2. **SACI/ChromSA Postgraduate Research Colloquium**

   Title: Synthesis and characterization of the physicochemical properties of N-TiO_2/Bi_2O_3 heterojunction-structured nanomaterials

   Durban University of Technology, Durban Campus, 6 March 2019.

Signed:…… ……………….................…… Date:……23 August 2021…………………

Dedication

This dissertation is dedicated to my family and friends with modesty and deep gratitude. For not only did I make it, but, we have made it. On the road to success, there is always we, not I. There is always another person standing behind me, maybe not coming in the forefront but behind me, praying for me, showing the support; I will never lose that person, Never!

Acknowledgements

Firstly, I would like to thank God for his everlasting love and grace throughout my life and for the success of this dissertation.

Secondly, I would like to pass my gratitude and appreciation to my supervisors, Prof B.S. Martincigh and Prof. V.O. Nyamori, for their guidance and patience. They have highly supported me throughout this research project as well as during hard times with patience and knowledge, which has shaped me to be a better scientist. The role my supervisors have contributed throughout my master's research will forever be appreciated and acknowledged. I am grateful for their positive critique and for the support they have provided during the group presentations. I was able to learn new things during my interaction with them, and I have gained more knowledge, for which I am grateful.

Thirdly, I would like to thank Dr. Edigar Muchuweni for his support and guidance in this research project. The role he played through my lab work and write-up will forever be highly appreciated and acknowledged. This work would not have been possible without his wisdom. Also, I thank my colleagues and friends for their positive critical comments and for proofreading my dissertation with a keen eye, in particular, Mr. Mthokozisi Mkhize, Mr. Hassan Shoyiga, Mr. Nicholas Rono, Miss Nonjabulo Ngidi, Miss Samantha Ndlovu, and Mrs. Regina Egbele. I would also like to pass many thanks to the Nanotechnology Research Group for supporting and appreciating me throughout.

Fourthly, I would like to thank Thiloshini Naidoo and Unathi Bongoza for allowing me to use the instruments available in the School and their help. Gregory Moodley for his support by supplying me with some of the chemicals needed to carry out the lab work for this study. Also, thank you so much to the technical staff, academic staff and the Microscopy Unit for allowing me to use different microscopy techniques presented in this work.

I would like to thank my parents: Mr. Johnson Ngwenya and Ms. Busisiwe Nhlenyama, for their support, love, life lessons and that they believed in me from day one at university in 2014 until 2021. I am very thankful to my parents for understanding the importance of education.

Table of contents

Chapter 1

Introduction

Chapter 2

Literature review

74

Chapter 3

Synthesis and characterisation of the physicochemical properties of a N-doped TiO$_2$/Bi$_2$O$_3$ heterojunction-structured nanomaterial

108

Chapter 4

Incorporation of reduced graphene oxide into N-doped TiO$_2$/Bi$_2$O$_3$ nanoparticles

Chapter 5

Investigation of N-doped TiO$_2$/Bi$_2$O$_3$/rGO nanocomposite-based photoanodes for dye-sensitized solar cells

Chapter 6

Conclusions, recommendations and future work

List of tables

List of figures

Chapter 1

Chapter 2

Chapter 3

Chapter 5

List of abbreviations and symbols

Full name	Abbreviation/symbol
1 sun	100 mW cm^{-2}
Air mass	AM
Alternating current	AC
Arbitrary unit	a.u.
Brunauer-Emmett-Teller	BET
Conduction band	CB
Dye-sensitized solar cells	DSSCs
Electron volt	eV
Energy bandgap	E_g
Energy dispersive X-ray spectroscopy	EDX
Fill factor	FF
Fourier transform infrared	FTIR
Graphene oxide	GO
Hertz	Hz
Highest unoccupied molecular orbitals	HOMO
High-resolution transmission electron microscopy	HRTEM
Incident photon to current efficiency	IPCE
Indium tin oxide	ITO
Inductively coupled plasma-optical emission spectrometry	ICP-OES
Kilovolt	kV

Lowest unoccupied molecular orbitals	LUMO
Micrometre	μm
Mole percentage	Mol.%
Multiwalled carbon nanotube	MWCNT
Nitrogen-doped titanium dioxide	$N\text{-}TiO_2$
Nitrogen-doped titanium dioxide bismuth oxide	NTiBi
Ohms	Ω
Open-circuit voltage	V_{oc}
Photoluminescence	PL
Polyvinyl acetate	PVA
Powder X-ray diffraction	P-XRD
Power conversion efficiency	PCE
Quantum dot(s)	QDs
Reduced graphene oxide	rGO
Scanning electron microscopy	SEM
short-circuit current density	J_{sc}
Single-walled carbon nanotube	SWCNT
Thermogravimetric analysis	TGA
Three dimensional	3D
Titanium(IV) isopropoxide	TTIP
Valance band	VB
Volts	V
Watts	W

| Wavelength-dispersive X-ray spectroscopy | WDS |
| Weight percentage | Wt.% |

Chapter 1

Introduction

This chapter presents the overview, background, aim, objectives, problem statement, research approach, significance, limitations, and delimitations of the study adopted to accomplish the main principles of the research project.

1.1. Overview

The energy supply is an essential factor for social and economic development because many production and consumption activities involve energy as a basic input [1]. It plays a pivotal role in controlling the national economic growth and determines many aspects of human activity, including commercial trade, manufacturing, communication, transport, and the delivery of services, among other crucial events [2, 3]. In our modern society, electricity has many uses in our day-to-day life, from domestic to industrial usage, and from essential services to providing comfort to people. Thus, the increase in global energy consumption has plagued many countries with energy shortages due to the exhaustion of limited non-renewable energy sources used to generate electricity [4, 5]. Interestingly, many countries have already started to focus on alternative-clean electric energy generation technologies that may help to power the future [6, 7].

Renewable energy sources are energy sources that cannot be exhausted after use, such as, wind power, hydropower, biomass, geothermal and solar energy. Non-renewable energy sources can be exhausted, such as coal, oil, natural gases, and nuclear [8]. The world is highly dependent on coal-burning for electricity generation, while renewables contribute less [9, 10]. Hence, renewable energy is becoming an attractive and viable option [3, 11]. In addition, renewable energy is the most attractive investment due to the abundant natural resources from the sun and wind [12]. Therefore, the utilization of renewable energy sources can promote economic growth and improved environmental quality.

Dye-sensitized solar cells (DSSCs) offer a possible solution for electricity generation as a renewable power generation system. DSSCs are one of the most affordable devices in available solar cell technologies. However, each component of a DSSC heavily determines its cost and efficiency. In this present work, with the aim to meet the energy demand, the photoanode of a DSSC was revaluated with cost-effective, nontoxic, and highly-efficient graphene-based nanocomposites to improve the overall efficiencies of DSSCs further.

1.2. Background of the study

The study of carbon-nanostructures is extremely broad because of their unmatched properties and energy-related applications [13]. Well-known carbon forms are diamond and graphite. Numerous more allotropes and forms of carbon have been discovered and extensively researched. For instance, ball shapes, buckminsterfullerene, carbon nanotubes, and graphene, among others (see **Figure 1.1**).

(a) (0D) Fullerence   (b) (1D) SWCNT   (c) (1D) MWCNT

(d) (3D) Diamond

(e) (3D) Graphite
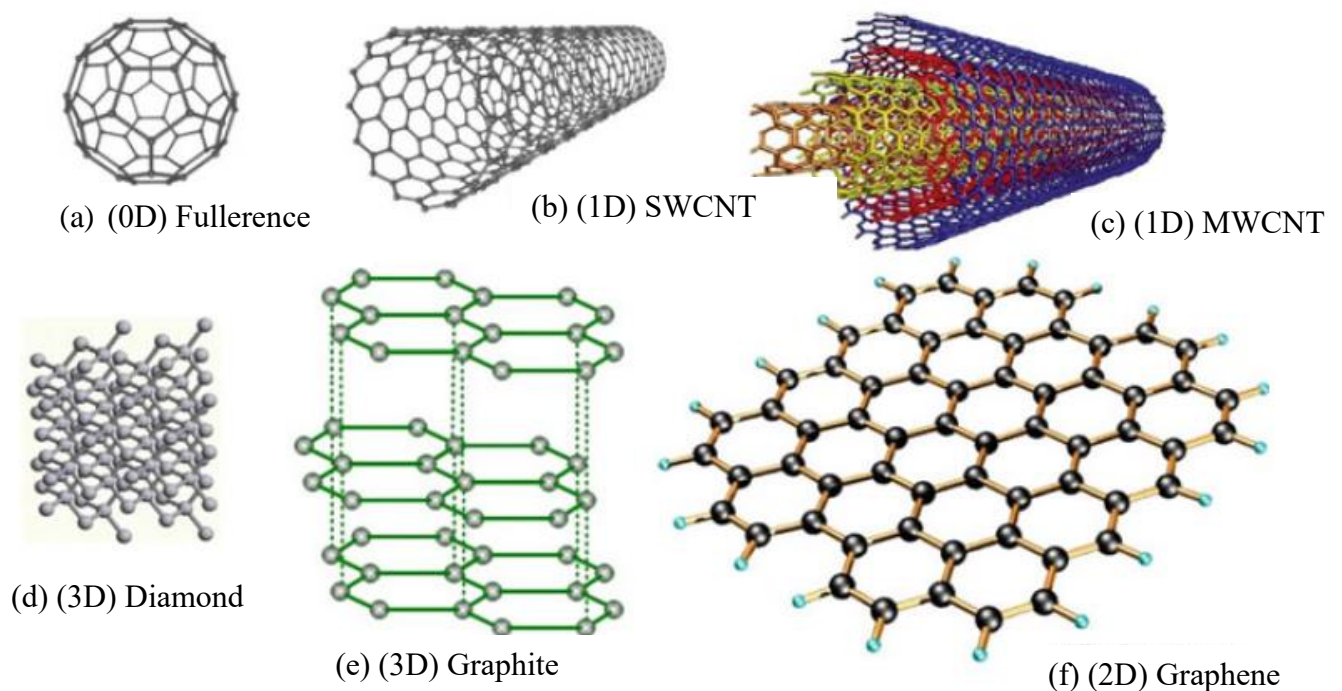
(f) (2D) Graphene

Figure 1.1: The various allotropes of carbon; (a) (0D) fullerene, (b) (1D) SWCNT, (c) (3D) diamond, (e) (3D) graphite and (f) (2D) graphene

Among these various allotropes of carbon materials, graphene has demonstrated great potential in many energy application fields due to its fascinating properties [14, 15]. Graphene can be considered a parent form for many carbon structures, like carbon nanotubes and fullerenes. The discovery of graphene has provided an immense boost and new dimension to materials research and nanotechnology. The multidisciplinary characteristics of graphene have a wide range of applications, such as in aerospace, building materials, mobile devices, solar energy devices, and many others [16]. Since 2004, graphene discovery is considered one of the most

wonderful achievements and has created a new and very promising scientific research area [17]. Graphene has excellent properties, such as electron transport, high optical transparency, flexible and environmental stability properties [18]. In addition, it is a cheaper material and has promising application in solar cells due to its excellent electron-transport properties and large surface area [19]. Several reviews on the basic research, efficient applications of graphene and graphene-based nanostructures have been reported [20]. For instance, Muchuweni et al. have reported an excellent review on the recent advancements of graphene-based materials for DSSCs [21]. Also, Alavi et al. reported the effects of graphene in DSSCs based on nitrogen-doped TiO_2 composites [22]. Reduced graphene oxide (rGO) modified-TiO_2 semiconductor materials for DSSCs have been reported [23]. Hence, these reports signify a promising strategy for effectively harvesting solar energy and converting it into electricity by means of graphene-based functional devices. Therefore, the present work proposed a promising approach to fabricate DSSCs with nitrogen-doped titanium dioxide/bismuth oxide/reduced graphene oxide (N-TiO_2/Bi_2O_3/rGO)-based high-efficiency photoanodes.

1.3. Problem statement

The problems that led to the creation and development of this study are:

I.   The increased global energy consumption has plagued many countries with energy shortages due to the exhaustion of the limited non-renewable energy sources used to generate electricity.

II. The increased rates of global warming, ozone depletion, and air pollution around the world resulted from the utilization of non-renewable energy resources.

III. The usage of high-cost devices to convert energy from sunlight into electricity.

IV. The TiO_2 semiconductor material of DSSCs has a major drawback of a high electron-hole recombination rate, which lowers the efficiency of the DSSC devices.

1.4. Aim and objectives

The main aim of this study was to synthesise and characterise N-TiO_2/Bi_2O_3/rGO nanocomposites, and investigate their photovoltaic performances as a photoanode material for DSSCs.

The following principal objectives achieved the aim of this study:

I. Synthesis and characterisation of N-doped TiO_2 *via* a coupled sol-gel and calcination treatment method. In these syntheses, the amount of urea was varied in titanium isopropoxide (TTIP) to achieve different nitrogen-doping amounts in TiO_2.

II. Synthesis and characterisation of nitrogen-doped titanium dioxide/bismuth oxide (N-TiO_2/Bi_2O_3) *via* a hydrothermal method, by varying the amounts of Bi_2O_3 added to the N-TiO_2 material with the optimal ratio in order to determine the best coupling ratio for both metal oxides.

III. Synthesis and characterisation of graphene oxide (GO) *via* Tour's method.

IV. Reduction of GO *via* a microwave-assisted method with ethanol as the reducing agent.

V. Varying the amount of rGO incorporated into the best ratio for N-TiO_2/Bi_2O_3 obtained in this work *via* a hydrothermal method.

VI. Evaluation of the photovoltaic performance of the fabricated DSSC based on a N-TiO_2/Bi_2O_3/rGO photoanode.

1.5. Research questions

In conducting this research, it was hoped to be able to answer a number of research questions as follows:

I. What is the optimal ratio for nitrogen-doping of TiO_2 that offers a good charge carrier separation?

II. What is the optimal ratio of the coupled N-doped TiO_2 with Bi_2O_3 to form a N-TiO_2/Bi_2O_3 composite that exhibits reduced charge carrier recombination?

III. What is the optimal ratio of rGO that should be incorporated into N-TiO_2/Bi_2O_3 that promotes a good occurrence of charge carrier separation for DSSC application purposes?

IV. Will the N-TiO_2/Bi_2O_3/rGO nanocomposite exhibit a better power conversion efficiency (PCE) when used as photoanode material in DSSCs?

1.6. Research approach

All the synthesis techniques that were used in this study were from standard synthetic chemistry. Syntheses were carried out in small batches and then scaled-up. A series of (10, 20, and 30 mol.%) N-doped TiO_2 materials were initially prepared *via* a combined sol-gel and calcination treatment. This was done by using titanium(IV) isopropoxide (TTIP) as the precursor of TiO_2, and urea as a nitrogen source. In these syntheses, urea was varied in TTIP to achieve different nitrogen-doping amounts in TiO_2. The materials obtained were evaluated for their light absorption and photogenerated charge carrier separation. The material that offered the best charge carrier separation was chosen to be further coupled with Bi_2O_3. The N-TiO_2/Bi_2O_3 nanocomposites were prepared *via* a hydrothermal method, by varying the Bi_2O_3 amounts. The materials obtained were washed with ethanol and double-distilled water, and then dried in the oven overnight at 50 °C. Overall, the materials prepared were denoted as NTiBi x%, where x% refers to the Bi_2O_3 to N-TiO_2 mass ratios such as 1, 3, and 5 wt.%. The NTiBi materials obtained were also evaluated for their charge carrier separation, and the one that exhibited the least charge carrier recombination was selected for incorporation with reduced-graphene oxide.

The modified graphene sheets were prepared by exfoliation of GO, and the highest quality of graphene sheets was controlled by the microwave-assisted synthesis technique employed. According to the experimental procedure, the oxidation-reduction method was proclaimed as an efficient and cheaper method to prepare exfoliated graphene sheets from graphite powder. Tour's method was employed to initial chemically convert graphite into GO, which was further reduced *via* microwave-assisted synthesis with ethanol as the reducing agent. Fourier transform infrared (FTIR) spectroscopy was used to rapidly monitor the synthesis of rGO, whereby the formation of GO as an intermediate was observed by the appearance of oxygenated functionalities such as hydroxyl, carboxyl, and epoxy peaks in the spectrum. The formation of rGO was indicated by a tremendous decrease or even disappearance of the oxygenated functionality peaks in the FTIR spectrum. The rGO obtained was introduced into the best optimal ratio of NTiBi nanoparticles prepared in this work. In this synthesis, rGO was varied into NTiBi to prepare samples containing different amounts of rGO. This included NTiBi/rGO (3, 5, 10, and 15 wt.%) nanocomposites. These NTiBi/rGO (3, 5, 10, and 15 wt.%) nanocomposites were then used to prepare photoanodes *via* the Doctor Blade method, and employed with an aluminium counter electrode to fabricate the complete DSSC.

A variety of characterisation techniques were used to elucidate the chemical structure of the NTiBi/rGO nanocomposites prepared. Standard spectroscopic techniques including FTIR, Raman spectroscopy, UV-Vis, and photoluminescence, and ICP-OES, and elemental analysis, XRD, SEM, TEM, HRTEM, EDX, TGA, and BET were used. The photovoltaic performance of the DSSC devices fabricated with photoanodes based on the NTiBi/rGO nanocomposites was evaluated with a solar simulator.

1.7. Significance of the study

The significance of this study was to find a graphene-based nanomaterial that can be developed into a photovoltaic semiconductor material for DSSCs. Hence, systematic synthesis and characterisation of the NTiBi/rGO nanocomposites is essential in discovering and developing cheaper and highly-efficient photovoltaic semiconductor materials for DSSCs. The conclusion cannot be more reliable than the data set they rely on. The results of this present work have a significant potential impact on socio-economic research in the world. Also, this research contributes to affordable and clean energy technology since it involves the use of graphene as a cost-effective and non-toxic material.

1.8. Limitations

The shortcomings, conditions, or influences that cannot be controlled in this study that place restrictions on the methodology and conclusions are outlined as follows:

- It is challenging to identify the type of N-doping in the TiO_2 structure, that is, whether it is interstitial or substitutional; this would be possible with X-ray photoelectron spectroscopy (XPS).
- The evaluation of the presence of both titanium and nitrogen in the nanocomposites with energy dispersive X-ray spectroscopy (EDX) was complex due to the overlapping nature of their peaks in the spectrum obtained. This may be due to the fact that the titanium (L = 0.452) and nitrogen (K = 0.392) energies are very close. Also, since nitrogen is one of the lightest elements it is challenging to detect with EDX, however, this would be possible with wavelength-dispersive X-ray spectroscopy (WDS).
- The evaluation of the photovoltaic performance of the DSSCs with varying rGO a solar simulator was done in an uncontrolled environment since a glove box was not available.

1.9.   Delimitations

The boundaries of this study based on the decisions made to narrow the study to make it more manageable and relevant to what we were trying to achieve are as follows:

- When synthesising N-TiO$_2$, solvents in the reaction mixture were evaporated on a hot plate and the material was dried at 130 ℃ in the oven. This was necessary because decanting the top liquid from the gel formed or centrifuging to separate the suspension would have caused nitrogen-containing compounds to be lost in the gel.
- A solvent-assisted microwave reduction method coupled with prior mild annealing was employed to reduce GO. Prior mild annealing of GO at 300 °C for 1 h was necessary before microwaving to eliminate amorphous carbon, which can be formed during oxidation. However, at this temperature, some of the C=O functionalities in the plane of the sheet may be removed.
- Surfactants were not used to disperse the starting materials of the nanocomposites prior to the synthesis to eliminate any possible interferences.
- A proper dispersion was achieved by ultra-sonication of the starting material mixtures prepared separately and further sonicated after both mixtures were mixed together in the synthesis.
- Binder was not used in the deposition of the nanocomposites onto ITO-coated glass in order to eliminate any possible interferences of the binder in electron transport.
- The anatase phase in TiO$_2$ was retained by nitrogen-doping and Bi$_2$O$_3$ coupling.

1.10.   Structure of the dissertation

This dissertation consists of six chapters, and mainly focused on developing a highly-efficient photoanode for DSSCs based on a graphene material on account of its good charge carrier separation, high electron transportation, high surface area, and good thermal stability. The dissertation starts with Chapter 1 that briefly introduces the study, and ends with Chapter 6 that concludes the overall work presented, together with proposed future topics for study. The content of each chapter is highlighted as follows:

Chapter 1

This chapter briefly presents the overview, background, aim, objectives, problem statement, research approach, limitations, and delimitations that were adopted to accomplish the main principles of the study.

Chapter 2

This chapter briefly introduces the background of the study, and expresses the need for renewable energy resources as an alternative energy source. Subsequently, a detailed literature review on DSSCs and some of their limitations is presented. Current and further approaches for optimizing the efficiency of DSSCs, such as employing N-TiO_2 incorporated with graphene for a photoanode material, are also discussed.

Chapter 3

This chapter presents a brief introduction to titanium dioxide (TiO_2) and, subsequently, details the synthesis and characterisation of the NTiBi nanoparticles. The results of the characterisation are presented and discussed. In the present work, the preparation of the NTiBi was divided into two parts. Firstly, TiO_2 was doped with nitrogen, and secondly, this was followed by coupling of N-TiO_2 with Bi_2O_3.

Chapter 4

This chapter presents a brief introduction on graphene-based materials and, subsequently, discusses the incorporation of rGO into NTiBi nanoparticles to form NTiBi/rGO nanocomposites with the different amounts of rGO. It also includes the characterisation of the materials prepared.

Chapter 5

This chapter briefly introduces the development of photoanodes for dye-sensitized solar cells (DSSCs), and the fabrication of a complete DSSC by making use of a NTiBi/rGO-based photoanode. It also presents the results and discussion of the photovoltaic performances of the fabricated DSSCs.

Chapter 6

This chapter presents a summary of the findings, and an overall conclusion of the study. Recommendations and future work are also discussed.

References

1. T. Zahid, N. Arshed, M. Munir and K. Hameed, *Role of energy consumption preferences on human development: a study of SAARC region*, Economic Change and Restructuring, 2021, **54**, 121-144.

2. Z. Wang, M. M. Asghar, S. A. H. Zaidi, K. Nawaz, B. Wang, W. Zhao and F. Xu, *The dynamic relationship between economic growth and life expectancy: contradictory role of energy consumption and financial development in Pakistan*, Structural Change and Economic Dynamics, 2020, **53**, 257-266.

3. M. Tvaronaviciene, J. Baublys, J. Raudeliuniene and D. Jatautaite, *Chapter 1-Global energy consumption peculiarities and energy sources: role of renewables*, in *Energy transformation towards sustainability*, eds. M. Tvaronaviciene and B. Slusarczyk, Elsevier, Amsterdam, Netherlands, 2020, 1-49.

4. M. Shahbaz, C. Raghutla, K. R. Chittedi, Z. Jiao and X. V. Vo, *The effect of renewable energy consumption on economic growth: evidence from the renewable energy country attractive index*, Energy, 2020, **207**, 118162.

5. J. Meng, X. Hu, P. Chen, D. M. Coffman and M. Han, *The unequal contribution to global energy consumption along the supply chain*, Journal of Environmental Management, 2020, **268**, 110701.

6. I. Batarseh and K. Alluhaybi, *Emerging opportunities in distributed power electronics and battery integration: setting the stage for an energy storage revolution*, IEEE Power Electronics Magazine, 2020, **7**, 22-32.

7. G. Yilan, M. N. Kadirgan and G. A. Ciftcioglu, *Analysis of electricity generation options for sustainable energy decision making: the case of Turkey*, Renewable Energy, 2020, **146**, 519-529.

8. A. Sharif, S. A. Raza, I. Ozturk and S. Afshan, *The dynamic relationship of renewable and nonrenewable energy consumption with carbon emission: a global study with the application of heterogeneous panel estimations*, Renewable Energy, 2019, **133**, 685-691.

9. A. K. Aliyu, B. Modu and C. W. Tan, *A review of renewable energy development in Africa: a focus in South Africa, Egypt and Nigeria*, Renewable and Sustainable Energy Reviews, 2018, **81**, 2502-2518.

10. C. Magazzino, F. V. Bekun, M. U. Etokakpan and G. Uzuner, *Modeling the dynamic nexus among coal consumption, pollutant emissions and real income: empirical*

evidence from South Africa, Environmental Science and Pollution Research, 2020, **27**, 8772-8782.

11.   K. Sun, H. Xiao, S. Liu, S. You, F. Yang, Y. Dong, W. Wang and Y. Liu, *A review of clean electricity policies-from countries to utilities*, Sustainability, 2020, **12**, 7946.

12.   T. Cook and D. Elliott, *Renewable energy in africa: changing support systems*, in *Renewable energy and sustainable buildings: selected papers from the world renewable energy congress wrec 2018*, ed. A. Sayigh, Springer International Publishing, Cham, Switzerland, 2020, 235-244.

13.   C. Ngo, M. A. Fitzgerald, M. J. Dzara, M. B. Strand, D. R. Diercks and S. Pylypenko, *3D atomic understanding of functionalized carbon nanostructures for energy applications*, ACS Applied Nano Materials, 2020, **3**, 1600-1611.

14.   S. K. Tiwari, S. Sahoo, N. Wang and A. Huczko, *Graphene research and their outputs: status and prospect*, Journal of Science: Advanced Materials and Devices, 2020, **5**, 10-29.

15.   M. I. Fadlalla, P. S. Kumar, V. Selvam and S. G. Babu, *Emerging energy and environmental application of graphene and their composites: a review*, Journal of Materials Science, 2020, **55**, 7156-7183.

16.   C. H. A. Tsang, H. Huang, J. Xuan, H. Wang and D. Y. C. Leung, *Graphene materials in green energy applications: recent development and future perspective*, Renewable and Sustainable Energy Reviews, 2020, **120**, 109656.

17.   K. S. Novoselov, A. K. Geim, S. V. Morozov, D. Jiang, M. I. Katsnelson, I. V. Grigorieva, S. V. Dubonos and A. A. Firsov, *Two-dimensional gas of massless Dirac fermions in graphene*, Nature, 2005, **438**, 197.

18.   W. Yu, L. Sisi, Y. Haiyan and L. Jie, *Progress in the functional modification of graphene/graphene oxide: a review*, RSC Advances, 2020, **10**, 15328-15345.

19.   M. Coroş, F. Pogăcean, L. Măgeruşan, C. Socaci and S. Pruneanu, *A brief overview on synthesis and applications of graphene and graphene-based nanomaterials*, Frontiers of Materials Science, 2019, **13**, 23-32.

20.   J. Wang, J. Song, X. Mu and M. Sun, *Optoelectronic and photoelectric properties and applications of graphene-based nanostructures*, Materials Today Physics, 2020, **13**, 100196.

21.   E. Muchuweni, B. S. Martincigh and V. O. Nyamori, *Recent advances in graphene-based materials for dye-sensitized solar cell fabrication*, RSC Advances, 2020, **10**, 44453-44469.

22.   M. Alavi, R. Rahimi, Z. Maleki and M. Hosseini-Kharat, *Improvement of power conversion efficiency of quantum dot-sensitized solar cells by doping of manganese into a ZnS passivation layer and cosensitization of zinc-porphyrin on a modified graphene oxide/nitrogen-doped TiO$_2$ photoanode*, ACS omega, 2020, **5**, 11024-11034.

23.   A. Merazga, J. Al-Zahrani, A. Al-Baradi, B. Omer, A. Badawi and S. Al-Omairy, *Optical band-gap of reduced graphene oxide/TiO$_2$ composite and performance of associated dye-sensitized solar cells*, Materials Science and Engineering: B, 2020, **259**, 114581.

Chapter 2

Literature review

This chapter provides a brief introduction to the background of the study, expressing the need for renewable energy resources as an alternative energy source. Subsequently, it provides a detailed literature review on dye-sensitized solar cells (DSSCs) as an emerging technology of the third generation of solar cells and some of their major limitations. Current and further approaches for optimizing the efficiency of DSSCs, such as employing nitrogen-doped titanium dioxide (N-TiO$_2$) incorporated with graphene for a photoanode material, are also discussed.

2.1. Introduction

The current energy system is mainly dependent on fossil fuels, such as coal, natural gas, and oil, that contribute significantly to global electricity generation [1]. However, these energy sources are non-renewable, and their increased consumption rate, due to the rapid increase in the global energy demand, arising from the human population and economic growth, may eventually lead to their exhaustion [2, 3]. Consequently, the development of renewable energy sources has attracted remarkable research attention in recent years. Particularly, solar energy has emerged as a potential energy source to overcome this challenge due to the ability of the sun to provide energy in the form of heat and radiation, which makes the production of thermoelectric power and electricity possible. Therefore, solar energy is a renewable energy source that plays a significant role in reducing the demand for fossil fuels, eventually minimizes greenhouse gas emissions.

2.2. Solar energy as a source of renewable energy

Solar energy sources operate through the conversion of energy from sunlight into electricity and heat, either directly through photovoltaic (PV) devices or indirectly by using thermoelectric generators [4]. Solar energy provides the largest source of clean energy that is most reliable, readily available, and renewable. Unlike fossil fuels which produce harmful gas emissions, which affect air, water and soil, solar energy produces no pollution. The sun delivers 120,000 terawatts of energy to the earth in an hour [5], and hence, it is an unlimited source of energy that does not strip the landscape or harm the ozone layer. Also, the use of renewable energy

resources lowers the cost of global electrical energy production. Therefore, there is an urgent need to make use of renewable energy resources in global electricity production.

2.3. Photovoltaic cells

Photovoltaics (PV) is a method for the conversion of solar radiation into electrical power by using semiconductors that exhibit the photovoltaic effect. Becquerel, in 1839, was the first to observe the PV effect, through the investigation of the light effect on a silver-coated platinum electrode immersed in an electrolyte [6]. Subsequently, in 1941, Russel Ohl patented the first modern solar cell made of silicon [7]. The earlier photovoltaic cells were made from thin silicon wafers that converted solar energy into electrical power. However, modern photovoltaic technology is governed by the principle of electron-hole creation in each cell consisting of two different layers (p-type and n-type materials) of semiconductor materials, as shown in Figure 2.1. The n-type semiconductor is where the excess electrons are generated, and the p-type material has excess holes. The generated free electrons are attracted towards the positive terminal, whereas generated holes are attracted towards the negative terminal.
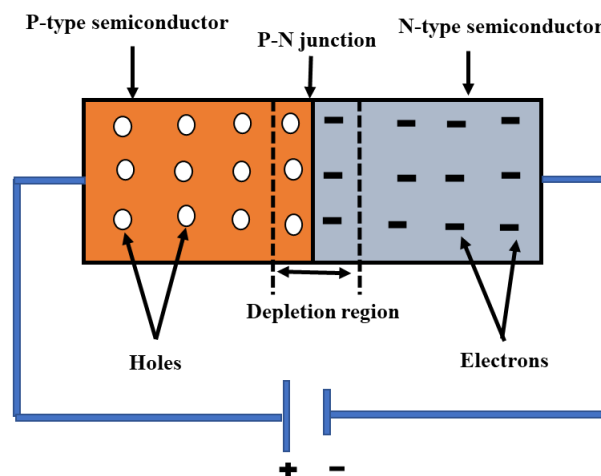
Figure 2.1: The p-n junction of the PV cell

Commonly, there are three types of PV cell technologies that dominate the world market: first-generation, second-generation, and third-generation technologies. The first-generation solar cells are the oldest and most popular used technology due to their high-power efficiencies and are produced from silicon wafers. First-generation solar cells are further categorized into two

subclasses namely; single-crystalline silicon and polycrystalline silicon solar cells. Second-generation solar cells are made from thin films solar cells or amorphous silicon (a-Si), and are more affordable as compared to the first-generation silicon wafer solar cells [8]. Thin-film solar cells are classified as a-Si, cadmium telluride (CdTe), and copper indium gallium di-selenide (CIGS). Third-generation solar cells are the new promising technologies, and well-developed solar cell types, and this includes quantum dots (QD) solar cells, polymer-based solar cells, dye-sensitized solar cells (DSSCs), and perovskite solar cell [9, 10]. Among these, DSSCs are currently the most efficient emerging third-generation solar cells, as shown in Figure 2.2, and represent a cheap and clean technology to harness solar energy efficiently.

Figure 2.2 is a chart reported by the National Renewable Energy Laboratory (NREL) that summarises the highest confirmed efficiencies for research cells for a range of PV technologies from 1976 to the present. Devices included in this chart have efficiencies that are corroborated by independent, recognized test laboratories and are reported on a standardized basis. The measurements for new entries are with respect to a standard test or acceptable reporting condition.
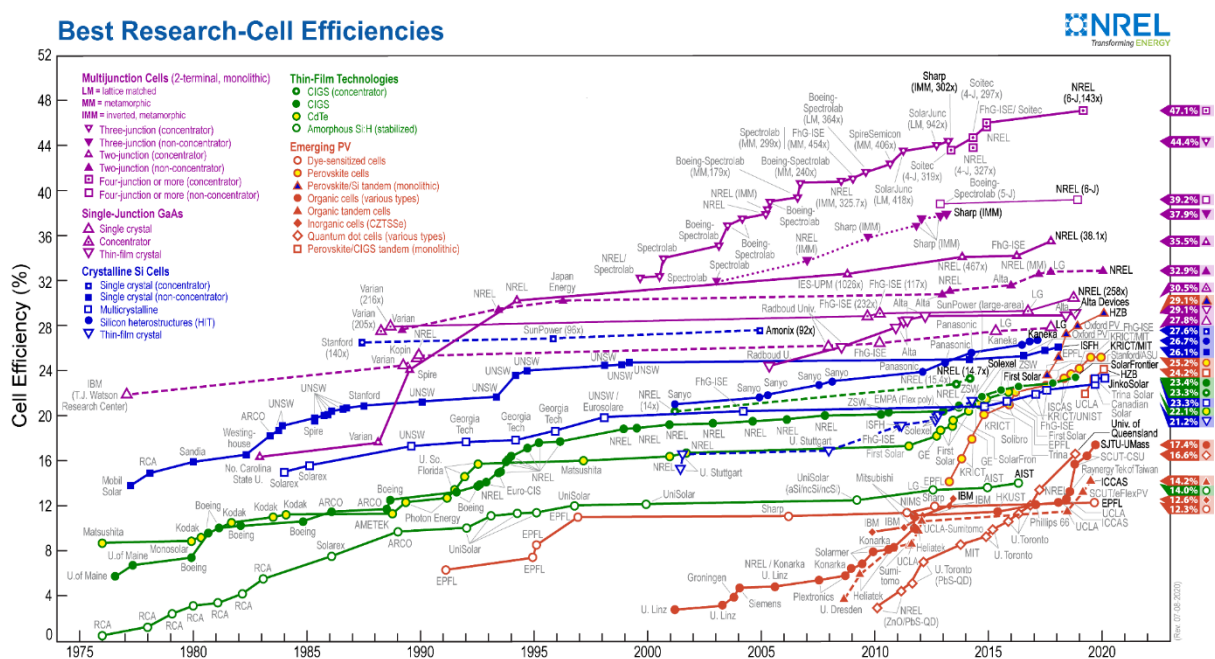
Figure 2.2: Timeline of PV cell energy conversion efficiencies [11]

2.4.   Background

O'Regan and Gratzel, in 1988, were originally the co-inventers of the DSSC and reported the first high efficiency DSSCs in 1991 [12]. A DSSC is also known as a Gratzel cell, whereby it was developed from the discovery that illumination of organic dyes generates electricity at oxide electrodes in electrochemical cells. The effort to understand the primary process in the photosynthesis phenomenon was studied by using chlorophyll extracted from spinach [13]. This study demonstrated electric power generation by using the principles of DSSCs [14]. The structure and working principles of DSSCs are discussed in Section 2.5.

2.5.   Structure of DSSCs and operational principles

DSSC devices consist of four key components, which are: the working electrode (photoanode), sensitizer (dye), redox-mediator (electrolyte), and counter electrode (cathode), as shown in Figure 2.3.
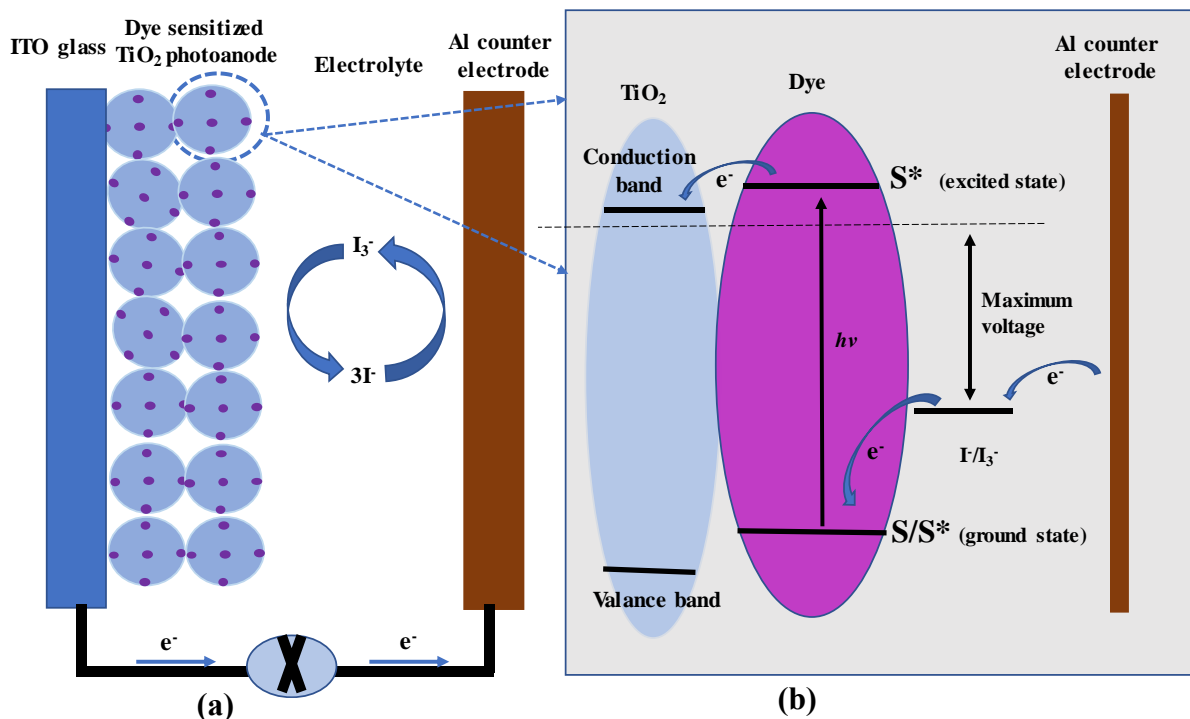
Figure 2.3: (a) Structure and (b) working mechanism of a DSSC device

The working principle of a DSSC is defined by four mechanisms: light absorption, electron injection, transportation of carriers, and collection of current. The following mechanisms are involved in the conversion of the energy of the photons into an electrical current [15]:

- Firstly, a photon of incident light strikes a dye molecule; if the photon of light has enough energy, it excites an electron from the dye molecule.

- Due to the absorption of photon energy, electrons are promoted from the ground state (S) to the excited state (S^*) of the dye. The absorption of most dyes is typically in the visible range of 400-700 nm, which corresponds to a photon energy of about 1.72 eV.

- Excited electrons with a lifetime in the nanosecond range are injected into the conduction band of the nanoporous TiO_2 electrode, which lies below the excited state of the dye. The TiO_2 itself only absorbs a small fraction of solar photons from the UV region [16].

The mechanism of dye excitation and electron injection into TiO_2 are depicted as follows:

Photoexcitation of the dye as seen in Equation (1):

$$S + h\nu \rightarrow S^* \tag{1}$$

Injection of electron as see in Equation (2):

$$S^* \rightarrow S^+ + e^- (TiO_2) \tag{2}$$

Electron passes through the external circuit as seen in Equation (3):

$$(e^-)\, TiO_2 \rightarrow (e^-)\, Al \tag{3}$$

These injected electrons are transported between the TiO_2 nanoparticles, and diffuse towards the transparent conducting oxide (TCO) back contact and flow through the external circuit to the counter electrode.

- The original state of the dye is restored by accepting an electron from I^-, the two I^- are oxidized to I_2 that then reacts with I^- to form the triiodide, I_3^-.

- The oxidized mediator (I_3^-) diffuses towards the counter electrode and is reduced to I^- ion.

The mechanism for the restoration of the original state of the dye molecule and iodide ions (I^-) are depicted as follows:

Regeneration of dye as seen in Equation (4):

$$2S^+ + 2e^- \rightarrow 2S \tag{4}$$

Regeneration of iodide ion as Equation (5) and (6):

$$2I^- \rightarrow I_2 + 2e^-$$ (5)

$$I_2 + I^- \rightarrow I_3^-$$ (6)

2.5.1. Transparent conducting glass

The transparent conducting glass plays an essential role in determining the transmission and photoconductive properties, as well as the efficiency of solar cells. DSSCs are typically fabricated with two conductive transparent materials, which help as a substrate for the deposition of the semiconductor material and, also, act as current collectors. There are two critical requirements a substrate needs to meet for DSSCs. Firstly, the substrate should be more than 80% transparent to allow an optimum amount of sunlight to reach the active area of the cell [17]. Secondly, it should have a high electrical conductivity for efficient charge transfer and reduced energy loss in DSSCs. Fluorine-doped tin oxide (FTO, SnO_2: F) and indium-doped tin oxide (ITO, In_2O_3: Sn) are commonly employed as the TCO on glass substrates in DSSCs [18, 19]. These TCO substrates consist of soda-lime glass coated with layers of ITO and FTO. The ITO films have a transmittance > 80% and 18 Ω cm^{-2} of sheet resistance, while FTO films show a lower transmittance of ~ 75% in the visible region and sheet resistance of 8.5 Ω cm^{-2} [20]. Hence, ITO-coated glass is the preferred substrate for use in DSSCs.

2.5.2. Electrodes

Electrodes are a particular class of solid electrical conductors that carry electric current into non-metallic solids, liquids, gases, vacuums, or plasmas. The electrode at which oxidation occurs is called the anode, while the one at which reduction occurs is the cathode. Commonly, in DSSCs, a porous nanocrystal TiO_2 coated electrode is used as the photoanode (anode), whereas platinum (Pt), aluminium (Al) or a carbon (C) coated electrode is employed as the counter electrode (cathode) [21].

2.5.2.1. The working electrode (photoanode)

The working electrode is the main component in DSSCs, which converts solar energy into electrical energy *via* a photovoltaic phenomenon. The working electrode is typically fabricated by depositing a thin layer of a wide bandgap (3 - 3.2 eV) semiconductor oxide, such as titanium dioxide (TiO_2) [22], zinc oxide (ZnO) [23, 24], niobium pentoxide (Nb_2O_5) [25, 26], tin oxide (SnO_2) [27] and nickel oxide (NiO) [28], on a transparent conducting glass plate made of FTO or ITO. Among these, the application of anatase TiO_2 is preferable as compared to the rutile

phase [29], due to its wide energy bandgap of 3.2 eV, while the rutile phase has a bandgap of about 3 eV. Furthermore, TiO_2 is non-toxic, chemically stable, cost-effective, and readily available. These semiconducting layers absorb only a small fraction of light in the UV region; hence, working electrodes are normally immersed in a mixture of dye molecules and a solvent. When the TiO_2 film is immersed in the dye solution, the dye becomes covalently bonded to the TiO_2 surface [30], which renders the working electrode with a large surface area and a highly porous structure for effective photon harvesting and efficient carrier transport.

2.5.2.2. Counter electrode

The counter electrode collects and transfers electrons from the external circuit. It catalyses the reduction of the I^-/I_3^- liquid electrolyte and significantly influences the photovoltaic performance and long-term stability of the device. Commonly, it is fabricated from Pt, Al or C, but Pt is the most widely used and demonstrates higher efficiencies. However, the replacement of Pt is much needed due to its higher cost and scarcity.

2.5.3. Photosensitizer (dye molecule)

The photosensitizer is an essential material for the fabrication of the working electrode in DSSCs, and it is accountable for the maximum absorption of solar energy. Dye molecules are usually coloured organic molecules, typically applied to the TiO_2 photoanode. The dye material to be used in DSSCs should meet the following photophysical and electrochemical properties [21, 31]:

- The dye material should be luminescent.
- The absorption spectrum of the dye should cover the ultraviolet-visible (UV-Vis) and near-infrared (NIR) regions.
- The highest occupied molecular orbital (HOMO) should be located far from the surface of the conduction band of TiO_2, and the lowest unoccupied molecular orbital (LUMO) should be located as close to the surface of the TiO_2 as possible, and subsequently should be higher with respect to the TiO_2 conduction band potential.
- The HOMO level should lie lower than that of the redox electrolyte.
- The periphery of the dye should be hydrophobic to enhance the long-term stability of the cells, as it minimizes the direct contact between the electrolyte and the anode; otherwise, water-induced distortion of the cells will occur.

2.5.4.   Electrolyte

The electrolyte is defined as a chemical compound that ionizes when dissolved or in a molten state to produce an electrically conductive medium. It is also the main component of the DSSCs, so it is vital to look at its characteristics to improve the efficiency of the cell. Hence, an electrolyte to be used in DSSCs should demonstrate the following features [32, 33]:

1. The redox couple should be able to regenerate the oxidized dye efficiently.
2. It should have long-term chemical, thermal, and electrochemical stability.
3. It should be non-corrosive to the DSSC components.
4. It should be able to permit fast diffusion of charge carriers, enhance conductivity, and create an effective contact between the working and counter electrodes.
5. Its absorption spectrum should not overlap with the absorption spectrum of the dye.

Electrolytes such as I^-/I_3^-, bromine/bromide (Br_2/Br^-), SCN^-/SCN^{2-}, and Co(II)/Co(III)) have been reported with the aforementioned characteristics. Among these, I^-/I_3^- has been demonstrated to be a highly efficient electrolyte, but there are certain limitations associated with its application in DSSCs. The I^-/I_3^- electrolyte corrodes glass/TiO_2/Pt; it is highly volatile, responsible for photodegradation and dye desorption, and has poor long-term stability [34, 35].

Also, the effect of the solvent in liquid electrolytes for DSSCs has been investigated. These include acetonitrile as a solvent for the water contamination effect on liquid acetonitrile/TiO_2 anatase interface for durable DSSCs [36]. The changing of the electrolyte solvent from acetonitrile to a series of solvents, such as N-methylpyrrolidine (NMP), valeronitrile (VN), propionitrile (PN), 3-methoxypropionitrile(MPN) or *N*-methylpyrrolidone (NMP), have been reported. The electrolytes with mixed solvents, e.g., comprising the addition of PN, VN, or MPN to AN, reveal the optimal solvent is an AN:PN mixture with volume ratios of 3:1 or 1:1. This mixed solvent results in enhanced performance and long-term stability of *p*-type DSSCs with a cycloruthenated dye [37]. Ethylene carbonate and propylene carbonate have also been tested as useful solvents for an effective electrolyte system with long-term stability in DSSCs [38].

The effect of additives on liquid electrolytes of DSSCs has also been investigated. The additive 4-*tert*-butylpyridine (TBP) shifted the conduction band of TiO_2 upwards [39], which increases the value of the open-circuit voltage (V_{oc}), reduces the short-circuit current density (J_{sc}), and lowers the injection driving force. It is believed that TBP on a TiO_2 surface can reduce

recombination through back transfer to the electrolyte. Therefore, solvent, electrolytes and additives are essential aspects vital for improving the stability and efficiency of DSSCs.

2.6. Evaluation of the performance of DSSCs

Investigating solar cell parameters is very important for industrial considerations as well as for scientific research. Evaluation of the performance of a DSSC can be performed by using various techniques. However, one of the most widely used approaches is the use of current-voltage (I-V) characteristics under illumination or in darkness. The main parameters of this technique include measurements of the V_{oc}, I_{sc}, maximum power (P_{max}) and fill factor (FF), and these are used to define the efficiency of solar cells [40]. These parameters are depicted on the I-V curve shown in Figure 2.4, where the current expressed in amperes (A), is on the y-axis, and voltage in volts (V), is on the x-axis. The I-V curve of a photovoltaic device is based on the device being under standard conditions, i.e., 1,000 watts per square meter [41], and device temperature of 25 °C, assuming that there is no shading on the device.
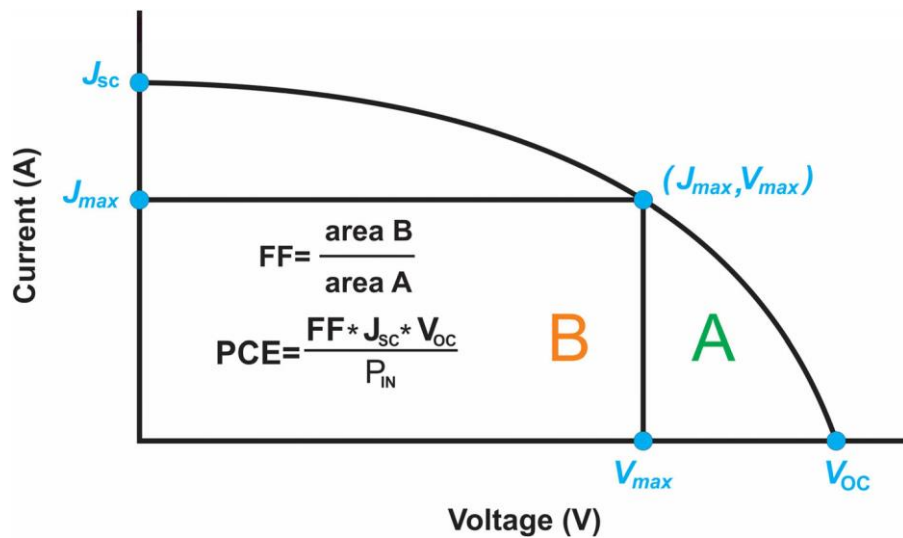
Figure 2.4: I-V curve for evaluation of the cell performance [21]

The maximum power output (P_{max}) is the power of the cell delivered to the load upon conversion of sunlight into electricity. It is located on the knee of the I-V curve, as shown in Figure 2.4, and is given by a product of $J_{mp} \times V_{mp}$. The ratio of maximum power output to the product ($V_{oc} \times J_{sc}$) gives FF, and is defined by using Equation (7):

$$FF = \frac{Area\ A}{Area\ B} = \frac{J_{mp} \times V_{mp}}{J_{sc} \times V_{oc}}$$

Also, the overall power conversion efficiency PCE (%) is defined as the percentage of energy output from the solar cell to input energy (P_{in}) from the sun (shining on a photovoltaic (PV) device), and is defined by using Equation (8):

$$PCE\ (\%) = \frac{V_{oc} \times J_{sc} \times FF}{P_{in}}$$

(8)

The external quantum efficiency (also known as IPCE) is the ratio of the number of electrons flowing through the external circuit to the number of photons of a given energy shining on the surface of the cell at any wavelength (λ) [42]. It is determined by using Equation (9):

$$IPCE = 1240 \times \frac{J_{sc}}{P_{in} \times \lambda}$$

(9)

The equivalence circuit model is used to define the entire I-V curve of a single solar cell. Although an ideal solar cell may be modelled by a current source in parallel with a diode, in practice, no solar cell is ideal, so a shunt and series resistance component is added to the model. The resulting equivalent circuit of a solar cell is shown in Figure 2.5. In this figure, I_{ph} represents the photogenerated current, I_D represents the voltage-dependent current lost to recombination, and I_{sh} represents the current loss due to shunt resistances. In this single diode model, I_D is modelled using the Shockley equation for an ideal diode.
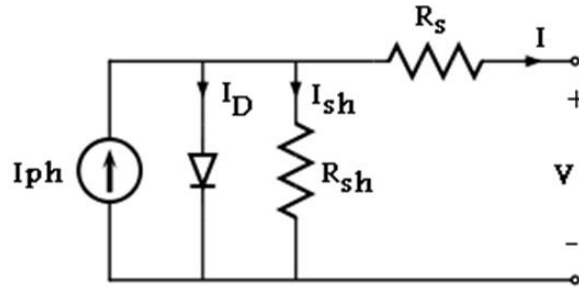
Figure 2.5: The equivalence circuit of a single solar cell [43]

2.7.   Limitation of DSSCs

Recently, many reports have presented comparable efficiencies for DSSCs [44-47]. However, much work is still to be done due to some of the limitations associated with these cells. The major limitations of DSSCs include slow electron transport, fast electron-hole recombination

rate in the TiO$_2$ photoanode, and the use of a liquid electrolyte that has temperature stability problems since the electrolyte can freeze at low temperatures, halting power production and potentially leading to physical damage. The stability failure can be divided into two classes; firstly, limitation towards extrinsic stability and, secondly, limitation towards intrinsic stability [48]. The DSSCs need to be intrinsically stable as well extrinsically stable to be comparable to Si-solar cells and fulfil market needs and commercialization. The limitations towards stability, electron transport, and recombination are discussed in the sections that follow.

2.7.1. Limitation towards extrinsic stability

Extrinsic stability occurs when a sealant material is used for sealing solar cells to make them airtight or watertight. It is the electrolyte that needs to be protected from the external environment and leakage. Also, moisture permeation into the cell should be restricted. Hence, to ensure better longevity of the cell, effective sealing is required. Commonly, Surlyn® and Bynel® hotmelt foils are employed as sealant materials in DSSCs to seal the cells [49]. The pressure build-up inside the cell results in a decrease in the sealing efficiency. If the cell is being exposed within a cyclic or regular temperature variation, the efficiency of the sealant material also decreases. However, the use of Surlyn® and Bynel® hotmelt foils cannot be restricted due to cost-effectiveness and easy processability. Hence, there is work that needs to be done to enhance their adhesion efficiency with glass by pre-treatment of the glass with metal oxide particles. Significant research effort has been devoted to developing an alternative sealant material. Consequently, sealants based on low melting glass frits have been prepared to offer high stability, but these sealants are not suitable for large area module production [50-52]. This has led to the further development of free-glass frit sealant materials; however, the electrolyte reacted with the glass [53]. Later, the concept of microfluidic sealing was introduced to DSSCs [54, 55], of which the sealed cell was found to be more sustainable.

2.7.2. Limitation towards intrinsic stability

Intrinsic stability refers to material stability that is dependent mainly on the fundamental chemical composition and structure of the material. Among the several works reported on thermal stability, an accelerating ageing test in experiments was carried out for 1000 h revealed the thermal stability of the dye, electrolyte, and Pt-counter electrode at 80 °C storage [56]. Through these experiments, it was found that a small test cell can maintain 90% of the initial efficiency under elevated temperatures. Comparably, light soaking exposure for 3000 h

followed by 2000 h at 85 °C induced a PCE reduction of only 10% when a tetraglyme-based electrolyte was employed as a non-nitrile solvent [57]. Also, under AM 1.5 and 55-60 °C moderate temperatures, the fabricated device displays stability for 1000 h.[50] When both the stress factors, such as a temperature of about 80 °C and light soaking, were combined, a rapid degradation in the performance of the cell was observed. Therefore, a significant improvement in the intrinsic stability of the cell is required as 80 °C temperature can be easily attained during sunny days.

2.7.3. Limitation towards electron transport and recombination

Electron transport and recombination in DSSCs are the major limitations of the cell's performance and stability [58, 59]. The influence of charge transport and recombination toward the performance of DSSCs has been investigated by using organic electrolytes, ionic liquids, and organic-hole conductors as hole transport materials (HTM) [60]. The device based on a volatile electrolyte demonstrated benefits of long electron lifetimes, fast electron diffusion through the TiO_2 nanoparticle network, and long charge carrier diffusion lengths, yielding improved photovoltaic performance. The electron transport and recombination in DSSCs made from single-crystal rutile TiO_2 nanowires were reported [61]. They were found to be equivalent to those of DSSCs prepared from TiO_2 nanoparticles. The existence of competition between electron diffusion through the photoanode and recombination with I_3^- in the electrolyte determines the electron collection efficiency in DSSCs. Three factors that affect the electron transport rate across nanoparticle-based DSSCs are the residence time of electrons in traps, the network morphology of the nanoparticle, and structural defects [62, 63]. Therefore, understanding electron transport and recombination in dye-sensitized nanostructured TiO_2 solar cells is very important to hinder any limitations.

2.8. Key aspects of the efficiency of DSSCs

Significant optimization of the efficiency and stability of DSSCs focusses on the fundamental fabrication techniques and materials used. Various approaches to optimize the efficiency of DSSCs are discussed below [64-66]:

- The regeneration process of the dye molecule should take place in a nanosecond duration, which means it should be fast when compared with the oxidation process of dye.

- The formation of the dark current should be minimized by deposition of a uniform thin layer, e.g., TiO_2 nanoparticles, on the transparent conducting glass. In addition, the electrolyte should not have direct contact with the FTO or back contact and, hence, should not be reduced by the collector electrons, which prevents the formation of the dark current.

- The porosity of TiO_2 nanoparticles should be improved to maximize dye absorption on the working electrode.

- The interaction of nanoporous TiO_2 nanoparticles with the electrolyte solvent or TBP molecules should be inhibited for uniform sensitization of the working electrode by a sensitizer. If the entire surface of the nanoporous TiO_2 electrode is not uniformly coated with sensitizer, bare spots of nanoporous TiO_2 can be captured by TBP molecules or by an electrolyte solvent.

- Co-sensitization is another approach to optimize the performance of a DSSC, in which two or more sensitizing dyes with different absorption spectrum ranges are mixed together in order to broaden the spectra response range.

- Inserting phosphorescent or luminescent chromophores by adding a luminescent coating layer onto the glass of the photoanode, applying rare earth oxides into a DSSC can improve the efficiency of cells.

- Also, employing various electrolytes instead of a liquid electrolyte, such as a gel-electrolyte or a quasi-solid electrolyte improves the efficiency of the DSSCs.

- Alternatively, carbon-based materials can be employed as electrode, such as graphene, nanowires of carbon, or carbon nanotubes.

2.9. Current advancements in the efficiency of DSSCs

There is a need for optimizing the properties of each component of a DSSC to improve the overall efficiency. However, a major part is in developing highly effective electrodes (working and counter electrode. Hence, this section gives a brief account of the current studies as well as further studies on the optimization of working and counter electrodes of DSSCs.

2.9.1. Efficiency improvement using the photoanode

In 1991, Gratzel et al. initially reported the drastic optimization of the efficiency of DSSCs [67], in which 7-10% efficiencies were reported for DSSCs under AM 1.5 irradiation by using

a nanocrystalline TiO_2 thin film electrode. In 2000, Zhang et al. reported chemical treatments of the nanocrystalline porous TiO_2 electrodes, which improved the electron transport behaviour, interaction between dye molecules and TiO_2 surface, and increased the efficiency of the electrode [68]. In 2003, Islam et al. reported the molecular design of ruthenium(II) polypyridyl photosensitizers to improve the efficiency of nanocrystalline TiO_2 solar cells.[69] These studies have promoted a considerable increase in research interest in using transition metal complexes containing polypyridine ligands in DSSCs to improve their efficiency.

Also, incorporating binary metal-oxides into the photoanode appeared to improve the efficiency of DSSCs [70]. In 2016, Kunzmann et al. reported a binary indium-zinc oxide photoanode for efficient DSSCs [71]. Recently, photovoltaic studies of hybrid metal oxide semiconductors as photoanodes in DSSC were reported [70]. Modifying pristine TiO_2 by employing metals onto TiO_2 has been reported to improve the efficiency of DSSCs, such as Zn-TiO_2 [72, 73], Sn-TiO_2 [74], W-TiO_2 [75], and Cu-TiO_2 [76, 77]. Metal-doped metal oxides have also been employed to fabricate photoanodes, and DSSCs based on a Zn-SnO nanocomposite photoanode showed improved efficiency [78]. The transition from metal doping to non-metal element doping of TiO_2 has emerged as another promising approach to enhance the conversion efficiency in DSSCs [79-82].

Carbon-based materials have also been demonstrated to be promising alternatives in photoanode fabrication. Particularly, graphite-incorporated TiO_2 composite photoanodes have been reported for DSSCs, with a 30 % improvement in the conversion efficiency from 4.44 to 5.76% by using 0.01 weight percent (wt %) graphite–TiO_2 composite electrodes as compared to a pure TiO_2 electrode [83]. The J_{sc} value was increased from 9.03 to 12.59 mA cm^{-2} with 0.01 wt % of graphite content. Apart from TiO_2, carbon and its various allotropes have gained considerable interest in DSSC fabrication to fulfil the future need and have arisen as a perfect surrogate material for DSSCs. Some reports claimed that incorporating carbon nanotubes (CNTs) with TiO_2 by hydrothermal or sol-gel techniques tremendously enhanced the performance of the solar cell [84-87]. Another report on improving the interconnectivity between the TiO_2 and CNTs claimed that an increase in the IPCE could be found [87]. Further improvement of the PCE value from 7.35 to 8.15% was achieved on co-sensitized solar cells by employing a graphene-modified TiO_2 (G-TiO_2) photoanode, instead of a pure TiO_2 photoanode [88].

2.9.2.   Efficiency improvement using the counter electrode

Pt is the most preferred material to fabricate the counter electrode (CE) in DSSCs. However, there is a need for replacing Pt due to its high cost and low abundance. Carbon materials have emerged as an alternative material for the CE. These include carbon black, activated carbon, mesoporous carbon, CNTs, graphene, and fullerenes [65, 89, 90]. Organic polymers, as a family of the carbon-based materials, were proposed to be used as CE catalysts [91, 92]. More recently, several inorganic compounds were introduced into DSSCs as CE catalysts, including cobalt sulfide (CoS), nickel sulfide (NiS), and nickel nitride (Ni_3N) [93]. However, the truth remains that there are few alternatives to replace Pt in DSSCs, so three classes have been introduced, i.e., carbides (TMCs), nitrides (TMNs), and oxides (TMOs) of early-transition-metals [94, 95]. These catalysts display several strengths, including durability of the covalent solid, high melting temperatures of the ionic crystals, and the electrical and thermal conductivities of the transition metals.

A suitable binder combination was also investigated, where vanadium carbide (VC) with conductive carbon/*N*-methyl pyrrolidone (CC/NMP), NMP, CC/IPA (isopropanol) were studied and applied as CE catalysts. The vanadium carbide–CC/NMP binder displayed a high PCE of 3.9%, which was comparable to the photovoltaic performance of the DSSC using a Pt CE (4.0%) [96]. Furthermore, carbide catalysts displayed a higher catalytic activity as compared to Pt in regenerating a new organic redox couple and its disulfide dimer [97]. Therefore, this work expands the list of potential CE catalysts, which can be beneficial towards reducing the cost of DSSCs and thereby accelerating their fundamental research and commercial application. Recent studies suggested that the performance of the reduced graphene oxide (rGO) electrode towards I^-/I_3^- is comparable to that of the Pt electrode [98]. However, the catalytic performance of the rGO film towards the reduction of triiodide was not as good as the thermally decomposed Pt electrode. Hence, this prompts further study on improving the CE efficiency. Studies reporting promising materials for working and counter electrode materials are presented in Table 2.1, together with the PV parameters of the resulting DSSCs.

Table 2.1: PV parameters of DSSCs by applying various types of WE and CE materials

WE/CE	V_{oc}/V	J_{sc}/mA cm^{-2}	FF/%	PCE/%	Reference
WE: Al-doped TiO_2	0.58	13.39	55	4.27	**[99]**
WE: W-doped TiO_2	0.73	15.10	67	7.42	**[100]**
WE: Sn-doped TiO_2	0.72	16.01	71	8.31	**[74]**
WE: Zr doped TiO_2	0.45	0.13	34	0.02	**[101]**
WE: Fe doped TiO_2	0.29	0.22	27	1.72	**[101]**
WE: Ni doped TiO_2	0.67	10.44	39	2.78	**[102]**
WE: TiO_2-graphene	0.51	11.02	46	2.57	**[103]**
WE: N -doped TiO_2	0.75	11.16	56	1.54	**[104]**
WE: N-TiO_2-Graphene	0.68	15.93	58	6.30	**[105]**
WE: TiO_2 Carbon nanotubes	0.74	14.03	68	–	**[106]**
CE: $CoNi_2S_4$	0.54	11.24	67	4.04	**[46]**
CE: $CoFe_2O_4$/Graphene	0.77	22.08	51	–	**[105]**
CE: Graphite/conductive carbon black	0.63	13.44	63	5.32	**[65]**
CE: Acetylene carbon black-graphite	0.68	13.5	49	5.06	**[107]**

WE: working electrode, CE: counter electrode

2.10. Fabrication techniques of DSSCs

Fabrication techniques of DSSCs are also a significant aspect in determining the efficiency and cost of the cell. The well-known techniques for the fabrication are screen-printing, spin-coating, electrophoretic coating, and Doctor blade, as will be discussed in the subsequent sections.

2.10.1. Screen-printing

Screen-printing is one of the well-known techniques employed for coating different highly uniform structures and well-defined thin films on conducting substrates cost-effectively. In 2015, Luo et al. reported mixed-phase cobalt sulfide counter electrodes fabricated by adopting

a screen-printing approach [108], and fabricated DSSCs with a PCE of 7.2%. In 2020, Pattarith et al. reported silver (Ag) nanoparticles adhered to a reduced graphene oxide–platinum composite (Ag–rGO/Pt) as the counter electrode and TiO_2 on rGO sheets with Ag (TiO_2–rGO/Ag) as the photoanode, fabricated by a double screen-printing approach as shown in Figure 2.6 [109]. The DSSC based on the 1:2 Ag–rGO/Pt CE and 0.5 % TiO_2–rGO/Ag photoelectrode exhibited an overall highest PCE of 9.15% under 1.5 AM solar irradiation.
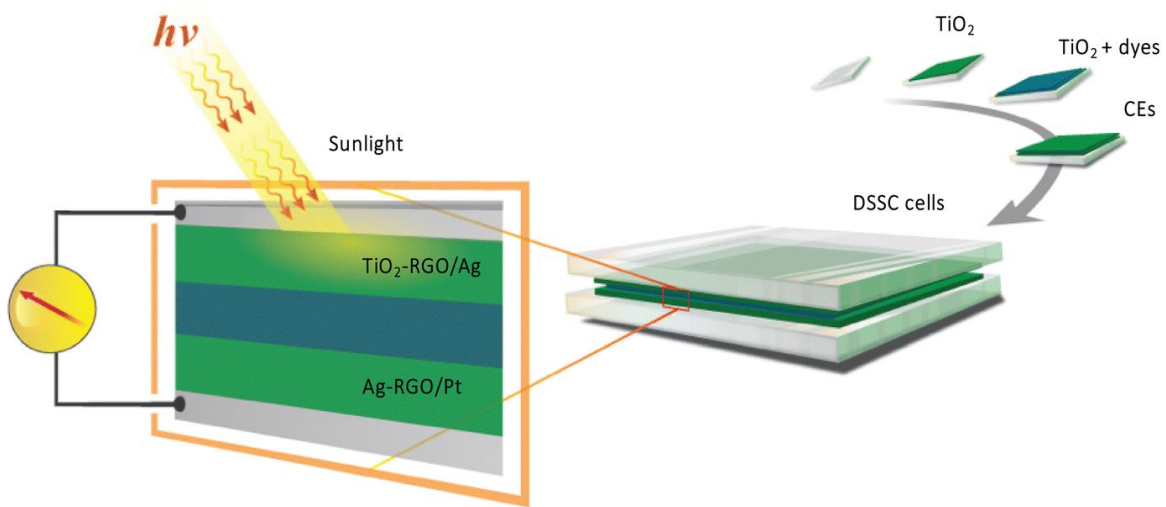
Figure 2.6: Fabrication of Ag nanoparticles adhered to rGO sheets on both electrodes of DSSCs by a screen-printing approach [109]

2.10.2. Spin-coating

Spin-coating is a simple process for rapidly depositing thin uniform coatings onto the surface of a substrate. This technique is performed in four main steps, namely; deposition, spin-up, spin-off, and solvent evaporating, as shown in Figure 2.7. In a typical procedure, in the first stage, a material solution to be deposited onto a substrate is prepared from a volatile solvent, then dropped onto the substrate surface at the centre and then spin-up and spin-off. The solvent evaporation stage occurs throughout the spin-up and spin-off process. The material solution is applied onto the surface of the substrate at the centre, and is distributed *via* centrifugal force. The second stage is the drying of the applied thin layer of the material on a glass substrate. The

thickness of the layer depends on many different parameters, which can be described by using Equation (10):

$$h = \left(1 - \frac{\rho_A}{\rho_{A0}}\right)\left(\frac{3\eta \times m}{2\rho_{A0} \times \omega^2}\right)^{\frac{1}{3}}$$

(10)

where h is the thickness, ρ_A is the density of a volatile liquid, η is the viscosity of the solution, m is the rate of evaporation, and ω is the angular speed. From this equation, it is seen that the angular speed, solution viscosity, and spinning time determine the thickness of the deposited film to be formed. The higher the spinning angular speed of the substrate, the thinner the film.
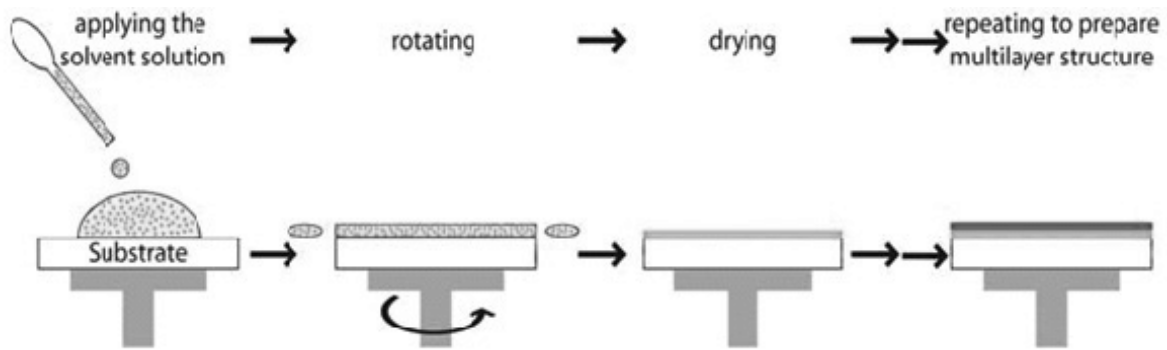
Figure 2.7: Schematic diagram of the spin-coating technique [110]

By employing a spin-coating approach, several works have been reported. For instance, in 2019, Yildiz et al. reported a thin-film TiO_2 photoanode fabricated by a spin-coating method for enhancement of the efficiency of natural and organic DSSCs [111].

2.10.3.   Electrophoretic deposition

Electrophoretic deposition (EPD) is a material processing technique, which involves the deposition of charged particles in a stable colloidal suspension onto a conductive substrate, acting as one of the two oppositely charged electrodes in the EPD cell. It is a quick and economical approach for coating a suitable solvent onto a conducting substrate surface. It involves four main steps, i.e., (a) dispersion, (b) electrochemical charging, (c) electrophoresis,

and (d) deposition (Figure 2.8). EPD is achieved from the motion of charged particles in an aqueous solution or solvent under the influence of an electric field. Recently, in 2019, Kyaw et al. reported the CdSe-TiO$_2$ nanocomposite film fabricated by EPD for quantum dot-sensitized solar cells.[112] Cao et al. have also reported the fabrication of mesoporous TiO$_2$ photoanodes by adopting the EPD technique and applied them in DSSCs [113].
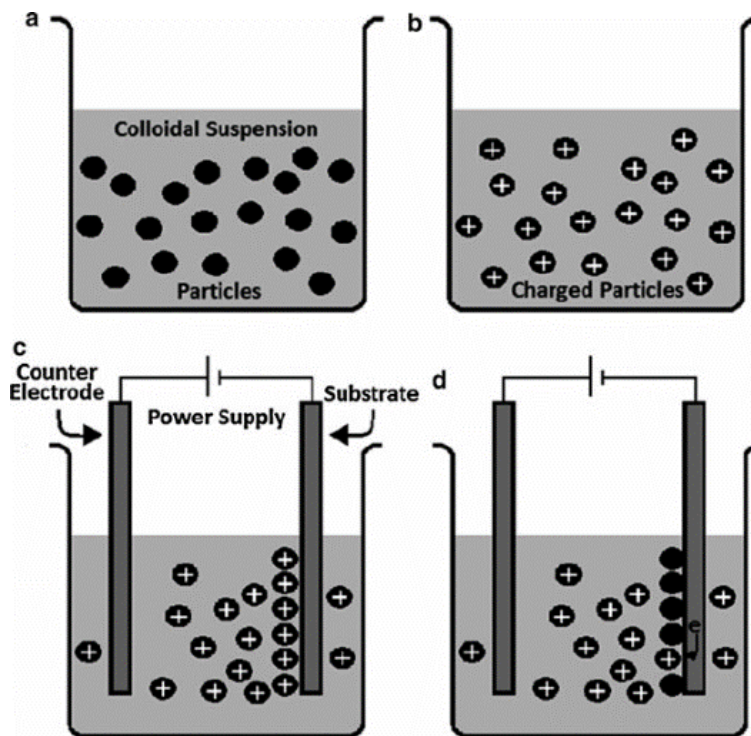
Figure 2.8: Schematic diagram of the four main steps of EPD [114]

2.10.4. Doctor-blade coating

Doctor-blade coating is a roll-to-roll compatible high-throughput thin film fabrication route with little solution wastage. This technique is widely applied for the development of a thin layer of the liquid substrate onto a conducting glass substrate, having a high surface area. It provides layers with thicknesses ranging from 10 to 150 μm, which can be controlled easily. Al-bahrani et al. adopted the Doctor-blade technique to fabricate counter electrodes for DSSCs. A nanocomposite of reduced graphene oxide/Multiwalled carbon nanotubes/nickel oxide (rGO/MWCNTs/NiO) was used [115]. Also, Kouhnavard et al. reported a potential counter electrode for DSSCs fabricated from hydrophilic carbon (HC)/TiO$_2$ colloid composite *via* Doctor-blade coating (Figure 2.9) [116]. The PCE of the cell was found to be 1.9% under standard test conditions. More recently, Sawant et al. reported Cu$_2$ZnSnS$_4$ counter electrodes in DSSCs fabricated *via* Doctor-blade coating [117]. This technique is economically and requires small amount of the starting materials over others. Thus, is considered as one of the most straightforward, low-cost process for semi-conductor paste deposition and simplest printing method available for modern electronics.
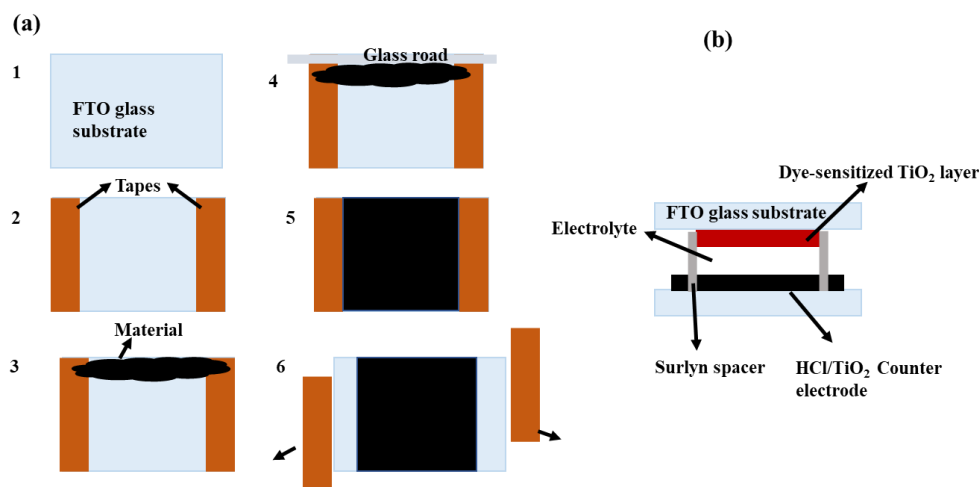
Figure 2.9: Illustration of the (a) deposition of (HC/TiO$_2$) counter electrodes by the Doctor blade approach and (b) complete assembly of a DSSC [116]

This technique is economical and requires small amounts of the starting materials over others. Thus, it is considered as one of the most straightforward, low-cost processes for semi-conductor paste deposition and the simplest printing method available for modern electronics.

2.11.   New design in photoanodes for further improvement

Nitrogen-doped titanium dioxide (N-TiO$_2$) electrodes bring a new design in the structure of photoanodes for DSSCs from the normal TiO$_2$ photoanodes to improve the efficiency of the cells. In addition, co-sensitizing the DSSCs using rGO in the N-TiO$_2$ photoanode tremendously enhances the efficiency, compared with a pure TiO$_2$ photoanode or a N-TiO$_2$ photoanode. In this work, a further approach to optimize the efficiency of DSSCs was adopted by introduced bismuth oxide (Bi$_2$O$_3$) into N-TiO$_2$-rGO photoanodes. Hence, the synthetic approaches of materials are also a challenging aspect, which requires appropriate methods to be employed.

2.12.   Chemistry of graphene

Graphene is defined as a single atomic layer of graphite, which is an allotrope of carbon composed of very tightly bonded sp^2 hybridized carbon atoms arranged in a hexagonal lattice. It possesses excellent electrical conductivity, electron mobility, high surface area, thermal stability, and mechanical strength. Graphene exists in two categories, i.e., pristine graphene and chemically modified graphene (CMG) (e.g., graphene oxide (GO) and rGO), as shown in Figure 2.10 [118].

(a) Graphite

(b) Graphene

(c) Graphene oxide

(d) Reduced graphene oxide
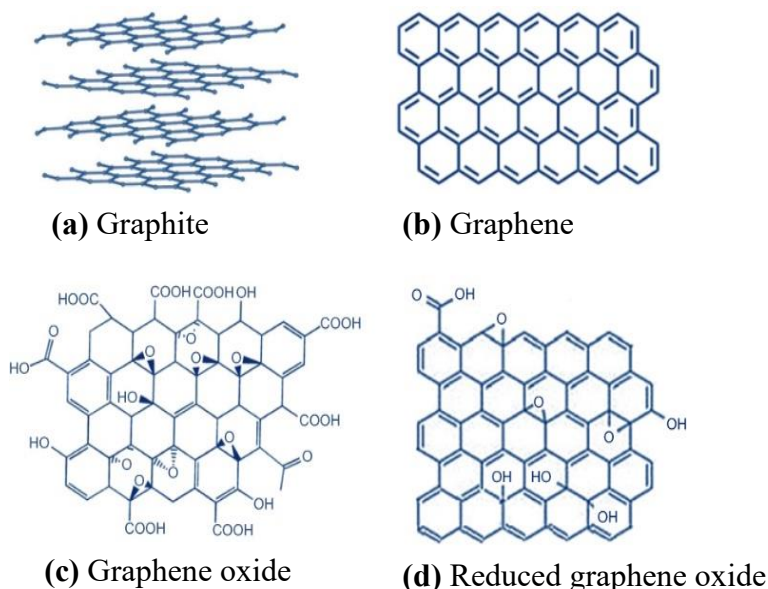
Figure 2.10: Chemical structures of graphite and graphene, including their common derivatives [119]

In order for pristine graphene to fulfill practical application requirements, it has frequently to be chemically modified. For instance, it is insoluble, unmanageable, and decomposes after melting. Thus, conventional material processing techniques cannot be employed to shape pristine graphene into its desired structures [120]. On the other hand, graphene layers can be physically stabilized on a solid-state support; these graphene layers tend to form wrinkles or stacking through π-π and hydrophobic interactions. Pristine graphene has a weak interaction with other small molecules or polymers and poor catalytic performance. Thus, considerable efforts have been made to modify the surfaces and electronic structure of pristine graphene sheets [120]. GO and rGO are regarded as two-dimensional (2D) conjugated macromolecules with larger molar masses, which possess supramolecular chemistry. GO sheet behaviour resembles an amphiphilic macromolecule, wherein basal planes are hydrophobic and edges are hydrophilic. Chemical functionalized rGO also possesses molecular behaviour. Subsequently, the CMG material can be assembled into a microscopic material with controlled composition and microstructure *via* hydrogen bonding, electrostatic, hydrophobic, and π-interactions between graphene sheets. Several excellent reviews [121-123] have summarized the chemistry of graphene, including covalent functionalization, noncovalent functionalization of graphene sheets, photochemistry, supramolecular chemistry, and catalytic chemistry.

2.12.1. Synthesis of graphene

Several approaches have been reported for graphene synthesis. These include the top-down approach and the bottom-up approach. The top-down approach involves modified graphene sheets produced *via* exfoliation of graphite or graphite derivative such as GO and graphite fluoride. The bottom-up approach involves piecing together alternative sources of carbon to give a graphene complex. Thus, to limit the length of this review, the top-down approach has been selected and is discussed. In the oxidation-reduction approach, the initial step is the oxidation of graphite to graphene oxide, followed by the reduction of GO to rGO [124].

2.12.1.1. Oxidation of graphite

The oxidation of graphite was initially reported by Brodie in 1856 [125], where he treated natural graphite with a solution of potassium chlorate in fuming nitric acid, in an attempt to determine the molecular weight of graphite. However, in 1957 Hummers and Hoffman developed a safer, faster, and more effective method called Hummer's method [126]. Briefly, this method employs a mixture of sulfuric acid with sodium nitrate and potassium

permanganate and is still used but with some modifications. GO can be synthesized *via* wet or dry methods. Hence, in the dry method, graphite is exposed to molecular oxygen under ultrahigh vacuum conditions and treated with ozone under ultraviolet light. However, the wet chemical method is inexpensive. Among several proposed methods, the three major methods are those of Brodie, Staudenmaier[127], and Hummer. These methods have been subjected to a variety of modifications to improve the overall yield and quality of the product.

Tour's method is one of the improved Hummer's methods, in which sodium nitrate has been replaced with phosphoric acid (H_3PO_4) in a mixture of H_2SO_4/H_3PO_4 (9:1) and an increasing amount of potassium permanganate ($KMnO_4$) [128]. This modification has successfully increased the yield and quality of the product, and it does not involve the evolution of toxic gases such as nitrogen dioxide (NO_2), dinitrogen tetroxide (N_2O_4), and residual sodium (Na^+) and nitrate (NO_3^-) ions. Researchers have claimed that GO produced with the Tour method has a higher degree of hydrophilic character as compared to that produced by Hummer's method, due to the presence of phosphoric acid [129]. $KMnO_4$ is a strong oxidizer in an acidic medium. Therefore, with its assistance, the complete intercalation of graphite with concentrated sulphuric acid (H_2SO_4) could be achieved. This results in graphite-bisulfate (H_2SO_4-GIC), whereby graphene layers are sandwiched with a bisulfate ion layer. This intercalation promotes the effective penetration of potassium permanganate into the graphene layers for the successful oxidation of graphite, and results in the formation of oxygen-containing functional groups, as shown in Figure 2.11.
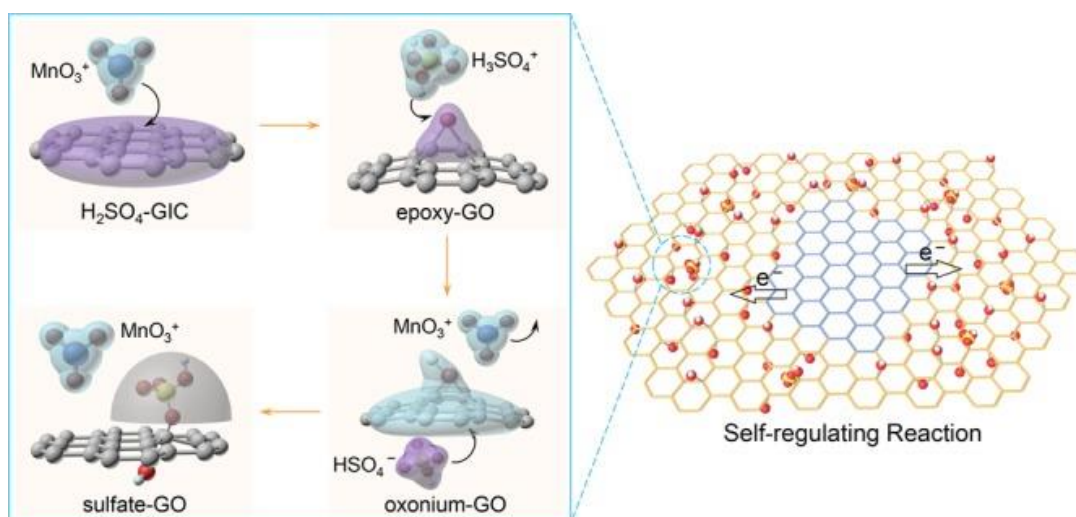
Figure 2.11: Schematic illustration of the intrinsic formation and conversion path of oxygen-containing functional groups during the graphite oxidation process [124]

2.12.1.2. Reduction of graphene oxide

After the discovery of graphite oxidation into GO in the past years, various attempts were made to remove the oxygen-containing groups on the surface of graphene oxide. This was done by adopting chemical reduction, but it did not occur until another approximately 80 years. In 1963, Brauer noticed the reduction of graphite oxide *via* treating graphite oxide with hydrazine, hydroxylamine, hydroiodic acid, tin(II), and iron(II) ions. Nowadays, the conversion of GO to rGO is simply achieved by electromagnetic radiation of high-energy and chemical reduction methods. High-energy radiation techniques for the reduction of GO are microwave, X-ray [130], gamma rays [131], ultraviolet [132], and camera flash radiation [133]. Upon gamma radiation, the reduction of GO in a mixture of water and alcohol molecules has demonstrated the conversion of water and alcohol molecules to highly reactive and reductive species, which act as a reducing agent [134]. Ultraviolet radiation has been reported to induce the reduction of GO very well under a mild hydrogen and nitrogen atmosphere, but after prolonged irradiation, ultraviolet radiation can destroy the epoxide groups on GO [135]. Flash camera reduction of GO under inert air has been reported by Cote et al., and it induced rapid heating that promotes the reduction of GO instantaneously [133]. Therefore, in this part of the review, the microwave-assisted method is discussed more in detail due to its low cost, ready availability, and short reaction time.

The microwave-assisted technique demonstrates a rapid exfoliation and reduction of GO by microwave irradiation. In 2015, Matsumoto et al. applied the microwave-assisted synthesis of rGO in a molecularly engineered oligomeric ionic liquid [136]. This approach demonstrated ultrahigh-efficiency exfoliation (93% yield) with high selectivity (95%) towards single-layer graphene (with thicknesses <1 nm) in 30 minutes, i.e., a short processing time. The isolated graphene sheets were readily re-dispersible in oligomeric ionic liquids up to approx. 100 mg mL^{-1}. Thereafter, the material forms a physical gel in which the anisotropic orientation of graphene sheets induced by a magnetic field is maintained. In 2016, Voiry et al. reported the efficacious reduction of GO by using 1-2 second-long microwave pulses [137]. Upon microwave irradiation, arcing was seen around GO, typically lasting 50-100 ms. The researchers correlated arcing seen around GO with a vigorous GO reduction. It was estimated to be a few thousand degrees celsius (°C) for the growth temperature of GO. Before microwaving, mild annealing was done at 300 °C for 1 h under an argon atmosphere. Microwaving with and without annealing at 300 °C was compared to the deduced preferable

method and it was concluded that prior annealing was essential. This rGO demonstrated a highly-disordered structure under examination with XPS and HRTEM with a negligible content of oxygen functional groups. Furthermore, the Raman spectrum of rGO was comparable with that of graphene, prepared *via* chemical vapour deposition (CVD). The rGO exhibited high-charge mobility greater than 1000 cm^2 V^{-1} s^{-1} in field-effect transistors and unanticipated low Tafel slopes of ~38 mV/decade for the rGO catalyst supported on oxygen molecules.

These oxygen functional groups leave the graphene sheet at their different temperatures and time (Figure 2.12a). For instance, the carbonyl group leaves first under mild annealing, and by raising the temperature, there is a removal of the carboxyl and epoxy groups. Upon the removal of the carbonyl groups, the graphene sheet is destroyed, and healing those holes is a challenge (Figure 2.12b). Hole formation should be avoided during graphite oxidation and further treatment of GO. The frequent structural defects observed upon microwave irradiation of GO include C-C bond breakage, carbonyl group formation, and bending of the sheet (Figure 2.12b-d.).
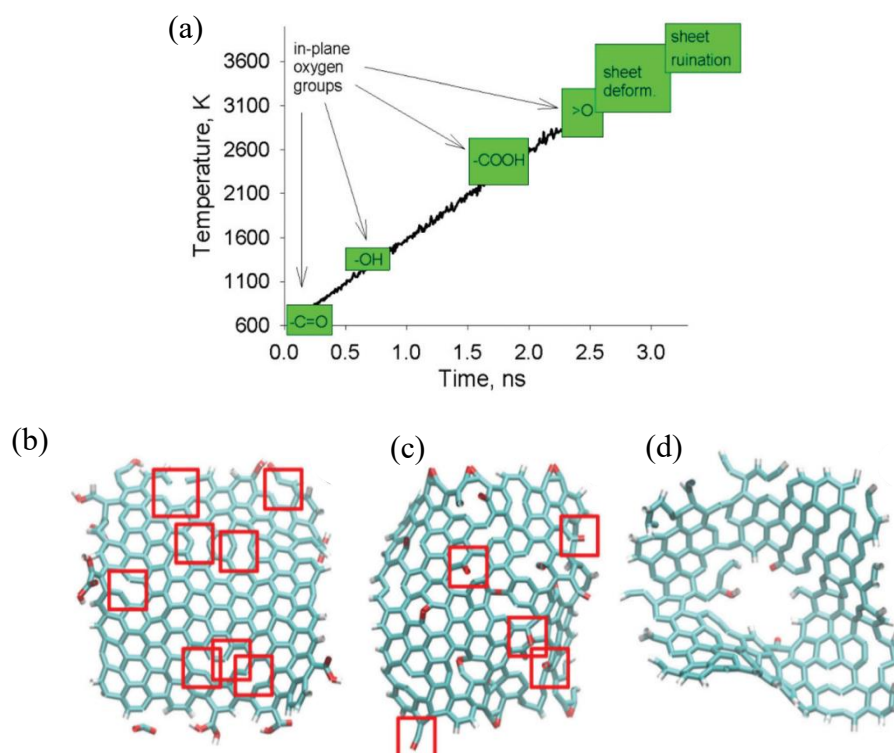
Figure 2.12: Structural defects observed upon microwave irradiation of GO: (a) diagram of GO reduction in nanosecond heating under vacuum, (b) carbon-carbon bond breakage; (c) carbonyl group formation and (d) bending of the sheet [137]

These frequently observed defects that occur during GO reduction (Figure 2.12), are usually impossible to remove, especially the oxygen-containing groups without disturbing the GO sheet structure. C-C bond breakage is the most common defect. However, it does not destroy the sheet because if a reactant is supplied, these defects can play an essential role in molecular combination reactions. Therefore, a microwave technique for the reduction of GO is still much preferred due to the defects formed that provide benefits for rGO. In another work, an effective reduction of GO *via* a hybrid microwave heating technique using mildly reduced graphene oxide (MG) as an external susceptor has also been reported [138]. In this study, MG was prepared by annealing of GO at 300 °C for 1 h under nitrogen in a horizontal heating furnace (which is a conventional heating method), and reduction of GO was subsequently achieved by covering the GO powder with a MG membrane in different mass ratios of MG to GO and microwaved under argon at 2000 W for 30 s. Therefore, this technique accelerates the reduction of GO in a more cost-effective and beneficial manner in a short time.

2.13.   N-TiO$_2$ photoanode

Several efforts have been made to optimize the structure and electron transport of nanocrystalline TiO$_2$. These include the preparation of a scattering layer on the TiO$_2$ photoanode to reduce recombination [139], and a sensible design morphology on the photoanode to improve photoelectrochemical performance [140]. Among these, changing the band structure or surface states of nanocrystalline TiO$_2$ by the doping technique has attracted considerable research interest recently. Doping with chromium (Cr) [141, 142], tin (Sn) [143], magnesium (Mg) [144], zinc (Zn) [145, 146], niobium (Nb) [147], and tantalum (Ta) [145, 148, 149], elements has been reported. However, replacing traditional metal doping of TiO$_2$ with a non-metal, such as nitrogen atom doping, to improve the performance in DSSCs has gained attention since 2005, but still needs to be studied [150]. Nitrogen doping is quite encouraging, and it changes not only the crystal structure but also reduces the electron-hole recombination rate of TiO$_2$.

The enhanced photocurrent of a N-TiO$_2$ electrode-based DSSCs has been reported with an efficiency of 4.86% [151]. The enhancement of the conversion efficiency was mostly ascribed to the increase of light absorption in the near-visible region, and partially to the morphological characteristics of the N-TiO$_2$ film. N-ion-implanted TiO$_2$ photoanodes in a quantum dot-DSSC have been reported, and the photoanode performances was improved with post-N-ion doping

through ion implantation. The authors concluded that N-TiO$_2$ electrodes are promising for light-driven energy devices [152]. The embedded multifunctional N-TiO$_2$ scattering particles in the mesoporous photoanode of DSSCs have been reported with a PCE of 7.98% [153]. The use of a high-surface N-TiO$_2$ in a mesoporous photoelectrode of DSSCs improves the PCE compared with commercial photoelectrodes without additives. Thus, these novel multifunctional photoelectrodes may be suitable for nanostructured solar cells.

A comparative study of DSSCs based on N-TiO$_2$ and TiO$_2$-graphene composite electrodes was reported to improve the efficiency [154]. From this work, the photoanode of N-doped TiO$_2$ modified with graphene showed the highest energy-conversion efficiency in comparison to pure TiO$_2$ and N-TiO$_2$ photoanodes. The improvement in the conversion efficiency of the graphene-based DSSC was attributed to the formation of electron bridges between TiO$_2$ and FTO, which minimises the recombination rate of electron-hole pairs and increases the rate of electron transport. Recently, N-TiO$_2$/graphene nanofibers as DSSC photoanodes have been reported with a promising PCE of 5.01%, which was an increase of 26% when compared with the nitrogen-free device [155]. Therefore, these analyses confirmed that co-sensitisation is another approach to optimize the performance of a DSSC further, as introducing graphene into N-TiO$_2$ showed improved efficiency. Hence, more studies are needed on N-doped TiO$_2$/rGO employed as a photoanode for DSSCs.

2.13.1. Strategy for the preparation of N-TiO$_2$

A number of techniques have been introduced to incorporate nitrogen into the lattice structure of TiO$_2$, including sputtering, ball milling, plasma or ion implantation [156], solvothermal, sol-gel [157], and hydrothermal methods [158, 159], direct hydrolyses of organic/inorganic salts, and oxidation of titanium nitride. Among these techniques, sol-gel is the most widely used approach due to its simplicity. However, various types of sol-gel can be employed with a wide modification regarding the method of application. The main advantage of this technique is the use of low temperatures, which makes it cost-effective. Furthermore, the sol-gel technique can be employed without the use of special equipment, and hence, the experimental procedures for sol-gel can be widely modified. The following section focusses on a few reports that describe these modifications.

Barkul et al. prepared N–TiO$_2$ by a sol-gel technique from titanium *tert*-butoxide (Ti(C$_4$H$_9$O)$_4$) and urea (CH$_4$N$_2$O) [160]. This was done by preparing two solutions separately, a titanium

solution and a urea solution, then mixing them together and regulating the pH to 10 with ammonia solution. The solution was stirred over three hours and then cooled. The resulting precipitate was dispersed in distilled water and continuously stirred under the same conditions. Thereafter, the gel obtained was dried at 110 °C and further calcined at 400 °C for over 5 h. This approach presents a low aging time, but the pH of the solution has to be regulated. On the other hand, the calcination time has to be longer.

Zhao et al. prepared N-TiO$_2$ by a sol-gel technique from Ti(C$_4$H$_9$O)$_4$ and CH$_4$N$_2$O as the nitrogen source [161]. The aging time was 24 h, and the gel formed was dried at 100 °C in an oven for 12 h and crushed into a powder. The powder was treated further under a nitrogen (N$_2$) atmosphere in a homemade dielectric barrier discharge (DBD) plasma reactor for 30 min and then calcined in N$_2$ in a tube furnace. It was concluded that the N$_2$ plasma treatment had the smallest particle size of TiO$_2$, (calculated crystallite sizes of N-TiO$_2$, N-TiO$_2$ (NTP) and TiO$_2$ of 6.9, 4.9, and 11.2 nm, respectively) and better dispersion (Figure 2.13). Moreover, it was speculated that the newly formed TiO$_2$ precursors in plasma are primarily negatively charged, which prevents particle agglomeration during thermal treatment [162].
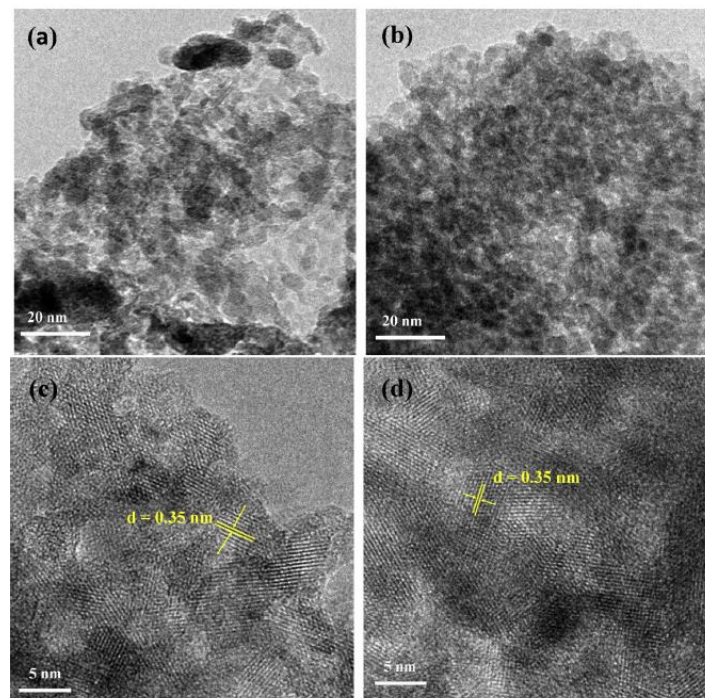
Figure 2.13: TEM image of (a) N-TiO$_2$ and (b) N-TiO$_2$ (NTP). HRTEM images of (c) N-TiO$_2$ and (d) N-TiO$_2$ (NTP) [161]

Recently, Sturini et al. prepared N-doped TiO_2 by a sol-gel method using titanium isopropoxide $[Ti[OCH(CH_2)_2]_4$ and an aqueous solution of ammonia [163]. In this process, they obtained a gel after 4 h of vigorous magnetic stirring, and the resulting mixture was dried at 100 °C for 12 h. It was then subsequently calcined in a muffle furnace at 350 °C for 1 h to achieve the crystallization of TiO_2, from the amorphous to the anatase phase. Hence, these reports provide evidence that the sol-gel method can be employed with a wide range of modifications depending on the application.

2.14.   Nanocomposite preparation techniques

There are a wide range of approaches for the synthesis of nanocomposites. These include liquid-phase, gas-phase, and solid-phase synthesis. The liquid phase approaches include co-precipitation, sol-gel, hydrothermal/solvothermal, microemulsion/micelle method, thermochemical/flame decomposition of metal-organic precursors, and the microwave-assisted method [164, 165]. Among these, the sol-gel and hydrothermal methods are selected and discussed, due to their simplicity and easy hybridization with other techniques.

2.14.1.   Sol-gel approach

The sol-gel approach is a wet-chemical technique that uses a colloidal suspension (sol) to produce an integrated network (gel). Sol denotes that the solution consists of very fine particles, while the gel is a semi-rigid mass formed when the solvent from the solution starts to evaporate, and fine particles or ions left behind begin to join together in a continuous network. The typical procedure involves the first step of hydrolysis, followed by polycondensation as a second step and finally, a dry gel is obtained. Liang et al. adopted the sol-gel approach to incorporate nitrogen into the lattice structure of TiO_2 by hydrolysis and the aging of $(Ti(C_4H_9O)_4)$ [166].

2.14.2.   Hydrothermal approach

This is the technique of crystallising or synthesising substances from a high-temperature aqueous solution at high vapour pressure. The reactants are dissolved in water or another solvent (solvothermal) in a closed vessel, then heated above ambient temperature and pressure. Hydrothermal synthesis involves water acting both as a catalyst and occasionally as a component of solid phases during the synthesis at elevated temperature and pressure. It offers

many advantages, such as relatively mild operating conditions (reaction temperatures < 300 °C), and average nanoparticle size can be controlled by adjusting the processing time and temperature. Hence, a wide variety of graphene-based nanocomposites have been prepared by adopting the hydrothermal technique. Shen et al. demonstrated an environmentally friendly and efficient route for the preparation of TiO_2-rGO composites by adopting a one-step hydrothermal method using glucose as the reducing agent [167]. Suwannaruang et al. reported that the hydrothermal method enhances the integration of nitrogen species into TiO_2 [168]. Particle deposition has often been achieved with hydrothermal synthesis, and hydrothermal synthesis has revealed an excellent deposition of nanoparticles onto the surfaces of materials. In a related report, Kilic et al. reported graphene-TiO_2 nanostructures and CuO nanorods produced on FTO substrates using the cost-effective hydrothermal growth method [169]. The major advantage of the hydrothermal technique is that it can be hybridized with other processes to gain enhancement of crystallizing substances, such as microwave-hydrothermal, sol-gel hydrothermal, and ultrasound-assisted hydrothermal crystallisation, but is not limited to these.

2.15. Characterisation techniques for nanomaterials

Once nanomaterials have been prepared, they need to be characterised in order to ascertain their identity, structural features, and textural properties. The typical characterisation techniques mostly employed to study nanoparticles or nanocomposites are scanning electron microscopy (SEM), transmission electron microscopy (TEM), high-resolution transmission electron microscopy (HRTEM), X-ray diffraction (XRD), thermogravimetric analysis (TGA), Brunauer-Emmett-Teller (BET) surface area analysis, ultraviolet-visible spectroscopy (UV-Vis), photoluminescence (PL) spectroscopy, Raman spectroscopy, Fourier-transform infrared spectroscopy (FTIR), and inductively coupled plasma-optical emission spectrometry (ICP-OES), but are not limited to these. Hence, in this section, these aforementioned techniques are the ones that have been explained in detail for their operational principles.

2.15.1. Scanning electron microscopy

Scanning electron microscopy (SEM) is a powerful non-destructive investigative tool that applies a focussed beam of electrons to produce complex, and high magnification images of the surface topography of a sample (Figure 2.14). Once an area of interest has been spotted on the sample and is evaluated using SEM, it can also provide deeper insight into the elemental

analysis of the material by using energy-dispersive x-ray spectroscopy (EDXS). This technique is used very effectively in microanalysis and failure analysis of solid inorganic materials.
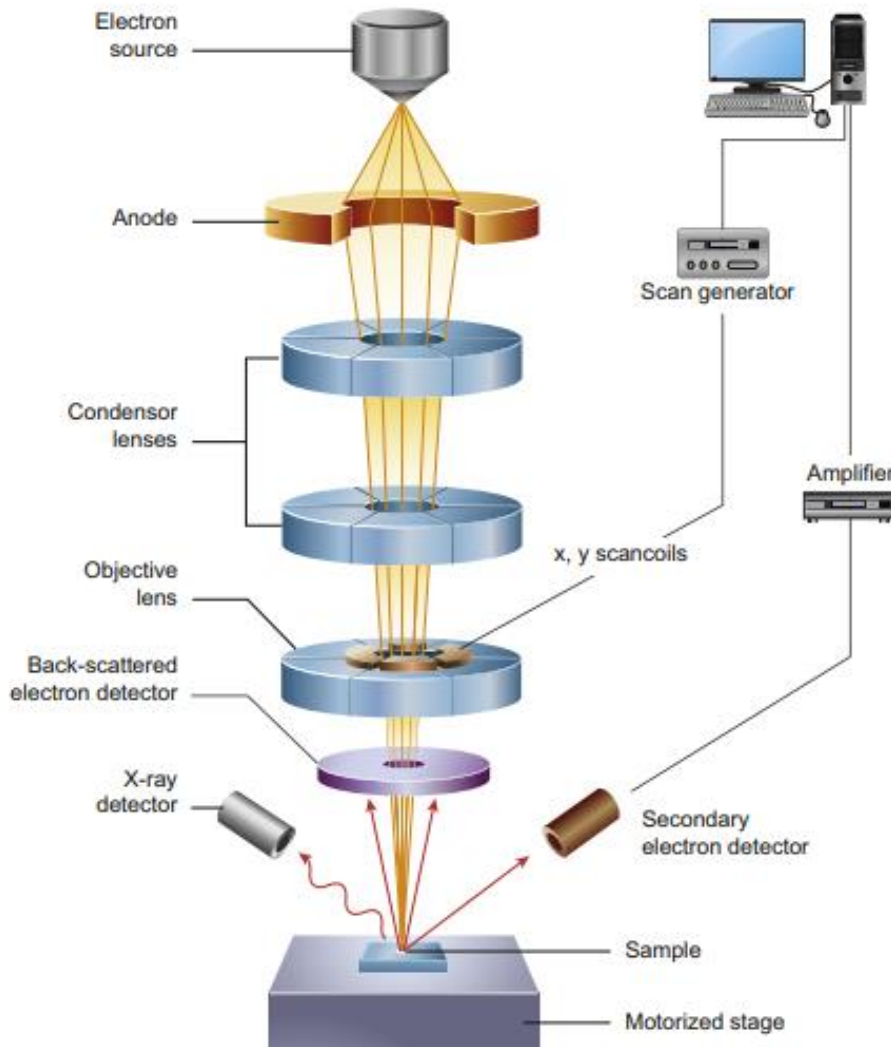
Figure 2.14: Schematic diagram of the core components of a SEM microscope [170]

2.15.2. Transmission electron microscopy

Transmission electron microscopy (TEM) is a powerful non-destructive tool for material sciences, in which a high energy beam of electrons is shone through a very thin sample, as shown in Figure 2.15. The interactions between the electrons and the atoms can be used to observe features such as the crystal structure, and features in the structure like dislocations and grain boundaries can be investigated. Chemical analysis can also be performed. TEM can also

be used to study the growth of layers, their composition, and defects in semiconductors. High-resolution TEM can analyze the quality, shape, size, and density of quantum wells, wires, and dots. TEM operates on the same basic principles as the light microscope but uses electrons instead of light. Since the wavelength of electrons is much smaller than that of light, the optimal resolution attainable for TEM images is many orders of magnitude better than that of a light microscope. Thus, TEM can reveal the finest details of the internal structure in some cases as small as individual atoms.
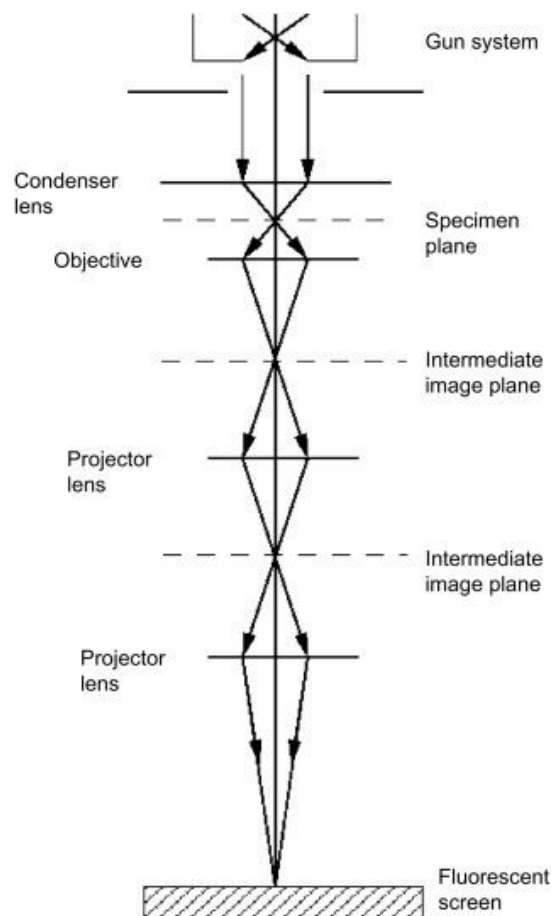
Figure 2.15: Schematic diagram of the core components of a TEM microscope [171]

2.15.3.   Powder X-ray diffraction

Powder X-ray diffraction (P-XRD) is a powerful non-destructive technique for studying the crystal structures of materials. It is used to provide information about the structures, crystalline phases, and crystal orientations present in a material, and other structural parameters such as crystallinity, strain, crystal defects, and average grain size. XRD is based on the constructive

interference of monochromatic X-rays and a crystalline sample. These X-rays are generated by a cathode ray tube, filtered to produce monochromatic radiation, collimated to concentrate, and directed toward the sample, as shown in Figure 2.16. The interaction of the incident rays with the sample produces constructive interference (and a diffracted ray) when conditions satisfy Bragg's law with Equation (11):

$$n\lambda = 2dsin\theta$$

(11)

where n is an integer, λ is the wavelength of the X-rays, d is the interplanar spacing generating the diffraction, and θ is the diffraction angle.

This law relates the wavelength of electromagnetic radiation to the diffraction angle and the lattice spacing in a crystalline sample. These diffracted X-rays are then detected, processed, and counted. Scanning the sample through a range of 2θ angles, all possible diffraction directions of the lattice should be attained due to the random orientation of the powdered material. Conversion of the diffraction peaks to d-spacings allows identification of the compound because each compound has a set of unique d-spacings. Commonly, this is achieved by comparison of d-spacings with standard reference patterns.
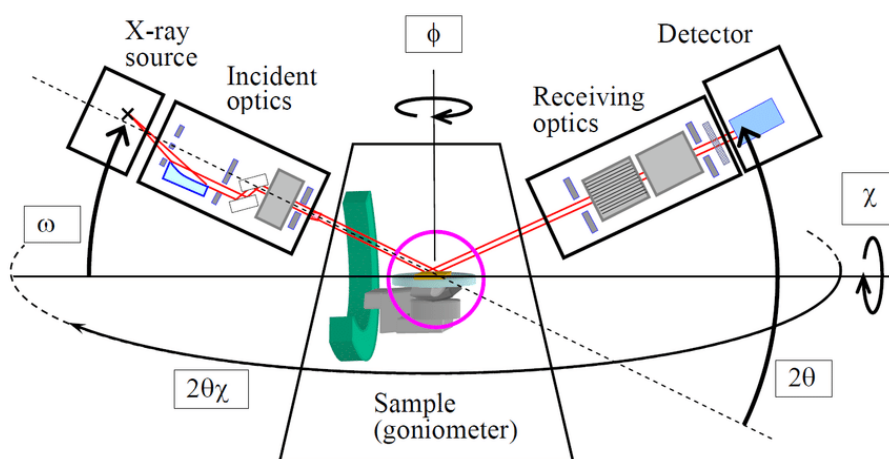
Figure 2.16: Schematic diagram of the X-ray diffractometer system [172]

2.15.4. Thermogravimetric analysis

Thermogravimetric analysis (TGA) is a technique for thermal analysis carried out by gradually raising the temperature of a sample in a furnace under a controlled atmosphere, as shown in Figure 2.17. The weight of the sample is measured on an analytical balance and is used to

study the thermal stability of the material and its composition. The mass loss is observed if a thermal event involves the loss of a volatile component. Chemical reactions, such as combustion, involve mass losses, whereas physical changes, such as melting, do not. The weight of the sample is depicted against temperature or time to present thermal transitions in the materia, such as loss of solvent, the water of hydration in inorganic materials, and finally, decomposition of the materials
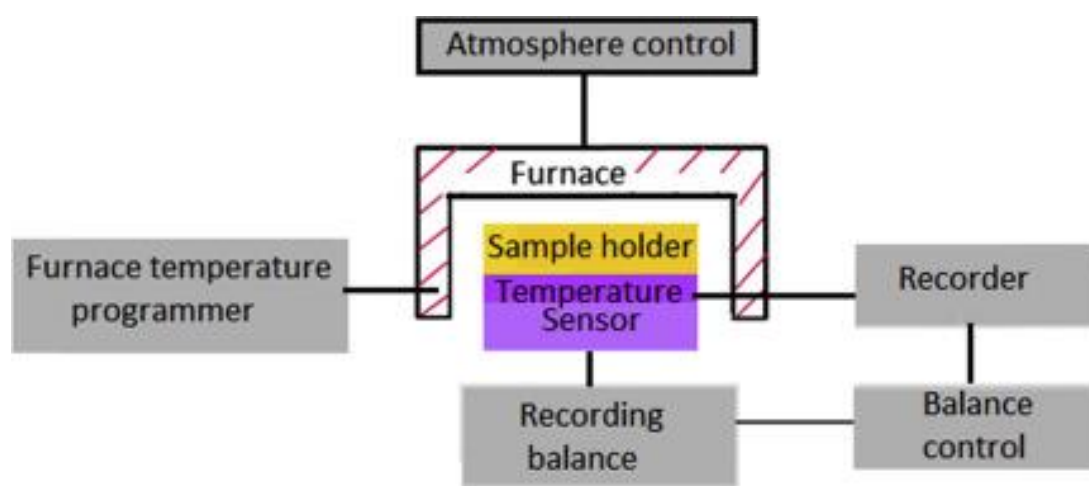
Figure 2.17: Schematic diagram of a thermobalance [173]

TGA has been used to study a synthesized TiO_2 nanocrystals for a photoanodes tested in large area DSSCs [174]. They have concluded that the TGA method allows to completely separate the crystallinity resulted in room temperature, and the crystal size, which remained restricted because of the lack of a high-temperature treatment for a TiO_2. Therefore, by using a TGA, a fully dehydrated material can be easily seen, and dehydrated materials are a compulsory requirement for use in DSSCs. TGA has also been used to determine the amount of rGO in the photoanode of DSSCs [175].

2.15.5.   Brunauer-Emmett-Teller surface area analysis

Brunauer-Emmett-Teller (BET) is a technique of measuring the specific surface area of a solid material. Among the few available techniques, none of them is as straightforward as the BET method for surface area analysis. The measurement of surface area by BET is relatively simple. However, the mathematics and physics behind the BET method are a little more complicated,

and so understanding the result can be difficult. BET measures the surface area based on gas adsorption, such as nitrogen gas. More specifically, it allows the determination of the overall specific external and internal surface area of the sample, e.g., nano-powders or porous solids, by measuring the amount of physically adsorbed gas according to the BET method. Commonly, the adsorbate (nitrogen gas) on the solid material is measured at its boiling point of -196 °C. At that stage, the nitrogen gas is below the critical temperature. It is assumed that the gas condenses onto the surface in a monolayer. When the size of the gas atom/molecule is known, the amount of adsorbate (condensed) gas can be correlated to the total surface area of the particles, including pores at the surface (inaccessible pores are not detected). It is this correlation calculation and volume of the adsorbate to the surface area that BET theory provides by using Equation (12).

$$\frac{1}{V\left[\left(\frac{p^\circ}{p}\right) - 1\right]} = \frac{C-1}{V_m\,C}\left(\frac{p}{p^\circ}\right) + \frac{1}{V_m\,C}$$

(12)

where V_m is the volume of the monolayer for the adsorbate, p^0 is the saturation pressure of adsorbate, p is the equilibrium pressure of adsorbate, and c is the BET constant (E_1-E_L/RT). E_1 is the heat of adsorption for the first layer, and E_L is the heat of vaporization.

From the volume of the monolayer for adsorbate (V_m), the total and specific surface area can be determined by using Equations (13) and (14), respectively.

$$S_T = \frac{V_m \times N \times A_{cs}}{M}$$

(13)

where S_T is the total surface area of the material, N is Avogadro's number (6.02×10^{23} molecules mol^{-1}), A_{CS} is the cross-sectional area of the adsorbate nitrogen (16.2 Å), and M is the molecular mass of nitrogen gas.

$$S_T = \frac{S_T}{w}$$

(14)

where S_{BET} is a specific surface area, and w is the mass of the sample material.

2.15.5.1. Porosity analysis

Porous materials are described in terms of their adsorption properties. The International Union of Pure and Applied Chemistry (IUPAC) classification of adsorption isotherms is illustrated in Figure 2.18; the six types of isotherms are characteristic of adsorbents that are microporous (type I), nonporous or macroporous (types II, III, and VI), or mesoporous (types IV and V).
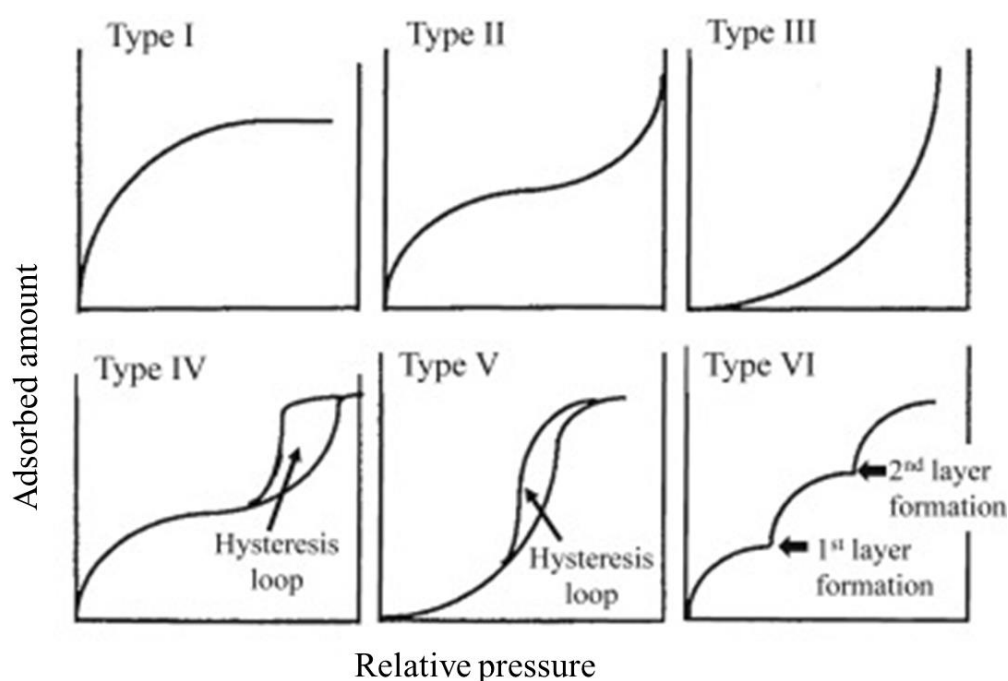
Figure 2.18: Schematic representation of the six types of sorption isotherms drawn to match the IUPAC classification [176-178]

Figures (IV and V) show an adsorption hysteresis, and it is commonly accepted that there is a relation between the shape of the hysteresis loop and the texture, e.g., pore size distribution, pore geometry, and connectivity of a mesoporous material.

The classification of hysteresis loops is given by IUPAC, and presented in Figure 2.19, which were originally introduced by de Boer [177]. The H1 loop is ascribed to a porous material that consists of well-defined cylindrical-like pore channels or agglomerates of approximately uniform spheres. On the other hand, the type H2 loop is widely associated with a disordered

material, in which the distribution of pore sizes and shapes is not well defined and also indicative of bottleneck constrictions. H3 hysteresis is given by materials that have slit-shaped pores, and this isotherm does not show any limiting adsorption at high P/P^o, which is observed with non-rigid aggregates of plate-like particles. Type H4 hysteresis is also commonly associated with narrow slit pores [178]. The dashed curves in the hysteresis loops shown in Figure 2.19, reflect low-pressure hysteresis, which may be associated with the change in volume of the adsorbent.
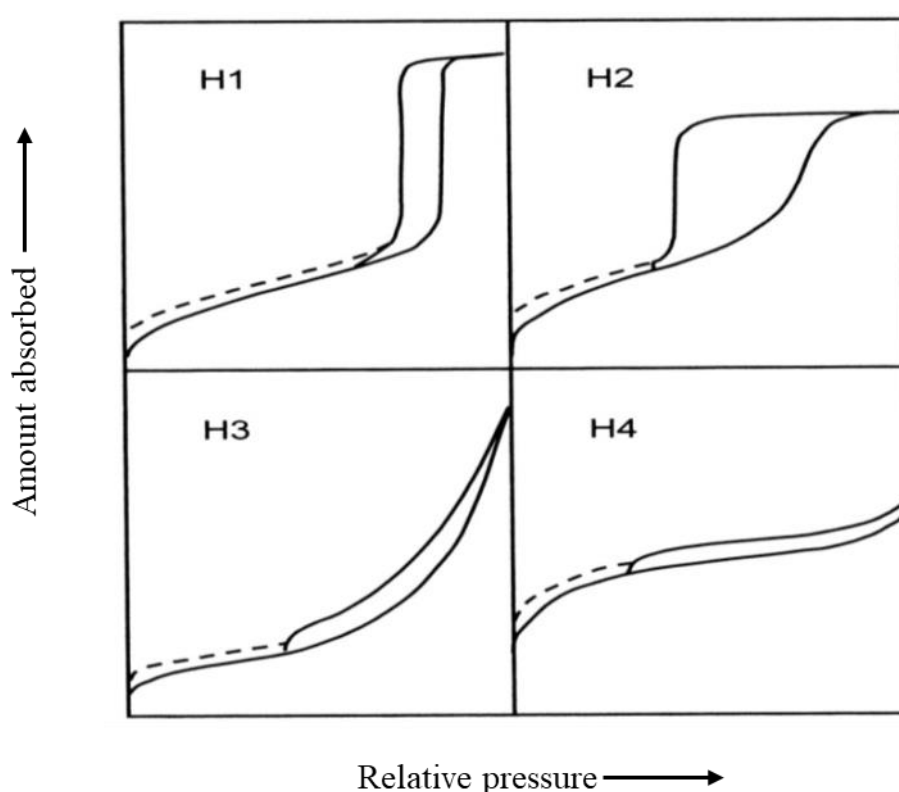
Figure 2.19: The relationship between the pore shape and the adsorption-desorption isotherm [179]

The analysis of pores is commonly done by using the Barrett-Joyner-Halenda (BJH) method, and the porous solid materials are classified by IUPAC: Microporous materials are those have pore diameters up to 2.0 nm, mesoporous materials have pore sizes intermediate between 2.0 and 50.0 nm, while microporous materials have pore sizes exceeding 50.0 nm, as shown in Figure 2.20 [180].
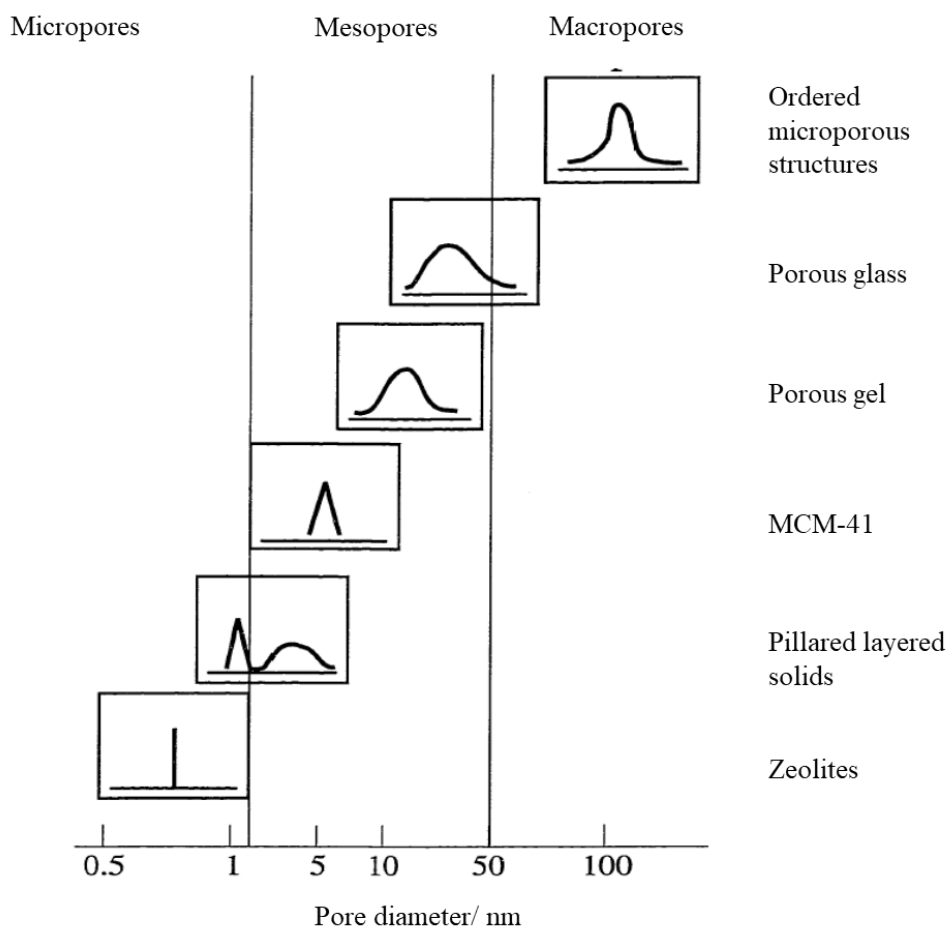
Figure 2.20: Schematic illustrating pore size distribution of different porous materials [179]

2.15.6. Ultraviolet-visible diffuse reflectance spectroscopy

Ultraviolet-visible diffuse reflectance spectroscopy (UV-Vis DRS) is a type of spectroscopy in which the diffuse reflection of light from the surface of the sample is typically measured in the UV-Vis range (190-800 nm). Commonly, this technique is routinely used for studying the optical properties of solid material (opaque). Since light cannot penetrate opaque (solid) samples, it is reflected from the surface of the samples. The surface is built from a non-absorbing powder, and most materials exhibit a mixture of diffuse and specular reflection from their surface. Diffuse reflection is not often caused by the roughness of the surface of the solid material. The flat surface gives specular reflection, but it does not prevent diffuse reflection.

In diffuse reflection, the incident light is reflected in many angles, unlike in specular reflection, where the incident light is reflected at just one angle, as shown in Figure 2.21.
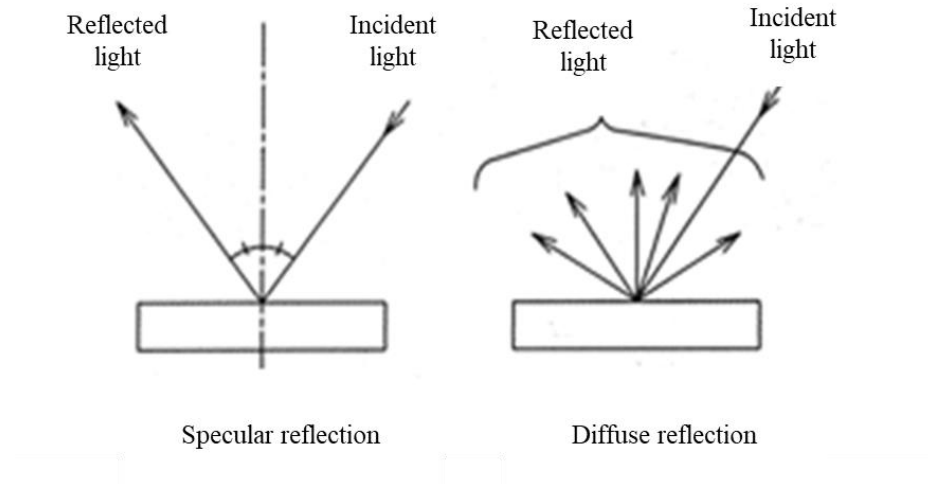
Figure 2.21: Illustration of specular and diffuse reflection [181]

The use of integrating spheres enables the measurement to be carried out. When the light is directed to the sample at an angle of 0°, the existing specular reflected light in the sphere is not measured; only diffuse reflected light is measured. However, available models of integrating spheres with a different angle of incident light make it possible to measure both specular and diffuse reflected light.

Among the developed theories attempted to explain the optical phenomenon resulting from diffuse reflectance, the Kubelka Munk theory is well-known and widely used. This theory is based on light absorption and partial scattering. It was formulated to model the resultant light emerging from translucent and opaque media, assuming that only two light channels are travelling in opposite directions, including absorbed and scattered light. The Kubelka-Munk equation is expressed by using Equation (15):

$$F(R) = \frac{(1 - R_\infty)^2}{2R_\infty} = \frac{k}{s} = \frac{2.303\varepsilon C}{s}$$

(15)

where R_∞ is the reflectance at infinite thickness, k is the absorption coefficient (twice the Beer's law absorption coefficient), s is twice the scattering coefficient of the sample, ε is the molar absorptivity, and C is the analyte concentration.

Estimation of the optical bandgap energy of nanoparticles is simply carried out from the recorded diffuse UV-Vis data by plotting (F(R) energy) against energy (hν).

2.15.7.   Photoluminescence spectroscopy

Photoluminescence (PL) spectroscopy is a type of light emission spectroscopy in which the light emission results from a process called photoexcitation, as shown in Figure 2.22. When light is directed onto a sample, the electrons within the material becomes promoted into excited states (photoexcitation). When the electrons fall from the excited states to their equilibrium states, energy can be released in the form of light. The intensity of the emitted light is plotted against the wavelength on the spectrum. PL spectroscopy is useful in determining the electronic structure and properties of materials as it gives the peak light intensity that materials can emit at a specific wavelength.
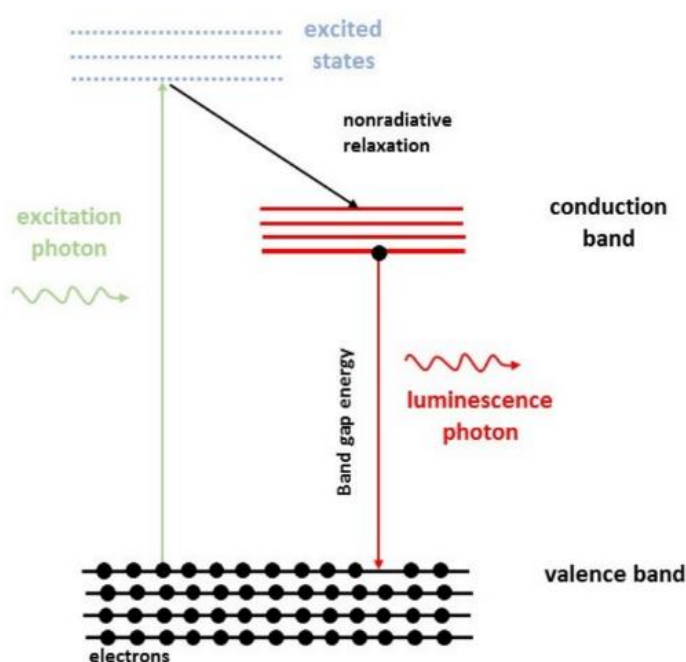
Figure 2.22: Schematic representation of photoluminescence excitation [182]

PL spectroscopy can be employed to evaluate electron-hole recombination in nanomaterials, as the emission signals in the PL spectra are given by the recombination phenomenon of the free electrons and holes generated. PL spectroscopy has been used to study the physical properties of the photogenerated carriers of Bi_2O_3 after being coupled with N-TiO_2 [183]. PL spectroscopy was adopted to evaluate the electron trapping efficiency on the surface-modified TiO_2 incorporated with GO for DSSC application [184].

2.15.8. Raman spectroscopy

Raman spectroscopy is an analytical technique where scattered light is used to measure the vibrational energy modes of a sample, as shown in Figure 2.23. It is named after the Indian physicist C. V. Raman who, together with his research partner K. S. Krishnan, were the first to observe Raman scattering in 1928. Raman spectroscopy provides both chemical and structural information, as well as the identification of substances through their characteristic Raman 'fingerprint'. Raman spectroscopy extracts this information through the detection of Raman scattering from the sample. Raman has been reported as a useful technique to determine the crystalline phases present and the chemical structure of titania [185].
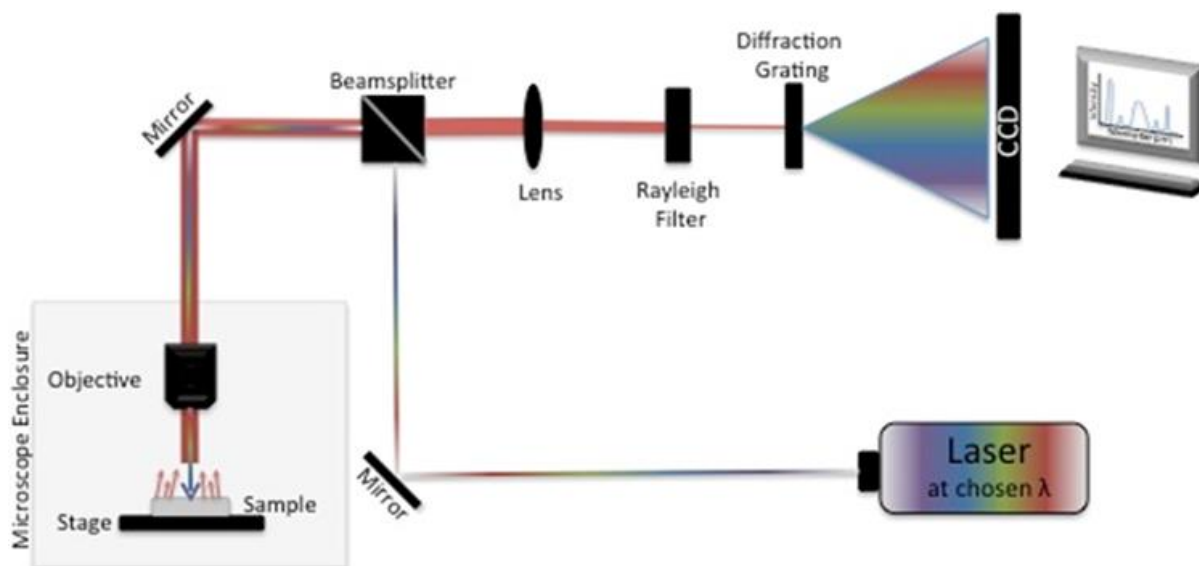
Figure 2.23: A schematic diagram of the Raman instrument [186]

2.15.9. Fourier transform infrared spectroscopy

Fourier transform infrared (FTIR) spectroscopy is a preferred non-destructive technique of infrared spectroscopy, routinely used to identify a functional group present in a material (gas, liquid, and solid) by applying a beam of infrared radiation, as shown in Figure 2.24. The instrument measures the absorption of IR radiation made by each bond in the molecule. It gives a spectrum which is plotted as percent transmittance versus wavenumber (cm^{-1}). A wide range of materials containing covalent bonds absorb electromagnetic radiation in the IR region. The determination of functional groups in a molecule has to be carried out in IR active molecules. An IR-active molecule is one that has a permanent dipole moment. When IR radiation interacts with the covalent bond of the material having an electric dipole, the molecule absorbs energy, and the bond starts back and forth oscillations.
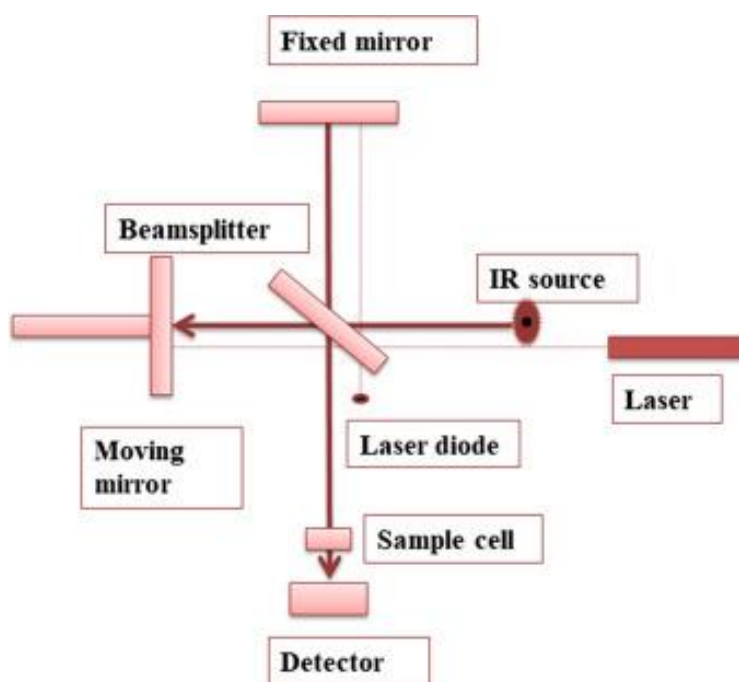
Figure 2.24: Schematic diagram of the FTIR instrument [187]

2.15.10. Inductively coupled plasma-optical emission spectrometry

Inductively coupled plasma-optical emission spectrometry (ICP-OES) is an elemental analysis technique that uses the emission spectra to identify and quantify the elements present in a sample. The sample is introduced into the plasma torch in a process that desolvates, ionizes, and excites atomic species, as shown in Figure 2.25. The constituent elements are then identified by their characteristic emission lines and quantified by the intensity of the same lines. The technique has been commercially available since 1974. Recently, that technique has been employed in the compositional analysis of semiconductor materials [188]. It has demonstrated a drastic influence on the accuracy and reproducibility of the result.
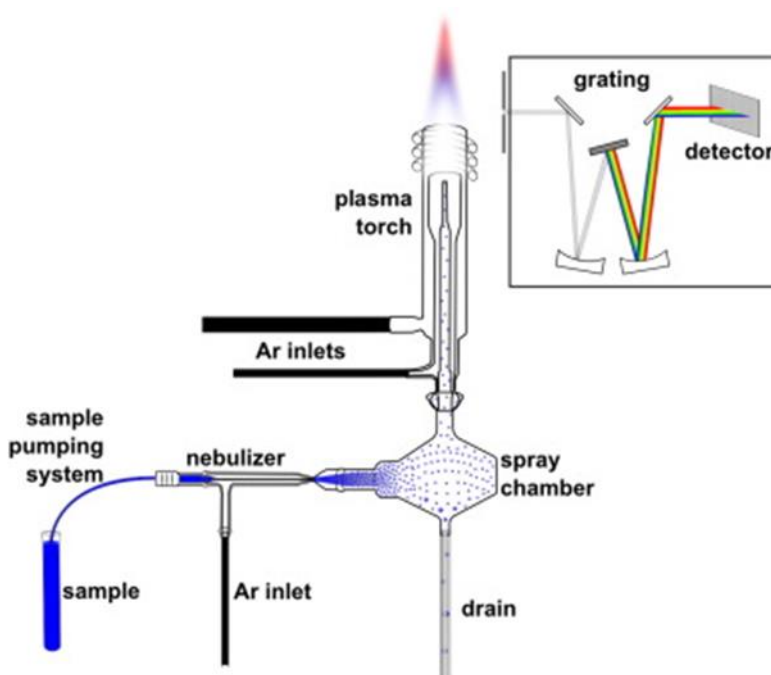
Figure 2.25: Schematic diagram of ICP-OES instrumentation [189]

2.16. Conclusion

In summary, solar energy has emerged as an alternative energy source, and it provides the largest source of clean energy that is most reliable, readily available, and renewable. DSSCs, as one of the devices that convert solar energy into electricity, have become popular, and represent the cutting edge of solar technologies with high efficiency and low production cost. The comparable efficiencies of DSSCs reported have indicated that much work has to be done due to some of the limitations associated with DSSCs, such as electron transport, recombination, and stability. Optimal device efficiency has to be reached by looking at each component of the DSSC and working on it to improve the overall efficiency. The major part of optimizing the efficiency of the DSSCs is to first study and improve the electrodes (working and counter electrodes). It has been shown that the transition from metal doping of titania to non-metal doping, coupled with a carbon material, has drastically improved the overall efficiency of the electrodes further. The reports on graphene incorporated with N-TiO_2 for photoanodes of DSSCs provide evidence that more studies are needed on this material. Hence, in this dissertation, Bi_2O_3 was introduced into N-TiO_2-rGO photoanodes to optimize the efficiency of DSSCs further.

References

1. G. Mutezo and J. Mulopo, *A review of Africa's transition from fossil fuels to renewable energy using circular economy principles*, Renewable and Sustainable Energy Reviews, 2021, **137**, 110609.

2. K. Nwaigwe, P. Mutabilwa and E. Dintwa, *An overview of solar power (PV systems) integration into electricity grids*, Materials Science for Energy Technologies, 2019, **2**, 629-633.

3. S. M. Jowitt, G. M. Mudd and J. F. H. Thompson, *Future availability of non-renewable metal resources and the influence of environmental, social, and governance conflicts on metal production*, Communications Earth & Environment, 2020, **1**, 13.

4. A. K. Pandey, R. K. R and M. Samykano, *Chapter 1 - Solar energy: direct and indirect methods to harvest usable energy*, in *Dye-sensitized solar cells*, eds. A. K. Pandey, S. Shahabuddin and M. S. Ahmad, Academic Press, Massachusetts, United States, 2022,, pp. 1-24.

5. G. Keru, P. G. Ndungu and V. O. Nyamori, *A review on carbon nanotube/polymer composites for organic solar cells*, International Journal of Energy Research, 2014, **38**, 1635-1653.

6. M. Becquerel, *Memoire sur les effets electriques produits sous l'influence des rayons solaires*, Comptes Rendus Hebdomadaires Des Seances De l'Academie Des Sciences, 1839, **9**, 561-567.

7. R. S. Ohl, *Light* sensitive electric device, US patent No. 2,402, 662, priority date 1941.

8. M. M. A. Moon, M. Rahman, J. Hossain and A. B. M. Ismail, *Comparative study of the second generation a-Si:H, CdTe, and CIGS thin-film solar cells*, Advanced Materials Research, 2019, **1154**, 102-111.

8. N. A. Tegegne and F. G. Hone, *Solar cell technology: challenges and progress*, in *Electrode materials for energy storage and conversion*, CRC Press, Boca Raton, United states, 2021, pp. 437-471.

10. Suman, P. Sharma and P. Goyal, *Evolution of PV technology from conventional to nano-materials*, Materials Today: Proceedings, 2020, **28**, 1593-1597.

11. N. Asim, K. Sopian, S. Ahmadi, K. Saeedfar, M. A. Alghoul, O. Saadatian and S. H. Zaidi, *A review on the role of materials science in solar cells*, Renewable and Sustainable Energy Reviews, 2012, **16**, 5834-5847.

12. B. O'Regan and M. Gratzel, *A low-cost, high-efficiency solar cell based on dye-sensitized colloidal TiO₂ films*, Nature, 1991, **353**, 737-740.

13. H. Tributsch and M. Calvin, *Electrochemistry of excited molecules: photo-electrochemical reactions of chlorophylls*, Photochemistry and Photobiology, 1971, **14**, 95-112.

14. H. Tributsch, *Reaction of excited chlorophyll molecules at electrodes and in photosynthesis*, Photochemistry and Photobiology, 1972, **16**, 261-269.

15. M. Gratzel, *Solar energy conversion by dye-sensitized photovoltaic cells*, Inorganic Chemistry, 2005, **44**, 6841-6851.

16. R. Katoh, A. Furube, K. Hara, S. Murata, H. Sugihara, H. Arakawa and M. Tachiya, *Efficiencies of electron injection from excited sensitizer dyes to nanocrystalline ZnO films as studied by near-IR optical absorption of injected electrons*, The Journal of Physical Chemistry B, 2002, **106**, 12957-12964.

17. J. Gong, J. Liang and K. Sumathy, *Review on dye-sensitized solar cells (DSSCs): fundamental concepts and novel materials*, Renewable and Sustainable Energy Reviews, 2012, **16**, 5848-5860.

18. D.-J. Kwak, B.-H. Moon, D.-K. Lee, C.-S. Park and Y.-M. Sung, *Comparison of transparent conductive indium tin oxide, titanium-doped indium oxide, and fluorine-doped tin oxide films for dye-sensitized solar cell application*, Journal of Electrical Engineering Technology, 2011, **6**, 684-687.

19. N. Al-Dahoudi and M. Aegerter, *Comparative study of transparent conductive In₂O₃:Sn (ITO) coatings made using a sol and a nanoparticle suspension*, Thin Solid Films, 2006, **502**, 193-197.

20 M. Aouaj, R. Diaz, A. Belayachi and F. Rueda, *Comparative study of ITO and FTO thin films grown by spray pyrolysis*, Materials Research Bulletin, 2009, **44**, 1458-1461.

21. K. Sharma, V. Sharma and S. S. Sharma, *Dye-sensitized solar cells: fundamentals and current status*, Nanoscale Research Letters, 2018, **13**, 381.

22. R. Keshavarzi, V. Mirkhani, M. Moghadam, S. Tangestaninejad and I. Mohammadpoor-Baltork, *Performance enhancement of dye-sensitized solar cells based on TiO₂ thick mesoporous photoanodes by morphological manipulation*, Langmuir, 2015, **31**, 11659-11670.

23.	D. I. Suh, S. Y. Lee, T. H. Kim, J. M. Chun, E. K. Suh, O. B. Yang and S. K. Lee, *The fabrication and characterization of dye-sensitized solar cells with a branched structure of ZnO nanowires*, Chemical Physics Letters, 2007, **442**, 348-353.

24.	R. Vittal and K.-C. Ho, *Zinc oxide based dye-sensitized solar cells: a review*, Renewable and Sustainable Energy Reviews, 2017, **70**, 920-935.

25.	F. Lenzmann, J. Krueger, S. Burnside, K. Brooks, M. Gratzel, D. Gal, S. Ruhle and D. Cahen, *Surface Photovoltage spectroscopy of dye-sensitized solar cells with TiO_2, Nb_2O_5, and $SrTiO_3$ nanocrystalline photoanodes: indication for electron injection from higher excited dye states*, The Journal of Physical Chemistry B, 2001, **105**, 6347-6352.

26.	M. Memari and N. Memarian, *Designed structure of bilayer TiO_2–Nb_2O_5 photoanode for increasing the performance of dye-sensitized solar cells*, Journal of Materials Science: Materials in Electronics, 2020, **31**, 2298-2307.

27.	I. Y.-Y. Bu, *Light harvesting, self-assembled SnO nanoflakes for dye sensitized solar cell applications*, Optik, 2017, **147**, 39-42.

28.	T. L. Chiang, C. S. Chou, D. H. Wu and C. M. Hsiung, *Applications of p-type NiO in dye-sensitized solar cells*, Advanced Materials Research, 2011, **239-242**, 1747-1750.

29.	N. G. Park, J. van de Lagemaat and A. J. Frank, *Comparison of dye-sensitized rutile- and anatase-based TiO_2 solar cells*, The Journal of Physical Chemistry B, 2000, **104**, 8989-8994.

30.	L. Yang, B. Xu, D. Bi, H. Tian, G. Boschloo, L. Sun, A. Hagfeldt and E. M. J. Johansson, *Initial light soaking treatment enables hole transport material to outperform spiro-OMeTAD in solid-state dye-sensitized solar cells*, Journal of the American Chemical Society, 2013, **135**, 7378-7385.

31.	C.-P. Lee, C.-T. Li and K.-C. Ho, *Use of organic materials in dye-sensitized solar cells*, Materials Today, 2017, **20**, 267-283.

32.	H. Kusama and H. Arakawa, *Influence of pyrazole derivatives in I^-/I_3^- redox electrolyte solution on Ru(II)-dye-sensitized TiO_2 solar cell performance*, Solar Energy Materials and Solar Cells, 2005, **85**, 333-344.

33.	Z. Yu, N. Vlachopoulos, M. Gorlov and L. Kloo, *Liquid electrolytes for dye-sensitized solar cells*, Dalton Transactions, 2011, **40**, 10289-10303.

34.	A. Petrocco, M. Liberatore, A. D. Carlo, A. Reale, T. M. Brown and F. Decker, *Thermal activation of mass transport and charge transfer at Pt in the I^-/I_3^- electrolyte of a dye-sensitized solar cell*, Physical Chemistry Chemical Physics, 2010, **12**, 10786-10792.

35. M. Toivola, F. Ahlskog and P. Lund, *Industrial sheet metals for nanocrystalline dye-sensitized solar cell structures*, Solar Energy Materials and Solar Cells, 2006, **90**, 2881-2893.

36. M. Sumita, K. Sodeyama, L. Han and Y. Tateyama, *Water contamination effect on liquid acetonitrile/TiO₂ anatase (101) interface for durable dye-sensitized solar cell*, The Journal of Physical Chemistry C, 2011, **115**, 19849-19855.

37. N. Marinakis, M. Willgert, E. C. Constable and C. E. Housecroft, *Optimization of performance and long-term stability of p-type dye-sensitized solar cells with a cycloruthenated dye through electrolyte solvent tuning*, Sustainable Energy & Fuels, 2017, **1**, 626-635.

38. A. Subramania, E. Vijayakumar, N. Sivasankar, A. R. Sathiya Priya and K.-J. Kim, *Effect of different compositions of ethylene carbonate and propylene carbonate containing iodide/triiodide redox electrolyte on the photovoltaic performance of DSSC*, Ionics, 2013, **19**, 1649-1653.

39. L. Yang, R. Lindblad, E. Gabrielsson, G. Boschloo, H. Rensmo, L. Sun, A. Hagfeldt, T. Edvinsson and E. M. J. Johansson, *Experimental and theoretical investigation of the function of 4-tert-butyl pyridine for interface energy level adjustment in efficient solid-state dye-sensitized solar cells*, ACS Applied Materials & Interfaces, 2018, **10**, 11572-11579.

40. H.-S. Kim and N.-G. Park, *Parameters affecting I–V hysteresis of CH₃NH₃PbI₃ perovskite solar cells: effects of perovskite crystal size and mesoporous TiO₂ layer*, The Journal of Physical Chemistry Letters, 2014, **5**, 2927-2934.

41. M. A. Munoz-Garcia, O. Marin, M. C. Alonso-Garcia and F. Chenlo, *Characterisation of thin film PV modules under standard test conditions: results of indoor and outdoor measurements and the effects of sunlight exposure*, Solar Energy, 2012, **86**, 3049-3056.

42. H. Ahmed, J. Doran and S. J. McCormack, *External quantum efficiency measurements and outdoor characterisation for PV luminescent downshifting devices*, in *Renewable energy and sustainable buildings*, ed. A. Sayigh, Springer International Publishing, Cham, Switzerland, 2020, 727-733.

43. A. K. lrazzaq, G. Bognar and B. Plesz, *Evaluation of different methods for solar cells/modules parameters extraction*, Solar Energy, 2020, **196**, 183-195.

44. S. Umale, V. Sudhakar, S. M. Sontakke, K. Krishnamoorthy and A. B. Pandit, *Improved efficiency of DSSC using combustion synthesized TiO₂*, Materials Research Bulletin, 2019, **109**, 222-226.

45. M.-E. Yeoh and K.-Y. Chan, *Efficiency enhancement in dye-sensitized solar cells with ZnO and TiO$_2$ blocking layers*, Journal of Electronic Materials, 2019, **48**, 4342-4350.

46 K. Subalakshmi, K. A. Kumar, O. P. Paul, S. Saraswathy, A. Pandurangan and J. Senthilselvan, *Platinum-free metal sulfide counter electrodes for DSSC applications: structural, electrochemical and power conversion efficiency analyses*, Solar Energy, 2019, **193**, 507-518.

47. F. Zhao, R. Ma and Y. Jiang, *Strong efficiency improvement in dye-sensitized solar cells by novel multi-dimensional TiO$_2$ photoelectrode*, Applied Surface Science, 2018, **434**, 11-15.

48. K. Sharma, V. Sharma and S. Sharma, *Dye-sensitized solar cells: fundamentals and current status*, Nanoscale Research Letters, 2018, **13**, 381.

49. S. Dai, K. Wang, J. Weng, Y. Sui, Y. Huang, S. Xiao, S. Chen, L. Hu, F. Kong and X. Pan, *Design of DSC panel with efficiency more than 6%*, Solar Energy Materials and Solar Cells, 2005, **85**, 447-455.

50. A. Hinsch, J. Kroon, R. Kern, I. Uhlendorf, J. Holzbock, A. Meyer and J. Ferber, *Long-term stability of dye-sensitised solar cells*, Progress in Photovoltaics: Research and Applications, 2001, **9**, 425-438.

51. R. Kern, N. Van Der Burg, G. Chmiel, J. Ferber, G. Hasenhindl, A. Hinsch, R. Kinderman, J. Kroon, A. Meyer and T. Meyer, *Long term stability of dye-sensitised solar cells for large area power applications*, Opto-Electronics Review, 2000, **8**, 284-288.

52. H. Y. Chen, S. R. Wang, H. Lin, G. Wang, S. H. Wang and G. J. Yang, *Stability of dye sensitized solar cells with glass frit sealant*, Key Engineering Materials, 2012, **512-515**, 1619-1624.

53. I. Lee, S. Hwang and H. Kim, *Reaction between oxide sealant and liquid electrolyte in dye-sensitized solar cells*, Solar Energy Materials and Solar Cells, 2011, **95**, 315-317.

54. A. Lamberti, A. Sacco, S. Bianco, E. Giuri, M. Quaglio, A. Chiodoni and E. Tresso, *Microfluidic sealing and housing system for innovative dye-sensitized solar cell architecture*, Microelectronic Engineering, 2011, **88**, 2308-2310.

55. G. P. Rutkowski and B. A. Grimes, *Microfluidically augmented dye-sensitized solar cells: integrating nanoscale materials with microfluidics for performance and longevity enhancement*, ACS Applied Energy Materials, 2019, **2**, 6311-6321.

56. P. M. Sommeling, M. Späth, H. J. P. Smit, N. J. Bakker and J. M. Kroon, *Long-term stability testing of dye-sensitized solar cells*, Journal of Photochemistry and Photobiology A: Chemistry, 2004, **164**, 137-144.

57. T. Stergiopoulos, A. G. Kontos, N. Jiang, D. Milliken, H. Desilvestro, V. Likodimos and P. Falaras, *High boiling point solvent-based dye solar cells pass a harsh thermal ageing test*, Solar Energy Materials and Solar Cells, 2016, **144**, 457-466.

58. H. Chen, N. Li, Y.-H. Wu, J.-B. Shi, B.-X. Lei and Z.-F. J. A. P. T. Sun, *A novel cheap, one-step and facile synthesis of hierarchical TiO₂ nanotubes as fast electron transport channels for highly efficient dye-sensitized solar cells*, Advance Power Technology, 2020, **31**, 1556-1563 .

59. A. Listorti, B. O'Regan and J. R. Durrant, *Electron transfer dynamics in dye-sensitized solar cells*, Chemistry of Materials, 2011, **23**, 3381-3399.

60. M. Wang, P. Chen, R. Humphry-Baker, S. M. Zakeeruddin and M. Gratzel, *The influence of charge transport and recombination on the performance of dye-sensitized solar cells*, ChemPhysChem, 2009, **10**, 290-299.

61. E. Enache-Pommer, B. Liu and E. S. Aydil, *Electron transport and recombination in dye-sensitized solar cells made from single-crystal rutile TiO₂ nanowires*, Physical Chemistry Chemical Physics, 2009, **11**, 9648-9652.

62. A. J. Frank, N. Kopidakis and J. Van De Lagemaat, *Electrons in nanostructured TiO₂ solar cells: transport, recombination and photovoltaic properties*, Coordination Chemistry Reviews, 2004, **248**, 1165-1179.

63. J. Bisquert, D. Cahen, G. Hodes, S. Rühle and A. Zaban, *Physical chemical principles of photovoltaic conversion with nanoparticulate, mesoporous dye-sensitized solar cells*, The Journal of Physical Chemistry B, 2004, **108**, 8106-8118.

64. T. Le Bahers, F. Labat, T. Pauporté, P. P. Lainé and I. Ciofini, *Theoretical Procedure for optimizing dye-sensitized solar cells: from electronic structure to photovoltaic efficiency*, Journal of the American Chemical Society, 2011, **133**, 8005-8013.

65. S. Zhang, J. Jin, D. Li, Z. Fu, S. Gao, S. Cheng, X. Yu and Y. Xiong, *Increased power conversion efficiency of dye-sensitized solar cells with counter electrodes based on carbon materials*, RSC Advances, 2019, **9**, 22092-22100.

66. S. Ananthakumar, D. Balaji, J. Ram Kumar and S. Moorthy Babu, *Role of co-sensitization in dye-sensitized and quantum dot-sensitized solar cells*, SN Applied Sciences, 2019, **1**, 186.

67. B. O'Regan and M. Gratzel, *A low-cost, high-efficiency solar cell based on dye-sensitized colloidal TiO$_2$ films*, Nature, 1991, **353**, 737-740.

68. D. Zhang, Y. Liu, W. Wang and X. Xiao, *Chemical treatments of the nanocrystalline porous TiO$_2$ electrodes*, Chinese Science Bulletin, 2000, **45**, 1956-1959.

69. A. Islam, H. Sugihara and H. Arakawa, *Molecular design of ruthenium(II) polypyridyl photosensitizers for efficient nanocrystalline TiO$_2$ solar cells*, Journal of Photochemistry and Photobiology A: Chemistry, 2003, **158**, 131-138.

70. S. S. Kanmani, I. John Peter, A. Muthu Kumar, P. Nithiananthi, C. Raja Mohan and K. Ramachandran, *Binary semiconductor metal oxide as photoanodes, in Interfacial engineering in functional materials for dye-sensitized solar cells*, eds. K. B. Bhojanaa, K. Jothivenkatachalam, A. Pandikumar, John Wiley and Sons Inc., Hoboken, New Jersey, 2019, 163-192.

71. A. Kunzmann, M. Stanzel, W. Peukert, R. D. Costa and D. M. Guldi, *Binary indium–zinc oxide photoanodes for efficient dye-sensitized solar cells*, Advanced Energy Materials, 2016, **6**, 1501075.

72. F. Zhu, P. Zhang, X. Wu, L. Fu, J. Zhang and D. Xu, *The origin of higher open-circuit voltage in Zn-doped TiO$_2$ nanoparticle-based dye-sensitized solar cells*, ChemPhysChem, 2012, **13**, 3731-3737.

73. S. K. M. Saad, A. A. Umar, M. Y. A. Rahman and M. M. Salleh, *Porous Zn-doped TiO$_2$ nanowall photoanode: effect of Zn^{2+} concentration on the dye-sensitized solar cell performance*, Applied Surface Science, 2015, **353**, 835-842.

74. Y. Duan, N. Fu, Q. Liu, Y. Fang, X. Zhou, J. Zhang and Y. Lin, *Sn-Doped TiO$_2$ photoanode for dye-sensitized solar cells*, The Journal of Physical Chemistry C, 2012, **116**, 8888-8893.

75. S. Thogiti, J. Y. Park, C. T. Thanh Thuy, D. K. Lee, B.-K. Min, H. J. Yun and J. H. Kim, *High-performance dye-sensitized solar cells through graded electron transport in band-engineered W-TiO$_2$ cascade layer*, ACS Sustainable Chemistry & Engineering, 2018, **6**, 13025-13034.

76. L. Zhou, L. Wei, Y. Yang, X. Xia, P. Wang, J. Yu and T. Luan, *Improved performance of dye sensitized solar cells using Cu-doped TiO$_2$ as photoanode materials: band edge movement study by spectroelectrochemistry*, Chemical Physics, 2016, **475**, 1-8.

77. M. Dhonde, K. Sahu and V. Murty, *Cu-doped TiO$_2$ nanoparticles/graphene composites for efficient dye-sensitized solar cells*, Solar Energy, 2021, **220**, 418-424.

78. A. N. El-Shazly, A. E. Shalan, M. M. Rashad, E. A. Abdel-Aal, I. A. Ibrahim and M. F. El-Shahat, *Solid-state dye-sensitized solar cells based on $Zn_{1-x}Sn_xO$ nanocomposite photoanodes*, RSC Advances, 2018, **8**, 24059-24067.

79. H. Melhem, P. Simon, J. Wang, C. Di Bin, B. Ratier, Y. Leconte, N. Herlin-Boime, M. Makowska-Janusik, A. Kassiba and J. Boucle, *Direct photocurrent generation from nitrogen doped TiO_2 electrodes in solid-state dye-sensitized solar cells: towards optically-active metal oxides for photovoltaic applications*, Solar Energy Materials and Solar Cells, 2013, **117**, 624-631.

80. K. Li, Q. Sun, S. Wu, D. You, T. Zang, L. Yu, L. Sui and L. Dong, *The remarkable morphology regulatory effect of NH_4^+ ions on TiO_2 nanorod arrays and their application in dye-sensitized solar cells*, Applied Physics A, 2019, **125**, 245.

81. W. Guo, Y. Shen, G. Boschloo, A. Hagfeldt and T. Ma, *Influence of nitrogen dopants on N-doped TiO_2 electrodes and their applications in dye-sensitized solar cells*, Electrochimica Acta, 2011, **56**, 4611-4617.

82. A. Subramanian and H.-W. Wang, *Effects of boron doping in TiO_2 nanotubes and the performance of dye-sensitized solar cells*, Applied Surface Science, 2012, **258**, 6479-6484.

83. X. Hu, K. Huang, D. Fang and S. Liu, *Enhanced performances of dye-sensitized solar cells based on graphite–TiO_2 composites*, Materials Science and Engineering: B, 2011, **176**, 431–435.

84. S. Kim, O. Dovjuu, S.-H. Choi, H. Jeong and J.-T. Park, *Photovoltaic characteristics of multiwalled carbon nanotube counter-electrode materials for dye-sensitized solar cells produced by chemical treatment and addition of dispersant*, Coatings, 2019, **9**, 250.

85. S. D. Delekar, A. G. Dhodamani, K. V. More, T. D. Dongale, R. K. Kamat, S. F. Acquah, N. S. Dalal and D. K. Panda, *Structural and optical properties of nanocrystalline TiO_2 with multiwalled carbon nanotubes and its photovoltaic studies using Ru (II) sensitizers*, ACS Omega, 2018, **3**, 2743-2756.

86. S. Muduli, W. Lee, V. Dhas, S. Mujawar, M. Dubey, K. Vijayamohanan, S.-H. Han and S. Ogale, *Enhanced conversion efficiency in dye-sensitized solar cells based on hydrothermally synthesized $TiO_2-MWCNT$ nanocomposites*, ACS Applied Materials & Interfaces, 2009, **1**, 2030-2035.

87.   K.-M. Lee, C.-W. Hu, H.-W. Chen and K.-C. Ho, *Incorporating carbon nanotube in a low-temperature fabrication process for dye-sensitized TiO₂ solar cells*, Solar Energy Materials and Solar Cells, 2008, **92**, 1628-1633.

88.   G. Sharma, D. Daphnomili, K. Gupta, T. Gayathri, S. Singh, P. Angaridis, T. Kitsopoulos, D. Tasis and A. Coutsolelos, *Enhancement of power conversion efficiency of dye-sensitized solar cells by co-sensitization of zinc-porphyrin and thiocyanate-free ruthenium (II)-terpyridine dyes and graphene modified TiO₂ photoanode*, RSC Advances, 2013, **3**, 22412-22420.

89.   X. Luo, Y. Zhang and S. H. Kim, *Incorporation of nanostructured carbon composite materials into counter electrodes for highly efficient dye-sensitized solar cells*, Nanoscale Research Letters, 2018, **13**, 274.

90.   S. Thomas, T. G. Deepak, G. S. Anjusree, T. A. Arun, S. V. Nair and A. S. Nair, *A review on counter electrode materials in dye-sensitized solar cells*, Journal of Materials Chemistry A, 2014, **2**, 4474-4490.

91.   M. Wu and T. Ma, *Recent progress of counter electrode catalysts in dye-sensitized solar cells*, The Journal of Physical Chemistry C, 2014, **118**, 16727-16742.

92.   S. S. B. Gunasekera, I. R. Perera and S. S. Gunathilaka, *Conducting polymers as cost effective counter electrode material in dye-sensitized solar cells*, in *Solar energy*, eds. C. P. Tyagi H., Powar S., Agarwal A., Springer, Singapore, Asia, 2020, 345-371.

93.   J. Yang, Y. Niu, J. Huang, L. Liu and X. Qian, *N-doped C/CoSe₂@Co–FeSe₂ yolk-shell nano polyhedron as superior counter electrode catalyst for high-efficiency Pt-free dye-sensitized solar cell*, Electrochimica Acta, 2020, **330**, 135333.

94.   X. Zhang, X. Chen, K. Zhang, S. Pang, X. Zhou, H. Xu, S. Dong, P. Han, Z. Zhang and C. Zhang, *Transition-metal nitride nanoparticles embedded in N-doped reduced graphene oxide: superior synergistic electrocatalytic materials for the counter electrodes of dye-sensitized solar cells*, Journal of Materials Chemistry A, 2013, **1**, 3340-3346.

95.   M. Wu, X. Lin, Y. Wang, L. Wang, W. Guo, D. Qi, X. Peng, A. Hagfeldt, M. Gratzel and T. Ma, *Economical Pt-free catalysts for counter electrodes of dye-sensitized solar cells*, Journal of the American Chemical Society, 2012, **134**, 3419-3428.

96.   P. Vijayakumar, R. Govindaraj, N. Santhosh, M. S. Pandian, A. Pandikumar and P. Ramasamy, *Investigation of suitable binder combination and electrochemical charge transfer dynamics of vanadium carbide nanoparticles-based counter electrode in Pt-free dye-sensitized solar cell*, Journal of Materials Science, 2018, **53**, 4444-4455.

97. M. Wu, J. Bai, Y. Wang, A. Wang, X. Lin, L. Wang, Y. Shen, Z. Wang, A. Hagfeldt and T. Ma, *High-performance phosphide/carbon counter electrode for both iodide and organic redox couples in dye-sensitized solar cells*, Journal of Materials Chemistry, 2012, **22**, 11121-11127.

98. S. Sarker, K.-S. Lee, H. W. Seo, Y.-K. Jin and D. M. Kim, *Reduced graphene oxide for Pt-free counter electrodes of dye-sensitized solar cells*, Solar Energy, 2017, **158**, 42-48.

99. Neetu, I. C. Maurya, A. K. Gupta, P. Srivastava and L. Bahadur, *Extensive enhancement in power conversion efficiency of dye-sensitized solar cell by using Al-doped TiO_2 photoanode*, Journal of Solid State Electrochemistry, 2017, **21**, 1229-1241.

100. Z. Tong, T. Peng, W. Sun, W. Liu, S. Guo and X.-Z. Zhao, *Introducing an intermediate band into dye-sensitized solar cells by W^{6+} doping into TiO_2 nanocrystalline photoanodes*, The Journal of Physical Chemistry C, 2014, **118**, 16892-16895.

101. F. A. Unal, S. Ok, M. Unal, S. Topal, K. Cellat and F. Şen, *Synthesis, characterisation, and application of transition metals (Ni, Zr, and Fe) doped TiO_2 photoelectrodes for dye-sensitized solar cells*, Journal of Molecular Liquids, 2020, **299**, 112177.

102. D.-T. Nguyen, Y. Kurokawa and K. Taguchi, *Enhancing DSSC Photoanode performance by using Ni-Doped TiO_2 to fabricate scattering layers*, Journal of Electronic Materials, 2020, **49**, 2578-2583.

103. R. Ghayoor and M. N. S. Rad, *Facile preparation of TiO_2 nanoparticles decorated by the graphene for enhancement of dye-sensitized solar cell performance*, Journal of Materials Research, 2019, **34**, 2014-2023.

104. M. Motlak, M. S. Akhtar, N. A. M. Barakat, A. M. Hamza, O. B. Yang and H. Y. Kim, *High-efficiency electrode based on nitrogen-doped TiO_2 nanofibers for dye-sensitized solar cells*, Electrochimica Acta, 2014, **115**, 493-498.

105. M. Mousa, M. Khairy and H. Mohamed, *Dye-sensitized solar cells based on an n-doped TiO_2 and TiO_2-graphene composite electrode*, Journal of Electronic Materials, 2018, **47**, 6241-6250.

106 M. Mohammadnezhad, G. S. Selopal, Z. M. Wang, B. Stansfield, H. Zhao and F. Rosei, *Role of carbon nanotubes to enhance the long-term stability of dye-sensitized solar cells*, ACS Photonics, 2020,**7**, 653-664.

107. M. F. Don, P. Ekanayake, H. Nakajima, A. H. Mahadi, C. M. Lim and A. Atod, *Acetylene carbon black-graphite composite as low-cost and efficient counter electrode for dye-sensitized solar cells (DSSCs)*, Ionics, 2019, **25**, 5585-5593.

108. Y. Luo, J. Shen, R. Cheng, X. Chen, Y. Chen, Z. Sun and s. Huang, *Facile synthesis of mixed-phase cobalt sulfide counter electrodes for efficient dye sensitized solar cells*, Journal of Materials Science: Materials in Electronics, 2014, **26**, 42-48.

109. K. Pattarith and Y. Areerob, *Fabrication of Ag nanoparticles adhered on rGO based on both electrodes in dye-sensitized solar cells (DSSCs)*, Renewables: Wind, Water, and Solar, 2020, **7,** 1-10.

110. J. Weszka, M. Szindler, M. Szczęsna and M. Szindler, *Influence of solvent on the surface morphology and optoelectronic properties of a spin coated polymer thin films*, Journal of Achievements in Materials and Manufacturing Engineering, 2013, **61**, 302-307.

111. Z. K. Yildiz, A. Atilgan, A. Atli, K. Ozel, C. Altinkaya and A. Yildiz, *Enhancement of efficiency of natural and organic dye sensitized solar cells using thin film TiO_2 photoanodes fabricated by spin-coating*, Journal of Photochemistry and Photobiology A: Chemistry, 2019, **368**, 23-29.

112. H. M. Aung Kyaw, K. A. Yaacob, A. F. Mohd Noor, A. Matsuda and G. Kawamura, *Effect of deposition time $CdSe$-TiO_2 nanocomposite film by electrophoretic deposition for quantum dot sensitized solar cell*, Materials Today: Proceedings, 2019, **17**, 736-742.

113. D. Cao, H. Yin, X. Yu, J. Zhang, Y. Jiao, W. Zheng, B. Mi and Z. Gao, *Role of modifying photoanodes by organic titanium on charge collection efficiency enhancement in dye-sensitized solar cells*, Advanced Engineering Materials, 2019, **22**, 1901071.

114. P. Amrollahi, J. S. Krasinski, R. Vaidyanathan, L. Tayebi and D. Vashaee, *Electrophoretic deposition (EPD): fundamentals and applications from nano- to microscale structures, in Handbook of nanoelectrochemistry: electrochemical synthesis methods, properties, and characterization techniques*, eds. M. Aliofkhazraei and A. S. H. Makhlouf, Springer International Publishing, Cham, Switzerland, 2016, 561-591.

114. M. R. Al-bahrani, W. Ahmad, H. F. Mehnane, Y. Chen, Z. Cheng and Y. Gao, *Enhanced electrocatalytic activity by rGO/MWCNTs/NiO counter electrode for dye-sensitized solar cells*, Nano-Micro Letters, 2015, **7**, 298-306.

116. M. Kouhnavard, N. A. Ludin, B. V. Ghaffari, S. Ikeda, K. Sopian and M. Miyake, *Hydrophilic carbon/TiO_2 colloid composite: a potential counter electrode for dye-sensitized solar cells*, Journal of Applied Electrochemistry, 2016, **46**, 259-266.

117. J. P. Sawant and R. B. Kale, *CZTS counter electrode in dye-sensitized solar cell: enhancement in photo conversion efficiency with morphology of TiO₂ nanostructured thin films*, Journal of Solid State Electrochemistry, 2020, **24**, 461-472.

118. W. Yu, L. Sisi, Y. Haiyan and L. Jie, *Progress in the functional modification of graphene/graphene oxide: a review*, RSC Advances, 2020, **10**, 15328-15345.

119. R. G. Bai, K. Muthoosamy, S. Manickam and A. Hilal-Alnaqbi, *Graphene-based 3D scaffolds in tissue engineering: fabrication, applications, and future scope in liver tissue engineering*, International Journal of Nanomedicine, 2019, **14**, 5753.

120 X. Wang and G. Shi, *An introduction to the chemistry of graphene*, Physical Chemistry Chemical Physics, 2015, **17**, 28484-28504.

121. D. R. Dreyer, A. D. Todd and C. W. Bielawski, *Harnessing the chemistry of graphene oxide*, Chemical Society Reviews, 2014, **43**, 5288-5301.

122. C. K. Chua and M. Pumera, *Covalent chemistry on graphene*, Chemical Society Reviews, 2013, **42**, 3222-3233.

123. T. Torres, *Graphene chemistry*, Chemical Society Reviews, 2017, **46**, 4385-4386.

124. C. Li, X. Chen, L. Shen and N. Bao, *Revisiting the oxidation of graphite: reaction mechanism, chemical stability, and structure self-regulation*, ACS Omega, 2020, **5**, 3397-3404.

125. B. C. Brodie, *XIII. On the atomic weight of graphite*, Philosophical Transactions of the Royal Society of London, 1859, **149**, 249-259.

126. W. S. Hummers Jr and R. E. Offeman, *Preparation of graphitic oxide*, Journal of the American Chemical Society, 1958, **80**, 1339-1339.

127. L. Staudenmaier, *Verfahren zur darstellung der graphitsaure*, Berichte Der Deutschen Chemischen Gesellschaft, 1898, **31**, 1481-1487.

128. D. C. Marcano, D. V. Kosynkin, J. M. Berlin, A. Sinitskii, Z. Sun, A. Slesarev, L. B. Alemany, W. Lu and J. M. Tour, *Improved synthesis of graphene oxide*, ACS Nano, 2010, **4**, 4806-4814.

129. D. Marcin Behunová, G. Gallios, V. Girman, H. Kolev, M. Kaňuchová, S. Dolinská and M. Václavíková, *Electrophoretic deposition of graphene oxide on stainless steel substrate*, Nanomaterials, 2021, **11**, 1779.

130. Y. Zhang, H.-L. Ma, Q. Zhang, J. Peng, J. Li, M. Zhai and Z.-Z. Yu, *Facile synthesis of well-dispersed graphene by γ-ray induced reduction of graphene oxide*, Journal of Materials Chemistry, 2012, **22**, 13064-13069.

131. L. F. Dumée, C. Feng, L. He, Z. Yi, F. She, Z. Peng, W. Gao, C. Banos, J. B. Davies, C. Huynh, S. Hawkins, M. C. Duke, S. Gray, P. D. Hodgson and L. Kong, *Single step preparation of meso-porous and reduced graphene oxide by gamma-ray irradiation in gaseous phase*, Carbon, 2014, **70**, 313-318.

132. G. Williams, B. Seger and P. V. Kamat, *TiO₂-graphene nanocomposites. UV-assisted photocatalytic reduction of graphene oxide*, ACS Nano, 2008, **2**, 1487-1491.

133. L. J. Cote, R. Cruz-Silva and J. Huang, *Flash reduction and patterning of graphite oxide and its polymer composite*, Journal of the American Chemical Society, 2009, **131**, 11027-11032.

134. W. Wang, Y. Wu, Z. Jiang, M. Wang, Q. Wu, X. Zhou and X. Ge, *Formation mechanism of 3D macroporous graphene aerogel in alcohol-water media under gamma-ray radiation*, Applied Surface Science, 2018, **427**, 1144-1151.

135. Y. Matsumoto, M. Koinuma, S. Y. Kim, Y. Watanabe, T. Taniguchi, K. Hatakeyama, H. Tateishi and S. Ida, *Simple photoreduction of graphene oxide nanosheet under mild conditions*, ACS Applied Materials & Interfaces, 2010, **2**, 3461-3466.

136. M. Matsumoto, Y. Saito, C. Park, T. Fukushima and T. Aida, *Ultrahigh-throughput exfoliation of graphite into pristine 'single-layer' graphene using microwaves and molecularly engineered ionic liquids*, Nature Chemistry, 2015, **7**, 730-736.

137. D. Voiry, J. Yang, J. Kupferberg, R. Fullon, C. Lee, H. Y. Jeong, H. S. Shin and M. Chhowalla, *High-quality graphene via microwave reduction of solution-exfoliated graphene oxide*, Science, 2016, **353**, 1413-1416.

138. S. Tang, S. Jin, R. Zhang, Y. Liu, J. Wang, Z. Hu, W. Lu, S. Yang, W. Qiao, L. Ling and M. Jin, *Effective reduction of graphene oxide via a hybrid microwave heating method by using mildly reduced graphene oxide as a susceptor*, Applied Surface Science, 2019, **473**, 222-229.

139. F. Xie, G. Dong, K. Wu, Y. Li, M. Wei and S. Du, *In situ topological transformation of hierarchical TiO₂ hollow nanobricks as efficient scattering layer for dye-sensitized solar cells*, Chemical Physics Letters, 2020, **739**, 136996.

140. X. Cao, C. Xu, X. Liang, J. Ma, M. Yue and Y. Ding, *Rationally designed/assembled hybrid BiVO₄-based photoanode for enhanced photoelectrochemical performance*, Applied Catalysis B: Environmental, 2020, **260**, 118136.

141. C. Kim, K.-S. Kim, H. Y. Kim and Y. S. Han, *Modification of a TiO₂ photoanode by using Cr-doped TiO₂ with an influence on the photovoltaic efficiency of a dye-sensitized solar cell*, Journal of Materials Chemistry, 2008, **18**, 5809-5814.

142. S. B. Humam, H. H. Nguyen, C. Regmi, G. Gyawali, B. Joshi and S. W. Lee, *Effect of Cr-doping on the physicochemical properties of blue TiO$_2$ and its application in dye-sensitized solar cells via low-temperature fabrication process*, Ceramics International, 2019, **45**, 4230-4236.

143. S. Ni, F. Guo, D. Wang, S. Jiao, J. Wang, Y. Zhang, B. Wang, P. Feng and L. Zhao, *Modification of TiO$_2$ nanowire arrays with Sn doping as photoanode for highly efficient dye-sensitized solar cells*, Crystals, 2019, **9**, 113.

144. S. Iwamoto, Y. Sazanami, M. Inoue, T. Inoue, T. Hoshi, K. Shigaki, M. Kaneko and A. Maenosono, *Fabrication of dye-sensitized solar cells with an open-circuit photovoltage of 1-V*, ChemSusChem: Chemistry Sustainability Energy and Materials, 2008, **1**, 401-403.

145. H. Usui, Y. Domi, K. Takama, Y. Tanaka and H. Sakaguchi, *Tantalum-doped titanium oxide with rutile structure as a novel anode material for sodium-ion battery*, ACS Applied Energy Materials, 2019, **2**, 3056-3060.

146. S. Iwamoto, Y. Sazanami, M. Inoue, T. Inoue, T. Hoshi, K. Shigaki, M. Kaneko and A. Maenosono, *Fabrication of dye-sensitized solar cells with an open-circuit photovoltage of 1-V*, ChemSusChem: Chemistry & Sustainability Energy & Materials, 2008, **1**, 401-403.

147. J.-M. Song, P.-J. Wang, L.-H. Chan, C.-M. Chen, W.-F. Ho and S.-Y. Chen, *Efficiency enhancement of dye-sensitized solar cells using Ti–Nb alloy photoanodes with mesoporous oxide surface*, Journal of the Electrochemical Society, 2020, **167**, 046501.

148. X. Feng, K. Shankar, M. Paulose and C. A. Grimes, *Tantalum-doped titanium dioxide nanowire arrays for dye-sensitized solar cells with high open-circuit voltage*, Angewandte Chemie International Edition, 2009, **48**, 8095-8098.

149. H. Krysova, P. Mazzolini, C. S. Casari, V. Russo, A. L. Bassi and L. Kavan, *Electrochemical properties of transparent conducting films of tantalum-doped titanium dioxide*, Electrochimica Acta, 2017, **232**, 44-53.

150. T. Ma, M. Akiyama, E. Abe and I. Imai, *High-efficiency dye-sensitized solar cell based on a nitrogen-doped nanostructured titania electrode*, Nano Letters, 2005, **5**, 2543-2547.

151. S. H. Kang, H. S. Kim, J.-Y. Kim and Y.-E. Sung, *Enhanced photocurrent of nitrogen-doped TiO$_2$ film for dye-sensitized solar cells*, Materials Chemistry and Physics, 2010, **124**, 422-426.

152. P. Sudhagar, K. Asokan, E. Ito and Y. S. Kang, *N-ion-implanted TiO₂ photoanodes in quantum dot-sensitized solar cells*, Nanoscale, 2012, **4**, 2416-2422.

153. S. Shogh, R. Mohammadpour, A. Iraji zad and N. Taghavinia, *A new strategy on utilizing nitrogen doped TiO₂ in nanostructured solar cells: embedded multifunctional N-TiO₂ scattering particles in mesoporous photoanode*, Materials Research Bulletin, 2015, **72**, 64-69.

154. M. A. Mousa, M. Khairy and H. M. Mohamed, *Dye-sensitized solar cells based on an N-Doped TiO₂ and TiO₂-graphene composite electrode*, Journal of Electronic Materials, 2018, **47**, 6241-6250.

155. N. Gao, T. Wan, Z. Xu, L. Ma, S. Ramakrishna and Y. Liu, *Nitrogen doped TiO₂/graphene nanofibers as dsscs photoanode*, Materials Chemistry and Physics, 2020, **255**, 123542.

156. A. Ghicov, J. M. Macak, H. Tsuchiya, J. Kunze, V. Haeublein, L. Frey and P. Schmuki, *Ion implantation and annealing for an efficient N-doping of TiO₂ nanotubes*, Nano Letters, 2006, **6**, 1080-1082.

157. J. Marques, T. D. Gomes, M. A. Forte, R. F. Silva and C. J. Tavares, *A new route for the synthesis of highly-active N-doped TiO₂ nanoparticles for visible light photocatalysis using urea as nitrogen precursor*, Catalysis Today, 2019, **326**, 36-45.

158. F. Peng, L. Cai, L. Huang, H. Yu and H. Wang, *Preparation of nitrogen-doped titanium dioxide with visible-light photocatalytic activity using a facile hydrothermal method*, Journal of Physics and Chemistry of Solids, 2008, **69**, 1657-1664.

159. S. Hu, A. Wang, X. Li and H. Löwe, *Hydrothermal synthesis of well-dispersed ultrafine N-doped TiO₂ nanoparticles with enhanced photocatalytic activity under visible light*, Journal of Physics and Chemistry of Solids, 2010, **71**, 156-162.

160. R. Barkul, V. Koli, V. Shewale, M. Patil and S. Delekar, *Visible active nanocrystalline N-doped anatase TiO₂ particles for photocatalytic mineralization studies*, Materials Chemistry and Physics, 2016, **173**, 42-51.

161. W. Zhao, S. Liu, S. Zhang, R. Wang and K. Wang, *Preparation and visible-light photocatalytic activity of N-doped TiO₂ by plasma-assisted sol-gel method*, Catalysis Today, 2019, **337**, 37-43.

162. Z. Wang, Y. Zhang, E. C. Neyts, X. Cao, X. Zhang, B. W. L. Jang and C.-J. Liu, *Catalyst preparation with plasmas: how does it work?*, ACS Catalysis, 2018, **8**, 2093-2110.

163. M. Sturini, F. Maraschi, A. Cantalupi, L. Pretali, S. Nicolis, D. Dondi, A. Profumo, V. Caratto, E. Sanguineti and M. Ferretti, *TiO₂ and N-TiO₂ sepiolite and zeolite composites for photocatalytic removal of ofloxacin from polluted water*, Materials, 2020, **13**, 537.

164. L. A. Kolahalam, I. K. Viswanath, B. S. Diwakar, B. Govindh, V. Reddy and Y. Murthy, *Review on nanomaterials: synthesis and applications*, Materials Today: Proceedings, 2019, **18**, 2182-2190.

165. U. Riaz, T. Mehmood, S. Iqbal, M. Asad, R. Iqbal, U. Nisar and M. Masood Akhtar, *Historical background, development and preparation of nanomaterials*, in *Nanotechnology: trends and future applications*, eds. M. B. Tahir, M. Rafique and M. Sagir, Springer, Singapore, Asia, 2021, 1-13.

166. Y. Liang, S. Sun, T. Deng, H. Ding, W. Chen and Y. Chen, *The preparation of TiO₂ film by the sol-gel method and evaluation of its self-cleaning property*, Materials, 2018, **11**, 450.

167. J. Shen, B. Yan, M. Shi, H. Ma, N. Li and M. Ye, *One step hydrothermal synthesis of TiO₂-reduced graphene oxide sheets*, Journal of Materials Chemistry, 2011, **21**, 3415-3421.

168. T. Suwannaruang, K. Kamonsuangkasem, P. Kidkhunthod, P. Chirawatkul, C. Saiyasombat, N. Chanlek and K. Wantala, *Influence of nitrogen content levels on structural properties and photocatalytic activities of nanorice-like N-doped TiO₂ with various calcination temperatures*, Materials Research Bulletin, 2018, **105**, 265-276.

169. B. Kılıç, *Interface effect of graphene–TiO₂ photoanode with CuO nanorod counter electrode on solar conversion efficiency and enhanced external quantum efficiency*, Optical and Quantum Electronics, 2019, **51**, 208.

170. B. J. Inkson, *2-Scanning electron microscopy (SEM) and transmission electron microscopy (TEM) for materials characterization*, in *Materials characterisation using nondestructive evaluation (NDE) methods*, eds. G. Hubschen, I. Altpeter, R. Tschuncky and H.-G. Herrmann, Woodhead Publishing, Cambridge, England, 2016, 17-43.

171. H. Ardebili and M. G. Pecht, *Chapter 6-Defect and failure analysis techniques for encapsulated microelectronics, in Encapsulation technologies for electronic applications*, eds. H. Ardebili and M. G. Pecht, William Andrew Publishing, Oxford, UK, 2009, 287-350

172. K. Inaba, S. Kobayashi, K. Uehara, A. Okada, S. Reddy and T. Endo, *High resolution X-ray diffraction analyses of (La,Sr)MnO₃/ZNO/sapphire(0001) double heteroepitaxial films*, Advances in Materials Physics and Chemistry, 2013, **3**, 72-89.

173. S. Loganathan, R. B. Valapa, R. K. Mishra, G. Pugazhenthi and S. Thomas, *Chapter 4-Thermogravimetric analysis for characterization of nanomaterials*, in *Thermal and rheological measurement techniques for nanomaterials characterization*, eds. S. Thomas, R. Thomas, A. K. Zachariah and R. K. Mishra, Elsevier, Amsterdam, Netherlands, 2017, 67-108.

174. A. Hegazy, N. Kinadjian, B. Sadeghimakki, S. Sivoththaman, N. K. Allam and E. Prouzet, *TiO$_2$ nanoparticles optimized for photoanodes tested in large area dye-sensitized solar cells (DSSC)*, Solar Energy Materials and Solar Cells, 2016, **153**, 108-116.

175. L. Liu, Y. Zhang, B. Zhang and Y. Feng, *A detailed investigation on the performance of dye-sensitized solar cells based on reduced graphene oxide-doped TiO$_2$ photoanode*, Journal of Materials Science, 2017, **52**, 8070-8083.

176. K. S. Sing, *Reporting physisorption data for gas/solid systems with special reference to the determination of surface area and porosity (recommendations 1984)*, Pure and Applied Chemistry, 1985, **57**, 603-619.

177. Z. Alothman, *A review: fundamental aspects of silicate mesoporous materials*, Materials, 2012, **5**, 2874-2902.

178. Y. Hu, *Nitrogen doping of mesoporous carbon materials, in Carbon and metal oxides based nanomaterials for flexible high performance asymmetric supercapacitors*, ed. Y. Hu, Springer, Singapore, Asia, 2018, 35-47.

179. Z. Alothman, *A review: fundamental aspects of silicate mesoporous materials*, Materials, 2012, **5**, 2874-2902.

180. X. S. Zhao, G. Lu and G. J. Millar, *Advances in mesoporous molecular sieve MCM-41*, Industrial & Engineering Chemistry Research, 1996, **35**, 2075-2090.

181. M. Hafez, I. Yahia and S. Taha, *Study of the diffused reflectance and microstructure for the phase transformation of KNO$_3$*, Acta Physica Polonica, A., 2015, **127**.

182. V. Mahalingam, *Synthesis, growth and characterisation of piperazinium p-aminobenzoate and piperazinium p-chlorobenzoate nonlinear optical single crystals,* Master of Science in Physics, Alagappa University, Karaikudi, India, 2018.

183. X. Fan, N. Hua, H. Jia, Y. Zhu, Z. Wang, J. Xu and C. Wang, *Synthesis and evaluation of visible-light photocatalyst: nitrogen-doped TiO$_2$/Bi$_2$O$_3$ heterojunction structures*, Science of Advanced Materials, 2014, **6**, 1892-1899.

184. S. W. Chong, C. W. Lai, J. C. Juan and B. F. Leo, *An investigation on surface modified TiO₂ incorporated with graphene oxide for dye-sensitized solar cell*, Solar Energy, 2019, **191**, 663-671.

185. D. Bersani, G. Antonioli, P. P. Lottici and T. Lopez, *Raman study of nanosized titania prepared by sol–gel route*, Journal of Non-Crystalline Solids, 1998, **232-234**, 175-181.

186. D. Regonini, *Anodised TiO₂ nanotubes: synthesis, growth mechanism and thermal stability*, Doctor of Philosophy, University of Bath, Bath, UK, 2008.

187. D. Titus, E. James Jebaseelan Samuel and S. M. Roopan, *Chapter 12-Nanoparticle characterization techniques*, in *Green synthesis, characterization and applications of nanoparticles*, eds. A. K. Shukla and S. Iravani, Elsevier, Amsterdam, Netherlands, 2019, 303-319.

188. C. Morrison, H. Sun, Y. Yao, R. A. Loomis and W. E. Buhro, *Methods for the ICP-OES analysis of semiconductor materials*, Chemistry of Materials, **32**, 1760-1768, 2020.

189. F. Caruso, S. Mantellato, M. Palacios and R. J. Flatt, *ICP-OES method for the characterisation of cement pore solutions and their modification by polycarboxylate-based superplasticizers*, Cement and Concrete Research, 2017, **91**, 52-60.

Chapter 3

Synthesis and characterisation of the physicochemical properties of a N-doped TiO$_2$/Bi$_2$O$_3$ heterojunction-structured nanomaterial

This chapter presents a brief introduction to titanium dioxide (TiO$_2$) and, subsequently, details the synthesis and characterisation of the N-TiO$_2$/Bi$_2$O$_3$ nanomaterial. The results of the characterisation are presented and discussed. In the present work, the preparation of the N-TiO$_2$/Bi$_2$O$_3$ was divided into two parts. Firstly, TiO$_2$ was doped with nitrogen and, secondly, this was followed by coupling of N-TiO$_2$ with Bi$_2$O$_3$.

3.1. Introduction

Titanium dioxide (TiO$_2$) is an important material for photovoltaic [1] and photocatalytic [2] applications. However, the rapid recombination of the electron-hole pairs in TiO$_2$ lowers its photocatalytic activity [3]. Hence, enormous efforts have been undertaken to improve the efficiency of TiO$_2$ by suppressing the recombination of electron-hole pairs. These include doping with non-metal elements [4] and coupling with suitable semiconductors, as two alternative ways to enhance the photocatalytic activity by suppressing the recombination of electron-hole pairs [5, 6]. As a results, N-doped TiO$_2$ has become realizable and appears to enhance the photocatalytic activity of TiO$_2$ [7]. Also, coupling with another semiconductor, such as Bi$_2$O$_3$, favours the occurrence of good separation and transport of the charge carriers photogenerated to inhibit recombination in TiO$_2$ due to the photosensitisation effect of Bi$_2$O$_3$ [8]. Consequently, to the best of our knowledge, the preparation of N-TiO$_2$/Bi$_2$O$_3$ heterojunction-structured nanomaterials can provide deep insight into the intrinsic and extrinsic fundamentals of enhancing the photocatalytic activity of TiO$_2$. Thus, this work aimed to prepare and characterise a N-TiO$_2$/Bi$_2$O$_3$ nanomaterial with different amounts of Bi$_2$O$_3$ in weight percent, and deduce that it exhibits a good charge carrier separation.

3.2. Experimental

This section provides details on the materials used to synthesise the targeted materials and, subsequently, provides the synthetic and characterization approaches.

3.2.1. Materials

All the chemicals, solvents and reagents used in the synthesis were used as received without further purification, and their sources and purity or grade are listed in Table 3.1. The water used in the syntheses was from a double-distilled machine.

Table 3.1: Chemicals, solvents and reagents used in the synthesis

Reagent/solvents	Supplier	Grade/Purity percentage
Titanium(IV) isopropoxide	Sigma Aldrich	97.0
Sodium hydroxide	Prommark Chemicals	99.8
Urea	Sigma Aldrich	99.5
Absolute ethanol	Sigma Aldrich	95.0
Glacial acetic acid	Rochelle Chemicals	Analytical grade
Bismuth(III) nitrate pentahydrate	Sigma Aldrich	98.0
Nitric acid	Sigma Aldrich	65.0
Sulfuric acid	Promark Chemicals	98

3.2.2. Synthesis of N-TiO$_2$ photocatalyst

A series of N-TiO$_2$ materials with different doping amount of nitrogen were synthesised by varying amount of urea into titanium(IV) isopropoxide (10, 20 and 30 mole% urea) *via* a combined sol-gel and calcination treatment. Titanium(IV) isopropoxide (TTIP) was used as the precursor of TiO$_2$, and urea was used as a nitrogen source. A stable reaction mixture was obtained by the addition of a urea solution (urea was dissolved into 20 mL double-distilled water and vigorously stirred until complete dissolution) into the TTIP mixture (TTIP in absolute 10 mL ethanol and 3 mL glacial acetic acid) under vigorous stirring at room temperature. The reaction mixture was stirred at room temperature for 3 h with a magnetic stirrer, and the gel obtained was aged at room temperature for 24 h for complete hydrolysis.

The solvents in the reaction mixture were evaporated by heating the gel on a hot plate for 10 min, and then dried at 130 °C in the oven overnight. The product obtained with a white colour was then pulverized and calcined at a 450 °C in muffle furnace for 5 h to obtain a yellow product, indicating nitrogen-doped TiO_2. Yellow solid produced had an increasing intensity of the colour as the N/Ti ratio increased (see in Appendix F). The masses and volumes of reagents used to prepare the N-TiO_2 materials are detailed in Table 3.2. This is followed by a sample calculation to show how the amounts of urea required for doping were calculated.

Table 3.2: Masses and volumes of reagents used to prepared different N-TiO_2 materials

Material	Volume of TTIP/cm^3	Mass of urea/g
10 mol.% N-TiO_2	10	0.2254
20 mol.% N-TiO_2	10	0.5070
30 mol.% N-TiO_2	10	0.8693

The sample calculation for the amounts of reagents required for the preparation of 10 mole% N-TiO_2 are detailed below:

10 cm^3 of titanium isopropoxide used contains:

$$n = \left(\frac{0.96 \ g \ cm^{-3} \times 10 \ cm^3}{284.219 \ g \ mol^{-1}} \right) = \ 0.03378 \ mole \ TTIP$$

$$mole\% = \left(\frac{moles \ of \ urea}{total \ number \ of \ moles} \right) 100\%$$

$$10 \ mole\% = \left(\frac{n}{n + 0.03378 \ mol} \right) 100\%$$

$$n = 0.0037533 \ mol \ of \ Urea$$

$$Mass \ of \ urea \ required \ = \ 0.0037533 \ mol \ \times \ 60.05 \ g \ mol^{-1} = 0.2254 \ g$$

3.2.3.   Synthesis of Bi$_2$O$_3$

Bi$_2$O$_3$ was initially prepared by dissolving 3 g bismuth nitrate pentahydrate in 10 mL 65% nitric acid and 5 mL double-distilled water under vigorous stirring, followed by the slow addition of 1 g NaOH pellets until a yellowish suspension was observed. The mixture was vigorously stirred overnight at room temperature and, subsequently, transferred into a Teflon-lined autoclave. The Teflon-lined autoclave containing the reaction mixture was heated in an oven at 180 °C for 6 h. The Bi$_2$O$_3$ formed was filtered, washed three times with double-distilled water and dried at 80 °C overnight.

3.2.4.   Synthesis of N-TiO$_2$/Bi$_2$O$_3$ nanomaterial

Nitrogen-doped TiO$_2$/Bi$_2$O$_3$ was synthesised *via* a hydrothermal method. Two suspensions were prepared separately, i.e., N-doped TiO$_2$ in double-distilled water and Bi$_2$O$_3$ in double-distilled water. The two suspensions were combined and stirred for about 10 minutes with a stirrer bar. The reaction mixture was then transferred into a Teflon-lined autoclave and heated in an oven at 180 °C for 12 h. The product obtained was washed with the 10 mL ethanol and 10 mL double-distilled water three times with each, and then dried in the oven overnight at 50 °C. A similar procedure was adopted to prepare more samples containing different amounts of Bi$_2$O$_3$. Overall, the samples prepared were denoted as NTiBi x%, where x% refers to the Bi$_2$O$_3$ to N-TiO$_2$ mass ratio such as 1, 3, and 5 wt.%. For these syntheses, only the 20 mol.% N-TiO$_2$ was used. The masses and volumes of reagents used to prepare the NTiBi materials are detailed in Table 3.3. This is followed by a sample calculation to show how the amounts of Bi$_2$O$_3$ required were calculated.

Table 3.3: Masses and volumes of reagents used to prepared different Bi$_2$O$_3$ materials

Material	Mass of 20 mol.% N-TiO$_2$/g	Mass of Bi$_2$O$_3$/g
NTiBi 1 wt.%	1.0087	0.0102
NTiBi 3 wt.%	1.0056	0.0311
NTiBi 5 wt.%	1.0075	0.0530

A sample calculation for the mass of Bi_2O_3 required to prepare NTiBi 1 wt.% with 1.0087 g of 20 mol.% N-TiO$_2$ follows:

$$1\,wt.\,\% = \left(\frac{x}{x + 1.0087\ g}\right) 100\%$$

$$x = 0.01012\ g\ Bi_2O_3$$

3.2.5. Characterisation of the materials

The techniques used to characterise the physicochemical properties of the N-TiO$_2$ and NTiBi heterojunction-structured nanomaterials synthesised are discussed in the subsequent sections.

3.2.5.1. Electron dispersive X-ray spectroscopy

Electron dispersive X-ray spectroscopy (EDX) was employed as a qualitative technique to evaluate the elemental compositions of the N-TiO$_2$ and NTiBi materials. The instrument model used for EDX was a Zeiss Ultra Plus coupled with a JEOL JSM 6100 SEM instrument. While capturing images, only selected random areas were measured. An EDX scanning rate between 5 – 10 kilocounts per second at an acceleration voltage of 20 kV with a working distance of 5 – 10 mm was used. The results obtained from the EDX Aztec software were in the form of EDX spectra, and a qualitative table was generated with the weight percentage of elements in the sample. The magnification of images was at 2.5 μm, and the scans lasted for 5 min.

3.2.5.2. Elemental analysis

Elemental analysis was employed for quantitative analysis to determine the presence of nitrogen in N-TiO$_2$ and NTiBi. The measurements were carried out with an Elementar vario EL cube CHNSO elemental analyser.

3.2.5.3. Inductively coupled plasma-optical emission spectrometry

The bismuth content of the NTiBi samples prepared by varying the amount of bismuth oxide in N-TiO$_2$ was examined with inductively coupled plasma-optical emission spectrometry (ICP-OES). A standard solution of bismuth (100 mg L^{-1}) was prepared by dilution of an ICP standard solution of 1000 mg L^{-1} (Merck, Germany), and the working standards were prepared by diluting this standard solution. The working standards were used to obtain the calibration

curves for the determination of the bismuth concentrations. The samples to be analysed were firstly heated in muffle furnace at 600 °C for 3 h to gives carbon-free material, and digestion was difficult. Enormous efforts were made to prepare different sulfuric acid (98% H_2SO_4): nitric acid (65% HNO_3) ratios until a mixing ratio that offered the best bismuth solubility was identified. A 50 mg mass of carbon-free NTiBi nanoparticles was accurately weighed and digested with a mixture of H_2SO_4:HNO_3 (10:1 v/v) by heating on a hotplate up to 400 °C whilst stirring for 5 min to give a clear solution. The digested solution was quantitatively transferred to a 100 mL volumetric flask and made to volume with double-distilled water. The digestion vessels were washed with double-distilled water and the washings added to the volumetric flask before making to volume. A 1 mL aliquot of this solution was then diluted into a 100 mL volumetric flask with double-distilled water. Also, double distilled water was used as a blank solution. The ICP-OES reading of the prepared sample was substituted as a y-value into the calibration equation that resulted from the standard bismuth calibration to obtain a concentration in mg L^{-1}. For instance, the ICP-OES reading for NTiBi 1 wt.% was 150.92367 and calculations were performed as follows:

$y = 1777.6x + 36.585$, where x is the [Bi] and y is the ICP-OES reading

$$[Bi] = \left(\frac{150.92367 - 36.585}{1777.6} \right)$$

$$[Bi] = 0.06432 \ mg \ L^{-1}$$

$$Dilution \ factor \ was \ = \frac{100 \ mL}{1 \ mL} = 100$$

$$Wt.\% = \left(\frac{0.06432 \ mg \ L^{-1} \times 0.1 \ L \times 100}{50.0 \ mg} \right) 100 \ \% \ = \ 1.29 \ wt.\%$$

A similar procedure, as above was adopted for the NTiBi 3 wt.% and NTiBi 5 wt.% ICP-OES readings; of 326.77831 and 497.86348, respectively. The ICP-OES instrument parameters are listed in Table 3.4.

Table 3.4: The ICP-OES operating parameters for determination of Bi content

Parameters	Conditions
Incident power/kW	1.20
Plasma gas flow rate/L min^{-1}	15
Auxiliary gas flow rate/L min^{-1}	1.5
Nebulizer gas flow rate/L min^{-1}	0.2
Pump flow rate/mL min^{-1}	0.8
Wavelength/nm	223.061

3.2.5.4. Ultraviolet-visible spectroscopy

Ultraviolet-visible (UV-Vis) spectroscopy was employed to study the optical absorption of the sample suspensions. The samples were suspended in double-distilled water, sonicated for 1 h, and after sonication, measurements were performed immediately. Spectra were acquired with a Shimadzu UV-3600 UV-Vis-NIR spectrophotometer. The samples were contained in quartz cuvettes.

3.2.5.5. Diffuse reflectance ultraviolet-visible spectroscopy

Diffuse reflectance ultraviolet-visible (DRS-UV/Vis) spectroscopy was employed to study optical properties such as optical absorption. Spectra were acquired with a PerkinElmer Lambda 35 UV/Vis spectrophotometer in conjunction with a Labsphere integrating sphere.

3.2.5.6. Photoluminescence spectroscopy

Photoluminescence spectroscopy (PL) was employed to study the recombination phenomenon of the photogenerated charge carriers. Measurements were performed on a PerkinElmer LS55 fluorescence spectrometer. A LS55 series front surface accessory was used since the samples were in a solid-state. Excitation was done at 300 nm, and the emission spectra were recorded from 300 to 800 nm, with an excitation slit of 15 nm, an emission slit of 10 nm, and a scan

speed of 120 nm min^{-1}. The software used for data acquisition was FL Winlab version 4.00.03 from PerkinElmer Inc.

3.2.5.7. Powder X-ray diffraction

Powder X-ray diffraction (XRD) was employed to investigate the crystal structures of titania doped with nitrogen and coupled with Bi_2O_3. XRD analysis was performed with a D8 Advance diffractometer supplied by BRUKER AXS, Germany. Measurements were performed with a θ-θ scan in locked coupled mode. Monochromatic Cu-K ($\lambda K\alpha_1 = 1.5406$ Å) radiation was used together with a positive, sensitive detector (Lybe-Eye) that records diffraction data at a typical speed of 0.5 sec/step which is equivalent to an effective time of 92 seconds per step for a scintillation counter. The instrument software was from the International Centre for Diffraction Data (ICDD) database for 1999, and EVA software from BRUKER was used for data evaluation.

3.2.5.8. High-resolution transmission electron microscopy

High-resolution transmission electron microscopy (HRTEM) was employed to provide much higher resolution than is possible with any light-based imaging techniques by observing the existence of lattice fringes on titania doped with nitrogen and NTiBi. The instrument model used for these measurements was a JEOL JEM 2100 high-resolution transmission electron microscopy with an accelerating voltage of 200 kV.

3.2.5.9. Raman spectroscopy

Raman spectroscopy was employed to determine the crystalline phases present and the chemical structure of titania doped with nitrogen and coupled with Bi_2O_3. Measurements were carried out on a Delta Nu Advantage 532™ Raman spectrometer with a 2D CCD detector at 1800 lines per grating. The sample holder was positioned under the laser at a focal length of 16.50 mm, and the laser power was 15 mW.

3.2.5.10. Scanning electron microscopy

Scanning electron microscopy (SEM) was employed to investigate the surface morphologies of titania doped with nitrogen and coupled with Bi_2O_3. The measurements were performed with a JEOL JSM 6100 instrument. The accelerating voltage was 10 kV, aluminium stubs were used as sample holders, and the required sample size was sprinkled on top of carbon tape. The

optimum working distance was about 7 mm, and the aperture size was 30 μm. The images were produced by scanning the focussed beam of electrons on the surface of the material. The electrons interact with atoms in the sample, producing various signals that reveal information about the sample's surface topography and composition. The software package employed in the data acquisition and analysis from the instrument was Zeiss Smart SEM version 5.03.06.

3.2.5.11. Transmission electron microscopy

Transmission electron microscopy (TEM) was employed to evaluate the morphology of the materials further. In addition, this technique was used to measure the nanoparticle size of titania doped with nitrogen and coupled with Bi_2O_3. The measurements were performed with a JEOL JEM 1010 transmission electron microscopy using lacey or holey carbon-coated copper grids. The images were taken at different magnifications by using the Megaview 3 camera. Samples for analysis were prepared by ultrasonication in a water bath. The samples were dispersed in 1 mL of ethanol for 10 min. The grids were then dipped into the ethanolic dispersion and allowed to dry prior to insertion in the specimen chamber.

3.2.5.12. Fourier-transform infrared spectroscopy

Fourier-transform infrared (FTIR) spectroscopy was employed to investigate the functional groups and bonding within the structure of titania doped with nitrogen and coupled with Bi_2O_3. FTIR is the most rapid available technique to monitor the formation of $N-TiO_2$, and the measurements were performed with a PerkinElmer Spectrum RX1 FTIR spectrometer with the samples pressed as KBr discs. A mass of 0.1500 g of powder was pressed into a pellet under a pressure of 10 Tons for about 2 min. The pellet consisted of a KBr:sample ratio of 500:1 weighed on a Shimadzu analytical balance. Background scanning was done to remove any CO_2 absorption in the background. Thereafter, the samples made into a KBr disc were scanned from 350 - 4000 cm^{-1}. The data from the instrument was initially saved as an ASCII file, and then further processed with Origin software.

3.2.5.13. Specific surface area and porosity

The Brunauer-Emmett-Teller (BET) isotherm was applied to obtain information on the surface area of the samples. The pore size distribution and pore volume were obtained by applying the Barrett–Joyner–Halenda (BJH) method. A Micromeritics TriStar II 3020 surface area and porosity analyser was employed to obtained nitrogen adsorption/desorption isotherms on the

photocatalysts at 77.35 K. Each sample was degassed at 100 °C in a Micromeritics flow degasser for at least 3 h prior to measurement. TriStar II 3020 Version 2 software was used to calculate the pore size distribution from the N_2 desorption isotherms.

3.2.5.14. Thermogravimetric analysis

Thermogravimetric analysis (TGA) was employed to study the thermal stability of the materials and their composition. The mass loss observed during the thermal event involves the loss of a volatile component. Chemical reactions, such as combustion, involve mass losses, whereas physical changes, such as melting, do not. The measurements were performed with a TA Instruments Q series^{TM} Thermal Analyser DSC/TGA (Q600). Samples were analysed under an air flow rate of 50 mL min^{-1}. The temperature was raised at a rate 10 °C min^{-1}, from room temperature to 1000 °C. TA Instruments 2000 universal software analysis was used to generate both the thermograms and first derivative plots. All the thermograms and first derivative plots obtained were reprocessed by using Origin software.

3.3. Results and discussion

This section discusses the characterisation results and the physicochemical properties of the N-TiO_2 and NTiBi materials synthesised.

3.3.1. Elemental composition

The elemental composition of the samples was investigated with EDX coupled to a SEM. Also, the content of nitrogen and bismuth present in the samples prepared was confirmed with elemental analysis (CHNS) and ICP-OES, respectively.

3.3.1.1. Qualitative analysis

EDX, as a qualitative technique, was used to confirm the presence of the expected elements; namely, titanium, bismuth, oxygen and nitrogen. Each element was observed through the EDX spectrum collected, with its unique peaks on the electromagnetic emission spectrum. Figure 3.1 (a) displays the EDX spectrum for 20 mol.% $N-TiO_2$. It is seen that titanium, oxygen and nitrogen are present in 20 mol.% $N-TiO_2$ prepared. However, the peaks for titanium and nitrogen overlap during the energy of the X-ray emitted from the sample after excitation with an electron beam. This may be due to the fact that the titanium (L = 0.452) and nitrogen (K = 0.392) energies are very close. Figure 3.1 (b) displays the EDX spectrum for NTiBi 3 wt.%, and each element is observed with its unique peaks. The nitrogen peak persistently overlapped with the titanium peak even after the introduction of Bi_2O_3. Hence, these results strongly provide evidence for the presence of titanium, bismuth and oxygen. The presence of nitrogen was challenging to verify, according to the EDX results obtained. The elemental mapping image resulting from the NTiBi 3 wt.% photocatalyst prepared is presented in Figure 3.1 (c). According to the elemental mapping titanium, bismuth, and oxygen were present in good distribution in the samples prepared.
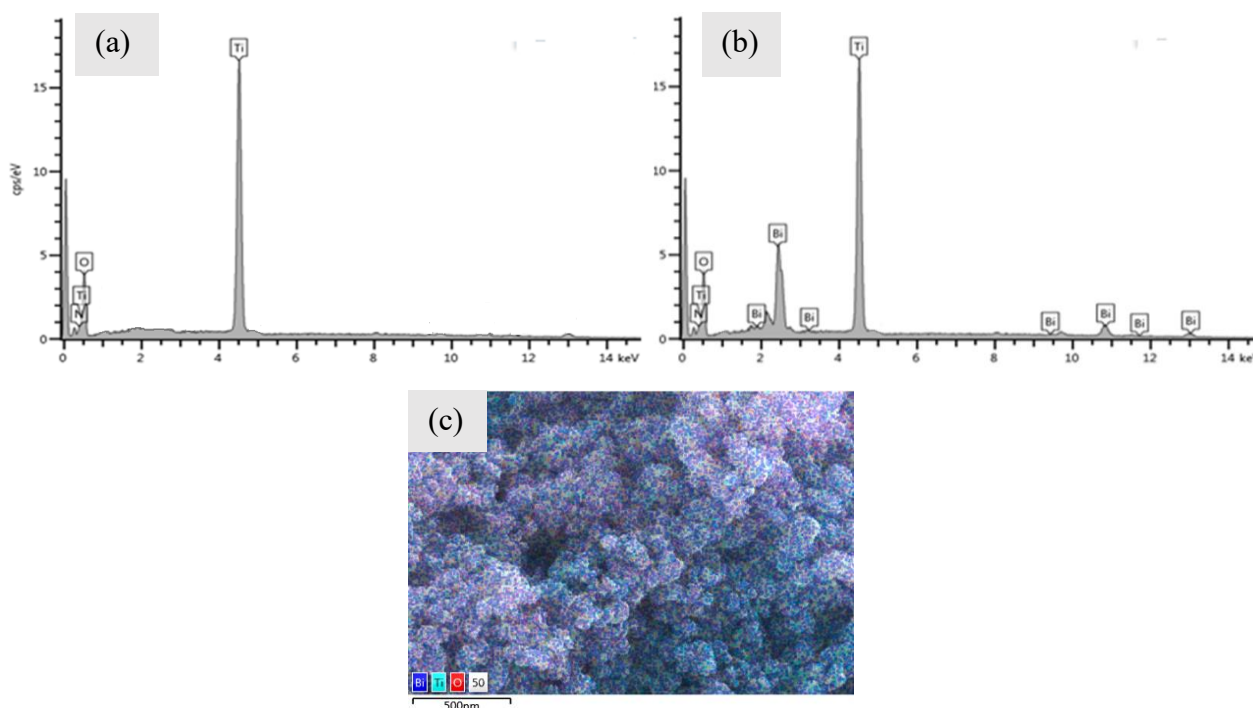
Figure 3.1: EDX spectrum of (a) 20 mol.% $N-TiO_2$, (b) NTiBi 3 wt.% and elemental mapping of (c) NTiBi 3 wt.%

3.3.1.2. Nitrogen content

The nitrogen content of the samples was determined by elemental analysis (CHNS). The results obtained are shown in Table 3.5, and highlight that nitrogen content in N-TiO_2 increases with increased loading of urea, and this is consistent with a previous report [9]. Notably, not all nitrogen atoms in urea are incorporated into the crystal lattice of titania. Some of the nitrogen can be lost during heating under calcination in the form of oxides of nitrogen [9, 10]. It is also seen that as the N-TiO_2 is coupled with Bi_2O_3, there is a decrease in nitrogen content with a higher loading of Bi_2O_3. The loss of doped nitrogen is assumed to be caused by further treatment of N-TiO_2 with Bi_2O_3, such as solubilization, washing, and heating processes, etc., that could result in a decrease of nitrogen content. Also, the loss of doped nitrogen upon higher loading of Bi_2O_3, was thought to arise through chemical reaction during heating [10]. As the Bi_2O_3 loading increases, the sample become richer with Bi and O elements, while other elements become less.

Table 3.5: The nitrogen content of the samples prepared

Sample	Nitrogen content/%
10 mol.% N-TiO_2	0.78
20 mol.% N-TiO_2	2.82
30 mol.% N-TiO_2	4.81
NTiBi 1 wt.%	2.61
NTiBi 3 wt.%	1.82
NTiBi 5 wt.%	0.85

3.3.1.3. Bismuth content

Figure 3.2 shows the calibration curve resulting from the bismuth standards prepared to determine the bismuth concentration in the NTiBi nanoparticles by ICP-OES. It can be seen

that the calibration curve showed good linearity ($R^2 = 0.998$) between the intensity of bismuth and each concentration of the working standard solutions prepared. This was achieved over a 0.05 - 1 mg L^{-1} concentration range. This calibration curve was used in the determination of the bismuth concentration in the samples prepared. Three replicates were measured for each sample, and the average values were used. The bismuth concentrations determined were then used to compute the weight percentage of bismuth present in the NTiBi, and the results obtained are summarized in Table 3.6 with their percentage relative standard deviation (%RSD) that indicates the precision. Therefore, these results confirm that the loaded bismuth was within the expected range (see Table 3.6). For instance, the targeted 1.0, 3.0 and 5.0 wt.% bismuth loaded onto N-TiO$_2$ were found experimentally to be 1.29, 3.27 and 5.19 wt.%, respectively. These experimental values are in good agreement with the targeted composition.
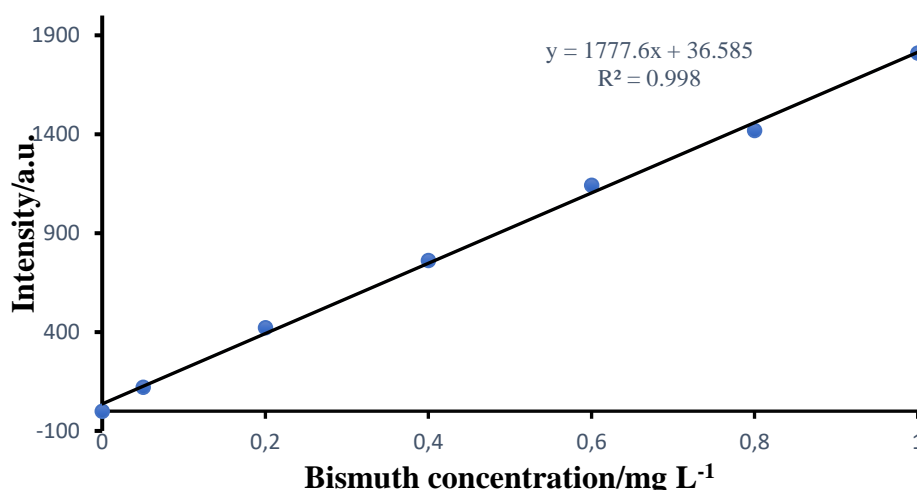
Figure 3.2: Standard calibration curve for the determination of the bismuth concentration in the NTiBi nanoparticles by ICP-OES

Table 3.6: The targeted and experimentally determined bismuth content in the NTiBi nanoparticles

Sample	Targeted Bi/wt.%	Experimental Bi/wt.%	RSD/%
NTiBi 1 wt.%	1.00	1.29	24.88
NTiBi 3 wt.%	3.00	3.27	18.72
NTiBi 5 wt.%	5.00	5.19	15.13

3.3.2. Optical properties

The optical properties of the N-TiO_2 and NTiBi materials synthesised were evaluated by using ultraviolet-visible, diffuse reflectance ultraviolet-visible and photoluminescence spectroscopy techniques.

3.3.2.1. Ultraviolet-visible spectroscopy

Figure 3.3 depicts the UV-Vis absorption spectra of the 20 mol.% N-TiO_2 and NTiBi materials synthesized. The absorption spectra of N-doped TiO_2 showed a stronger absorption towards the visible light region, which reveals enhancement of visible light absorption by the modified TiO_2 doped with nitrogen compared with the un-doped TiO_2. Accordingly, these results indicate that the nitrogen atoms are incorporated into the lattice of TiO_2. In addition, the incorporation of Bi_2O_3 extended the maximum absorption further towards the visible region. However, the measurement of the spectra of suspensions of the samples was challenging due to the scattering of reflected light by fine particles in the solution. This prevents 100% of the light from reaching the detector, making it more difficult for a clear spectrum to be obtained. Therefore, the measurement was carried out with an integrating sphere (UV/Vis DRS) where the samples are in their solid state, and the results were compared (see Section 3.3.2.2).
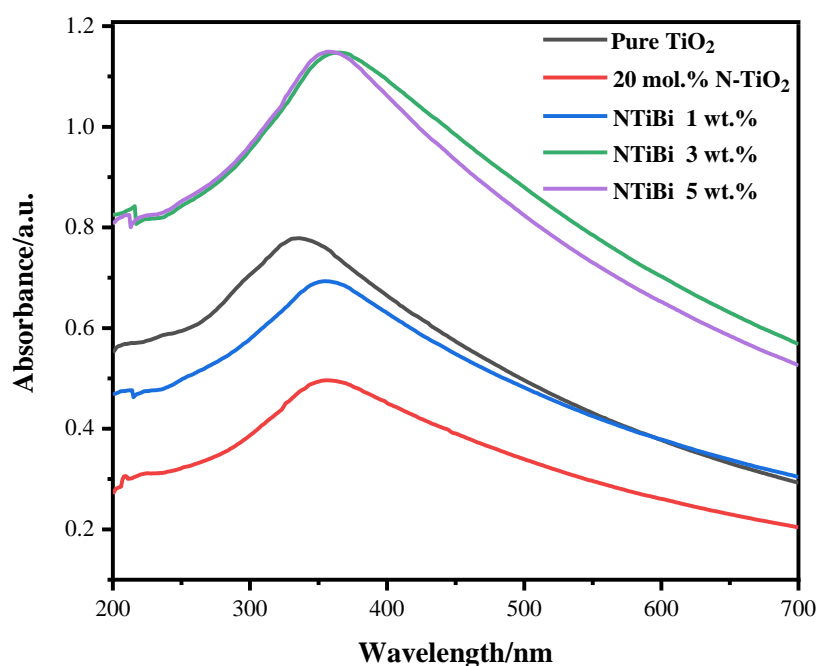
Figure 3.3: UV–Vis spectra of TiO_2-based nanoparticles in a water suspension

3.3.2.2. Diffuse reflectance spectroscopy

Ultraviolet-visible diffuse reflectance spectroscopy (UV-Vis DRS) was employed to characterise the light absorption and further extrapolate the bandgap energies of the photocatalysts from the Kubelka Munk function. The Kubelka Munk function (F(R)) is proportional to the absorption coefficient (α). Therefore, by knowing the F(R) behaviour, the absorption can be deduced. The samples were studied to know the electronic transitions and shift in the bandgap energies. The UV-Vis DR spectra of the 20 mol.% N-TiO_2 and NTiBi materials synthesized are presented in Figure 3.4 (a). The maximum absorption of pure titania was observed at 312 nm. After doping TiO_2 with nitrogen, this maximum absorption band was extended towards the visible region. The extension of the absorption edge was attributed to the substitution of oxygen atoms with nitrogen atoms in the TiO_2 lattice; these allow the *p*-orbitals of the nitrogen atoms to overlap with the *p*-orbitals of the oxygen atoms in the valence band of TiO_2 [11, 12]. Previously, it has been reported that the bandgap energy of TiO_2 becomes narrower, and the absorption edge is shifted to lower energy through nitrogen doping of TiO_2 [13]. Photo-absorption of NTiBi showed a significant increase in absorption. It can be clearly seen from the spectrum for 3 wt.% of Bi_2O_3 into N-TiO_2. The extrapolated optical bandgap energies from the Kubelka Munk plot in Figure 3.5 (b) are presented in Table 3.7 (see

additional information in Appendix F). These results confirmed that the optical bandgap energy was narrowed by coupling 20 mol.% N-TiO$_2$ with Bi$_2$O$_3$. The band gap narrowing of the NTiBi composites synthesized was attributed to the N-doping and coupling effect of N-TiO$_2$ with a narrowed band gap Bi$_2$O$_3$ semiconductor, and this is consistent with previous reports [14, 15]. Thus, this significantly promotes the good separation of photogenerated charge carriers and suppresses their recombination. This was confirmed by PL analyses (see Section 3.3.2.3).
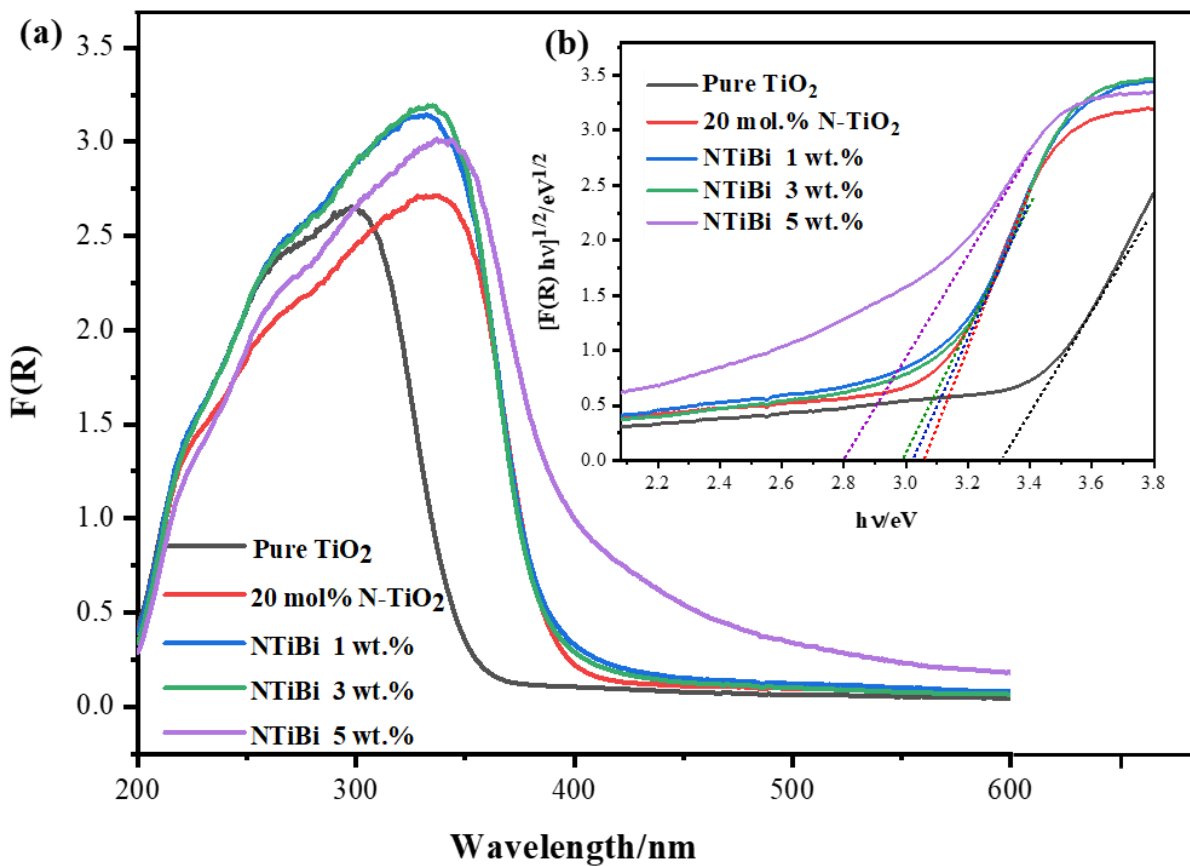
Figure 3.4: The (a) UV/Vis diffuse reflectance spectra and (b) Kubelka Munk plot for 20 mol.% N-TiO$_2$ and NTiBi composites

Table 3.7: The optical bandgap energies of the photocatalysts prepared

Sample	Energy bandgap/eV
Pure TiO_2	3.30
20 mol.% $N\text{-}TiO_2$	3.06
NTiBi 1 wt.%	3.00
NTiBi 3 wt.%	2.98
NTiBi 5 wt.%	2.80

3.3.2.3. Photoluminescence spectroscopy

It is well-known that the emission signals in the photoluminescence (PL) spectra result from the recombination phenomenon of the photogenerated charge carriers. Therefore, PL was used to investigate the separation and recombination rate of the photogenerated charge carriers from the photocatalysts. A higher intensity of the PL peaks implies a high recombination rate of the photogenerated charge carriers, which could lower the photocatalytic performance of the material [16]. There are three peaks (R1, R2 and R3) observed in Figure 3.5 (a) and (b); peak R2 was used to examine the peak intensity behaviour, that is, whether it increases or decreases with N-doping in TiO_2 and the Bi_2O_3 coupling effect. Peaks R1 and R3 were not used since they showed no defined trend in their intensity changes with N-doping content and the coupling effect, thus it indicates that there is luminescence quenching, which is assumed to play a significant role on the PCE.

Figure 3.5 (a) displays PL spectra of pure TiO_2 and a series of $N\text{-}TiO_2$ prepared. A drastic decrease in the R2 intensity was observed in the 20 mol.% $N\text{-}TiO_2$ material from the series of $N\text{-}TiO_2$ prepared. This material was selected to couple with Bi_2O_3 due to the good occurrence of charge separation observed, since a material that exhibits a lower recombination rate is designed for operation under solar light [17]. In addition, a high amount of nitrogen incorporated into TiO_2 showed high charge carrier recombination, and this was clearly observed in 30 mol.% $N\text{-}TiO_2$. Figure 3.5 (b) displays the PL spectra of the NTiBi materials prepared. It is obviously seen that the NTiBi 3 wt.% nanocomposites exhibit significantly

weaker PL intensities than either pure TiO_2, 20 mol.% $N-TiO_2$ and NTiBi (1 and 5 wt.%). This provides evidence that coupling of $N-TiO_2$ with Bi_2O_3 results in good separation of photogenerated charge carriers and a poor recombination rate of the photogenerated charge carriers. However, the use of excessive Bi_2O_3 into $N-TiO_2$ may result in a higher recombination rate of photogenerated charger carriers, as is clearly seen from 5 wt.% of Bi_2O_3 into $N-TiO_2$. The good occurrence of charge carriers separation observed can be attributed to the matched band potentials and interconnected nanocrystal heterojunction of $N-TiO_2$ and Bi_2O_3.
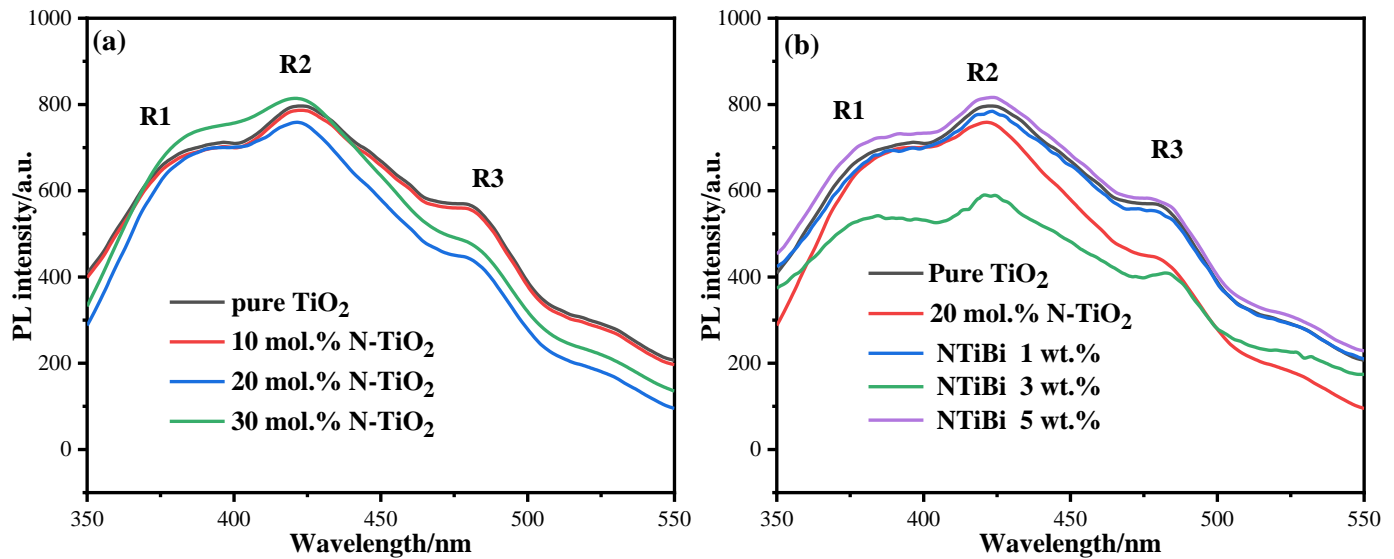
Figure 3.5: The PL spectra of the (a) $N-TiO_2$ and (b) NTiBi materials prepared

3.3.3. Crystallinity and phases

The crystallinity of the titania and bismuth oxide phases present in the materials synthesised ($N-TiO_2$ and NTiBi) in this work were investigated through HRTEM, SAED, powder X-ray diffraction and Raman spectroscopy.

3.3.3.1. Powder XRD

Figure 3.6 displays the powder X-ray diffractograms of the 20 mol.% $N-TiO_2$ and NTiBi materials synthesized. The strong diffraction peak at 25.25° in Figure 3.6 (a) confirms the presence of the TiO_2 anatase structure from the N-doped TiO_2 synthesized, and it corresponds to the (101) Miller indices plane. Generally, the presence of the rutile phase in TiO_2 is indicated by the appearance of a diffraction peak around 27°, and other peaks that are adjacent to the

anatase peaks [18, 19]. Hence, Figure 3.6 (a) confirms the presence of pure anatase phase in the N-TiO$_2$ prepared, and this is in good agreement with the standard diffraction data [18]. The diffractograms of NTiBi in Figure 3.6 (b) shows no significant shift of the principal anatase peak, since the Bi atom (103 pm) is much bigger than the Ti atom (61 pm), and indicates that the Bi-species are present in a separated phase of Bi$_2$O$_3$ [20]. The presence of Bi$_2$O$_3$ in the composites prepared is confirmed with four peaks observed at 26.86°, 30.22°, 33.24° and 52.27° corresponding to the (120), (121), (112), and (221) planes of pristine Bi$_2$O$_3$, respectively [21]. The diffraction peaks in Figure 3.6 (b-d) that are observed at 26.86°, and 33.24° indicate the α-Bi$_2$O$_3$ phase structure, and those at 33.24°, 52.27° indicate the β-Bi$_2$O$_3$ phase [22]. It is well-known that a high intensity of the XRD peaks indicates a high degree of crystallinity of the material, and peak broadness indicates low crystallinity [23]. Therefore, from an inspection of the diffractograms presented in this work, it is visibly seen that a high loading of bismuth oxide lowers the peak intensities. This suggests that the crystallinity of the NTiBi nanoparticles is affected by the high loading amount of Bi$_2$O$_3$.

The Debye-Scherrer formula was adopted to calculate the average crystallite sizes in the nanoparticles prepared from the anatase peaks by peak broadening. The inter-planar spacing between atoms (*d*-spacing) is computed from Bragg's Law and is enumerated in Table 3.8. The crystallite size of the anatase structure in 20 mol.% N-TiO$_2$ was found to be 18 nm. The crystallite size of the anatase structure in the NTiBi nanoparticles decreased with a high loading of Bi$_2$O$_3$, as presented in Table 3.8. The smaller crystallite size of NTiBi synthesized will be beneficial in enhancing the PCE of the DSSCs [24]. The *d*-spacing of the anatase structure in the 20 mol.% N-TiO$_2$ and NTiBi nanoparticles prepared was found to 0.35 nm in all samples.

The lattice parameters (*a* and *c*) for the TiO$_2$ anatase structure were calculated from Equation (16), for the (200) and (101) peak positions.

$$\frac{1}{d^2} = \frac{h^2 + k^2}{a^2} + \frac{l^2}{c^2} \tag{16}$$

where, (*h k l*) are the Miller indexes, and *d* is the interplanar distance. The calculated values are presented in Table 3.9, and are consistent with a previous report [25]. The lattice parameters for α-Bi$_2$O$_3$ (monoclinic) and β-Bi$_2$O$_3$ (tetragonal) were also calculated and are presented in Table 3.9; again, the values obtained are consistent with the literature [26]. Therefore, it is evident that N-TiO$_2$ was coupled with Bi$_2$O$_3$.
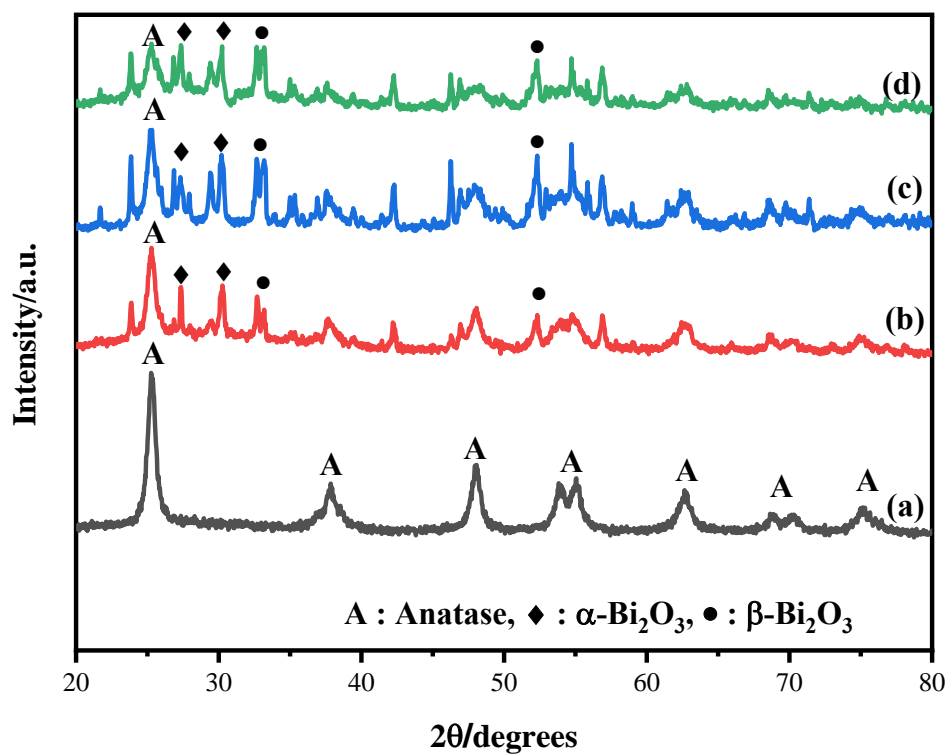
Figure 3.6: Powder X-ray diffractograms of (a) 20 mol.% N-TiO$_2$, (b) NTiBi 1 wt.%, (c) NTiBi 3 wt.%, and (d) NTiBi 5 wt.%

Table 3.8: XRD data for the TiO$_2$ anatase structure

Sample	Peak position 2θ/degree	FWHM/radian	Crystallite size/nm	d-spacing/nm
20 mol.% N-TiO$_2$	25.28	0.008015	18.07	0.35
NTiBi 1 wt.%	25.31	0.09915	14.61	0.35
NTiBi 3 wt.%	25.25	0.009985	14.50	0.35
NTiBi 5 wt.%	25.29	0.01028	14.09	0.35

Table 3.9: The lattice parameters of the anatase TiO_2, β-Bi_2O_3, and α-Bi_2O_3 synthesized materials

Samples	Lattice parameters/Å		
	TiO_2 anatase structure		
	$a = b$	c	$V = a \times b \times c$ (Å³)
TiO_2	3.784	9.512	136.199
N-TiO_2	3.782	9.468	135.405
NTiBi 1 wt.%	3.783	9.467	135.444
NTiBi 3 wt.%	3.779	9.466	135.169
NTiBi 5 wt.%	3.776	9.459	134.858
	β-Bi_2O_3 (tetragonal)		
	$a = b$	c	$V = a \times b \times c$ (Å³)
NTiBi 1 wt.%	7.737	5.636	337.551
NTiBi 3 wt.%	7.737	5.636	337.551
NTiBi 5 wt.%	7.738	5.637	337.552
	α-Bi_2O_3 (monoclinic)		
	a	b	c	$V = a \times b \times c \sin\beta$(Å³)

Samples	a	b	c	$V = a \times b \times c \sin\beta$(Å³)
NTiBi 1 wt.%	5.847	8.166	7.508	330.15
NTiBi 3 wt.%	5.847	8.166	7.508	330.15
NTiBi 5 wt.%	5.848	8.166	7.509	330.16

3.3.3.2. HRTEM and SAED analysis

The HRTEM images showed various lattice fringes and allowed for the identification of the crystallographic spacings for N-TiO_2 and NTiBi. Figure 3.7 (a) and (b) present the HRTEM images obtained for 20 mol.% N-TiO_2 and NTiBi 3 wt.% respectively (see additional information in Appendix A). The lattice fringes of $d = 0.36$ nm found in both images matched well with the (1 0 1) crystallographic plane of anatase TiO_2, while the fringes of $d = 0.32$ nm and $d = 0.27$ nm in Figure 3.4 (b) matched the (1 2 0) and (1 2 1) crystallographic planes of the Bi_2O_3 nanoparticles, respectively. Figure 3.7 (c-d) illustrates the SAED ring patterns of 20 mol.% N-TiO_2 and NTiBi, and further confirm the crystallinity of the nanoparticles prepared. The interlayer spacings provided by the SAED ring patterns of N-TiO_2 and NTiBi 3 wt.% are

well-matched with the TiO_2 anatase phase *d*-spacing. This indicates the presence of the anatase phase in the nanoparticles prepared. The interlayer spacings obtained with this technique are in good agreement with the results from XRD measurements.
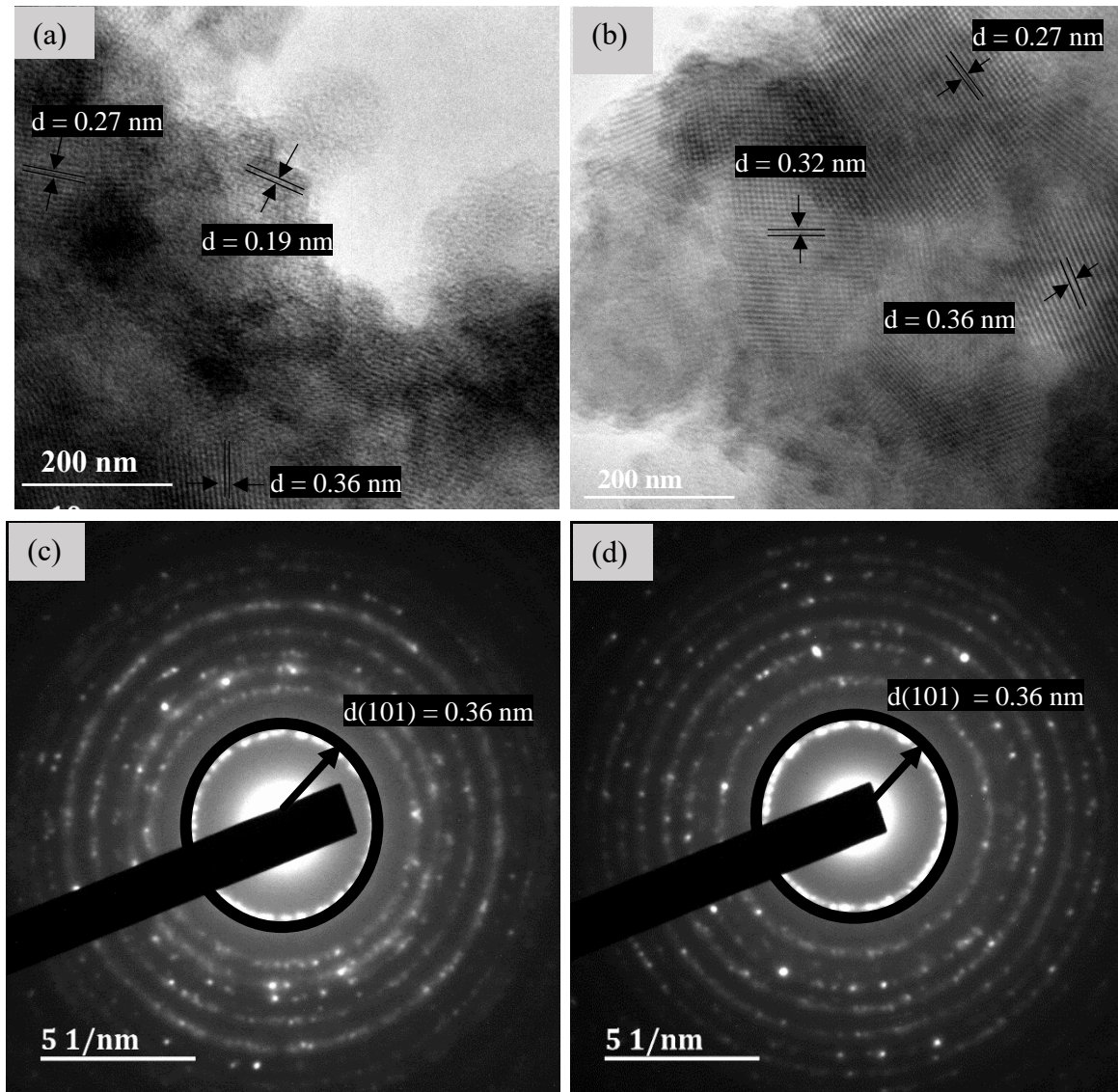
Figure 3.7: The (a-b) HRTEM images and (c-d) SAED pattern of 20 mol.% N-TiO_2, and NTiBi 3 wt.%

3.3.3.3. Raman analysis

The Raman study highlighted the principal vibrational lattice dynamics of the nanoparticles prepared. This involves the O, Ti and Bi atoms in the vibrations concerned. Figure 3.8 depicts the Raman spectra of 20 mol.% N-TiO$_2$ and NTiBi with different amounts of Bi$_2$O$_3$. According to the Raman spectrum obtained for the N-TiO$_2$ nanoparticles, four Raman peaks are observed within the 150 – 630 cm^{-1} range. This confirms the presence of the anatase phase of TiO$_2$ in the N-TiO$_2$ prepared, and these peaks constantly appeared in the NTiBi prepared. These Raman peaks can be assigned as 152 cm^{-1} (E$_g$), 393 cm^{-1} (B$_{1g}$), 515 cm^{-1} (A$_{1g}$+B$_{1g}$) and 626 cm^{-1} (Eg) [27-28]. In addition, anatase TiO$_2$ commonly exhibits four characteristic Raman-active modes [29]. Therefore, characteristic vibrational frequencies observed and their intensity ratios confirmed the presence of pure anatase phase in N-TiO$_2$ and NTiBi. The α-Bi$_2$O$_3$ and β-Bi$_2$O$_3$ phases exhibit Raman features in the 50 - 600 cm^{-1} range, while γ-Bi$_2$O$_3$ and δ-Bi$_2$O$_3$ feature in the 50-900 cm^{-1} range, and the ε-Bi$_2$O$_3$ phase does not have any Raman data reported yet [30, 31]. According to the Raman spectra of NTiBi, it can be clearly seen that the NTiBi nanoparticles synthesized could contain one of these phases (α-Bi$_2$O$_3$ and β-Bi$_2$O$_3$) or both as the Raman band shifts were seen in the 100 - 600 cm^{-1} range. It was also observed that with an increasing amount of Bi$_2$O$_3$ in N-TiO$_2$, the peaks of the NTiBi nanocomposites become broader and weaker. The decrease in the intensity of the Raman peaks can be associated with the decrease in the crystallinity of the NTiBi nanoparticles. These results are in good agreement with previous reports [32] and are consistent with the XRD measurements.
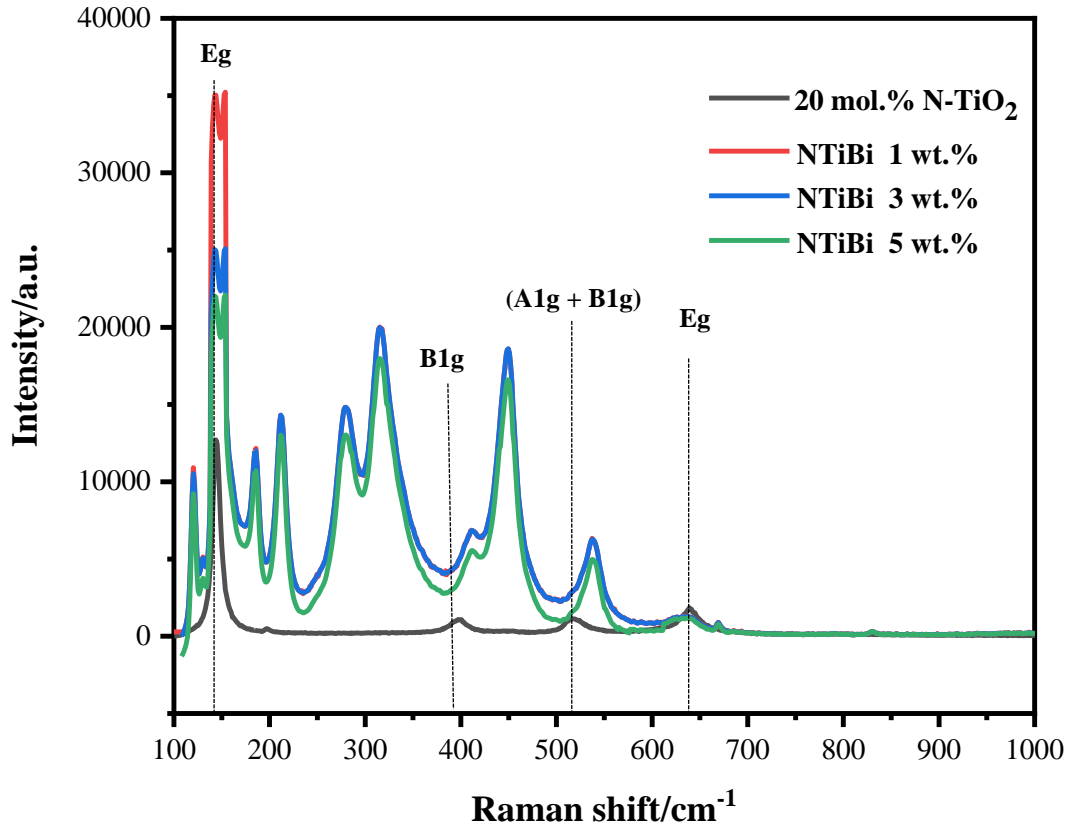
Figure 3.8: Raman spectra of 20 mol.% N-TiO$_2$ and NTiBi (1, 3 and 5 wt.% Bi$_2$O$_3$)

3.3.4. Surface morphologies

Figure 3.9 (a) illustrates an SEM image for pure TiO$_2$ particles. It can be clearly seen that the particle structure of TiO$_2$ consists of approximately uniform spherically-shaped grains with regular morphology. Figure 3.9 (b) illustrates an SEM image for 20 mol.% N-doped TiO$_2$; most of the titania particles kept their original morphology; however, some agglomeration is observed. Figure 3.9 (c) illustrates a SEM image for NTiBi 3 wt.%, after coupling 20 mol.% N-TiO$_2$ with Bi$_2$O$_3$. This image revealed no significant changes in the texture of the composite as compared with the as-prepared materials.
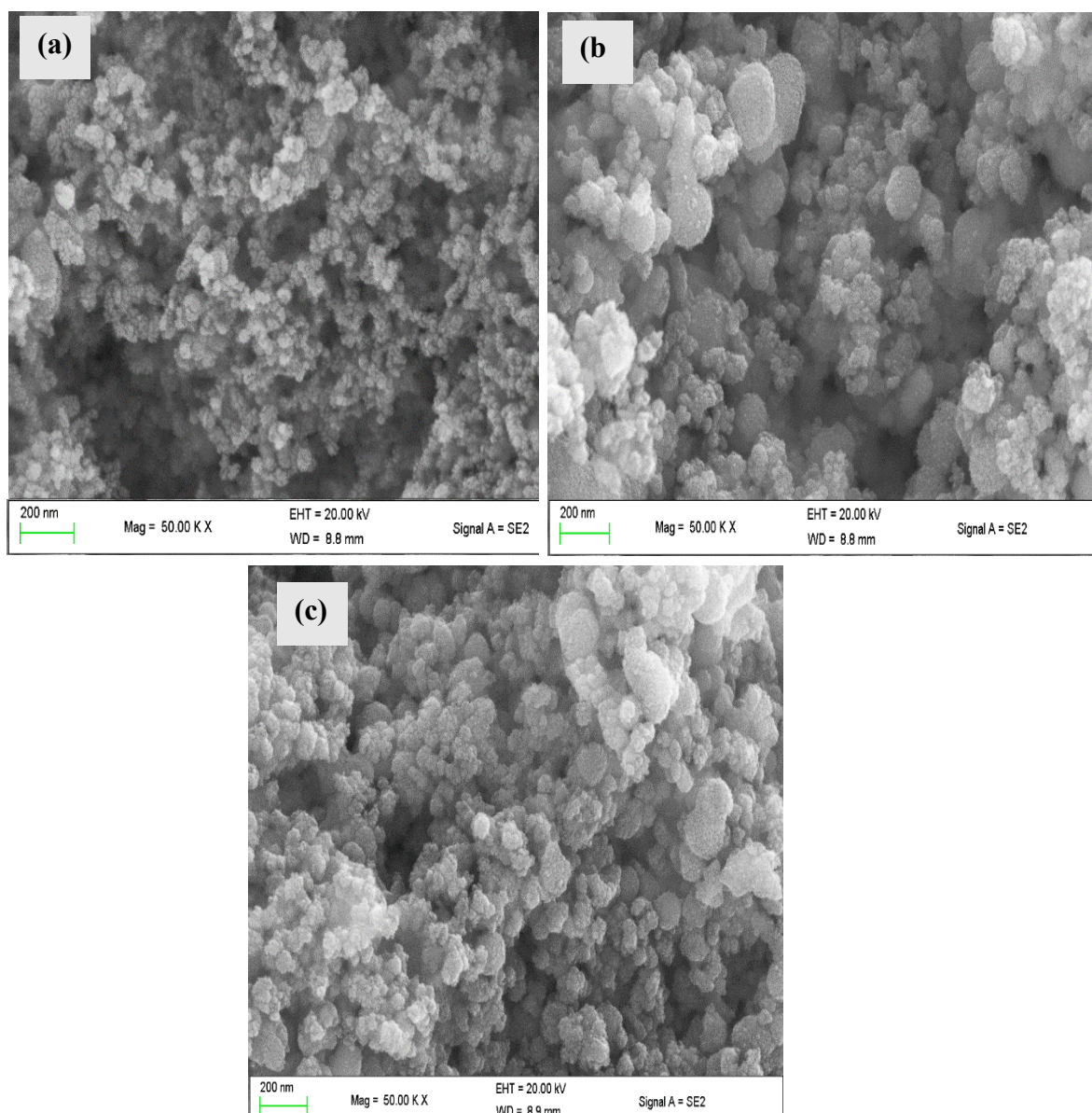
Figure 3.9: SEM images of (a) pure TiO$_2$, (b) 20 mol.% N-TiO$_2$ and (c) NTiBi 3 wt.%

The TEM images obtained from 20 mol.% N-TiO$_2$ and NTiBi 3 wt.% are shown in Figure 3.10 (a-b), which allows the examination of the surface morphology and, also, the direct measurement of nanoparticle size. It is clearly seen that the nanoparticles are spherical for both materials synthesized. These consist of approximately uniform spherically-shaped grains which overlap each other with regular morphology. Also, the average particles sizes were found to be in the 18 – 20 nm range.
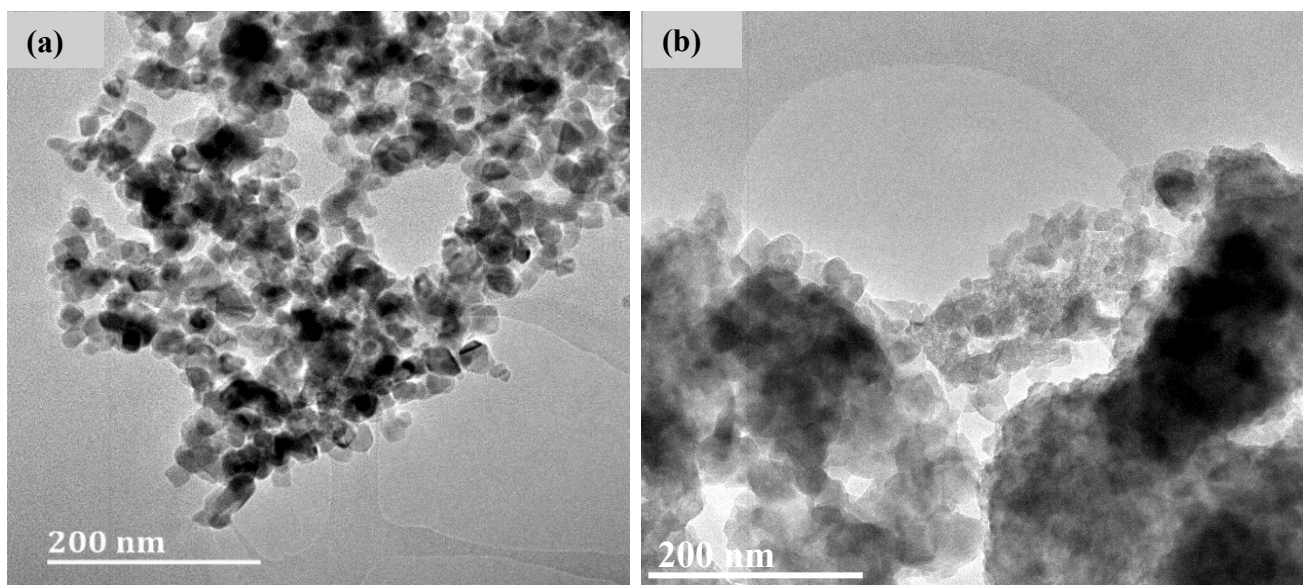
Figure 3.10: TEM images of (a) 20 mol.% N-TiO_2 and (b) NTiBi 3 wt.%

3.3.5. Functional groups

Figure 3.11 depicts the FTIR spectra of the pure TiO_2, N-TiO_2 and NTiBi nanoparticles (see additional information in Appendix F). According to Figure 3.11, it can be clearly seen that the patterns are similar. Figure 3.11 (a) shows the spectrum of pure TiO_2: A broad peak appears in the range of 400 - 1250 cm^{-1} with a sharp tip at 455 cm^{-1} that indicates the presence of Ti-O-Ti characteristic bonding of the anatase structure, while the bands at 1634 cm^{-1} as well as at 3367 cm^{-1} indicate the presence of O-H bending and stretching vibrations, respectively. The OH group vibration is attributed to the physisorbed water molecules present on the surface of TiO_2. Also, the band at 3367 cm^{-1} indicates the interaction of the T^{4+} ion with OH from the lattice structure. Figure 3.8 (b) depicts the spectrum of 20 mol.% N-TiO_2; this spectrum shows a slight shift of the Ti-O-Ti peak to higher wavenumbers and peak broadening compared with the same peak in the TiO_2 spectrum. This is likely because of the inclusion of the nitrogen atoms in the TiO_2 lattice structure, and the instrument detects the Ti-O and T-N characteristic bonding of the anatase structure at a similar position. This suggests that nitrogen is successfully doped into the TiO_2.

Figure 3.11 (c) depicts the spectrum of the NTiBi nanoparticles. According to this spectrum, the peak at the Ti-O-Ti peak position has slightly shifted towards a higher wavenumber and become broader than in the TiO_2 and N-TiO_2 spectra. This is expected since the Bi-O-Bi

bonding characteristic peak appears at the same position as the Ti-O and Ti-N peaks. This suggests that Bi_2O_3 was incorporated into N-TiO_2. However, this must be strongly confirmed by XPS analysis.
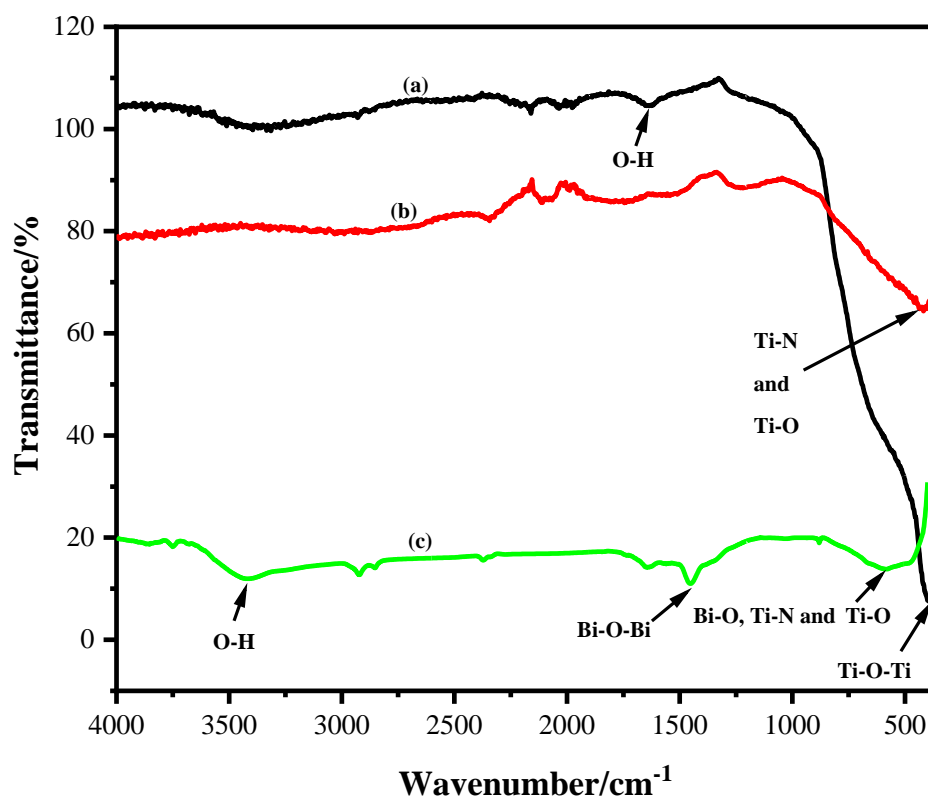
Figure 3.11: The FTIR spectra of (a) pure TiO_2, (b) 20 mol.% N-TiO_2 and (c) NTiBi (3 wt.% Bi_2O_3) nanoparticles

3.3.6.   Surface area and porosity

Figure 3.12 (a-b) presents the nitrogen adsorption-desorption isotherms of the NTiBi 3 wt.% nanoparticles (see additional information in Appendix B). These isotherms reveal that all the samples exhibit a Type III characteristic. Figure 3.12 (a) shows a hysteresis loop that is classified as H1, which is associated with the formation of slit-shaped pores in aggregates of nanoparticles. The surface areas of the nanoparticles synthesised are presented in Table 3.9. N-doped TiO_2 showed a surface area of 35.20 $m^2 g^{-1}$, whereas NTiBi nanoparticles exhibited larger surface areas, in the range of 45 – 57 $m^2 g^{-1}$. This suggests that the high surface area might be contributed by the mesoporous structure and nano-size of the particles. NTiBi samples show an increasing trend of surface area with increasing Bi_2O_3 loadings. This is likely

because the Bi_2O_3 particles hindered the agglomeration of N-TiO_2 nanoparticles and result in larger surface areas.

Figure 3.12 (c-d) depicts the BJH pore size distribution curves of the 20 mol.% N-doped TiO_2 and NTiBi 3 wt.%. The pore diameters for all nanoparticles prepared are within the range of 2 – 50 nm, which reveals that these materials are mesoporous. An inspection of the results obtained suggests that as the surface areas increased, the pore sizes and pore volumes decreased with the introduction of Bi_2O_3 (see summarized results in Table 3.9). Thus, differences in the surface area and porosity of particles of the same material, which may otherwise have the same physical characteristics, can greatly influence its performance characteristics.
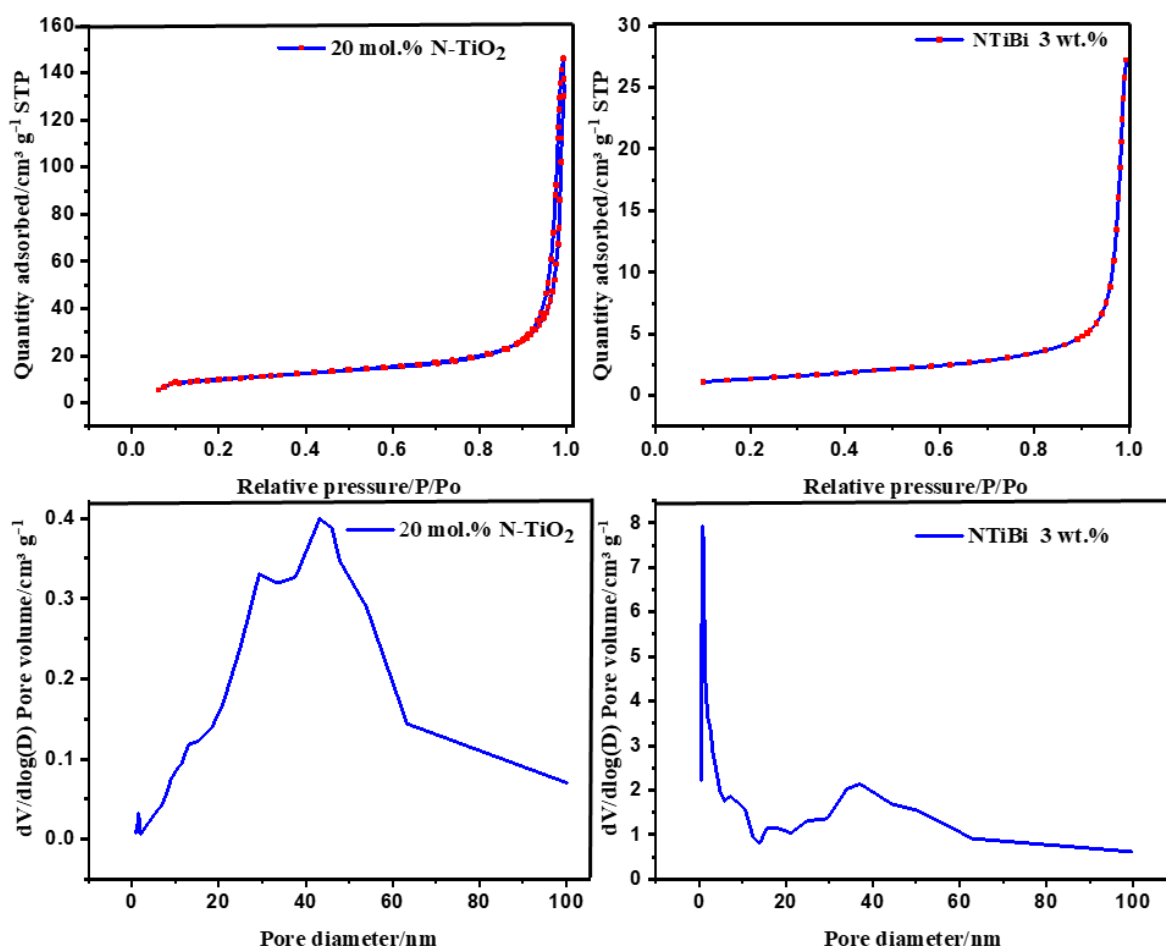
Figure 3.12: (a-b) N_2 absorption-desorption isotherms and (c-d) BJH pore size distribution curves for 20 mole.% N-TiO_2 and NTiBi 3 wt.% nanoparticles, respectively

Table 3.10: BET surface areas, and pore sizes and volumes of the photocatalysts

Sample	S_{BET}/m^2 g^{-1}	Pore diameter/nm	Pore volume/cm^3 g^{-1}
TiO$_2$	33.25	62.66	0.8756
20 mol.% N-TiO$_2$	35.20	34.56	0.2240
NTiBi 1 wt.%	45.27	33.25	0.06845
NTiBi 3 wt.%	55.21	32.28	0.04258
NTiBi 5 wt. %	57.04	30.15	0.01253

3.3.7. Thermal stability

The thermal behaviour of the N-TiO$_2$ and NTiBi nanoparticles synthesized was investigated through TGA. Figure 3.13 depicts the thermograms of urea and N-TiO$_2$ prepared by means of varying the amount of urea into TiO$_2$: The decomposition profile of N-TiO$_2$ with various amounts of mole% N is tabulated in Table 3.11. Urea was totally decomposed at 410 °C, which reveals that the synthesis of N-TiO$_2$ during the calcination process should not be more than 450 °C, and it involves three decomposition steps. According to the decomposition profile of the N-TiO$_2$ photocatalysts prepared, it is clearly seen that N-TiO$_2$ involves two weight loss steps. The first step can be attributed to the loss of physically adsorbed water molecules on the surface of the photocatalyst. The second step involves the loss of loss organic residues, and nitrogen since urea was totally decomposed at 410 °C and this is consistent with literature [33]. Moreover, it is obviously seen that loading more urea results in a lower thermal stability of the N-TiO$_2$ photocatalyst, as shown in Figure 3.13 (a).

Thermograms of the NTiBi nanoparticles synthesized are presented in Figure 3.13 (b), and the decomposition profile in Table 3.11. Thermograms of the NTiBi shows the two decomposition steps, the first step involves the loss of physically absorbed water molecules, whereas the second step is attributed to the loss of nitrogen. Also, it is clearly seen that coupling of N-TiO$_2$ with Bi$_2$O$_3$ increases the thermal stability of photocatalyst. According to the series of NTiBi (1, 3, 5 wt.% Bi$_2$O$_3$) nanoparticles synthesized the 5 wt.% composition shows a lower weight loss in TGA. Hence, a high loading of bismuth oxide increases the thermal stability of the NTiBi nanoparticles.
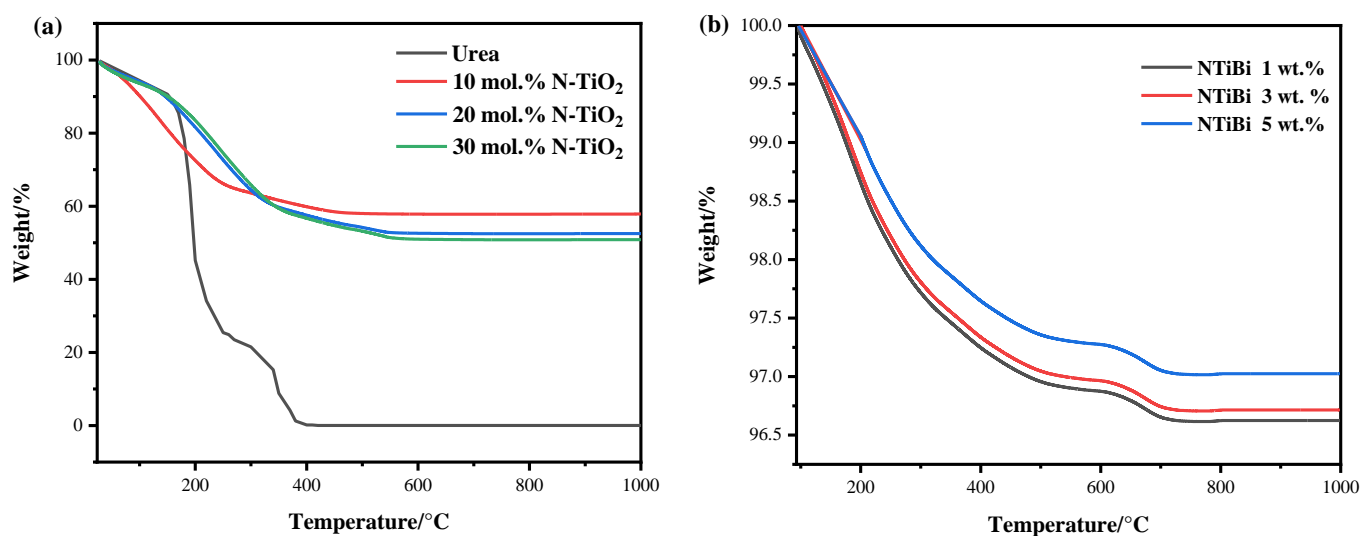
Figure 3.13: TGA curves of the (a) N-TiO$_2$ and (b) NTiBi

Table 3.11: The weight loss percentage of the samples at different temperature ranges

Sample	Sample temperature/°C	Weight loss/%
	28 – 159	5.4586
Urea	210 – 370	74.4385
	371 – 410	19.6698
10 mol.% N-TiO$_2$	38 – 115	5.0421
	116 –542	37.8015
20 mol.% N-TiO$_2$	37 – 160	8.8526
	161 – 539	38.2685
30 mol.% N-TiO$_2$	37 – 161	9.9851
	162 – 469	38.5889
NTiBi 1 wt.%	30 – 460	3.1251
	462 –710	0.2643
NTiBi 3 wt.%	30 – 461	2.9852
	462 -710	0.2938
	30 – 460	2.6874
NTiBi 5 wt.%	461 - 710	0.3165

3.4. Conclusion

A TiO_2-based nanocrystalline heterojunction with both N-doping and Bi_2O_3 coupling (NTiBi) was prepared and thoroughly characterised. The NTiBi was prepared *via* a combined sol-gel and annealing treatment method. The optical properties revealed that the initially prepared N-doped TiO_2 extended its absorption edge towards the visible region and had a narrowed energy bandgap compared with pure TiO_2. A good charge carrier separation was observed in the 20 mol.% $N-TiO_2$ material from the series of $N-TiO_2$ prepared, and this was used to prepare more samples with different amount of Bi_2O_3. When, 20 mol.% $N-TiO_2$ was coupled with a Bi_2O_3, the extension of the light absorption increased further towards the visible region and narrowed the bandgap energy. PL analyses revealed that 20 mol.% $N-TiO_2$ coupled with Bi_2O_3 had an improved electron-hole pair separation, as weaker intensities were observed. Particularly, this was seen in the NTiBi 3 wt.% nanocomposites which exhibited significantly weaker PL intensities than either pure TiO_2, 20 mol.% $N-TiO_2$ and NTiBi (1 and 3 wt.%). It was also seen that the use of excessive Bi_2O_3 into $N-TiO_2$ may result in a higher recombination rate of photogenerated charger carriers, as this was obviously seen from 5 wt.% of Bi_2O_3 into 20 mol.% $N-TiO_2$. The occurrence of the good charge carrier separation in NTiBi was attributed to the matched band potentials and the interconnected nanocrystalline heterojunction. The present work reports an important strategy to design and prepare high-performance TiO_2-based photocatalysts that are active in the visible region of the electromagnetic spectrum and have good charge carrier separation and transportation.

References

1.   Y. Bai, I. Mora-Sero, F. Angelis, J. Bisquert and P. Wang, *Titanium Dioxide Nanomaterials for Photovoltaic Applications*, Chemical reviews, 2014, **114**. 10095-10130.

2.   Y. Lan, Y. Lu and Z. Ren, *Mini review on photocatalysis of titanium dioxide nanoparticles and their solar applications*, Nano Energy, 2013, **2**, 1031-1045.

3.   V. Etacheri, C. Di Valentin, J. Schneider, D. Bahnemann and S. C. Pillai, *Visible-light activation of TiO_2 photocatalysts: Advances in theory and experiments*, Journal of Photochemistry and Photobiology C: Photochemistry Reviews, 2015, **25**, 1-29.

4.   A. Piątkowska, M. Janus, K. Szymanski and S. Mozia, *C-, N-and S-doped TiO$_2$ photocatalysts: a review*, Catalysts, 2021, **11**, 144.

5.   S. B. Rawal, S. Bera, D. Lee, D.-J. Jang and W. I. Lee, *Design of visible-light photocatalysts by coupling of narrow bandgap semiconductors and TiO$_2$: effect of their relative energy band positions on the photocatalytic efficiency*, Catalysis Science & Technology, 2013, **3**, 1822-1830.

6.   M. Humayun, F. Raziq, A. Khan and W. Luo, *Modification strategies of TiO$_2$ for potential applications in photocatalysis: a critical review*, Green Chemistry Letters and Reviews, 2018, **11**, 86-102.

7.   Y. Cong, J. Zhang, F. Chen and M. Anpo, *Synthesis and characterization of nitrogen-doped TiO$_2$ nanophotocatalyst with high visible light activity*, The Journal of Physical Chemistry C, 2007, **111**, 6976-6982.

8.   J. Yang, X. Wang, J. Dai and J. Li, *Efficient visible-light-driven photocatalytic degradation with Bi$_2$O$_3$ coupling silica doped TiO$_2$*, Industrial & Engineering Chemistry Research, 2014, **53**, 12575-12586.

9.   T. S. Natarajan, V. Mozhiarasi and R. J. Tayade, *Nitrogen doped titanium dioxide (N-TiO$_2$): synopsis of synthesis methodologies, doping mechanisms, property evaluation and visible light photocatalytic applications*, Photochem, 2021, **1**, 371-410.

10.   M. D'Arienzo, N. Siedl, A. Sternig, R. Scotti, F. Morazzoni, J. Bernardi and O. Diwald, *Solar light and dopant-induced recombination effects: photoactive nitrogen in TiO$_2$ as a case study*, The Journal of Physical Chemistry C, 2010, **114**, 18067-18072.

11.   G. Di Liberto, S. Tosoni and G. Pacchioni, *Nitrogen doping in coexposed (001)–(101) anatase TiO$_2$ surfaces: a DFT study*, Physical Chemistry Chemical Physics, 2019, **21**, 21497-21505.

12.   K. Wojtaszek, A. Wach, J. Czapla-Masztafiak, K. Tyrala, J. Sá, L. Yıldız Ozer, C. Garlisi, G. Palmisano and J. Szlachetko, *The influence of nitrogen doping on the electronic structure of the valence and conduction band in TiO$_2$*, Journal of synchrotron radiation, 2019, **26**, 145-151.

13.   T. Jia, F. Fu, D. Yu, J. Cao and G. Sun, *Facile synthesis and characterization of N-doped TiO$_2$/C nanocomposites with enhanced visible-light photocatalytic performance*, Applied Surface Science, 2018, **430**, 438-447.

14.   L. Dias, F. Correia, J. Ribeiro and C. Tavares, *Photocatalytic Bi$_2$O$_3$/TiO$_2$:N thin films with enhanced surface area and visible light activity*, Coatings, 2020, **10**, 445.

15. X. Fan, N. Hua, H. Jia, Y. Zhu, Z. Wang, J. Xu and C. Wang, *Synthesis and evaluation of visible-light photocatalyst: nitrogen-doped TiO$_2$/Bi$_2$O$_3$ heterojunction structures*, Science of Advanced Materials, 2014, **6**, 892-1899.

16. J. Liqiang, Q. Yichun, W. Baiqi, S. Li, J. Baojiang, Y. Libin, F. Wei, F. Honggang and S. Jiazhong, *Review of photoluminescence performance of nano-sized semiconductor materials and its relationships with photocatalytic activity*, Solar Energy Materials and Solar Cells, 2006, **90**, 1773-1787.

17. M. D'Arienzo, N. Siedl, A. Sternig, R. Scotti, F. Morazzoni, J. Bernardi and O. Diwald, *Solar light and dopant-induced recombination effects: photoactive nitrogen in TiO$_2$ as a case study*, The Journal of Physical Chemistry C, 2010, **114**, 18067-18072..

18. H. Ijadpanah-Saravy, M. Safari, A. Khodadadi-Darban and A. Rezaei, *Synthesis of titanium dioxide nanoparticles for photocatalytic degradation of cyanide in wastewater*, Analytical Letters, 2014, **47**, 1772-1782.

19. E. Filippo, C. Carlucci, A. L. Capodilupo, P. Perulli, F. Conciauro, G. A. Corrente, G. Gigli and G. Ciccarella, *Enhanced photocatalytic activity of pure anatase TiO$_2$ and Pt-TiO$_2$ nanoparticles synthesized by green microwave assisted route*, Materials Research, 2015, **18**, 473-481.

20. Z. Bian, J. Zhu, S. Wang, Y. Cao, X. Qian and H. Li, *Self-assembly of active Bi$_2$O$_3$/TiO$_2$ visible photocatalyst with ordered mesoporous structure and highly crystallized anatase*, The Journal of Physical Chemistry C, 2008, **112**, 6258-6262.

21. W. Peng, C. Yang and J. Yu, *Bi$_2$O$_3$ and g-C$_3$N$_4$ quantum dot modified anatase TiO$_2$ heterojunction system for degradation of dyes under sunlight irradiation*, RSC Advances, 2020, **10**, 1181-1190.

22. J. Hou, C. Yang, Z. Wang, W. Zhou, S. Jiao and H. Zhu, *In situ synthesis of α–β phase heterojunction on Bi$_2$O$_3$ nanowires with exceptional visible-light photocatalytic performance*, Applied Catalysis B: Environmental, 2013, **142-143**, 504-511.

23. M. Inoue and I. Hirasawa, *The relationship between crystal morphology and XRD peak intensity on CaSO$_4$·2H$_2$O*, Journal of Crystal Growth, 2013, **380**, 169-175.

24. M.-S. Liang, Y.-K. Fong, C.-C. Khaw, C.-C. Liu and S.-P. Chin, *Studies on the effects of crystallite sizes and scattering layers on the conversion efficiency of dye-sensitized solar cell*, Journal of Power and Energy Engineering, 2014, **2**, 18-24.

25. A. Khlyustova, N. Sirotkin, T. Kusova, A. Kraev, V. Titov and A. Agafonov, *Doped TiO$_2$: the effect of doping elements on photocatalytic activity*, Materials Advances, 2020, **1**, 1193-1201.

26. N. Azhar, M. Taib, O. Hassan, M. Yahya and A. Ali, *Structural, electronic and optical properties of Bi_2O_3 polymorphs by first-principles calculations for photocatalytic water splitting*, Materials Research Express, 2017, **4**, 034002.

27. O. Frank, M. Zukalova, B. Laskova, J. Kürti, J. Koltai and L. Kavan, *Raman spectra of titanium dioxide (anatase, rutile) with identified oxygen isotopes (16, 17, 18)*, Physical Chemistry Chemical Physics, 2012, **14**, 14567-14572.

28. E. J. Ekoi, A. Gowen, R. Dorrepaal and D. P. Dowling, *Characterisation of titanium oxide layers using Raman spectroscopy and optical profilometry: Influence of oxide properties*, Results in Physics, 2019, **12**, 1574-1585.

29. O. Frank, M. Zukalova, B. Laskova, J. Kurti, J. Koltai and L. Kavan, *Raman spectra of titanium dioxide (anatase, rutile) with identified oxygen isotopes (16, 17, 18)*, Physical Chemistry Chemical Physics : PCCP, 2012, **14**, 14567-14572.

30. L. Baia, R. Stefan, W. Kiefer and S. Simon, *Structural characteristics of B_2O_3-Bi_2O_3 glasses with high transition metal oxide content*, Journal of Raman Spectroscopy, 2005, **36**, 262-266.

31. A. Salazar-Perez, M. Camacho-Lopez, R. Morales-Luckie, V. Sanchez-Mendieta, F. Urena-Nunez and J. Arenas-Alatorre, *Structural evolution of Bi_2O_3 prepared by thermal oxidation of bismuth nano-particles*, Superficies Y Vacio, 2005, **18**, 4-8.

32. M. Malligavathy, S. Iyyapushpam, S. Nishanthi and D. P. Padiyan, *Remarkable catalytic activity of Bi_2O_3/TiO_2 nanocomposites prepared by hydrothermal method for the degradation of methyl orange*, Journal of Nanoparticle Research, 2017, **19**, 144.

33. M. S. Khan, J. A. Shah, M. Arshad, S. A. Halim, A. Khan, A. J. Shaikh, N. Riaz, A. J. Khan, M. Arfan and M. Shahid, *Photocatalytic decolorization and biocidal applications of nonmetal doped TiO_2: isotherm, kinetic modeling and in silico molecular docking studies*, Molecules, 2020, **25**, 4468.

Chapter 4

Incorporation of reduced graphene oxide into N-doped TiO$_2$/Bi$_2$O$_3$ nanoparticles

This chapter presents a brief introduction on graphene-based materials and subsequently discusses the incorporation of reduced graphene oxide (rGO) into N-TiO$_2$/Bi$_2$O$_3$ nanoparticles to form N-TiO$_2$/Bi$_2$O$_3$/rGO nanocomposites with the different amounts of rGO.

4.1. Introduction

Graphene, a two-dimensional (2D) semiconductor material consisting of individual sheets of *sp^2*-hybridized carbon atoms arranged in a hexagonal lattice structure, has attracted significant research attention due to its unique properties and potential applications [1]. Notably, graphene has been used to improve the photocatalytic performance of semiconductors due to its potential to promote good charge carrier separation and electron transfer [2, 3]. Also, graphene has the ability to broaden the optical absorption spectrum towards the visible region, thereby facilitating effective photon harvesting [4]. In addition, graphene is considered to be an excellent 2D catalytic support, and has been widely incorporated into TiO$_2$ to enhance the separation and transportation of charge carriers in photocatalytic reactions [5, 6].

Interestingly, N-TiO$_2$ coupled with Bi$_2$O$_3$ (discussed in Chapter 3) has also demonstrated enhanced charge separation and extension of the absorption spectrum, since Bi$_2$O$_3$ is one of the most potential visible light photocatalysts with a direct bandgap of 2.8 eV. Coupling N-TiO$_2$ and Bi$_2$O$_3$ does not only widen the absorption spectrum and inhibit the high recombination of photogenerated charge carriers, but also improves the thermal stability and surface area of the resulting composite material. For instance, the mostly reported Bi$_2$O$_3$/TiO$_2$ composites showed excellent photocatalytic performance [7]. Moreover, a strongly coupled TiO$_2$ with Bi$_2$O$_3$ resulting from a surface precleaning strategy for TiO$_2$ to facilitate coupling, has shown improved photochemical properties [8]. This study revealed that the interfacial coupling effect plays a significant role in tailoring the photochemical performance of heterostructured photocatalysts. Also, it provides deep insights into further improvements in suppressing the recombination of charge carriers.

Recently, a significant improvement in photocatalytic activity was observed after integrating graphene with TiO_2/Bi_2O_3. For example, nitrogen doped $GO-TiO_2/Bi_2O_3$ has been reported as a promising solar irradiated photocatalyst in the degradation of organic pollutants [9]. Also, to address the problem of rapid charge carrier recombination that usually lowers the photocatalytic activity of TiO_2, the incorporation of graphene into $N-TiO_2/Bi_2O_3$ has been proposed as a promising approach to suppress charge carrier recombination and further enhance the photocatalytic activity. Hence, the incorporation of reduced graphene oxide (rGO) into a new class of heterojunction nanostructured material ($N-TiO_2/Bi_2O_3$) is envisaged to be a promising strategy for enhancing the charger carrier separation and transportation, optical activity, surface area and thermal stability of the material.

4.2. Experimental

This section provides the details of all the materials used in the synthesis and characterization of the $N-TiO_2/Bi_2O_3/rGO$ nanocomposites, together with the intermediate nanomaterials formed during the synthesis.

4.2.1. Materials

All the chemicals, solvents and reagents used in the synthesis of the nanomaterials were used as received without further purification, and their sources and purity are listed in Table 4.1.

Table 4.1: Chemicals, solvents and reagents used in the synthesis of the nanomaterials

Reagent/solvents	Supplier	Purity/%
Graphite powder ($< 20\,\mu m$)	Sigma Aldrich	99.0
Potassium permanganate	Sigma Aldrich	99.4
Sulphuric acid	Promark Chemicals	98.0
Phosphoric acid	Rochelle Chemicals	85.0
Nitric acid	LabChem	65
Acetic acid glacial	Rochelle Chemicals	Analytical grade (99.8)
Hydrogen peroxide	Sigma Aldrich	98.0
Hydrochloric acid	Sigma Aldrich	98.0
Titanium dioxide	Sigma Aldrich	99.8

4.2.2.   Synthesis of graphene oxide

Graphene oxide (GO) was synthesised *via* Tour's method. A mass of 3 g of pure graphite powder was added into a mixture of sulphuric and phosphoric acids with a volume ratio of 9:1, under vigorous stirring. After 10 min, 18 g of potassium permanganate (KMnO$_4$) was slowly added into the reaction mixture, to make a 1:6 mass ratio of graphite:potassium permanganate. The reaction mixture was stirred for 6 h until it became brownish at temperatures below 50 °C to prevent the formation of explosive MnO$_2$. Then, the reaction mixture was allowed to cool and was transferred into 400 ml of ice-water. A few drops of hydrogen peroxide were added slowly, while stirring the mixture for 10 min, in order to eliminate excess KMnO$_4$. At this stage, an exothermic reaction took place and the reaction was cooled down in an ice bath. Then a mixture of 10 mL of HCl and 30 mL of deionized water was added, and the mixture was aged at room temperature to form the supernatant that was decanted away, while the residue was rewashed with HCl and deionized water. The final product was then further washed with double-distilled water until a pH of 6.4 was obtained, and dried in an oven at 50 °C for 2 days to obtain GO.

4.2.3.   Synthesis of rGO

A fast and simple solvent-assisted microwave reduction method coupled with prior mild annealing was used to reduce GO. In this method, GO was annealed at 300 °C for 1 h under an argon atmosphere before microwave reduction. Thereafter, GO was dispersed into a mixture of absolute ethanol and double-distilled water and microwave-reduced at 200 °C for 8 min with a power of 300 W. The product obtained was washed with double-distilled water and dried in an oven overnight at 50 °C.

4.2.4.   Synthesis of N-TiO$_2$/Bi$_2$O$_3$/rGO

The incorporation of rGO into N-TiO$_2$/Bi$_2$O$_3$ 3 wt.% was done *via* a hydrothermal method. This was done by preparing mixture A: rGO dispersed into double-distilled water and sonicated

for 30 min, and mixture B: N-TiO$_2$/Bi$_2$O$_3$ dispersed into double-distilled water and sonicated for 10 min. Mixture B was slowly added into mixture A to obtain a stable reaction mixture, and stirred for 30 min. Then, the reaction mixture was transferred into Teflon autoclaves and subjected to heating in an oven at 190 °C for 9 h. The product obtained was washed with double-distilled water and dried in an oven at 130 °C, overnight. A similar procedure was adopted to prepare more samples containing a different amount of rGO. Overall, the nanocomposites prepared were denoted by NTiBi/rGO x%, where x% represented the rGO weight ratios, such as 3, 5, 10 and 15 wt.%. For these syntheses only the NTiBi 3 wt.% prepared in Chapter 3 was used. The masses of reagents used to prepare NTiBi/rGO nanocomposites are detailed in Table 4.2. This is followed by a sample calculation to show how the amounts of rGO required for incorporation into NTiBi were calculated.

Table 4.2: Masses of reagents used to prepare different NTiBi/rGO nanocomposites

Material	Mass of NTiBi/g	Mass of rGO/g
NTiBi/rGO 3 wt.%	1.0014	0.03097
NTiBi/rGO 5 wt.%	1.0016	0.05272
NTiBi/rGO 10 wt.%	1.0015	0.1113
NTiBi/rGO 15 wt.%	1.0013	0.1767

A sample calculation for the mass of rGO required to prepare NTiBi/rGO 3 wt.% starting with a 1.0014 g of NTiBi:

$$3\ wt.\% = \left(\frac{x}{x + 1.0014\ g}\right) 100\%$$

$$x = 0.03097\ g$$

4.2.5. Characterisation of materials

The details of most of the characterisations for the physicochemical properties of the nanocomposites were discussed in Chapter 3, Section 3.3, except for the determination of the titanium and bismuth content in the nanocomposites. A titanium standard stock solution (600 mg L^{-1}) containing T^{4+} was prepared by heating 100 mg of pure TiO$_2$ in a mixture of 10 mL of sulfuric acid (98%) and 1 mL nitric acid (65%) on a hot plate up to 400 °C for 5 min. But, TiO$_2$ was initially annealed at 300 °C for 3 h before use to give a carbon-free material. The working standard solutions were then prepared by serial dilution from a 100 mg L^{-1} solution to fall within the 0.1 - 1 mg L^{-1} concentration range. Also, bismuth working standard solutions were prepared as described in Chapter 3 over a 0.05 – 1 mg L^{-1} concentration range. The nanocomposites were firstly heated in muffle furnace at 700 °C for 3 h to give a carbon-free material. Then, an accurately weighed amount of 50 mg of carbon-free material was mixed with 17 mg of potassium bisulphate (KHSO$_4$) in a crucible and heated over a Bunsen flame for approximately 10 minutes to fuse the mixture. The molten product was transferred into a mixture of H$_2$SO$_4$:HNO$_3$ (10:1 v/v) and heated on a hotplate up to 400 °C whilst stirring for 5 min to obtain a clear solution. The digest was cooled to room temperature and quantitatively transferred into a 100 mL volumetric flask. The digest residues were washed with double-distilled water and added to the same volumetric flask, and made to a volume of 100 mL with double-distilled water. A 1 ml aliquot of this solution was then diluted in a 100 ml volumetric flask with double-distilled water. Double-distilled water was used as a blank solution. The ICP-OES emission intensity readings of each element in the sample were substituted as the y-values into the calibration equations resulting from each standard calibration curve respectively to obtain a concentration in mg L^{-1}. For instance, the titanium ICP-OES reading in the NTiBi/rGO 3 wt.% was 1989.77167 and calculations were performed as follows:

$$y = 1988.7x - 8.3376 \quad \text{where } x \text{ is the [Ti] and } y \text{ is the ICP} - \text{OES reading}$$

$$[Ti] = \left(\frac{1989.77167 + 8.3376}{1988.7} \right)$$

$$[Ti] = 1.005 \; mg \; L^{-1}$$

$$Dilution \; factor \; was \; = \frac{100 \; mL}{1 \; mL} = 100$$

$$Wt.\% = \left(\frac{1.005 \; mg \; L^{-1} \times 0.1 \; L \times 100}{50.0 \; mg} \right) 100 \% = 20.09 \; wt.\%$$

A similar procedure was adopted for the NTiBi/rGO 5 wt.%, NTiBi/rGO 10 wt.% and NTiBi/rGO 15 wt.%, where the ICP-OES readings for Ti were 1969.57701, 1877.12701 and 1286.91289, respectively. Also, the ICP-OES readings for Bi were 177.29441, 167.80088, 158.90216, and 145.11663, for NTiBi/rGO (3, 5, 10 and 15 wt.% rGO, respectively). The calibration equation was $y = 1818.1\,x - 12.232$ for the bismuth concentration in the NTiBi/rGO samples. The ICP-OES instrument parameters are listed in Table 4.3.

Table 4.3: ICP-OES operating parameters for determination of Bi and Ti content

Parameters	Conditions
Incident power/kW	1.5
Plasma air flow rate/L min^{-1}	15
Auxiliary air flow rate/L min^{-}	1.5
Nebulizer gas flow rate/L min^{-1}	0.2
Pump flow rate/mL min^{-1}	0.8
Bismuth wavelength/nm	223.061
Titanium wavelength/nm	337.280

4.3. Results and discussion

This section discusses the results obtained from the characterization of the physicochemical properties of the NTiBi/rGO nanocomposites, together with the intermediate nanocomposites formed during the synthesis.

4.3.1. Elemental composition

The elemental composition analysis was performed qualitatively by using EDX-coupled with SEM microscopy and quantitatively with the aid of an elemental analyser (CHNSO) and ICP-OES.

4.3.1.1. Qualitatively analysis

EDX-coupled to SEM microscopy as a qualitative technique, was used to confirm the presence of the expected elements; including titanium, bismuth, carbon, oxygen, and nitrogen. The EDX

spectrum of rGO shown in Figure 4.1 (a) confirms the presence of carbon, and oxygen elements (see additional information in Appendix A). However, EDX is not suitable for detecting the lightest elements [10]; hence, hydrogen peaks could not be seen in the EDX spectrum due to it being the lightest element. In addition, hydrogen does not have core electrons to be removed, for X-ray emission to take place [11]. Figure 4.1 (b) displays the EDX spectrum of NTiBi/rGO 10 wt.%, in which each element was observed with its distinct peaks on the electromagnetic emission spectrum, indicating the formation of the NTiBi/rGO nanocomposite with the expected elements and of high purity. Figure 4.1 (c) displays the elemental mapping image of the NTiBi/rGO 10 wt.% nanocomposite. Each element of interest was defined with a unique colour, and it is clearly seen that there is a good distribution of the elements in the nanocomposite.
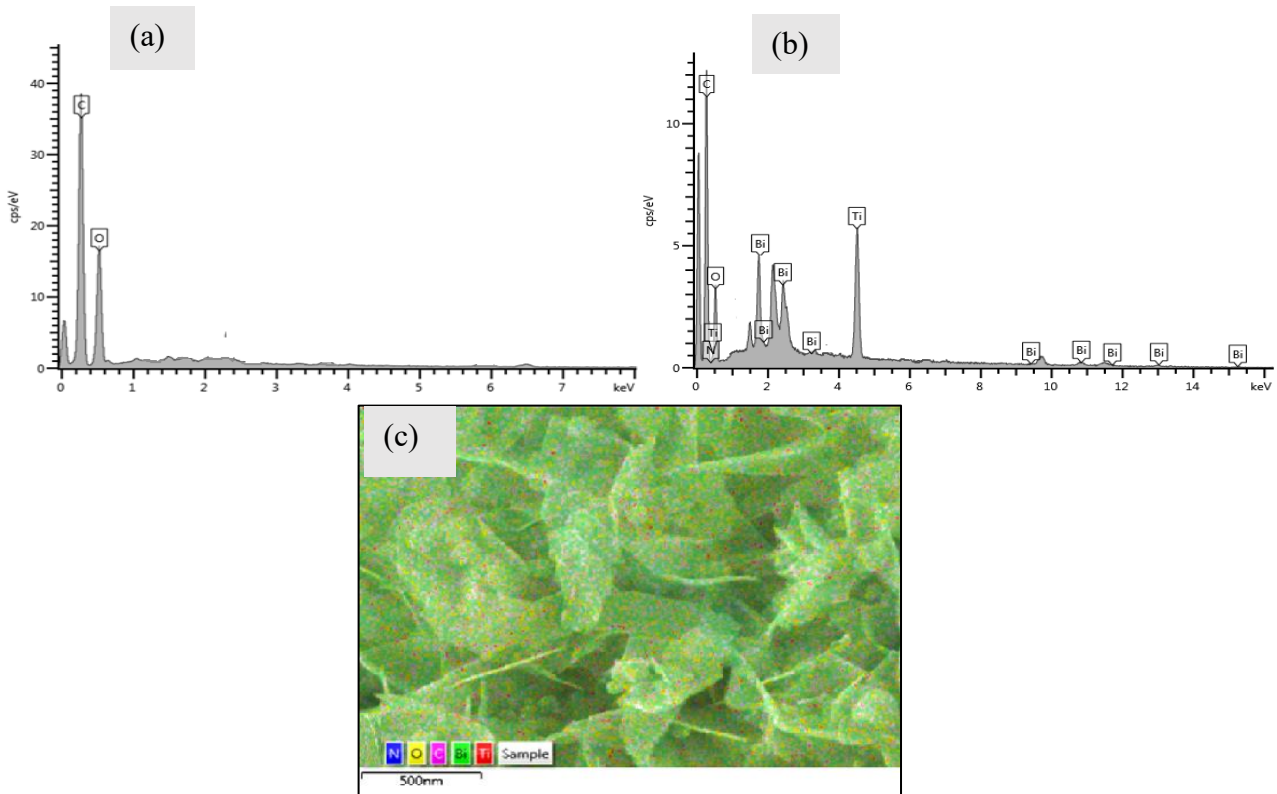

Figure 4.1: EDX spectra of (a) rGO and (b) NTiBi/rGO 10 wt.%, and (c) the elemental mapping of NTiBi/rGO 10 wt.%

4.3.1.2. Nitrogen content

Table 4.4 presents the amount of nitrogen, carbon, hydrogen and sulfur in the nanocomposites, determined with a CHNS elemental analyser and oxygen by difference. The oxygen content was determined by difference by including all elements, such as C, H, N, S, determined with the CHNS analyser, and Ti, Bi determined with ICP-OES, to the total composition. It is observed that as the content of rGO incorporated into NTiBi increases, there is a decrease in the nitrogen content in the nanocomposites. The decrease in nitrogen content is due to the subsequent treatment of N-TiO$_2$-based materials, since nitrogen in N-TiO$_2$ can be lost due to solubilization, heating, etc. [12, 13]. Also, as rGO loading increases, the sample become rich with rGO and other elements become less in the sample, and, thus, there is a decrease in N content. Through this technique, carbon, hydrogen, oxygen and sulfur elements were also observed. Among these, carbon, oxygen and hydrogen were expected to be seen in the nanocomposite. However, sulfur was not expected in the nanocomposites, but since it was observed at a very low amount its effects can be neglected. Moreover, the carbon content increases with the content of rGO in the nanocomposites. Hence, these results confirm the presence of nitrogen, carbon and hydrogen in the nanocomposites prepared.

Table 4.4: The content of nitrogen, carbon, oxygen, hydrogen and sulfur in the nanocomposites

Sample	N/%	C/%	H/%	S/%	O/%*
NTiBi/rGO 3 wt.%,	0.27	34.64	2.09	0.02	40.70
NTiBi/rGO 5 wt.%,	0.16	35.16	2.20	0.03	40.47
NTiBi/rGO 10 wt.%,	0.15	36.12	2.29	0.04	40.25
NTiBi/rGO 15 wt.%,	0.14	58.31	1.41	0.03	23.25

*Oxygen content determined by difference

4.3.1.3. Titanium and bismuth content in the nanocomposites

Figure 4.2 displays the standard calibration curve of titanium, obtained over a 0.1 - 1 mg L^{-1} concentration range with good linearity (R^2 = 0.9964). Also, Figure 4.3 displays the standard calibration curve for bismuth obtained over a 0.05 - 1 mg L^{-1} concentration range, with a good correlation coefficient (R^2 = 0.9945). Both calibration curves were suitable for the determination of titanium and bismuth concentrations in the nanocomposites. The amount of both elements in the nanocomposites, expressed as weight percentages, are tabulated in Table 4.5 with their respective percent relative standard deviation (%RSD). The amounts of titanium measured in these nanocomposites were 20.09, 19.89, 18.96 and 13.02 wt.% for NTiBi/rGO (3, 5, 10 and 15 wt.% rGO), respectively. From these results, it is clearly seen that the amount of titanium decreases with increasing rGO content. This is likely because the nanocomposites become rich with rGO upon loading more graphene. These results are in good agreement with the trend observed in the nitrogen content determined with the CHNS elemental analyser. Also, the bismuth content in the nanocomposite exhibited a similar trend as titanium as shown in Table 4.5.
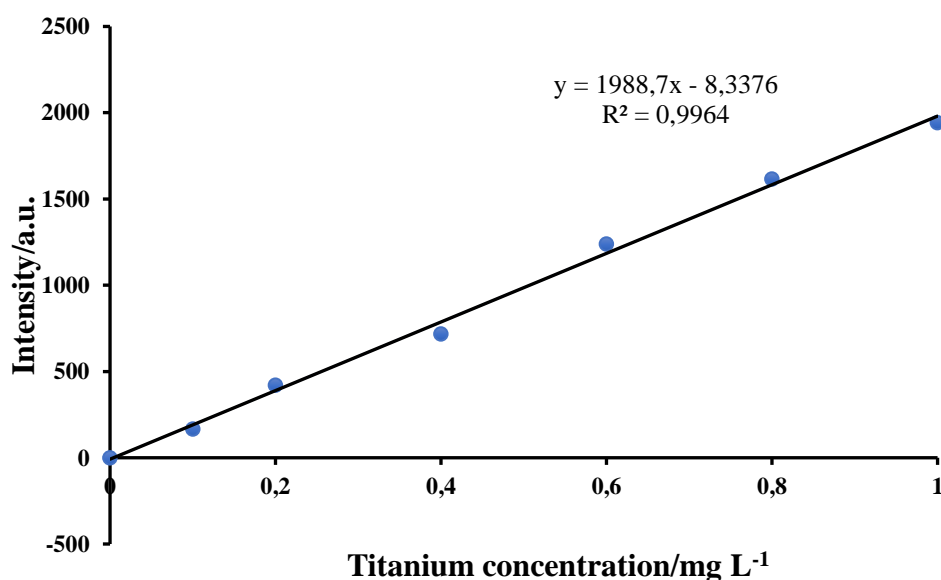
Figure 4.2: Standard calibration curve for the determination of titanium in the nanocomposites
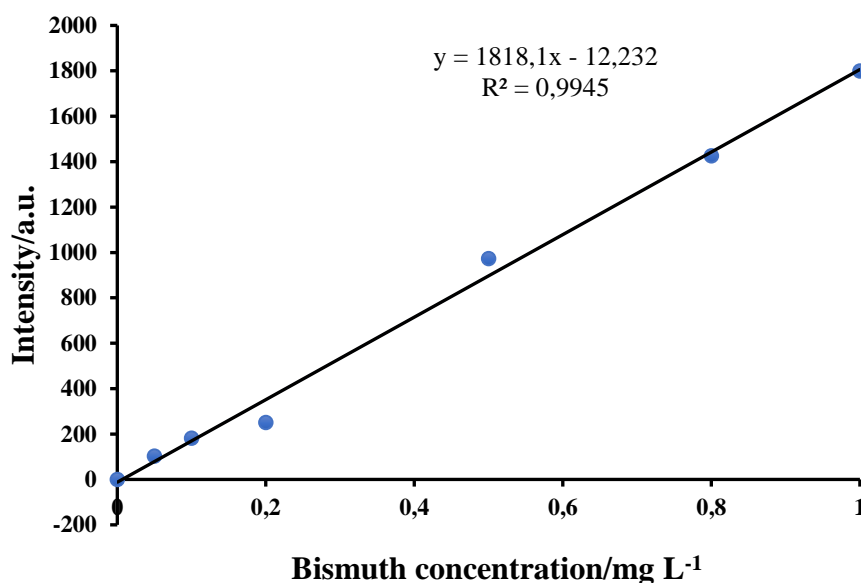
Figure 4.3: Standard calibration curve for the determination of bismuth in the nanocomposites

Table 4.5: The weight percentage of titanium and bismuth in the NTiBi/rGO nanocomposites

Sample	Experimental weight (RSD)/%	
	Ti	Bi
NTiBi/rGO 3 wt.%	20.09 (17.55)	2.19 (13.95)
NTiBi/rGO 5 wt.%	19.89 (15.28)	2.09 (13.69)
NTiBi/rGO 10 wt.%	18.96 (19.53)	1.99 (14.15)
NTiBi/rGO 15 wt.%	13.02 (23.74)	1.84 (12.25)

4.3.2. Optical properties

The optical properties of the NTiBi/rGO nanocomposites were evaluated by using ultraviolet-visible, diffuse reflectance ultraviolet-visible and photoluminescence spectroscopies.

4.3.2.1. Ultraviolet-visible spectroscopy

The ultraviolet-visible (UV-Vis) spectra of the samples as a suspension in double-distilled water were measured to characterise the light absorption properties of the nanocomposites prepared. Figure 4.4 depicts the UV-Vis spectra of the samples suspended in double-distilled water. The nanocomposites exhibited maximum absorption in the 351 - 363 nm range. Interestingly, rGO and NTiBi exhibited maximum absorption bands at 345 and 349 nm, respectively. Hence, these results confirm that incorporation of rGO into NTiBi extends light absorption towards the visible region. However, measurement of the UV-Vis spectra of these suspended samples was challenging to carry out due to the scattering of reflected light by fine particles in the suspension. This prevented 100% of the light from reaching the detector, thereby making it more difficult to obtain a clear spectrum; hence, resulting in some deviations of the maximum wavelength from the expected position. Therefore, the measurements were carried out with an integrating sphere (UV-Vis DRS) where the samples are in the solid-state, and the results were compared (see Section 4.3.2.2).
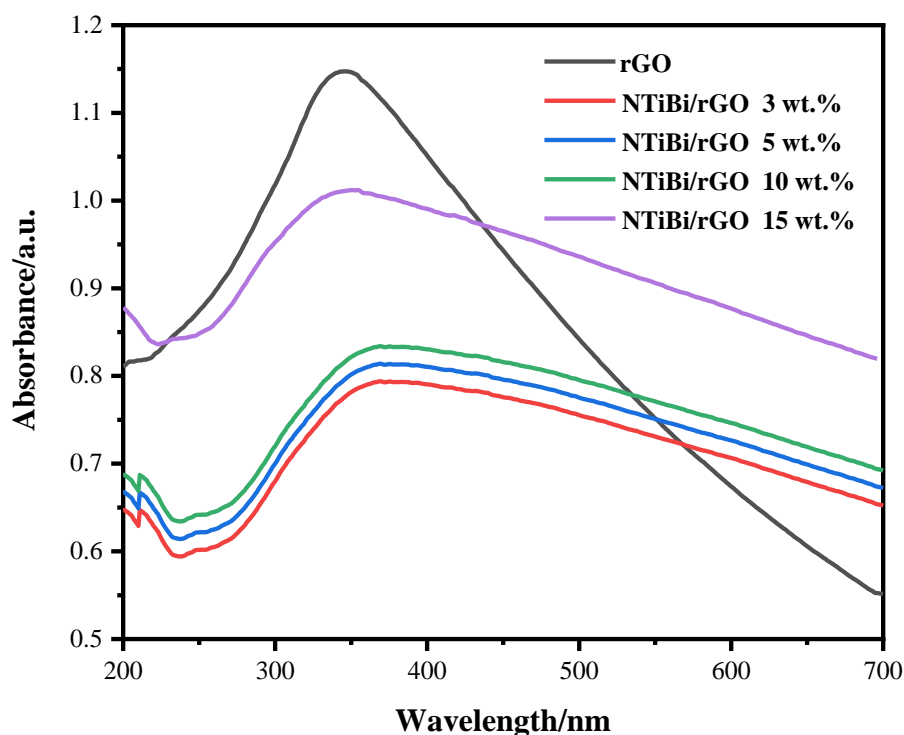

Figure 4.4: UV-Vis spectra of rGO and NTiBi/rGO (3, 5, 10 and 15 wt.%) nanocomposites suspended in double-distilled water

4.3.2.2. Diffuse reflectance ultraviolet-visible spectroscopy

The nanocomposites prepared were investigated for their electronic transitions and shift in the absorption band. Figure 4.5 (a) shows the UV-Vis diffuse reflectance spectra (DRS) of GO, rGO and NTiBi/rGO. The GO spectrum exhibits a maximum absorption band at 235 nm for a pi-pi* transition and a shoulder absorption band at 295 nm for a n-pi* transition [14]. However, in the rGO spectrum, the peak for the pi-pi* transition red-shifted to 265 nm [15]. This confirms that some of the oxygenated groups on the surface of GO were removed, and the conjugated structure was restored. For the NTiBi/rGO nanocomposite, light absorbance was extended towards the visible region, which increased light absorption. The red-shift and improved light absorbance are attributed to the introduction of rGO into NTiBi [16]. The plot resulting from the transformation based on the Kubelka-Munk function against the energy of light is presented in Figure 4.5 (b). The extrapolated bandgap energies are tabulated in Table 4.6, and these results reveal that the bandgap energy values of the nanocomposites decreased remarkably with increasing rGO content. Hence, incorporating a high amount of rGO into the NTiBi nanoparticles effectively increases the visible light absorption capacity [16, 17].
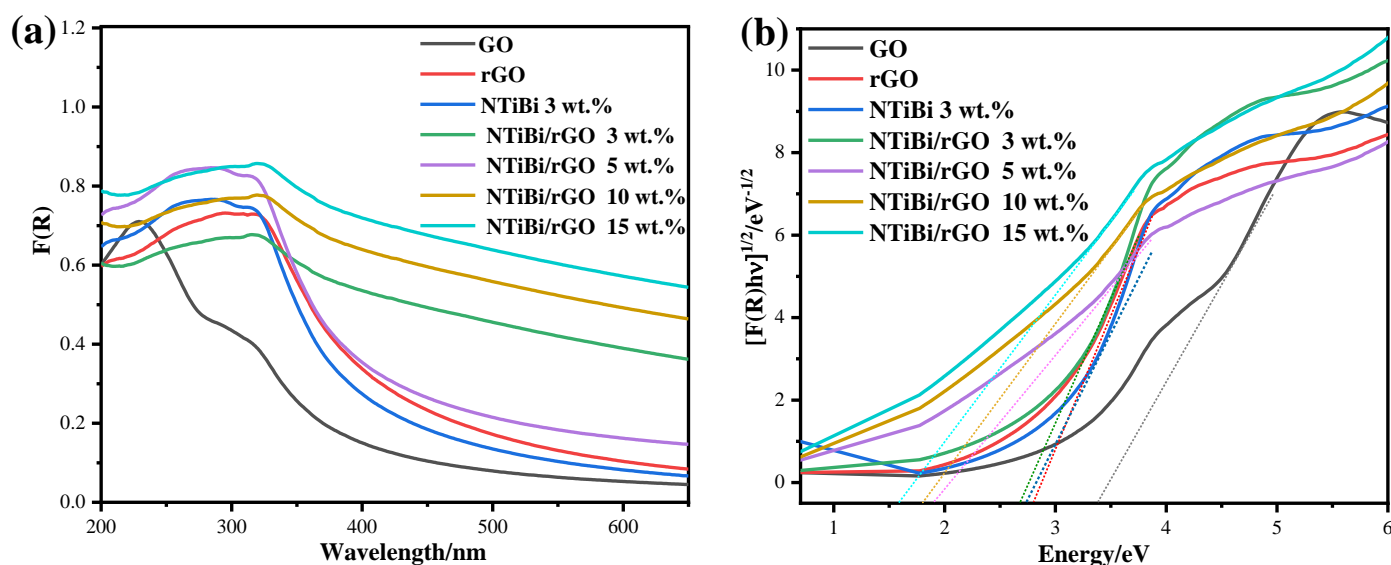

Figure 4.5: The (a) UV-Vis DRS spectra and (b) the corresponding Kubelka-Munk plots for GO, rGO, NTiBi 3 wt.% and NTiBi/rGO (3, 5, 10 and 15 wt.%) nanocomposites

Table 4.6: The optical bandgap energies for GO, rGO, NTiBi and NTiBi/rGO nanocomposite

Sample	Energy bandgap/eV
GO	3.4
rGO	2.9
NTiBi 3 wt.%	2.8
NTiBi/rGO 3 wt.%	2.7
NTiBi/rGO 5 wt.%	1.9
NTiBi/rGO 10 wt.%	1.8
NTiBi/rGO 15 wt.%	1.5

4.3.2.3. Photoluminescence spectroscopy

Figure 4.6 depicts the photoluminescence (PL) spectra of the samples. There are three peaks (R1, R2 and R3) observed in the spectra, and peak R2 that was used to examine the peak intensity behaviour, that is, whether it increased or decreased with incorporation of rGO. It is clearly seen that the incorporation of rGO into NTiBi drastically reduced the recombination of electrons and holes photogenerated in the nanocomposites. This is clearly seen in NTiBi/rGO 10 wt.% spectrum, since all peaks were decreased drastically. Thus, the optimal composition of the nanocomposite prepared is 10 wt.% of rGO into NTiBi/rGO, since it exhibited peaks with very low intensities. This suggests that a certain amount of rGO should be incorporated into NTiBi nanoparticles, as an excessive amount of rGO can lower the charger carrier separation ability. The promotion of good charger carrier separation with rGO in NTiBi/rGO was expected, since graphene materials exhibit excellent electron-accepting and electron transport capabilities [18].
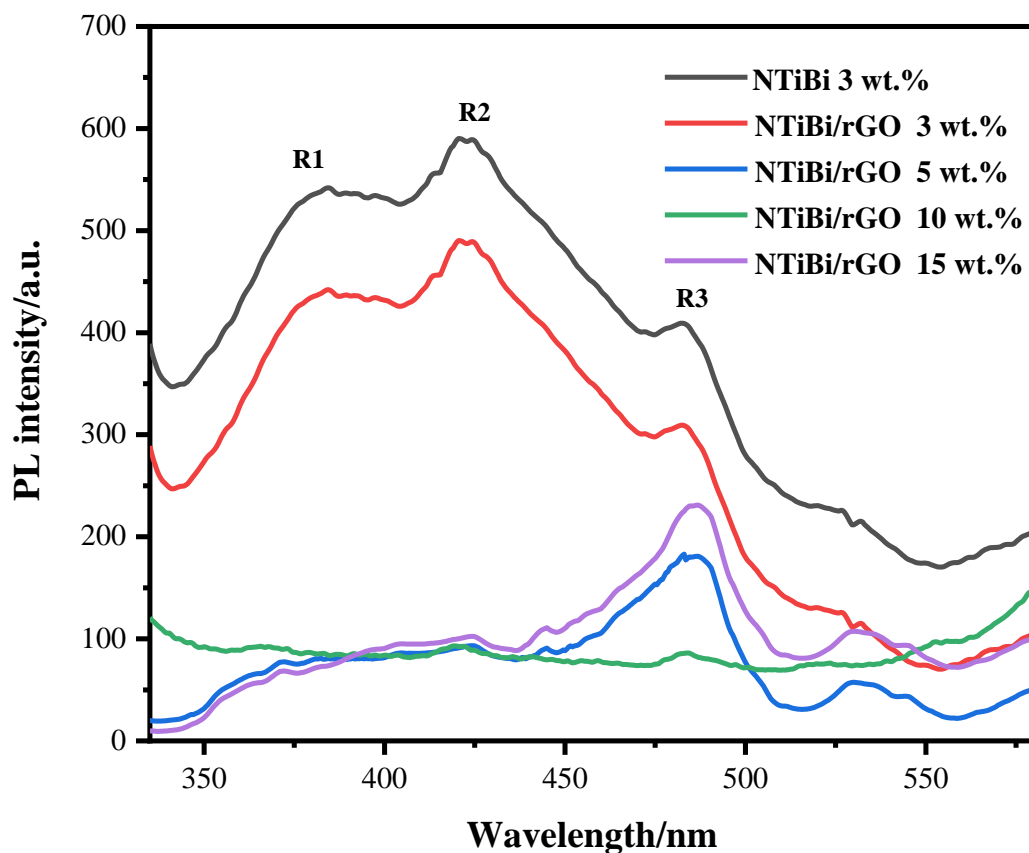
Figure 4.6: Photoluminescence spectra of the samples

4.3.3. Crystallinity and phases

The crystallinity and phases of titania, bismuth oxide and graphene derivatives present in the NTiBi/rGO nanocomposites were investigated by means of powder XRD, Raman spectroscopy, HRTEM and SAED.

4.3.3.1. Powder XRD

Figure 4.4 displays the powder X-ray diffractograms of the synthesized nanocomposites. The diffractogram of GO in Figure 4.7 (a) shows a strong diffraction peak at a 2θ angle of 9.9° with a $d_{(001)}$-spacing of 0.37 nm, as well as a low intensity peak at a 2θ of 42.0° with (100) plane, thereby confirming the successful synthesis of GO, and the efficiency of the oxidation reaction. The 2θ peak at 9.9° was expected for GO due to the increase in the interlayer spacing between

the nanoplatelets after the insertion of the oxygenated groups, while the low intensity 2θ peak at 42°, indicated the presence of some remaining graphite platelets [19]. After the thermal-microwave reduction of GO, rGO was obtained and its diffractogram in Figure 4.7 (b) showed the disappearance of the 2θ peak at 9.9°, while the 2θ peak at 42° continued to appear. In addition, the diffractogram of rGO is quite different from that of GO due to the appearance of a new peak at 24.13°, with an interplanar distance of 0.37 nm, which is smaller than 0.88 nm for GO. The decrease in interplanar distance was expected because of restacking of the graphene sheets after the partial removal of the oxygen-containing functional groups [20, 21].

Figures 4.7 (c-f) displays the diffractograms for the series of NTiBi/rGO nanocomposites prepared by varying the amount of rGO. The results clearly indicate that the diffraction peak of anatase TiO_2 in NTiBi/rGO overlaps with the rGO peak at 25°. The diffraction peaks of the phases of Bi_2O_3 were also observed at their respective positions. These occur at 2θ values of 26.86°, 30.22º, 33.24º and 52.27º. The 2θ values at 26.86° and 30.22° indicate the presence of the α-Bi_2O_3 phase structure, and those at 33.24°, and 52.27° indicate the β-Bi_2O_3 phase in the nanocomposites. In addition, there was no significant shift of the diffraction peaks for the NTiBi material in the diffractograms of the NTiBi/rGO nanocomposites obtained, after the incorparation of rGO. However, it has been observed that the incorporation of rGO into NTiBi reduced the peak intensities and the peaks also became broader. Moreover, incorporating a high amount of rGO showed a tremendous decrease in the peak intensities, indicating a decrease in the crystallinity. The presence of N-TiO_2, Bi_2O_3 and rGO diffraction peaks on the diffractograms confirm that the nanocomposite prepared is NTiBi/rGO. Hence, it is evident that the pure anatase phase of N-TiO_2 and both α-Bi_2O_3 and β-Bi_2O_3 phases are present in the NTiBi/rGO nanocomposites prepared.
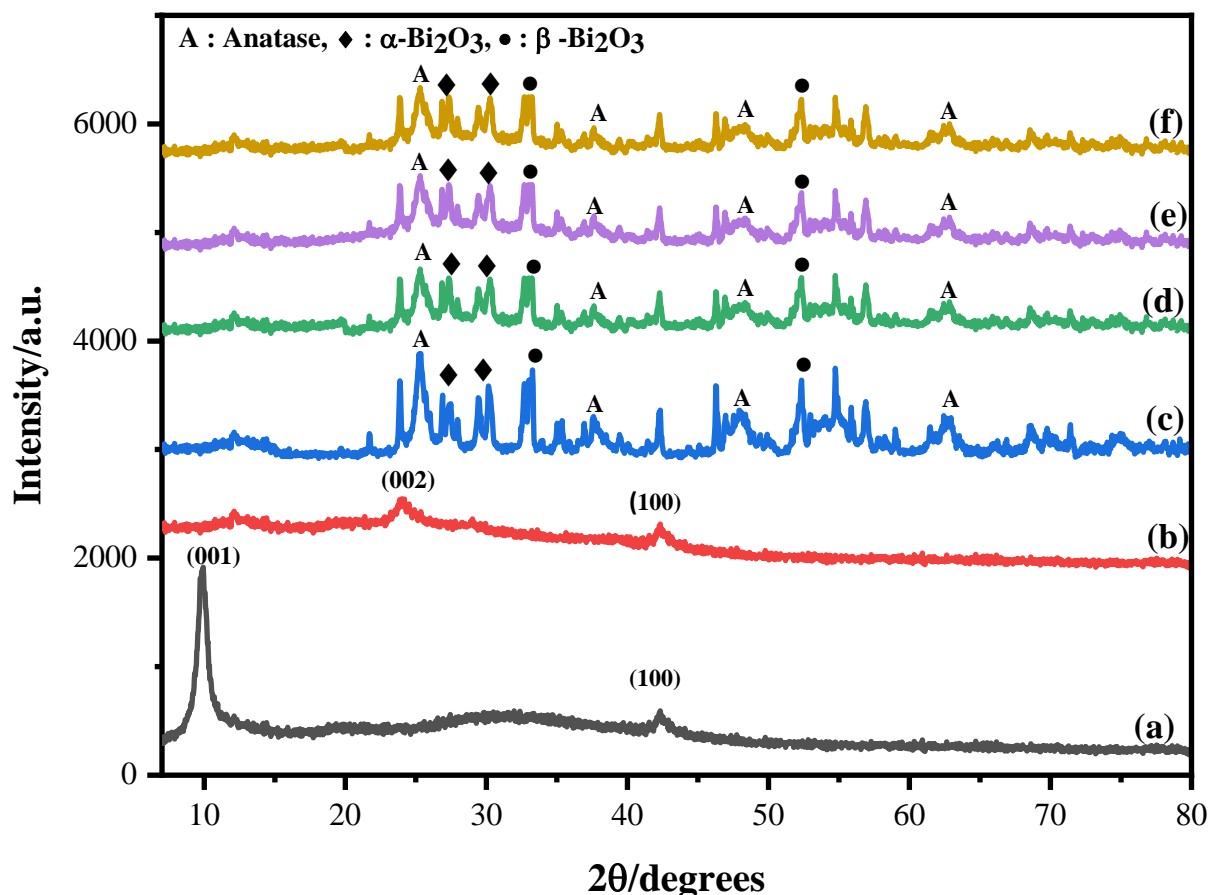
Figure 4.7: Powder X-ray diffractograms of (a) GO, (b) rGO and (c-f) NTiBi/rGO (3, 5, 10, 15 wt.% rGO)

By using the prominent XRD peaks, the average crystallite sizes of all the nanomaterials prepared were calculated with the aid of the Debye-Scherrer formula, by peak broadening and are listed in Table 4.7. It was noted that the average crystallite sizes of the nanocomposites decreased remarkably from those obtained for GO and rGO. This revealed that the incorporation of rGO inhibits the growth of the nanoparticles. Also, there is a slight decrease in crystallite size upon increasing the amount of rGO. These results are in good agreement with a previous report [22]. The inter-planar spacings between atoms (*d*-spacing) presented in Table 4.7 were computed from Bragg's Law, and confirmed the presence of the anatase phase of TiO_2 in the nanocomposites prepared.

Table 4.7: XRD data for GO, rGO and NTiBi/rGO

Material	2θ Peak position/degrees	FWHM/ radians	Crystallite size/nm	d-spacing/nm
GO	9.99	0.009329	15.52	0.88
rGO	24.13	0.01182	12.25	0.37
NTiBi/rGO 3 wt.%	25.35	0.01425	10.16	0.35
NTiBi/rGO 5 wt.%	25.36	0.01439	10.06	0.35
NTiBi/rGO 10 wt.%	25.37	0.01441	10.05	0.35
NTiBi/rGO 15 wt.%	25.37	0.01443	10.02	0.35

4.3.3.2. HRTEM and SAED analysis

The HRTEM image and SAED ring pattern of the NTiBi/rGO 10 wt.% nanocomposite are presented in Figure 4.8 (see additional information in Appendix B). The existence of various lattice fringes in Figure 4.8 (a) enables the identification of the phases present in the nanocomposites. The lattice fringes of $d = 0.35$ nm matched well with the anatase phase of TiO_2 (1 0 1), whereas the lattice fringes of $d = 0.33$, $d = 0.27$ and $d = 0.44$ nm matched well with the (120), (121) crystallographic planes of α-Bi_2O_3 and β-Bi_2O_3 nanoparticles, and (002) for rGO, respectively. In addition, to have a further crystallographic idea, selected area electron diffraction (SAED) was performed. Figure 4.8 (b) illustrates the SAED ring pattern obtained in NTiBi/rGO 10 wt.% with illuminating spots, and each spot corresponds to a lattice plane. The interlayer spacings were measured in both HRTEM and SAED for the nanocomposites, and are presented in Table 4.8. These results correspond well with the interplanar distances obtained by XRD. It is evident that the prepared nanocomposites consist of anatase N-TiO_2, α-Bi_2O_3, β-Bi_2O_3 phases and the rGO derivative.
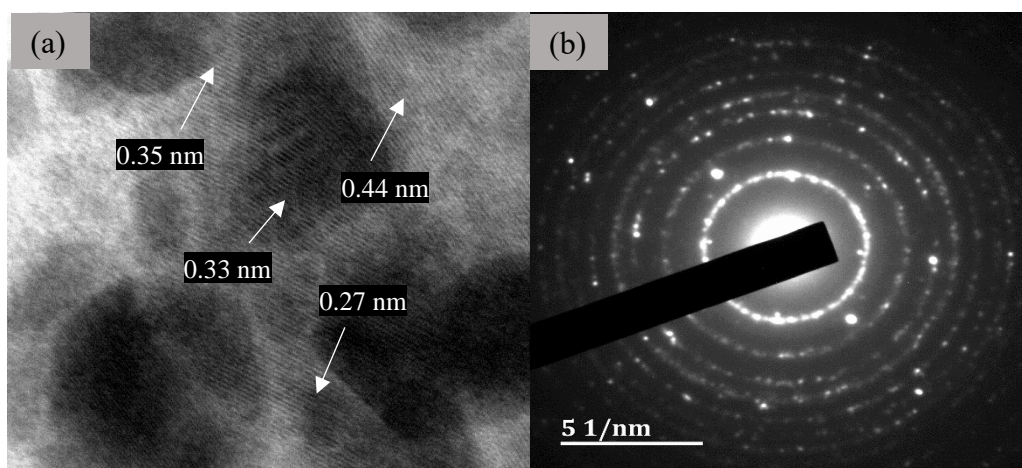
Figure 4.8: The (a) HRTEM image and (b) SAED of NTiBi/rGO 10 wt.%

Table 4.8: The interlayer spacing of GO, rGO and anatase phase in the nanocomposites

Material	HRTEM interlayer spacing/nm	SAED interlayer spacing/nm
GO	0.89	–
rGO	0.44	–
NTiBi/rGO 3 wt.%	0.35	0.36
NTiBi/rGO 5 wt.%	0.35	0.36
NTiBi/rGO 10 wt.%	0.35	0.36
NTiBi/rGO 15 wt.%	0.35	0.36

4.3.3.3.   Raman spectroscopy

Raman spectroscopy was used as a potential tool to investigate the ordered and disordered crystal structures of the nanocomposites. Figure 4.9 displays the Raman spectra of GO, rGO and NTiBi/rGO. The relevant data derived from the Raman characterization are presented in Table 4.9. Typically, the most prominent feature in the graphitic spectrum is the G band at around 1583 cm^{-1} that is attributed to the vibrations in the graphene structure, and a band at around 1370 cm^{-1} attributed to the disorder band [8]. The Raman spectra of GO, rGO and NTiBi/rGO exhibit the presence of wide D and G bands. By considering the D and G bands, it

is observed that introduction of rGO into NTiBi nanoparticles has broadened the peaks and this indicates a decrease in the crystallinity of the material. This is clearly seen in NTiBi/rGO 15 wt.%. Also, the I_D/I_G ratios were enumerated for all the nanocomposites by considering D and G band intensities, and are presented in Table 4.9. It is observed that the I_D/I_G ratios increased with the amount of rGO incorporated into the nanocomposites, demonstrating that the incorporation of high amounts of rGO into the nanocomposites causes more structural defects. The defects in the nanocomposites may act as electron traps and exist in grain boundaries at the contact points between nanoparticles [23]. Therefore, to prepare an efficient nanocomposite with high electron mobility and good charge carrier separation, excess loading of graphene into NTiBi should be avoided.
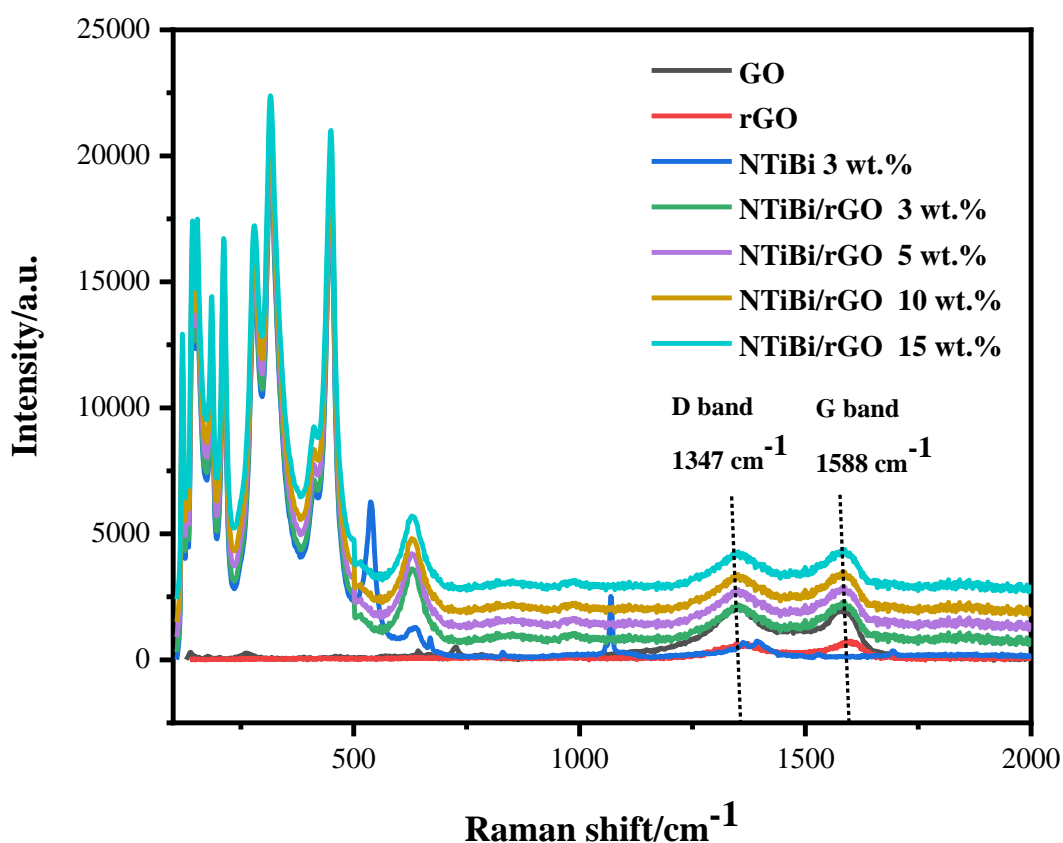

Figure 4.9: Raman spectra for GO, rGO and NTiBi/rGO

Table 4.9: Raman intensities of the D and G bands, and the computed I_D/I_G ratio in the nanocomposites

Materials	$I_{D\text{-band}}$	$I_{G\text{-band}}$	I_D/I_G ratio
GO	1705	1998	0.85
rGO	738	750	0.98
NTiBi/rGO 3 wt.%	1923	1985	0.97
NTiBi/rGO 5 wt.%	2713	2720	0.98
NTiBi/rGO 10 wt.%	3337	3360	0.99
NTiBi/rGO 15 wt.%	4402	4308	1.02

4.3.4. Surface morphologies and microstructural analyses

Figures 4.10 (a-c) show the SEM images of GO, rGO and NTiBi/rGO, respectively (see additional information in Appendix B). It can be clearly seen that both GO and rGO have a two-dimensional sheet-like structure. The distinction between GO and rGO is revealed by the size and shape of the sheets. The SEM image of GO in Figure 4.10 (a) exhibits randomly large sheets with distinct edges, wrinkled surfaces, and folding, whereas the SEM image of rGO in Figure 4.10 (b) exhibits some small layered aggregated sheets and folding. The observation of agglomerated sheets through a layered type of structure of rGO may be due to the partial removal of oxygen-containing functional groups. It is well-known that restacking of graphene sheets may be prevented, e.g., by functionalizing or preparing composites [24]. Hence, the graphene sheets should be prevented from restacking to exfoliate graphene sheets successfully. Figure 4.10 (c) shows the SEM image of NTiBi/rGO. It appears that the nanoparticles are aggregated on the surface of rGO. It is observed that the presence of nanoparticles on rGO acts as spacers that overcome the restacking of graphene sheets after the partial removal of oxygenated functional groups to enable proper exfoliation of the graphene sheets[25].

(a)

200 nm   Mag = 60.00 K X   EHT = 20.00 kV   Signal A = SE2
                                WD = 9.3 mm

(b)

200 nm   Mag = 20.00 K X   EHT = 20.00 kV   Signal A = SE2
                                WD = 7.2 mm

(c)   NTiBi

500nm
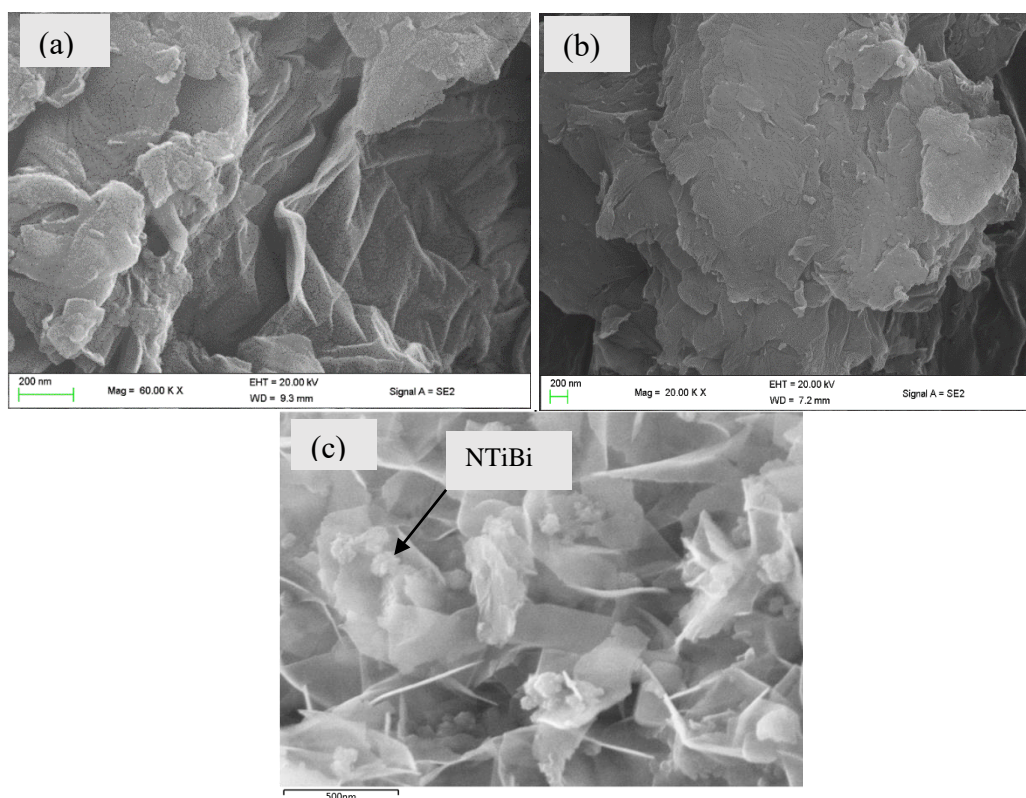
Figure 4.10. SEM images of (a) GO, (b) rGO and (c) NTiBi/rGO 10 wt.%

TEM has provided a deep insight into the microstructures of rGO and the nanocomposites. Figures 4.11 (a-b) show the TEM images of rGO and NTiBi/rGO 10 wt.% at a lower resolution, respectively (see additional information in Appendix A). The presence of transparent sheets of rGO is clearly observed in Figure 4.11 (a), and the NTiBi nanoparticles on the graphene sheets are also clearly observed in Figure 4.11 (b). This suggests that the NTiBi nanoparticles are well distributed on the graphene sheets.

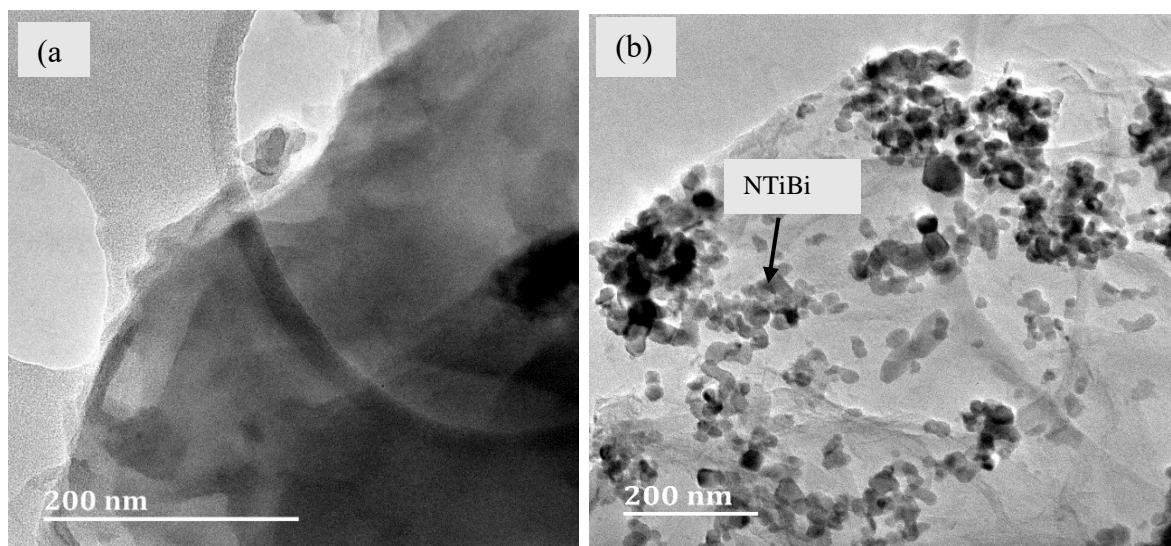**Figure 4.11**: TEM images of (a) rGO and (b) NTiBi/rGO 10 wt.%

4.3.5. Functional groups and bonding within the nanocomposites

Functional groups and bonding within the nanocomposites were investigated with FTIR spectroscopy. Figure 4.12 depicts the FTIR spectra of GO, rGO and the NTiBi/rGO 10 wt.% nanocomposites. The characteristic absorptions of GO were observed at 1708, 1627, 1381 and 1073 cm^{-1} are attributed to the stretching of C=O, C=C, C-O-C and C-O, respectively [26]. The more intense and broad peak at 3283 cm^{-1} is attributed to O-H stretching. The absorption peaks for C=O, C-O, C-O-C and O-H groups in the spectrum of rGO have decreased tremendously or even disappeared, while the peak of the carbonyl group at 1708 cm^{-1} was retained [27]. This confirms that the partial reduction of GO successfully occurred. The spectra of the NTiBi/rGO nanocomposites reveal a slight shift of the weaker peaks, including C-O and C=C, towards lower wavenumbers. This suggests that there is an interaction between the incorporated graphene sheets and the nanoparticles through the functional groups present. Moreover, upon increasing the amount of rGO in the nanocomposites, there is no significant change that is observed in their spectra.
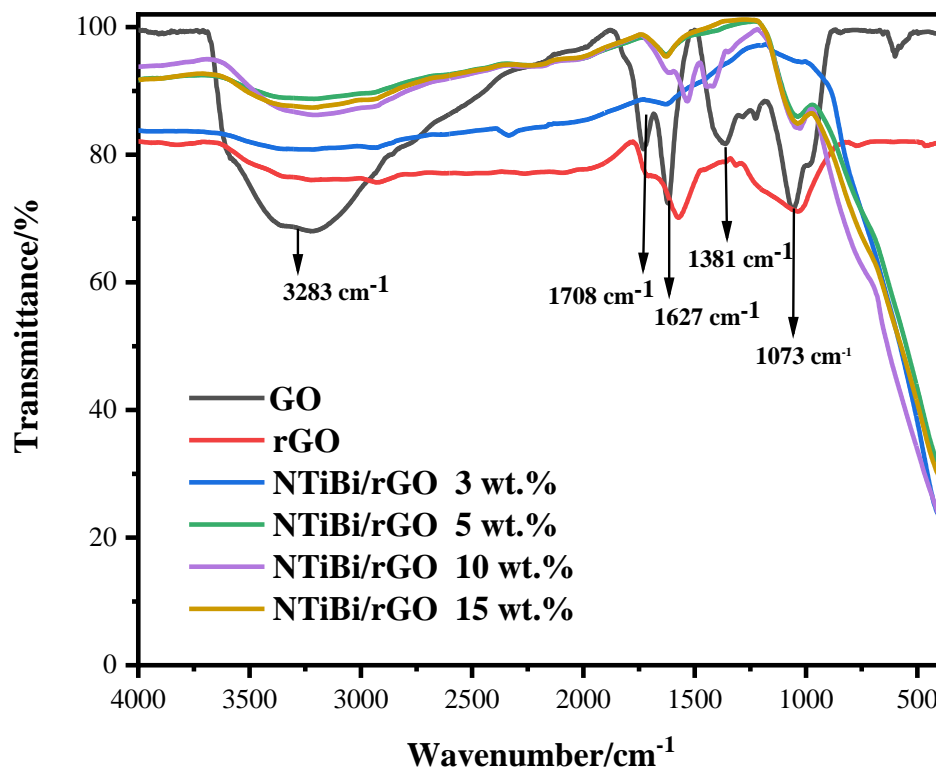
Figure 4.12: FTIR spectra of GO, rGO and NTiBi/rGO (3, 5, 10, 15 wt.% rGO)

4.3.6.   Surface area and porosity

Nitrogen adsorption-desorption isotherms were measured to determine the specific surface area of the nanocomposites. Figure 4.13 (a) depicts the nitrogen adsorption-desorption isotherm of the NTiBi/rGO 10 wt.% nanocomposite (see additional information in Appendix C). According to the IUPAC classification, the nanocomposites exhibit Type III isotherms, with the hysteresis loop classified as H1 [28]. The results summarized in Table 4.10 reveal that the NTiBi/rGO nanocomposites exhibit significantly increased surface areas up to 116.39 $m^2\,g^{-1}$, which are much greater than 55.21 $m^2\,g^{-1}$ for NTiBi. This is likely because graphene is well-known as a material with a larger specific surface area [29]. The NTiBi/rGO nanocomposites show an increasing trend of surface area, while the pore volume decreases with the increase in rGO loading. The BJH pore size diagram is plotted as an inset in Figure 4.13 (b), and the pore size in the nanocomposite was calculated to be 10 nm, which is smaller than 20 nm for NTiBi. This suggests that rGO results in small pores, as well as enlarging the surface area of the nanocomposite. Hence, this would surely facilitate higher loading of dye molecules in the

fabrication of the photoanode of a dye-sensitized solar cell (DSSC) [30]. Moreover, it provides a larger area for the mobilization of photogenerated charge carriers in the photoanode [31, 32].
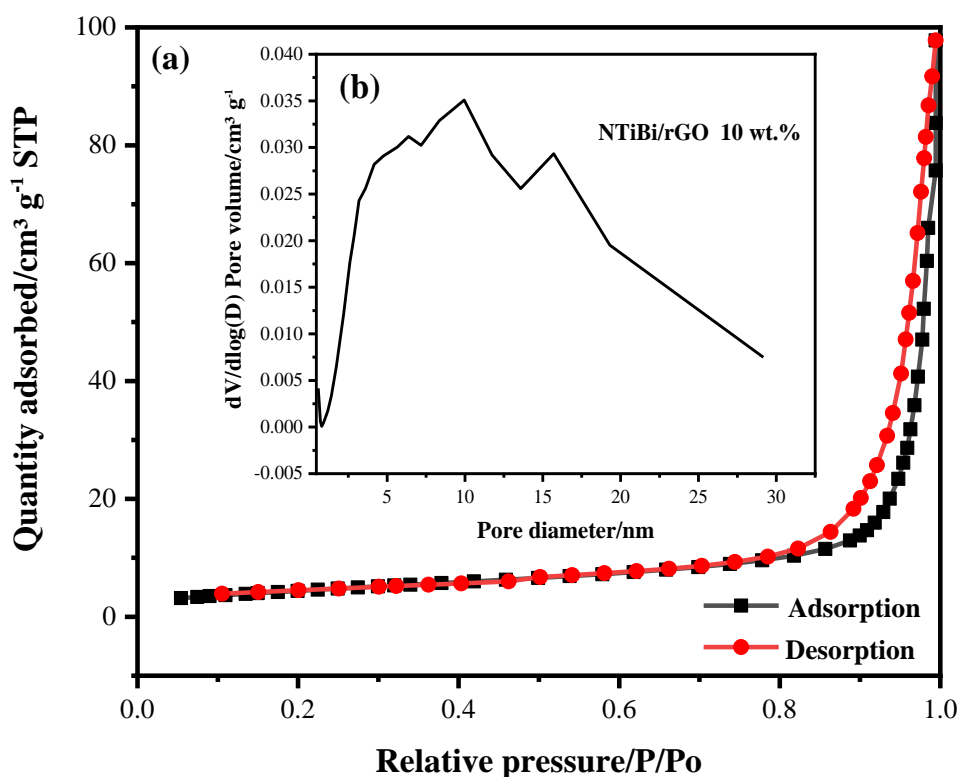
Figure 4.13: The (a) N_2 adsorption-desorption isotherm and (b) BJH pore size distribution curve of the NTiBi/rGO 10 wt.%

Table 4.10: BET surface areas, pore diameters and pore volumes for GO, rGO and NTiBi/rGO

Sample	BET surface area/m^2 g^{-1}	Pore diameter/nm	Pore volume/cm^3 g^{-1}
GO	80.53	6.52	0.4821
rGO	70.20	5.08	0.2240
NTiBi 3 wt.%	55.21	32.28	0.04258
NTiBi/rGO 3 wt.%	85.27	16.85	0.06852
NTiBi/rGO 5 wt.%	103.45	16.06	0.04258
NTiBi/rGO 10 wt.%	115.46	11.02	0.03856
NTiBi/rGO 15 wt.%	116.39	10.85	0.03042

4.3.7. Thermal stability

The thermal stability behaviour of the nanocomposites was deduced from TGA and analysis of the first derivative curves of the change in wt.% against temperature. Figure 4.14 depicts the thermograms for rGO and the NTiBi/rGO nanocomposites (see additional information in Appendix D). The decomposition profile of the materials is summarized in Table 4.11. It is observed that rGO decomposed completely at 650 °C, whereas NTiBi/rGO (3, 5, 10 and 15 wt.% rGO) nanocomposites exhibited 58.77, 58.82, 61.83 and 62.28% total weight losses at temperature ranges of 40 – 735, 39 – 735, 37 – 730, and 35 - 687 °C, respectively. NTiBi/rGO involves two decomposition steps, the first is attributed to loss of physically observed water molecules. The second step is attributed to the loss of nitrogen, organic residuals and rGO.

The highest thermal stability is observed in the NTiBi/rGO (3 and 5 wt.%) nanocomposites, since a lower total weight percent loss was observed. This suggests that incorporating a relatively high amount of rGO into the nanocomposite may lower the thermal stability. The percentage of the total weight of the residuals, presented in Table 4.11, can roughly estimate the amount of $N-TiO_2$ and Bi_2O_3 present in the nanocomposites since it is observed that rGO can undergo complete decomposition in TGA, whereas NTiBi does not decompose completely. From these results, it is evident that the synthesized nanocomposites demonstrated good thermal stability. The good stability of the nanocomposite synthesized will be beneficial
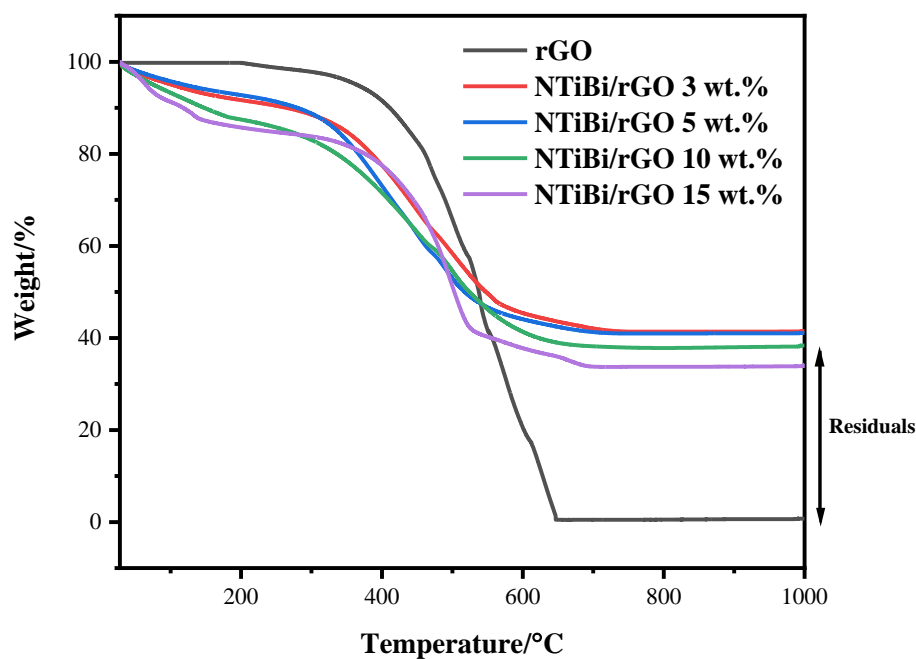
Figure 4.14: Thermograms for rGO and the NTiBi/rGO nanocomposites with different amounts of rGO

Table 4.11: Weight percentage losses and total residuals at different temperature ranges for rGO and the NTiBi/rGO nanocomposites

Sample	Sample temperature/°C	Weight loss/%	Total residual weight/%
rGO	215 – 650	99.98	0.02
NTiBi/rGO 3 wt.%	40 – 160	6.75	41.23
	161 – 735	52.05	
NTiBi/rGO 5 wt.%	39 – 161	6.43	41.18
	162 -–735	52.39	
NTiBi/rGO 10 wt.%	37 – 192	14.44	38.17
	193 – 730	47.39	
NTiBi/rGO 15 wt.%	35 – 193	14.02	37.72
	194 – 687	48.31	

4.4. Conclusion

A series of NTiBi/rGO (3, 5, 10 and 15 wt.%) nanocomposites were prepared *via* a hydrothermal method, and thoroughly characterised. UV-Vis spectroscopy revealed that excessive incorporation of rGO has significantly extended the light absorption capability of the resulting nanocomposites. Among the nanocomposites prepared, only the NTiBi/rGO 10 wt.% revealed a good occurrence of charge carrier separation and electron transfer. It was noted that a certain amount of rGO should be incorporated into NTiBi nanoparticles, as an excessive amount of rGO can lower the charger carrier separation ability. The enhancement of the charge carrier separation, in the NTiBi nanoparticles, was caused by the incorporation of rGO. In addition, the incorporation of rGO into the NTiBi nanocomposites also produced a significant increase in the surface area up to 116.39 $m^2\,g^{-1}$, and good thermal stability up to 735 °C. It can be concluded that the NTiBi/rGO nanocomposite material has good potential to be used in the design, and preparation of highly efficient photoanodes of dye-sensitized solar cells.

References

1. S. K. Tiwari, S. Sahoo, N. Wang and A. Huczko, *Graphene research and their outputs: status and prospect*, Journal of Science: Advanced Materials and Devices, 2020, **5**, 10-29.

2. J. Wang, G. Wang, J. Jiang, Z. Wan, Y. Su and H. Tang, *Insight into charge carrier separation and solar-light utilization: rGO decorated 3D ZnO hollow microspheres for enhanced photocatalytic hydrogen evolution*, Journal of colloid and interface science, 2020, **564**, 322-332.

3. N. Singh, S. Jana, G. P. Singh and R. Dey, *Graphene-supported TiO₂: study of promotion of charge carrier in photocatalytic water splitting and methylene blue dye degradation*, Advanced Composites and Hybrid Materials, 2020, **3**, 127-140.

4. P. Huo, X. Shi, W. Zhang, P. Kumar and B. Liu, *An overview on the incorporation of graphene quantum dots on TiO₂ for enhanced performances*, Journal of Materials Science, 2021, **51**, 1-21.

5.   Y.-B. Tang, C.-S. Lee, J. Xu, Z.-T. Liu, Z.-H. Chen, Z. He, Y.-L. Cao, G. Yuan, H. Song, L. Chen, L. Luo, H.-M. Cheng, W.-J. Zhang, I. Bello and S.-T. Lee, *Incorporation of graphenes in nanostructured TiO$_2$ films via molecular grafting for dye-sensitized solar cell application*, ACS Nano, 2010, **4**, 3482-3488.

6.   S. Chinnusamy, R. Kaur, A. Bokare and F. Erogbogbo, *Incorporation of graphene quantum dots to enhance photocatalytic properties of anatase TiO$_2$*, MRS Communications, 2018, **8**, 137-144.

7.   H. Rongan, L. Haijuan, L. Huimin, X. Difa and Z. Liuyang, *S-scheme photocatalyst Bi$_2$O$_3$/TiO$_2$ nanofiber with improved photocatalytic performance*, Journal of Materials Science & Technology, 2020, **52**, 145-151.

8.   Y. Pang, Q. Feng, Z. Kou, G. Xu, F. Gao, B. Wang, Z. Pan, J. Lv, Y. Zhang and Y. Wu, *A surface precleaning strategy intensifies the interface coupling of the Bi$_2$O$_3$/TiO$_2$ heterostructure for enhanced photoelectrochemical detection properties*, Materials Chemistry Frontiers, 2020, **4**, 638-644.

9.   S. Noor, S. Sajjad, S. A. K. Leghari, C. Flox and S. Ahmad, *Competitive role of nitrogen functionalities of N-doped GO and sensitizing effect of Bi$_2$O$_3$ QDs on TiO$_2$ for water remediation*, Journal of Environmental Sciences, 2021, **108**, 107-119.

10.   C. U. Ro, J. Osán and R. Van Grieken, *Determination of low-Z elements in individual environmental particles using windowless EPMA*, Analytical Chemistry, 1999, **71**, 1521-1528.

11.   N. Stojilovic, *Why can't we see hydrogen in X-ray photoelectron spectroscopy?*, Journal of Chemical Education, 2012, **89**, 1331-1332.

12.   T. S. Natarajan, V. Mozhiarasi and R. J. Tayade, *Nitrogen doped titanium dioxide (N-TiO$_2$): synopsis of synthesis methodologies, doping mechanisms, property evaluation and visible light photocatalytic applications*, Photochem, 2021, **1**, 371-410.

13.   M. D'Arienzo, N. Siedl, A. Sternig, R. Scotti, F. Morazzoni, J. Bernardi and O. Diwald, *Solar light and dopant-induced recombination effects: photoactive nitrogen in TiO$_2$ as a case study*, The Journal of Physical Chemistry C, 2010, **114**, 18067-18072.

14.   M. Ikram, A. Raza, M. Imran, A. Ul-Hamid, A. Shahbaz and S. Ali, *Hydrothermal synthesis of silver decorated reduced graphene oxide (rGO) nanoflakes with effective photocatalytic activity for wastewater treatment*, Nanoscale Research Letters, 2020, **15**, 1-11.

15. A. Kumar, A. M. Sadanandhan and S. L. Jain, *Silver doped reduced graphene oxide as a promising plasmonic photocatalyst for oxidative coupling of benzylamines under visible light irradiation*, New Journal of Chemistry, 2019, **43**, 9116-9122.

16. Y. Liu, *Hydrothermal synthesis of TiO2–rGO composites and their improved photocatalytic activity in visible light*, RSC Advances, 2014, **4**, 6040-36045.

17. L. Liu, C. Luo, J. Xiong, Z. Yang, Y. Zhang, Y. Cai and H. Gu, *Reduced graphene oxide (rGO) decorated TiO2 microspheres for visible-light photocatalytic reduction of Cr(VI)*, Journal of Alloys and Compounds, 2016, **690**, 771-776.

18. X.-F. Zhang and Q. Xi, *A graphene sheet as an efficient electron acceptor and conductor for photoinduced charge separation*, Carbon, 2011, **49**, 3842-3850.

19. G. Yasin, M. Arif, M. Shakeel, Y. Dun, Y. Zuo, W. Khan, Y. Tang, A. Khan and M. Nadeem, *Exploring the nickel–graphene nanocomposite coatings for superior corrosion resistance: manipulating the effect of deposition current density on its morphology, mechanical properties, and erosion-corrosion performance*, Advanced Engineering Materials, 2017, **7**, 1701166.

20. J. Shen, B. Yan, M. Shi, H. Ma and M. Ye, *One step hydrothermal synthesis of TiO2-reduced graphene oxide sheets*, Journal of Materials Chemistry, 2011, **21**, 3415-3421.

21. J. Gascho, S. Da Costa, A. Recco and S. Pezzin, *Graphene oxide films obtained by vacuum filtration: X-ray diffraction evidence of crystalline reorganization*, Journal of Nanomaterials, 2019, **2019**, 1-12.

22. P. Labhane, L. Patle, V. Huse, G. Sonawane and S. Sonawane, *Synthesis of reduced graphene oxide sheets decorated by zinc oxide nanoparticles: crystallographic, optical, morphological and photocatalytic study*, Chemical Physics Letters, 2016, **661**, 13-19.

23. F. Hao, H. Lin, C. Zhou, Y. Liu and J. Li, *Bifunctional single-crystalline rutile nanorod decorated heterostructural photoanodes for efficient dye-sensitized solar cells*, Physical Chemistry Chemical Physics, 2011, **13**, 15918-15924.

24. J. Li and M. Ostling, *Prevention of graphene restacking for performance boost of supercapacitors-a review*, Crystals, 2013, **3**, 163-190.

25. Y. Wang, Y. wu, Y. Huang, F. Zhang, Y. Ma and Y. Chen, *Preventing graphene sheets from restacking for high-capacitance performance*, The Journal of Physical Chemistry C, 2011, **115**, 23192–23197.

26. A. H. Labulo, B. Omondi and V. O. Nyamori, *Graphene/pyrrolic-structured nitrogen-doped CNT nanocomposite supports for Pd-catalysed heck coupling and chemoselective hydrogenation of nitroarenes*, SN Applied Sciences, 2019, **1**, 142.

27.   X. Shen, X. Chen, D. Sun, T. Wu and Y. Li, *Fabrication of a magnetite/diazonium functionalized-reduced graphene oxide hybrid as an easily regenerated adsorbent for efficient removal of chlorophenols from aqueous solution*, RSC Advances, 2018, **8**, 7351-7360.

28.   K. Sing and R. Williams, *Physisorption hysteresis loops and the characterisation of nanoporous materials*, Adsorption Science and Technology, 2004, **22**, 773-782.

29.   A. Iakunkov, V. Skrypnychuk, A. Nordenstrom, E. A. Shilayeva, M. Korobov, M. Prodana, M. Enachescu, S. H. Larsson and A. V.Talyzin, *Activated graphene as a material for supercapacitor electrodes: effects of surface area, pore size distribution and hydrophilicity*, Physical Chemistry Chemical Physics, 2019, **21**, 17901-17912.

30.   K. Fan, J. Yu and W. Ho, *Improving photoanodes to obtain highly efficient dye-sensitized solar cells: a brief review*, Materials Horizons, 2017, **4**, 319-344.

31.   W. Yan, M.-M. Huo, R. Hu and Y. Wang, *Working area effects on the energetic distribution of trap states and charge dynamics of dye-sensitized solar cells*, RSC Advances, 2019, **9**, 1734-1740.

32.   C. W. Kim, S. P. Suh, M. J. Choi, Y. S. Kang and Y. S. Kang, *Fabrication of SrTiO₃–TiO₂ heterojunction photoanode with enlarged pore diameter for dye-sensitized solar cells*, Journal of Materials Chemistry A, 2013, **1**, 11820-11827.

Chapter 5

Investigation of N-doped TiO$_2$/Bi$_2$O$_3$/rGO nanocomposite-based photoanodes for dye-sensitized solar cells

This chapter briefly introduces the development of photoanodes for dye-sensitized solar cells (DSSCs), and the fabrication of a complete DSSC by making use of a nitrogen-doped titanium dioxide/bismuth oxide/reduced graphene oxide (NTiBi/rGO)-based photoanode. It also presents the results and discussion of the photovoltaic performances of the fabricated DSSCs.

5.1. Introduction

DSSCs have attracted significant research attention, as a cost-effective alternative to silicon-based photovoltaic devices, for the conversion of solar energy into electricity [1]. Since the breakthrough of the solar energy conversion efficiency reported by Gratzel's group in 1991 [2], the development of DSSCs has been growing very rapidly. Interestingly, revamping the properties of each component in the DSSCs is necessary to improve further the overall efficiency of the cells [3]. Also, each component of DSSCs heavily determines their cost and efficiency [4]. However, great efforts have been made to find better photoanode materials further to improve the photovoltaic performance of DSSCs [5]. The photoanode plays a pivotal role in determining the photovoltaic performance of DSSCs, because of its function in collecting photoexcited electrons from the dye molecules and transferring them to the indium tin oxide (ITO) substrate [6, 7]. Furthermore, the photoanode serves as a scaffold layer to adsorb the dye molecules.

An efficient photoanode for DSSCs should possess features, such as a large surface area to increase the loading of dye molecules, favourable band alignment, and good photoexcited electron transport [8]. Typically, a photoanode is fabricated from various metal oxides, including tin dioxide (SnO$_2$) [9], zinc oxide (ZnO) [10, 11], and titanium dioxide (TiO$_2$) [12, 13]. Among these metal oxides, TiO$_2$ is the most important photoanode material due to its higher dye-loading capability, chemical stability, less toxicity, wide bandgap energy and larger surface area [14]. Also, its anatase phase is one of the most important and favourable phases in energy applications [15, 16]. However, TiO$_2$ has a major drawback in DSSCs, such as high charge carrier recombination rate [17]. To address this drawback, NTiBi/rGO nanocomposites

with high crystallinity have demonstrated a potential to replace the traditional TiO_2 photoanode. The optimization of light absorption properties was done by using a higher concentration of Eosin B dye, while the charge carrier transport properties were improved by using heterojunction structured materials (NTiBi) in which rGO was incorporated as a semiconductor, and PVA-doped with LiI as the electrolyte [18]. Also, the physical and chemical properties of TiO_2 were controlled not only by tuning its intrinsic electronic structure, but also by tailoring its size, organization, shape and surface properties [19, 20]. Consequently, the aspect of morphology control and functionalization of the NTiBi/rGO nanocomposites have been considered to improve further the power conversion efficiency (PCE) of DSSCs. Moreover, the proper orientation and packing of adsorbed Eosin B dye molecules on the semiconductor promoted a good injection process of photoexcited electrons [20].

5.2. Experimental

This section provides the details of all the materials used to fabricate the DSSC devices *via* the Doctor Blade method, and the photocurrent density-voltage (*J-V*) measurements of the fabricated devices.

5.2.1. Materials

All the materials used in the fabrication of the DSSC devices and their purities are listed in Table 5.1. In addition, the substrates used for the fabrication of the cells were cleaned before use.

Table 5.1: Substrates, chemicals, solvents and reagents used in the fabrication of DSSCs

Reagents/solvents	Supplier	Grade/Purity percentage/%
Absolute ethanol	Sigma Aldrich	97.0
Acetone	Sigma Aldrich	99.4
Acetonitrile	Sigma Aldrich	99.5
Methanol	Associated Chemical Enterprises	99.5
Eosin B	Sigma Aldrich	90.0

ITO glass	Sigma Aldrich	–
Lithium iodide	Sigma Aldrich	99.9
1-Methyl-1,3-propylimidazolium iodide	Sigma Aldrich	HPLC grade $\geq$ 98
4-Tert-butylpyridine	Sigma Aldrich	96.0
Guanidinium thiocyanate	Merck Shuchardt	$\geq$ 98
Polyvinyl acetate (PVA)	Sigma Aldrich,	MW = 100 000 g mol^{-1}

5.2.2. TiO$_2$ film preparation

The TiO$_2$ film was prepared *via* the Doctor Blade method. ITO glass was ultrasonicated for 30 min in a mixture of acetone, absolute ethanol and deionized water (10:10:5 v/v), and then washed with acetone, and thereafter dried in an oven, at 120 °C for 10 min. The conducting side of the ITO glass was identified by using a multimeter or an ultraviolet (UV) lamp. The ultrasonically cleaned ITO glass was kept on a flat surface, and an area of 2 cm $\times$ 2 cm was defined with Scotch tape, as shown in Figure 5.1 (a). A paste of TiO$_2$ prepared in absolute ethanol was applied with a small spatula, as shown in Figure 5.1 (b). The paste was then spread over the defined area with a glass rod, as shown in Figure 5.1 (c). The rod was pressed against the Scotch tape and quickly moved in a downward direction. This filled the area defined by the Scotch tape with the paste and resulted in the formation of a TiO$_2$ film. The glass rod was held firmly and moved quickly to ensure that nearly equal force or pressure was applied throughout the length of the rod to produce smooth and uniform films. If the pressure applied is not uniform, the resulting films will have an uneven texture, and significant variations in film thickness at different points will be obtained. The coating step can be perfected after a few initial attempts. After deposition, the Scotch tape was removed to obtain a uniform film, as shown in Figure 5.1 (d). The film was placed on a hot plate and slowly heated up to 300 °C for 30 min, as shown in Figure 5.1 (e), since a rapid increase in temperature may damage the film due to thermal shock. Hence, a slow increase in heat is crucial to obtain a crack-free film. This was achieved by slowly increasing the heat controller of the hot plate. After heating, the film was allowed to cool down to room temperature, as shown in Figure 5.1 (f). A mass of 0.2 g for nitrogen-doped titanium dioxide (N-TiO$_2$), nitrogen-doped titanium dioxide/bismuth oxide (NTiBi) or NTiBi/rGO nanocomposites was used to prepare the paste, where a similar procedure, as mentioned above for TiO$_2$ was adopted to prepare films of these materials.

5.2.3. Preparation of a DSSC photoanode

A few drops of 2 M Eosin B dye solution in methanol were dropped onto the prepared TiO_2 film. This allowed the dye molecules to be adsorbed onto the surface of the TiO_2 film, without allowing an excess or any aggregated dye solution on the TiO_2 film surface. The film was then dried in air for a few minutes in a dark room. After drying, the photoanode was ready for use, as shown in Figure 5.1 (g).

5.2.4. Preparation of counter electrodes

The counter electrode was prepared by making use of aluminium (Al) foil. Firstly, an ordinary glass was cut into a defined area that was equivalent to that of the ITO glass, and ultrasonicated for 30 min in a mixture of acetone, absolute ethanol, and deionized water (10:10:5 v/v), then secondly, washed with acetone, and dried in an oven at 50 °C for 10 min. Thereafter, the ultrasonically cleaned glass was covered with Al foil in such a way that a uniform surface was achieved, as shown in Figure 5.1 (h). Finally, the counter electrode was now ready for use.

5.2.5. Preparation of gel electrolyte

Polyvinyl acetate (PVAc)-doped with lithium iodide (LiI) gel electrolyte was prepared by mixing LiI (0.6695 g), iodine (0.6346 g), 1-methyl-3-propylimidazolium iodide (7.5623 g), 4-tert-butylpyridine (3.38 g), guanidinium thiocyanate (0.5914 g) and PVA (2.4986 g) and dissolving them in a 50 mL volumetric flask with acetonitrile as the solvent. The gel electrolyte obtained was stored in a fridge.

5.2.6. Assembly of DSSCs

A few drops of gel electrolyte were dropped and spread on the dye-sensitized TiO_2 film. Then, this dye-sensitized TiO_2 film with an electrolyte was sandwiched with the Al-counter electrode. Finally, the two electrodes were clamped together with binder clips, as shown in Figure 5.1 (i). This completed the fabrication and assembly procedure of a typical DSSC, and the device was now ready for testing.
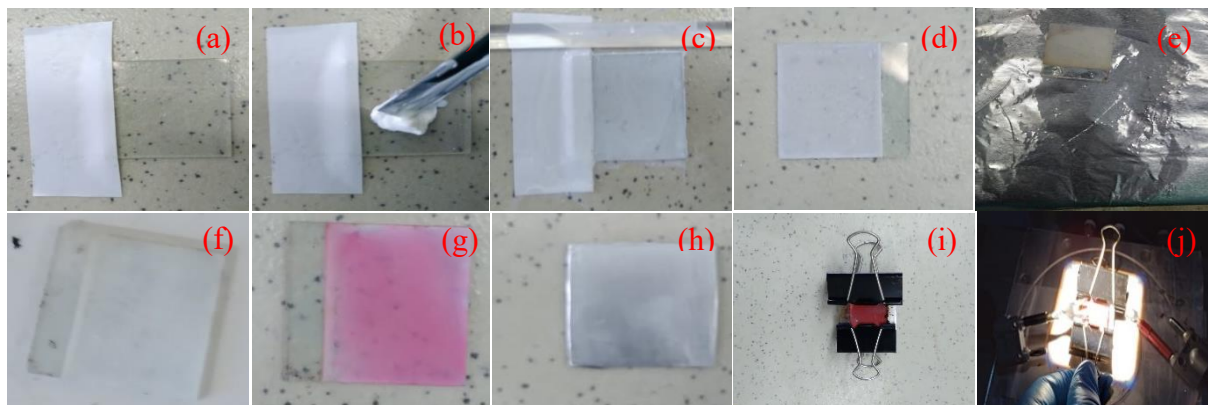
Figure 5.1: Images of the DSSC fabrication and testing: (a) Scotch tape applied to define the deposition area on an ITO substrate, (b) the TiO$_2$ paste applied with a spatula, (c) an evenly spread TiO$_2$ paste on an ITO substrate, (d) the deposited TiO$_2$ film on an ITO substrate after removing the Scotch tape, (e) the TiO$_2$ film being annealed on a hot plate, (f) the annealed TiO$_2$ film with a yellowish colour, (g) the TiO$_2$ film with the adsorbed dye, (h) the Al-coated counter electrode, (i) the complete assembly of the DSSC, and (j) the DSSC being tested with a solar simulator

5.2.7. Characterisation of the DSSCs

A solar simulator was employed to investigate the photovoltaic performance of the fabricated DSSC devices, as shown in Figure 5.1 (j). The measurements were performed with an Oriel LCS-100 solar simulator. The system employed a 100 W Xenon lamp with an integrated reflector, and controlled to a working distance of 8.0 inches (203 mm). The beam size was 38 × 38 mm, and an AM 1.5G filter was included operating at 1.0 sun output. The input power includes a 100 - 240 V AC voltage, a frequency of 50/60 Hz, and a maximum power of 130 W. A PVIV test solution was used for the complete IV measurements.

5.3. Results and discussion

This section presents the results and discussion for evaluating the photovoltaic performance of the fabricated DSSC devices using photoanodes based on NTiBi/rGO nanocomposites. In addition, the optical absorption of Eosin B dye at different concentrations is also discussed.

5.3.1. Optical absorption of Eosin B dye

Figure 5.2 depicts the UV-Vis absorption spectra of Eosin B dye solution prepared in methanol at different concentrations, with an inset showing the chemical structure of Eosin B. It is seen that Eosin B exhibits two absorption bands with maxima at 403 and 526 nm. The appearance of these bands verified that Eosin B absorbs light in the visible region, and it is observed that at a lower concentration, the band at 403 nm becomes very weak or even disappears, while the one at 526 nm is retained. Hence, the sample with a higher concentration of Eosin B was used to fabricate DSSCs due to its high absorption and high loading of dye molecules on the semiconductor surface. This dye demonstrated strong absorption in the visible range, as showed in Figure 5.2, and it is evident that this dye meets the requirements for DSSC fabrication. Interestingly, this dye has a large molecular weight and contains an extended system of conjugated double bonds, which allows for visible light absorption.
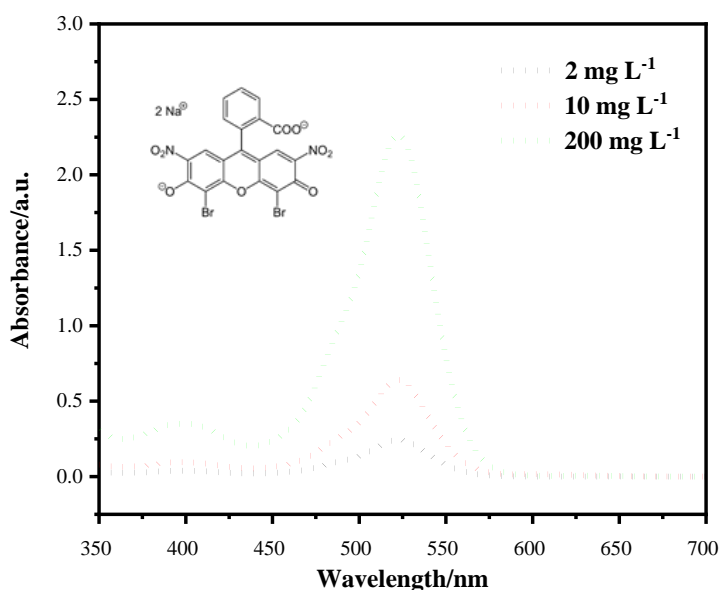

Figure 5.2: The spectra of Eosin B dye solution in methanol at different concentrations

5.3.2. Photovoltaic performance analysis

Figure 5.3 illustrates the *J-V* characteristics of the DSSCs fabricated with NTiBi/rGO nanocomposite-based photoanodes and Al counter electrodes (see additional information in Appendix F). The corresponding photovoltaic parameters are listed in Table 5.2. According to the results summarized in Table 5.2, it is clearly seen that the devices fabricated from

NTiBi/rGO-based photoanodes exhibit relatively high performance, resulting from the relatively high open-circuit voltage (V_{oc}), fill factor (FF) and short-circuit current density (J_{sc}) values. The devices fabricated from NTiBi/rGO (3, 5, 10 and 15 wt.%) nanocomposite-based photoanodes exhibited PCEs of 4.93, 5.65, 7.20 and 6.25%, respectively. These efficiencies are significantly higher than those of DSSCs fabricated with pure TiO_2, N-TiO_2 and NTiBi photoanode materials (Table 5.2). This suggests that the incorporation of rGO into NTiBi photoanodes significantly improved the photovoltaic performance of the devices. In particular, a comparison of the NTiBi/rGO photoanode-based DSCCs with the corresponding NTiBi photoanode-based devices shows that the PCE increased from 4.26% for DSSCs with the NTiBi photoanode up to 7.20% for NTiBi/rGO-based devices. Moreover, the FF, J_{sc} and V_{oc} also improved significantly.

A slight decrease in the photovoltaic performance of the devices was observed upon the incorporation of 15 wt.% of rGO into NTiBi. This suggests that an excess amount of rGO can lead to the absorption of more incoming light; hence, reducing the light-harvesting capability of the dye molecules, and thus inducing a negative effect on the PCE of the DSSCs [21]. Also, an excess amount of rGO can act as recombination centres, thereby reducing the FF and J_{sc}, which subsequently reduces the device performance [21]. Therefore, these results are consistent with the photoluminescence (PL) results (discussed in Chapter 4), which revealed that the incorporation of an excess amount of rGO could lower the separation of the photogenerated charge carriers. Interestingly, moving from TiO_2-based photoanodes to NTiBi/rGO-based photoanodes to fabricate DSSCs, has demonstrated a potential approach to significantly enhance the photovoltaic performance of DSSCs. These results demonstrate that there was a favourable band alignment and good interaction between the Eosin B dye molecules and the NTiBi/rGO nanomaterials. Thus, the recombination between injected photoexcited electrons and oxidized Eosin B dye molecules, which occurs after electron injection, was successfully suppressed. Also, there was a proper orientation and packing of the adsorbed dye molecules on the conduction band of the NTiBi/rGO nanocomposites, which promoted a good occurrence of charge carrier injection and separation processes.

The series resistance (*Rs*) is determined from the inverse of the slope of the *I-V* curve at the open circuit voltage and the shunt resistance (*Rsh*) from the inverse of the slope of the *I-V* curve at the short circuit condition [22, 23]. These parameters were calculated as follows and presented in Table 5.2.

$$Rs = \frac{I_{max} - 0}{V_{OC} - V_{max}} = \frac{\Delta I}{\Delta V} \tag{17}$$

$$Rsh = \frac{I_{SC} - I_{max}}{V_{max} - 0} = \frac{\Delta I}{\Delta V} \tag{18}$$

The shunt resistance increases from the TiO_2-based DSSC to the NTiBi/rGO 10 wt.%-based DSSC, but the NTiBi/rGO 15 wt.% cell shows a decrease. Therefore, this indicated that fabricated solar cells have the ability to minimize power loss, since a higher shunt resistance prevents power loss in solar cells by halting an alternate current path for the generated current. Moreover, an excess amount of rGO in the nanocomposites induces a negative effect on the PCE of the DSSCs such as in the case of the NTiBi/rGO 15 wt.% cell.
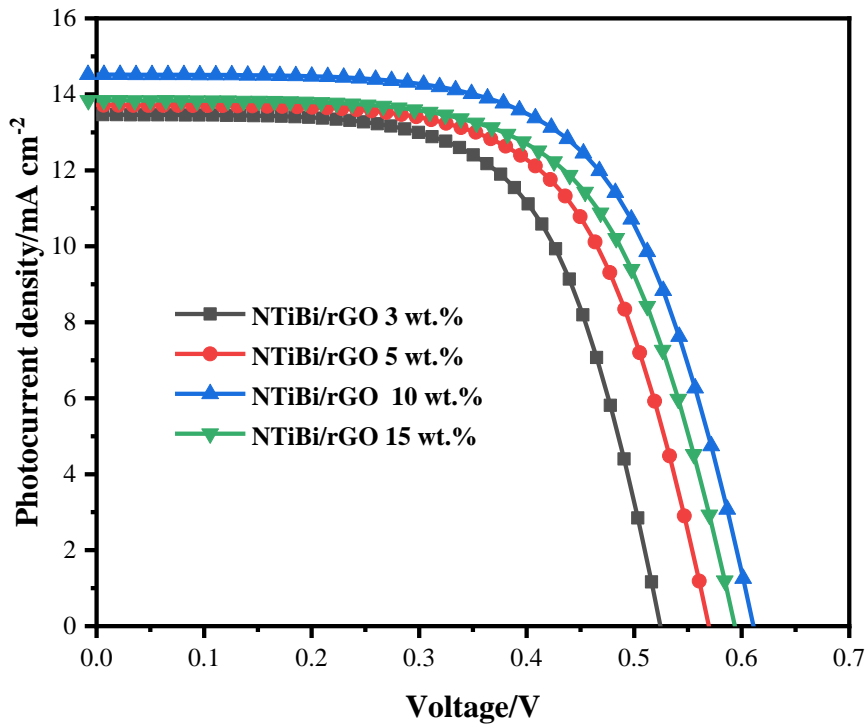
Figure 5.3: J–V curves of DSSCs with NTiBi/rGO-based photoanodes under illumination conditions

Table 5.2: Photovoltaic parameters of the DSSCs with different photoanode materials under illumination conditions

Material	Rsh/Ω cm^2	Rs/Ω cm^2	J_{sc}/mA cm^{-2}	V_{oc}/V	FF/%	PCE/%
TiO$_2$	1.35	0.00698	11.12	0.31	57.50	2.01
20 mol.% N-TiO$_2$	2.55	0.0054	13.08	0.42	60.05	3.29
NTiBi 3 wt.%	3.58	0.0045	13.83	0.48	63.58	4.26
NTiBi/rGO 3 wt.%	4.21	0.041	13.46	0.52	69.88	4.93
NTiBi/rGO 5 wt.%	4.58	0.0023	13.71	0.56	73.72	5.65
NTiBi/rGO 10 wt.%	6.25	0.0012	14.52	0.63	78.86	7.20
NTiBi/rGO 15 wt.%	3.85	0.0019	13.84	0.58	77.40	6.25

V_{oc}: open-circuit voltage, J_{sc}: short circuit current density, FF: fill factor, PCE: power conversion efficiency

On the other hand, the dark condition measurements were carried out, and the *J-V* curves are presented in Figure 5.4, with the corresponding photovoltaic parameters listed in Table 5.3. According to the results summarized in Table 5.3, it is clearly seen that the fabricated devices gave negligible values of FF and PCEs under dark illumination. However, the NTiBi/rGO (10 and 15 wt.% rGO)-based devices exhibited PCEs of 0.01048 and 0.01823%, respectively. These PCEs are very low when compared with those obtained under illuminated conditions (Table 5.2). Moreover, the high loading of rGO proved beneficial for a device to operate under dark conditions, since the NTiBi/rGO 15 wt.% device exhibited a relatively higher PCE than the NTiBi/rGO 10 wt.% device under darkness. This indicates that NTiBi/rGO devices can operate in cold weather, where there is less sunlight available, since these devices exhibited PCEs under dark conditions, where no light was available.
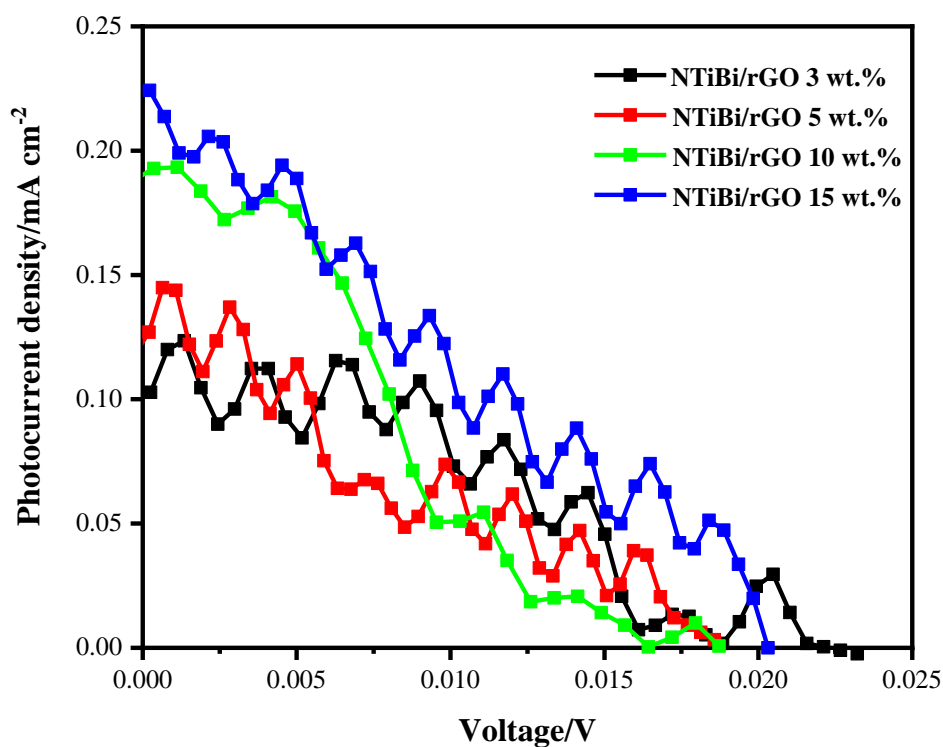
Figure 5.4: J–V curves of DSSCs with NTiBi/rGO-based photoanodes under dark conditions

Table 5.3: Photovoltaic parameters of DSSCs with different photoanode materials under dark conditions

Material	Rsh/Ω cm²	Rs/Ω cm²	Jsc/mA cm⁻²	Voc/V	FF/%	PCE/%
TiO₂	0.00065	68.42	0.0029	0.00254.	N/A	N/A
20 mol.% N-TiO₂	0.00060	64.55	0.0043	0.00980	N/A	N/A
NTiBi 3 wt.%	0.00085	63.5	0.0095	0.01253	N/A	N/A
NTiBi/rGO 3 wt.%	0.00064	48.58	0.1012	0.01981	N/A	N/A
NTiBi/rGO 5 wt.%	0.00056	48.25	0.1058	0.01983	N/A	N/A
NTiBi/rGO 10 wt.%	0.0024.	35.25	0.1988	0.01987	2.625	0.01048
NTiBi/rGO 15 wt.%	0.0018	28.56	0.2455	0.02155	3.256	0.01601

N/A means the device provided negligible values

5.3.3. Structure of DSSCs

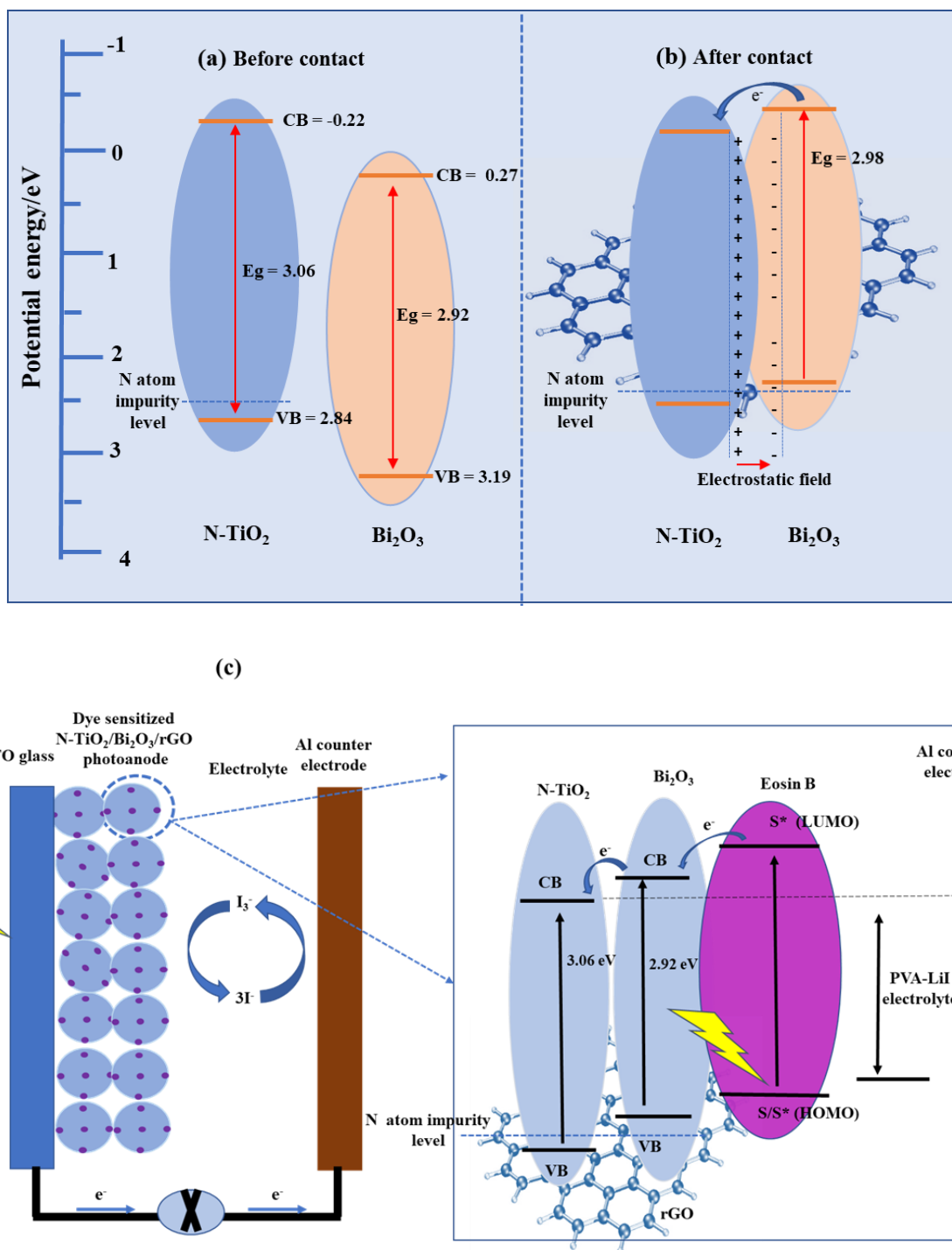On the basis of the above experimental results and discussion, a schematic diagram showing the band edge positions, electron–hole pair separation and transfer between the Bi_2O_3, N-TiO_2 heterojunction and rGO under light illumination: before contact and after formation of the heterojunction structure is presented in Figure 5.5 (a-b). The fabricated DSSC device is presented in Figure 5.5 (c), and consists of four key components, which are: NTiBi/rGO as semiconductor, Eosin B as sensitizer, PVA-doped with LiI as the electrolyte, and aluminium counter electrode. The band edge positions of a semiconductor at the point of zero charge were calculated by the following empirical equations 18 and 19.

$$E_{CB} = X - E^e - 0.5E_g \qquad\qquad\qquad\qquad\qquad (19)$$

$$E_{VB} = X - E^e + 0.5E_g \ldots\ldots\ldots\ldots\ldots\ldots\ldots\ldots\ldots\ldots\ldots\ldots\ldots\ldots(20)$$

where X is the absolute electronegativity of the semiconductor, E^e is the energy of free electrons on the hydrogen scale (about 4.5 eV); and E_g is the bandgap energy of the semiconductor. The X values for TiO_2 and Bi_2O_3 are ca. 5.81 and 6.23 eV, respectively. The experimental determined band-gap energy of N-TiO_2 is 3.06 eV, and of Bi_2O_3 is 2.92 eV.

Figure 5.5: Schematic diagram showing the band edge positions, electron–hole pair separation and transfer between the Bi_2O_3, N-TiO_2 heterojunction and rGO under light illumination: (a) before contact and (b) after formation of the heterojunction, (c) structure DSSC fabricated

5.4. Conclusion

A series of NTiBi/rGO (3, 5, 10 and 15 wt.%) nanocomposites was used to prepare different photoanodes *via* the Doctor Blade method, where Eosin B was employed as a dye for light absorption. These photoanodes with PVAc-doped with LiI gel electrolyte were assembled with an Al-coated counter electrode to fabricate the complete DSSCs. The NTiBi/rGO-based DSSCs exhibited PCEs of 4.93 - 7.20%, which were significantly greater than 4.26% for the pristine NTiBi-based DSSCs. The best optimal amount of rGO in NTiBi electrode was 10 wt.% of rGO, due to a higher PCE observed. Also, it was observed that excess amount rGO in NTiBi photoanodes can also absorb incoming light and act as recombination centre, negatively effecting the PCE of the DSSCs. The incorporation of rGO into the NTiBi photoanodes significantly enhances the PCE of DSSCs. On the other hand, the measurements carried out under dark conditions where there was no sunlight available, have demonstrated that these devices may operate in cold weather, upon high loading of rGO into the photoanodes.

References

1. M. Kokkonen, P. Talebi, J. Zhou, S. Asgari, S. A. Soomro, F. Elsehrawy, J. Halme, S. Ahmad, A. Hagfeldt and S. G. Hashmi, *Advanced research trends in dye-sensitized solar cells*, Journal of Materials Chemistry A, 2021, **9**, 10527-10545.

2. B. O'Regan and M. Gratzel, *A low-cost, high-efficiency solar cell based on dye-sensitized colloidal TiO$_2$ films*, Nature, 1991, **353**, 737-740.

3. N. Vlachopoulos, A. Hagfeldt, I. Benesperi, M. Freitag, G. Hashmi, G. Jia, R. A. Wahyuono, J. Plentz and B. Dietzek, *New approaches in component design for dye-sensitized solar cells*, Sustainable Energy & Fuels, 2021, **5**, 367-383.

4. N. Mariotti, M. Bonomo, L. Fagiolari, N. Barbero, C. Gerbaldi, F. Bella and C. Barolo, *Recent advances in eco-friendly and cost-effective materials towards sustainable dye-sensitized solar cells*, Green Chemistry, 2020, **22**, 7168-7218.

5. F. Babar, U. Mehmood, H. Asghar, M. H. Mehdi, A. U. H. Khan, H. Khalid, N. ul Huda and Z. Fatima, *Nanostructured photoanode materials and their deposition methods for efficient and economical third generation dye-sensitized solar cells: a comprehensive review*, Renewable and Sustainable Energy Reviews, 2020, **129**, 109919.

6. M. Z. H. Khan and X. Liu, *Role of nanostructured photoanode and counter electrode on efficiency enhancement of DSSCS*, Journal of Electronic Materials, 2019, **48**, 4148-4165.

7. H. Mohammadian-Sarcheshmeh, R. Arazi and M. Mazloum-Ardakani, *Application of bifunctional photoanode materials in DSSCs: a review*, Renewable and Sustainable Energy Reviews, 2020, **134**, 110249.

8. A. R. Lee and J.-Y. Kim, *Highly ordered TiO$_2$ nanotube electrodes for efficient quasi-solid-state dye-sensitized solar cells*, Energies, 2020, **13**, 6100.

9. S. Zainudin, H. Abdullah and M. Markom, *Electrochemical studies of tin oxide based-dye-sensitized solar cells (DSSC): a review*, Journal of Materials Science: Materials in Electronics, 2019, **30**, 5342-5356.

10. M. Ramya, T. Nideep, V. Nampoori and M. Kailasnath, *The impact of ZnO nanoparticle size on the performance of photoanodes in DSSC and QDSSC: a comparative study*, Journal of Materials Science: Materials in Electronics, 2021, **32**, 3167-3179.

11. A. Wibowo, M. A. Marsudi, M. I. Amal, M. B. Ananda, R. Stephanie, H. Ardy and L. J. Diguna, *ZnO nanostructured materials for emerging solar cell applications*, RSC Advances, 2020, **10**, 42838-42859.

12. Y. Bai, I. Mora-Sero, F. Angelis, J. Bisquert and P. Wang, *Titanium dioxide nanomaterials for photovoltaic applications*, Chemical Reviews, 2014, **114**, 10095-10130.

13. M. N. Islam and J. Podder, *The role of Al and Co co-doping on the band gap tuning of TiO_2 thin films for applications in photovoltaic and optoelectronic devices*, Materials Science in Semiconductor Processing, 2021, **121**, 105419.

14. R. S. Dubey, S. R. Jadkar and A. B. Bhorde, *Synthesis and characterization of various doped TiO_2 nanocrystals for dye-sensitized solar cells*, ACS Omega, 2021, **6**, 3470-3482.

15. R. Katal, S. Masudy-Panah, M. Tanhaei, M. H. D. A. Farahani and H. Jiangyong, *A review on the synthesis of the various types of anatase TiO_2 facets and their applications for photocatalysis*, Chemical Engineering Journal, 2020, **384**, 123384.

16. M. K. Hossain, A. Mortuza, S. Sen, M. Basher, M. Ashraf, S. Tayyaba, M. Mia and M. J. Uddin, *A comparative study on the influence of pure anatase and Degussa-P25 TiO_2 nanomaterials on the structural and optical properties of dye sensitized solar cell (DSSC) photoanode*, Optik, 2018, **171**, 507-516.

17. N. F. M. Sharif, M. Z. A. A. Kadir, S. Shafie, S. A. Rashid, W. Z. Wan Hasan and S. Shaban, *Charge transport and electron recombination suppression in dye-sensitized solar cells using graphene quantum dots*, Results in Physics, 2019, **13**, 102171.

18. A. Pallikkara and K. Ramakrishnan, *Efficient charge collection of photoanodes and light absorption of photosensitizers: a review*, International Journal of Energy Research, 2021, **45**, 1425-1448.

19. V. González-Verjan, B. Trujillo-Navarrete, R. M. Félix-Navarro, J. D. de Leon, J. Romo-Herrera, J. Calva-Yanez, J. Hernandez-Lizalde and E. Reynoso-Soto, *Effect of TiO_2 particle and pore size on DSSC efficiency*, Materials for Renewable and Sustainable Energy, 2020, **9**, 1-8.

20. L. Liu and X. Chen, *Titanium dioxide nanomaterials: self-structural modifications*, Chemical Reviews, 2014, **114**, 9890-9918.

21. L. Liu, Y. Zhang, B. Zhang and Y. Feng, *A detailed investigation on the performance of dye-sensitized solar cells based on reduced graphene oxide-doped TiO_2 photoanode*, Journal of Materials Science, 2017, **52**, 8070-8083.

22.   N. Kutlu, *Investigation of electrical values of low-efficiency dye-sensitized solar cells (DSSCs)*, Energy, 2020, **199**, 117222.

23.   A. Gholizadeh, A. Reyhani, P. Parvin and S. Z. Mortazavi, *Efficiency enhancement of ZnO nanostructure assisted Si solar cell based on fill factor enlargement and UV-blue spectral down-shifting*, Journal of Physics D Applied Physics, 2017, **50**, 11.

Chapter 6

Conclusion, recommendations and future work

This chapter presents the overall conclusion derived from the study conducted, and the recommendations and proposed future work based on the findings of this research.

6.1. Overall conclusion

The broad scope of this study was to develop a highly efficient photoanode for DSSCs based on NTiBi/rGO nanocomposites on account of their good charge carrier separation, high electron transportation, high surface area and good thermal stability. Experimental results discussed in Chapters 3, 4, and 5 show that the specific objectives of this study presented in Chapter 1 were successfully achieved. The novelty of the work is that NTiBi/rGO has been developed as photoanode material possessing simultaneously all the outstanding properties required for high performance in DSSCs. These include a high specific surface area, high crystallinity, good charge carrier separation and high electron transportation. Furthermore, the NTiBi/rGO nanocomposite has been found to possess a favourable conduction band position with Eosin B dye for a high open-circuit voltage, fill factor and efficiency. Interestingly, the major conclusions are:

A TiO_2-based nanocrystalline heterojunction with both N-doping and Bi_2O_3 coupling to form NTiBi was successfully prepared and thoroughly characterised. NTiBi was prepared *via* a hydrothermal method, whereas N-TiO_2 was initially prepared *via* a combined sol-gel and annealing treatment method. For these syntheses, only the 20 mol.% N-TiO_2 was used to couple with Bi_2O_3 due to the good occurrence of charge separation observed. From a series of NTiBi (1, 3 and 5 wt.% Bi_2O_3) nanocomposites prepared to contain different amounts of Bi_2O_3, only 5 wt.% of Bi_2O_3 exhibited enhanced charge carrier separation. It was concluded that N-TiO_2 coupled with Bi_2O_3 inhibits charge carrier recombination and widens the absorption band, since Bi_2O_3 is a visible light photocatalyst with a direct bandgap of 2.8 eV. Coupling N-TiO_2 with Bi_2O_3 not only widened the absorption band and inhibited the high recombination of photogenerated charge carriers, but also improved the thermal stability and surface area of the resulting composite material. The enhanced optical properties of NTiBi were attributed to the matched band potentials and the interconnected nanocrystalline heterojunction of NTiBi. The present work reports an important strategy to design and prepare high-performance TiO_2-based

photocatalysts that are active in the visible region of the electromagnetic spectrum and have good charge carrier separation and transportation.

Furthermore, the incorporation of rGO into a new class of heterojunction nanostructured material (NTiBi) was envisaged to be a promising strategy for further enhancing the optical activity, surface area and thermal stability of the materials. The NTiBi/rGO (3, 5, 10 and 15 wt.% rGO) nanocomposites were prepared *via* a hydrothermal method, and thoroughly characterized. Photoluminescence analyses revealed the good occurrence of charge carrier separation and electron transfer in the nanocomposites. Particularly good charge carrier separation was observed in the NTiBi/rGO 10 wt.% nanocomposite prepared, and it was concluded that an excess amount of rGO could lower the charge carrier separation. UV-Vis spectroscopy also revealed that incorporation of rGO into NTiBi nanoparticles significantly extended the light absorption capability of the resulting nanocomposites. The incorporation of rGO caused these enhanced optical properties of the NTiBi nanoparticles. Moreover, the incorporation of rGO into the NTiBi nanocomposites produced a significant increase in the surface area up to 116.39 $m^2\,g^{-1}$, and a good thermal stability up to 735 °C.

These NTiBi/rGO (3, 5, 10 and 15 wt.%) nanocomposites were used to prepare the different photoanodes via the Doctor Blade method, and were adopted to fabricate complete details DSSC devices with an aluminium counter electrode. The resulting photovoltaic performances were found to be significantly improved. The DSSC devices fabricated by making use of the nanocomposites (NTiBi/rGO) exhibited PCE values from 4.93 - 7.20%, which were significantly greater than 4.26% for the pristine NTiBi-based DSSC. The optimal amount of rGO into the NTiBi-based electrode was 10 wt.%, since it exhibited the largest PCE value of 7.20%. It was observed that excess rGO in the NTiBi photoanodes could absorb incoming light and act as a recombination centre, thus negatively affecting the PCE of the DSSCs. Thus, the incorporation of an optimal amount of rGO into the NTiBi photoanodes significantly enhances the PCE of DSSCs. On the other hand, the measurements carried out under dark conditions have demonstrated that these devices may operate in cold weather where there is less sunlight available, since these devices exhibited PCEs under dark conditions, where no light was available. However, this was observed with excess rGO in the NTiBi photoanodes, i.e., the NTiBi/rGO 15 wt.%-based DSSC. This NTiBi/rGO nanocomposite material has immense potential to be used for the design and preparation of highly efficient photoanodes for DSSCs.

6.2. Recommendations and future work

This study was found to be both interesting and challenging in some ways. It has shown great potential in fabricating NTiBi/rGO-based DSSC energy devices that can be utilized to generate electricity from solar energy efficiently. There is a good scope for this significant advancement. Hence, it will be fascinating to take this study further and possibly investigate the following areas:

Firstly, to study the effects of morphology on the NTiBi/rGO-based photoanode for DSSCs. Morphology has been reported as a critical aspect to be considered, and plays a pivotal role in electron transport, since surface defects can act as charge carrier traps influencing electron separation and transportation.

Secondly, the effect of various deposition techniques of nanocomposites onto ITO-coated glass, such as spin-coating, can improve our understanding of an ideal morphology on the device.

Thirdly, the effect of incorporating rGO into CdS/TiO_2 for DSSCs to enhance efficiencies, because cadmium sulfide has been reported in previous work to improve light-harvesting.

Fourthly, identify the type of N-doping type in the TiO_2 structure, that is, whether it is interstitial or substitutional by means of the XPS technique.

Other possible areas of investigation are the effect of dye interactions on the photoanode, such as the interaction of dye molecules with the photovoltaic semiconductor and the electrolyte. Also, to study the electron-hole recombination mechanism by means of PL decay and PL quantum efficiency (PLQE) measurements.

Appendices

Appendix A

Qualitative analysis
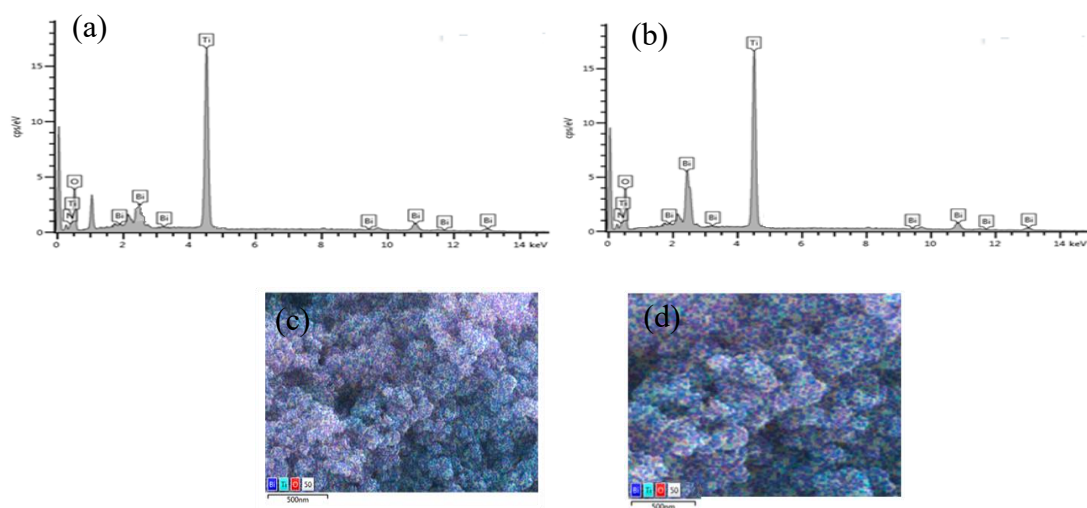
Figure A1: (a-b) EDX spectrum and (c-d) elemental mapping of the NTiBi 1 wt.% and NTiBi 5 wt.%, respectively
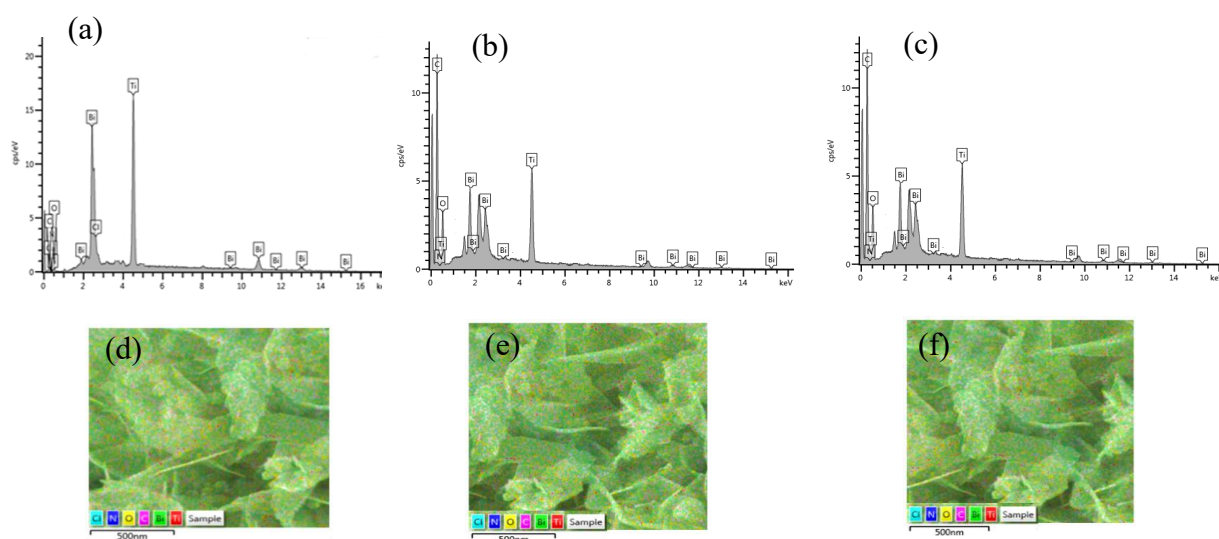
Figure A2: (a-c) EDX spectrum and (d-f) elemental mapping of the NTiBi/rGO 3 wt.%, NTiBi/rGO 5 wt.% and NTiBi/rGO 15 wt.%, respectively

Appendix B

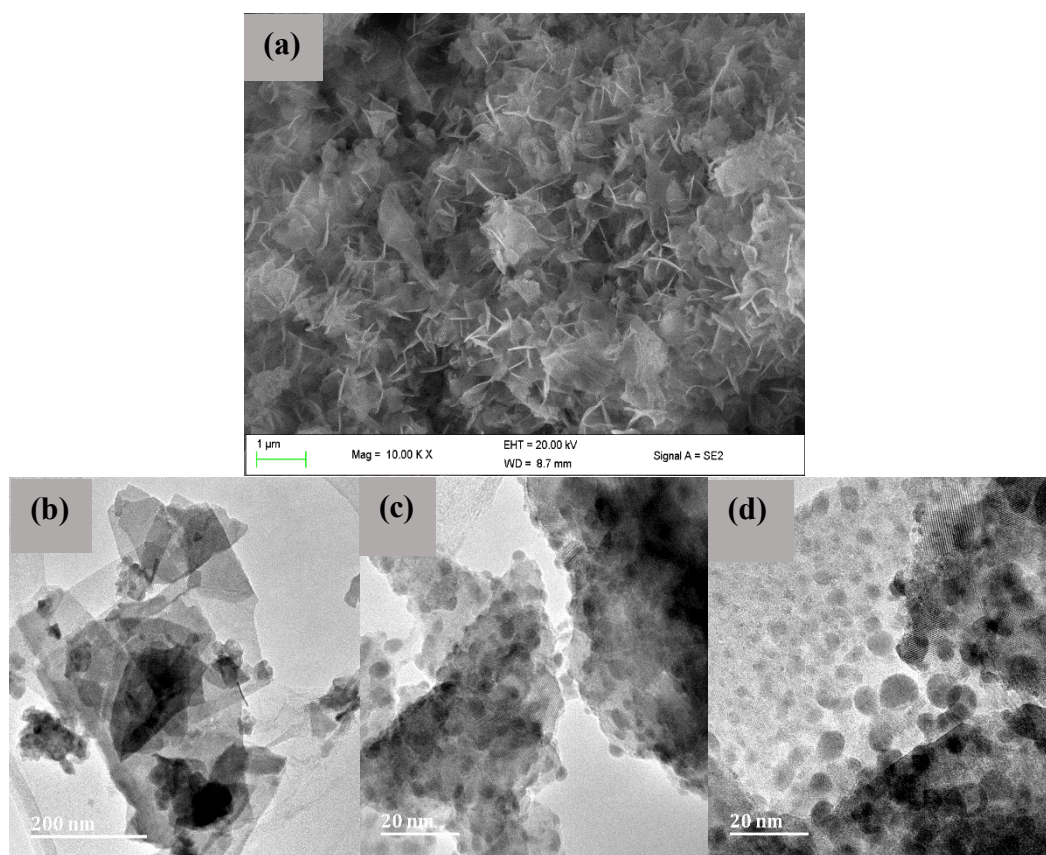## Surface morphology and microstructure analysis

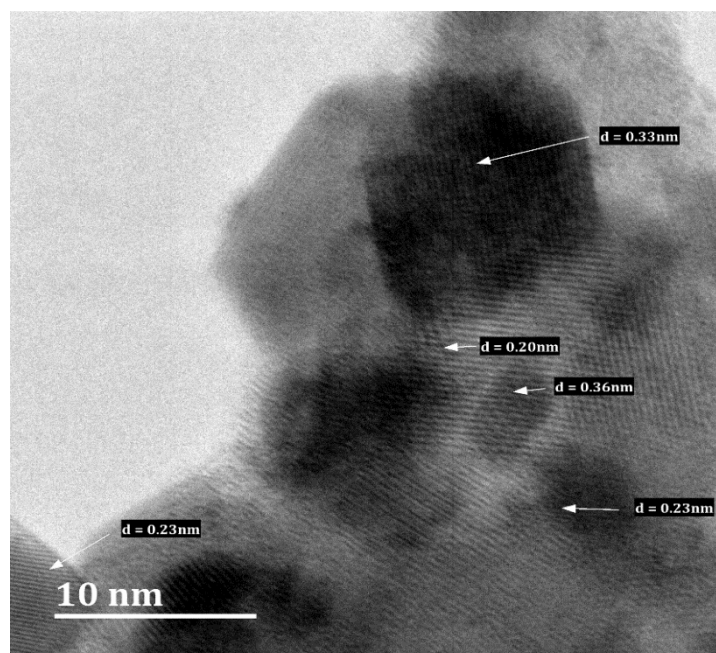**Figure B1**: The (a) SEM image of NTiBi/rGO 15 wt.%, (b-d) TEM images of NTiBi/rGO (3, 5 and 15 wt.% rGO, respectively

Figure B2: HRTEM image of NTiBi/rGO 15 wt.%

Appendix C

Surface area and pore size analysis
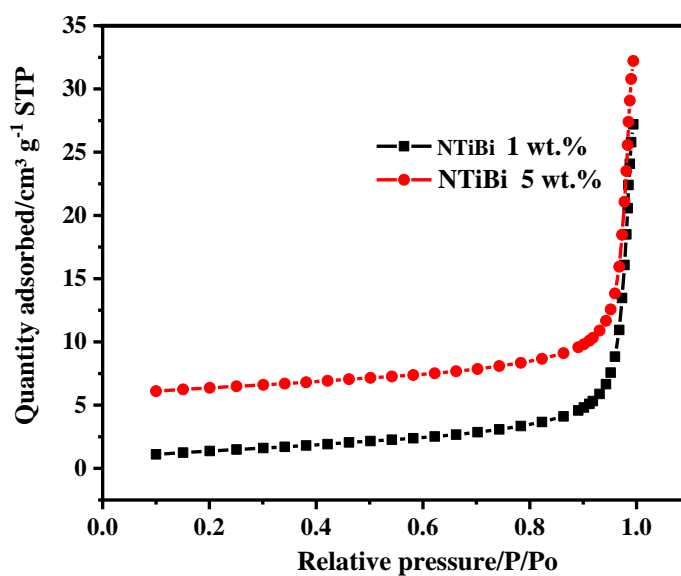
Figure C1: The N$_2$ absorption-desorption isotherm of 1 wt.% and 5 wt.% BiNTi, respectively
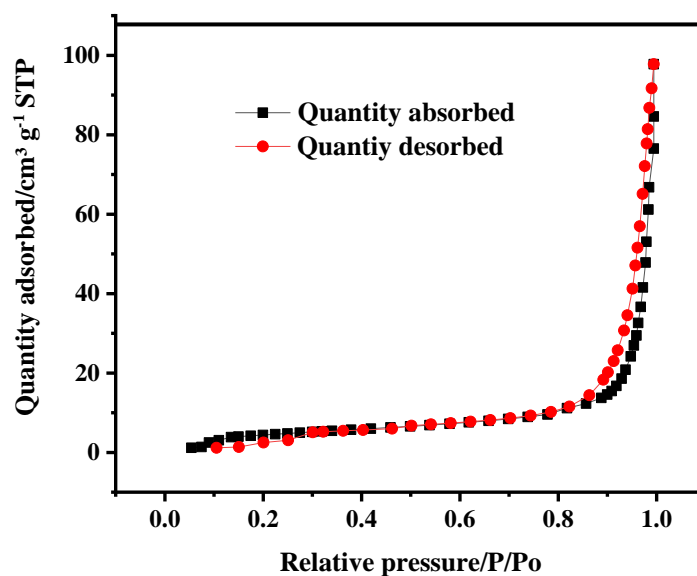
Figure C2: The N_2 absorption-desorption isotherm of NTiBi/rGO 3 wt.%
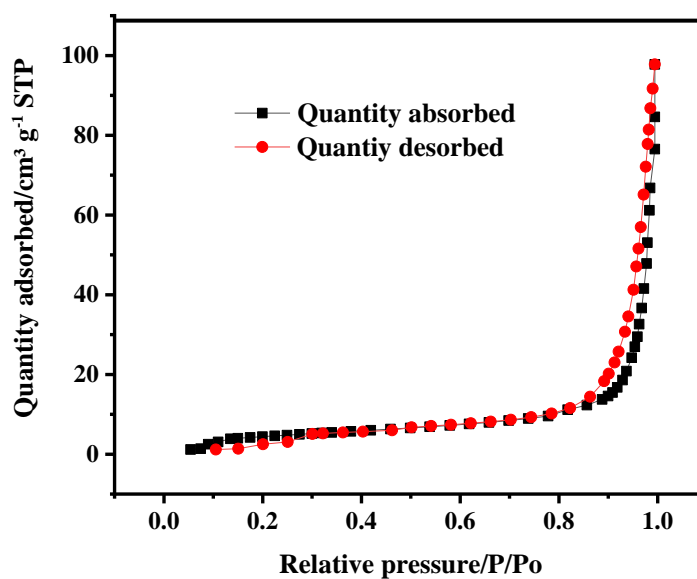
Figure C3: The N_2 absorption-desorption isotherm of NTiBi/rGO 5 wt.%
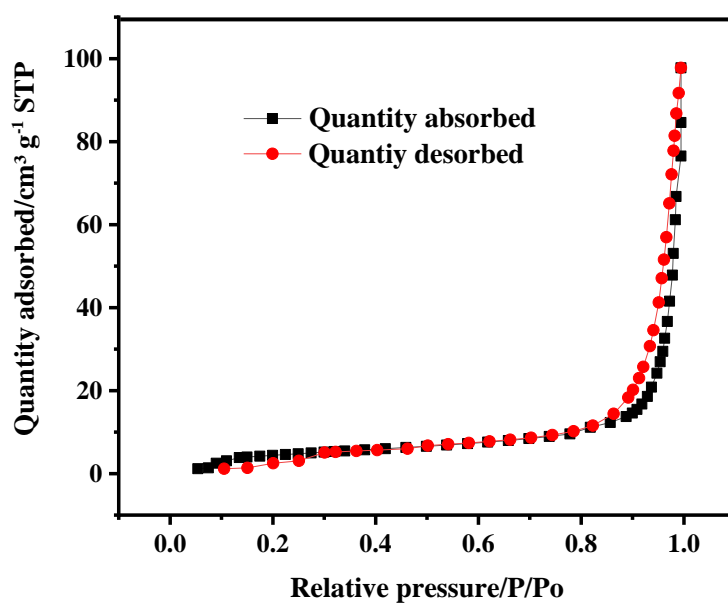
Figure C4: The N_2 absorption-desorption isotherm of NTiBi/rGO 15 wt.%
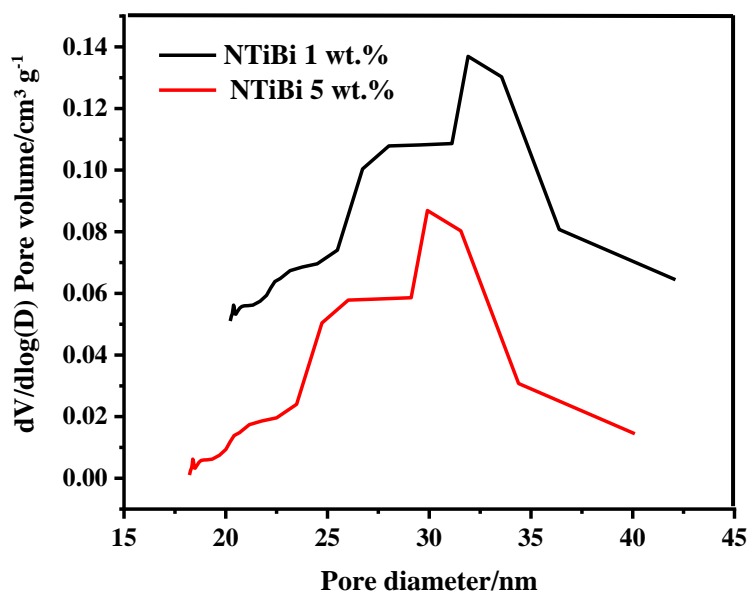
Figure C5: BJH pore size distribution curves of NTiBi (1 and 5 wt.% Bi_2O_3, respectively) nanoparticles
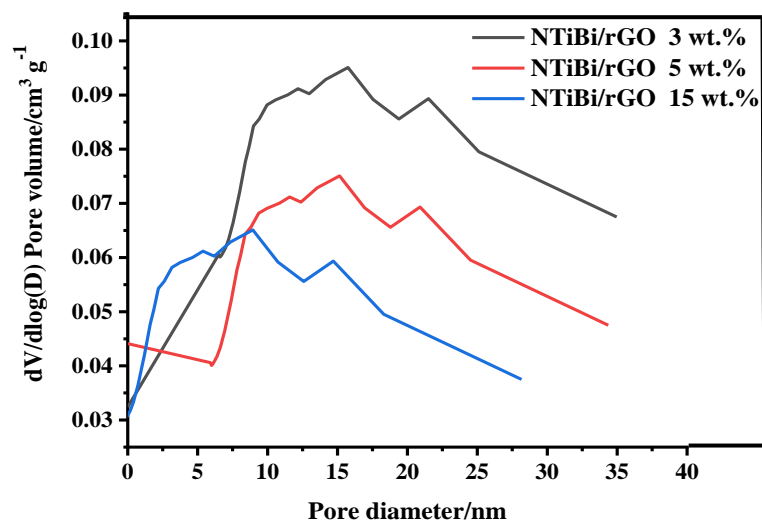
Figure C6: BJH pore size distribution curves of NTiBi/rGO (3, 5 and 15 wt.% rGO, respectively) nanocomposites

Appendix D

Thermal stability analysis
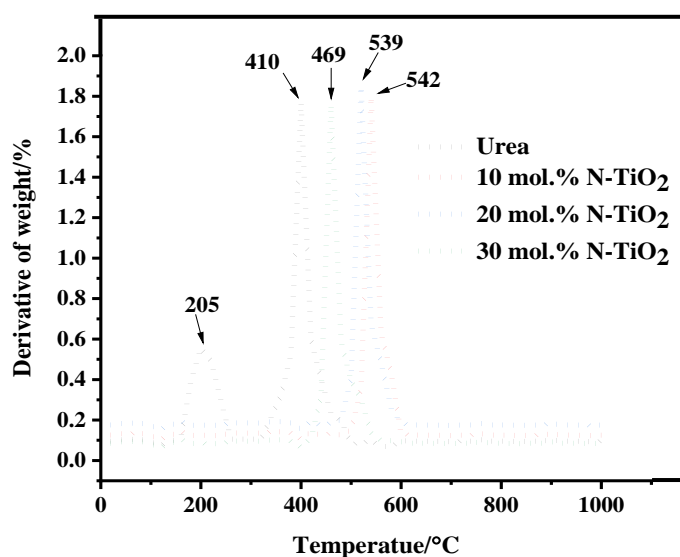
Figure D1: The first derivative curves of the change in weight percent against temperature for urea and N-TiO$_2$ (10, 20 and 30 mol.% N, respectively) nanoparticles
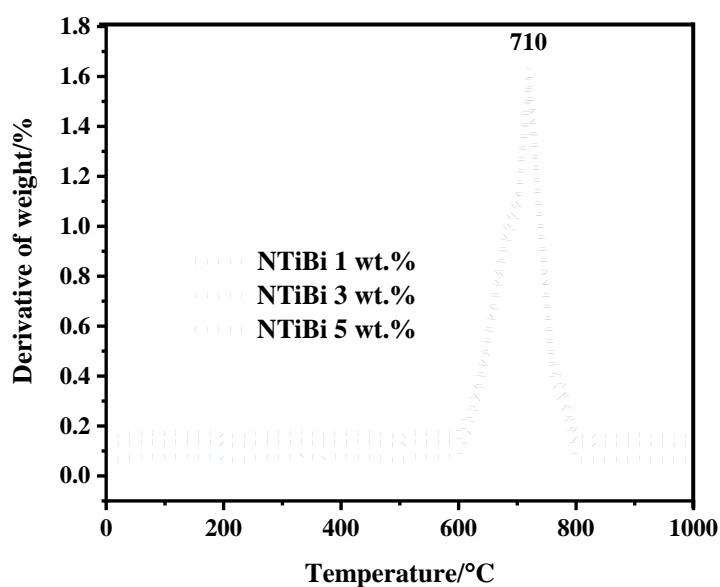
Figure D2: The first derivative curves of the change in weight percent against temperature for NTiBi (1, 3 and 5 wt.% Bi_2O_3, respectively) nanoparticles
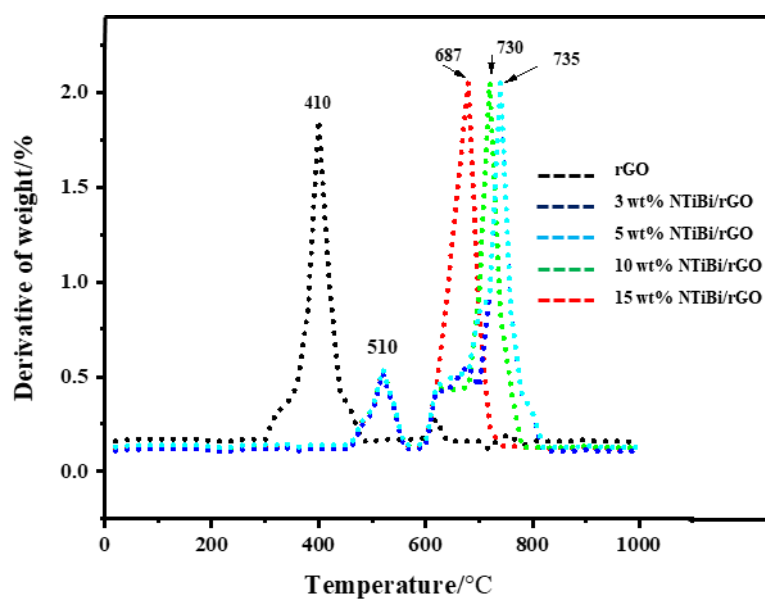

Figure D3: The first derivative curves of the change in weight percent against temperature for NTiBi/rGO (3, 5, 10 and 15 wt.% rGO, respectively) nanocomposites
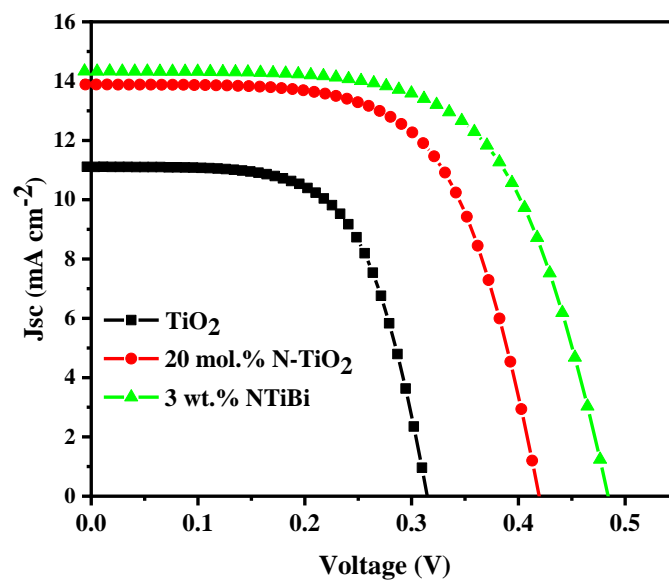
Appendix E

Photovoltaic performance analysis

Figure E1: Photocurrent density–voltage (J–V) curves of the DSSCs based on pure TiO_2, 20 mol.% $N\text{-}TiO_2$ and 3 wt.% NTiBi based photoanode under illuminated condition

Appendix F

Colour changes for N-TiO$_2$ with calcination

30 mol.% N-TiO$_2$
calcined
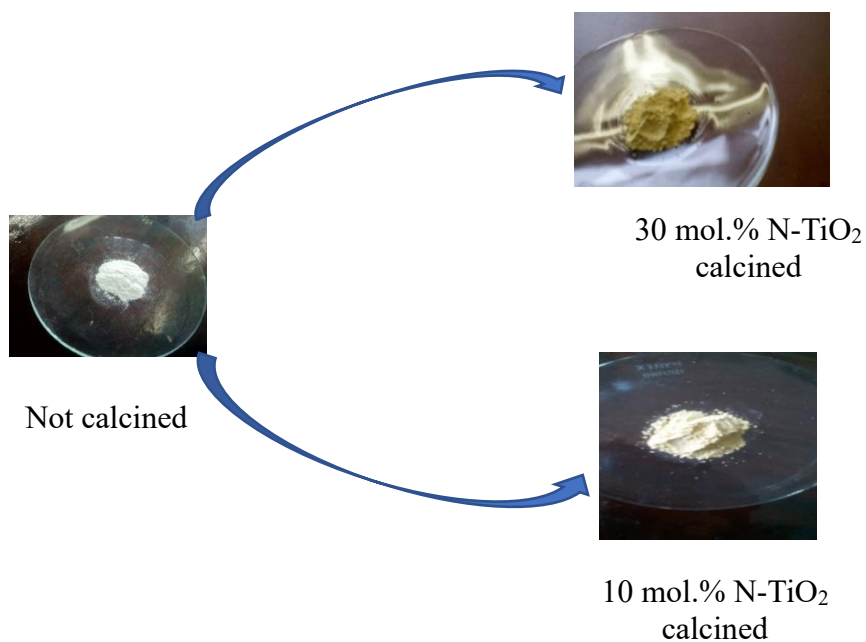
Not calcined

10 mol.% N-TiO$_2$
calcined

Figure F1: Images showing the colour of not calcined, calcined 10 mol.% and 30 mol.% N-TiO$_2$
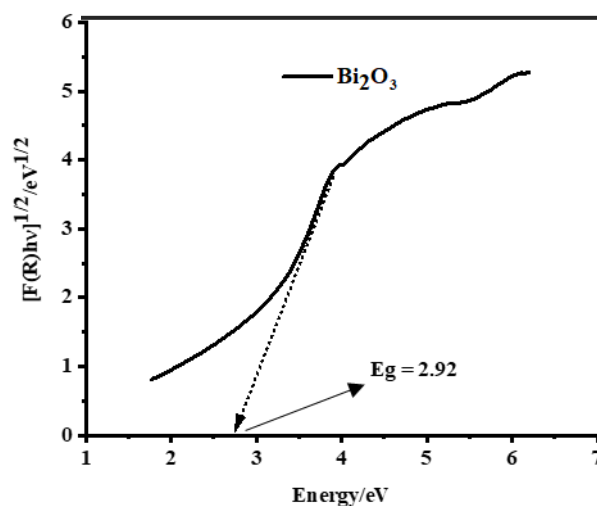
Appendix G
Diffuse reflectance spectroscopy

Figure G2: Kubelka Munk plot for Bi$_2$O$_3$